DISS. ETH NO. 26385

The Design of Experimentally Robust Pulse Sequences in Solid-State NMR

A thesis submitted to attain the degree of

Doctor of Sciences of ETH ZURICH

(Dr. sc. ETH Zurich)

presented by

Johannes Hellwagner

MSc ETH in Chemistry
born on July 26, 1991
Citizen of the Republic of Austria

accepted on the recommendation of
Prof. Dr. Matthias Ernst, examiner
Prof. Dr. Gunnar Jeschke, co-examiner

2019

THE MISTAKES OF THE FOOL ARE
KNOWN TO THE WORLD, BUT NOT
TO HIMSELF.
THE MISTAKES OF THE WISE MAN
ARE KNOWN TO HIMSELF, BUT NOT
TO THE WORLD.

Charles Caleb Colton

meiner Familie

Contents

Symbols and Abbreviations

$\delta_{i,j}$	Dipolar coupling between spin i and j
$\hat{\mathscr{H}}$	Hamilton operator
ϕ	Phase of rf pulse
T_2	Transverse relaxation time
τ_p	Time of rf pulse
τ_rise	Rise time of amplitude transient
ν_1	Nutation frequency
ω_eff	Effective field
ω_m	Modulation frequency
ω_r	Rotation frequency
ω_off	Electronic offset frequency of phase transient
AHT	Average Hamiltonian Theory
BCH	Baker-Campbell-Hausdorff
CM	Continuous phase Modulation
CP	Cross Polarization
CSA	Chemical-Shift Anisotropy
CW	Continuous Wave
DQ	Double Quantum
DUMBO	Decoupling Using Mind-Boggling Optimization
EM	Electron Microscopy
FID	Free Induction Decay
FSLG	Frequency-Switched Lee-Goldburg
FWHM	Full Width at Half Maximum
GAMMA	General Approach to Magnetic resonance Mathematical Analysis
LAB	Laboratory frame
MAS	Magic-Angle Spinning

MLF   Methionine-Leucine-Phenylalanine
MLS   Maximum-Length Sequence
NMR   Nuclear Magnetic Resonance
PAR   Proton-Assisted Recoupling
PAS   Principal-Axis System
PID   Proportional-Integral-Derivative
PMLG   Phase-Modulated Lee-Goldburg
POST   Permutationally Offset STabilized
ppm   parts-per-million
REDOR   Rotational Echo DOuble Resonance
RF   Radio Frequency
RFDR   Radio-Frequency Driven Recoupling
SNR   Signal-to-Noise Ratio
SPINAL   Small Phase INcremental ALternation
TROSY   Transverse Relaxation-Optimized SpectroscopY
TPPM   Two-Pulse Phase Modulation
XiX   X-inverse-X
ZQ   Zero Quantum

List of Chemicals

A list of all substances used for the work presented and their respective supplier or a quick description of the synthesis:

- **Phthalic acid-α,α-^{13}C$_2$:** purchased from Isotec
  Synthesis of di-ammonium phthalate: labelled phthalic acid was mixed with phthalic acid (natural abundance) in a ratio 1:7, an excess of aqueous ammonia was added, a white powder was obtained through lyophilization

- **N-formyl-U-[^{13}C-^{15}N]-Met-Leu-Phe-OH (MLF):** purchased from Giotto Biotech

- **1-^{13}C$_1$-^{15}N-glycine:** purchased from Cambridge Isotopes
  Labelled glycine was diluted in a ratio 1:9 with natural abundance glycine

- **1,2-^{13}C-^{15}N-glycine:** purchased from Sigma Aldrich
  Synthesis of **1,2-^{13}C-^{15}N-glycineethylester**: Ethanol and SOCl$_2$ were added to glycine for 2h under reflux conditions, the reaction mixture was rinsed with Toluol, subsequently the solvent was evaporated under vacuum yielding 1,2-^{13}C-^{15}N-glycineethylester as a white crystallite powder

- **2-^{13}C-^{15}N-glycine:** purchased from Sigma Aldrich
  Synthesis of **d8-2-^{13}C-^{15}N-glycineethylester**: d6-Ethanol (Sigma Aldrich) and SOCl$_2$ were added to 2-^{13}C-^{15}N-glycine for 2h under reflux conditions, the reaction mixture was rinsed with Toluol, subsequently the solvent was evaporated under vacuum yielding the glycineethylester derivate as a white crystallite powder

- **d5-2-^{13}C-^{15}N-glycineethylester:** d5-2-^{13}C-^{15}N-glycineethylester was synthesized from d8-2-^{13}C-^{15}N-glycineethylester by adding Methanol in an ultrasonic bath, subsequently the solvent was evaporated under vacuum yielding a white crystallite powder

Abstract

Solid-state NMR is a powerful tool for the study of the structural and dynamic proper-
ties of materials and biomolecules. The strength of solid-state NMR lies in the ability
to coherently manipulate the system Hamiltonian with the use of radio-frequency pulse
sequences and magic-angle spinning. This controlled perturbation is performed by in-
troducing multiple periodic time dependencies and allows for the measurement of the
correlation between nuclei and the identification of their local electronic environment.
In order to get reliable information and efficient experimental performance, the pulse
sequences need to be robust towards experimental uncertainties. Additionally, they
need to be highly specific to extract the desired interaction. In this thesis, a variety of
widely-used pulse sequences are examined with respect to pulse imperfections and pos-
sible approaches based on a theoretical understanding obtained by Floquet theory are
presented to tailor the pulse sequences in order to make them more reliably applicable.

In the first part of this thesis, the practical compensation of pulse imperfections is
studied and previously developed concepts are extended. A published theoretical model
of these imperfections, also known as pulse transients, is applied to physically measured
pulse shapes to find the origin of pulse imperfections in the spectrometer. Additionally,
small adjustments to the experimental setup are presented that ease the implementation
of pulse-transient compensation.
The second part of this thesis focuses on recoupling sequences, which are pulse sequences
designed to reintroduce the dipolar coupling, yielding important information about the
spatial proximity of two nuclei. One type of sequence, which includes Radio-Frequency
Driven Recoupling or Rotational Echo Double Resonance, uses an isolated π pulse as
a recoupling element. These sequences are widely used due the ease of experimental
implementation. Phase cycles are previously proposed modifications to stabilize these
sequences. In this thesis, these phase cycles are analysed using the concept of effective

Floquet Hamiltonians and numerical simulations to determine their robustness towards pulse imperfections. The advantages and disadvantages of various phase cycles are discussed and the experimental influence of pulse transients is understood using the theoretical concepts developed. A different kind of recoupling sequence uses symmetry-based pulse trains and is known as C or R sequence. A Floquet description of the recoupling sequence of interest, R26, shows inherent flaws in the design of the sequence that are also demonstrated experimentally. The influence of pulse transients is investigated and unexpected results are shown that are in stark contrast to the results found for RFDR and REDOR. A commonly used phase cycle shows great robustness towards any kind of experimental imperfection but calculations of the dipolar scaling coefficient show less recoupling efficiency than the basic sequence.

In the third part of this thesis, homo- and heteronuclear decoupling sequences are discussed. Decoupling sequences are designed to remove residual terms in the Hamiltonian that cause line broadening and thus these types of sequences are used to enhance spectral resolution. The homonuclear decoupling sequence frequency-switched Lee-Goldburg for proton-detected experiments is studied. Efficient decoupling is essential for proton detection because without it the lines are too broad to be distinguishable and do not yield reasonable information. This study focuses on the origin of performance degradation of the Lee-Goldburg sequence. Through the use of analytical calculations, numerical simulations, and experimental modifications, the residual line broadening is analysed. A concise conclusion of the origin of the performance degradation is presented for the first time, and it is understood why this sequence is still limited in its use. The heteronuclear decoupling sequence two-pulse phase modulation is investigated with respect to pulse transients. The requirement for the experimental use is a straightforward optimization and the implementation should be robust towards different conditions. Theoretical concepts to describe simple decoupling sequences with discrete phase modulations are presented and extended to understand the influence of pulse transients. The difference between continuous phase modulation and discrete phase jumps as well as a commonly-used phase cycle of the basic two-pulse sequence is investigated theoretically and experimentally.

In conclusion, this thesis generalises the concepts of pulse transients and the compensation, and draws conclusions on their influence on different kinds of pulse sequences. The removal of pulse imperfections allows the developed theoretical concepts to be validated

more accurately and inherent drawbacks of the pulse sequences are found experimentally. This results in suggested modifications and tailoring of the sequence to accommodate the experimental needs of more complex biological systems.

Zusammenfassung

Die Festkörper NMR ist eine leistungsfähige Methode zur Untersuchung von strukturellen und dynamischen Eigenschaften von Materialien und biologischen Molekülen. Die Stärke der Festkörper NMR liegt in der Fähigkeit den System-Hamiltonoperator durch die Anwendung von Radiofrequenz Pulssequenzen und Rotation um den magischen Winkel kohärent zu manipulieren. Diese kontrollierte Störung, welche zu mehrfachen Zeitabhängigkeiten führt, ermöglicht die Korrelationen zwischen Kernen zu messen und die elektronische Umgebung dieser Kerne zu bestimmen. Um verlässliche Informationen zu bekommen und effiziente experimentelle Reproduzierbarkeit zu erreichen, muss die Pulssequenz robust gegenüber experimentellen Unsicherheiten und Schwankungen sein sowie höchst spezifisch um die gewünschte Wechselwirkung zu bestimmen. In dieser Arbeit wird eine große Varietät von weitverbreiteten Pulssequenzen untersucht mit Hinblick auf Pulsimperfektionen und mögliche Herangehensweisen, basierend auf einer theoretischen Analyse mit Floquet Theorie, werden präsentiert um die Pulssequenzen zu verändern und sie somit verlässlicher zu machen.

In dem ersten Teil dieser Arbeit wird eine praktische Kompensation der Pulsimperfektionen untersucht und Konzepte erweitert, welche schon zuvor entwickelt wurden. Ein theoretisches Model dieser Imperfektionen, auch Pulstransienten genannt, welches in der Literatur vorgestellt wurde, wird auf experimentell gemessene Pulsformen angewandt um den Ursprung der Pulsimperfektionen im Spektrometer zu finden. Zusätzlich werden kleine Änderungen des experimentellen Setups diskutiert, welche zur einfacheren Implementierung der Pulstransienten-Kompensation führen können.

In dem zweiten Teil dieser Arbeit liegt der Fokus auf sogenannte Wiedereinkopplungssequenzen, welche Pussequenzen sind, die entwickelt wurden um die dipolare Kopplung selektiv wiedereinzukoppeln, und so Informationen über die räumliche Nähe von zwei Kernen zu liefern. Eine Art dieser Sequenzen, spezifisch 'Radio-Frequency Driven Re-

coupling' oder 'Rotational Echo Double Resonance', verwenden einen isolierten π Puls als Element, welches die Interaktion wiedereinkoppelt. Diese Sequenzen finden sehr weit verbreitete Anwendung, da die experimentelle Implementierung einfach ist. Zuvor vorgeschlagene Methoden und Veränderungen um diese Sequenzen robuster zu machen beinhalten Phasenzyklen. Diese Phasenzyklen werden theoretisch unter der Verwendung der Konzepte von effektiven Floquet Hamiltonoperatoren und numerischen Simulationen in Hinblick auf Robustheit gegenüber Pulsimperfektionen analysiert. Die Vor- und Nachteile von verschiedenen Phasenzyklen werden diskutiert und der experimentelle Einfluss von Pulstransienten ist mit Hilfe der entwickelten theoretischen Konzepte erklärbar.

Eine weitere Klasse von Wiedereinkopplungssequenzen verwendet auf Symmetrieargumenten basierende Pulsfolgen und sind bekannt als C- und R-Sequenzen. Eine Floquet Beschreibung der untersuchten Pulssequenz, R26, zeigt inhärente Fehler in dem Design der Sequenz, welche auch in Experimenten aufgezeigt werden. Der Einfluss von Pulsimperfektionen wird auch untersucht und unerwartete Resultate werden präsentiert, welche in direktem Kontrast zu den Ergebnissen von RFDR und REDOR stehen. Ein oft verwendeter Phasenzyklus zeigt hohe Robustheit in Hinblick auf jegliche experimentelle Imperfektion, jedoch zeigt die Berechnung des dipolaren Skalierungsfaktors, dass diese Implementierung theoretisch weniger effizient als die Basissequenz ist.

In dem dritten Teil dieser Arbeit werden homo- und heteronukleare Entkopplungssequenzen diskutiert. Entkopplungssequenzen sind entwickelt worden um residuale Terme des Hamiltonoperators zu entfernen, welche Linienverbreiterungen verursachen, und daher werden diese Art von Sequenzen zur Verbesserung der spektralen Auflösung verwendet. Die homonukleare Entkopplungssequenz 'frequency-switched Lee-Goldburg' für direkte Protonendetektion wird untersucht. Effiziente Entkopplung ist essentiell für Protonendetektion, da andererseits die Linien zu breit wären um sie separieren zu können. Die Analyse legt den Fokus auf den Ursprung der Leistungsverschlechterung der Lee-Goldburg Sequenz. Mit Hilfe von analytischen Berechnungen, numerischen Simulationen sowie experimentellen Modifikationen wird die verbleibende Linienverbreiterung analysiert. Eine präzise Zusammenfassung der verschiedenen Ursprünge der Verschlechterung wird zum ersten Mal diskutiert und es wird illustriert, wieso die praktische Applikation dieser Sequenz noch immer limitiert ist.

Die heteronukleare Entkopplungssequenz Zweipuls-Phasenmodulation wird untersucht mit Hinblick auf Pulstransienten. Die Optimierung dieser Art von Sequenzen muss simpel sein und die Implementierung robust gegenüber verschiedenen experimentellen Be-

dingungen. Theoretische Konzepte um einfache Entkopplungssequenzen zu beschreiben werden vorgestellt und erweitert um den Einfluss von Pulstransienten abschätzen zu können. Der Unterschied zwischen kontinuierlicher Phasenmodulation und diskreten Phasensprüngen wird theoretisch und experimentell untersucht sowie ein häufig gebrauchter Phasenzyklus der Zweipulssequenz.

Zusammenfassend versucht diese Arbeit die Konzepte von Pulstransienten und deren Kompensation zu verallgemeinern und Rückschlüsse auf den Einfluss auf verschiedene Arten von Pulssequenzen zu ziehen. Die Entfernung der Pulsimperfektionen erlaubt genauere und zuverlässige Validierung der entwickelten theoretischen Konzepte und ermöglicht die experimentelle Bestätigung von inhärenten Nachteilen der Pulssequenz. Dies führt zu möglichen Modifikationen und Veränderungen der Sequenzen um die experimentellen Anforderungen von komplexeren biologischen Systemen zu erfüllen.

1. Introduction

The quest for structure elucidation of material compounds and biomolecules is essential for understanding their properties and functions. In the last two decades, two techniques have been predominant for structure determination, namely X-ray diffraction [1] and liquid-state nuclear magnetic resonance (NMR) spectroscopy [2]. Very recently, cryo electron microscopy (EM) developed into a valuable technique for structure determination, and was rewarded with a Noble Prize in 2017 [3, 4]. However, despite the recent advances of these techniques, NMR, and especially solid-state NMR, is uniquely valuable for the study of dynamic processes in proteins. Solid-state NMR is particularly interesting for the study of neurodegenerative diseases that are related to protein aggregates or misfolding [5, 6]. It is especially powerful to study these effects due to its ability to determine short-range disorder, because chemical shifts yield information on local changes in the structure whereas the other analysis techniques yield mostly information on long-range ordering.

While very valuable, both X-ray diffraction and cryo-EM are limited by the sample preparation conditions needed to execute these techniques. X-ray diffraction requires single crystals for the structural studies. The crystal formation is especially challenging for larger proteins or molecular assemblies, which do not easily form such crystals. Amyloid fibrils and membrane proteins are prominent examples of structural motifs that are inaccessible by X-ray diffraction. On the other hand, cryo-EM is not limited by crystallisation, but can only yield sufficient resolution for studying such aggregates at cryogenic temperatures. These temperatures do not correspond to the natural environment of proteins and so all dynamic processes are halted. Nevertheless, it is claimed in the literature that the flash-freezing process traps the native state of the protein, and cryo-EM had recent success in determining a structural model for amyloid fibrils [7]. Liquid-state NMR is also limited in its use for large molecular assemblies and protein-protein complexes. Even if the biomolecules are soluble, a molecular weight higher than

approximately 40 kDa poses a challenge due to the increasingly long correlation time [8]. This correlation time induces an efficient transverse relaxation time, leading to significant loss of resolution in liquid-state NMR spectra. This problem can be circumvented by selectively labelling methyl-groups and performing Transverse Relaxation-Optimized Spectroscopy (TROSY) [9]. This yields highly specific structural information but requires specific labelling schemes.

Due to all of these drawbacks, solid-state NMR spectroscopy remains one of the predominant techniques for *de-novo* structure determination of large biomolecules and aggregates in atomic resolution [10–14]. A further advantage of solid-state NMR is the possibility of sedimented sample preparation, since micro-crystalline samples give good spectra but are not a necessity. Thus, most high-resolution spectra are obtained from sedimented samples since local ordering is all that is necessary for the NMR studies [15].

The most powerful approach for structure determination is, however, a hybrid approach in which two or more of the aforementioned methods are combined to determine high-resolution structures. The combination of X-ray diffraction or cryo-EM with NMR is of particular interest because NMR is a bottom-up approach in which the structure determination starts at the atomic level whereas X-ray diffraction or cryo-EM yield an overall structural model and improvement of the resolution can lead to elucidation of some detailed structure elements.

The versatility of solid-state NMR is based on the ability to manipulate the system Hamiltonian by radio-frequency (rf) irradiation and by mechanical rotation of the sample around an angle called the magic angle, i.e. magic-angle spinning (MAS) [16, 17]. These introduce a continuous time dependence and allow the removal of anisotropic interactions that usually cause very broad signals. Controlled interference of these two time dependences additionally allows the selective reintroduction of interactions of interest, such as the dipolar interaction, which contains information about internuclear distances, or the chemical-shift anisotropy (CSA), which contains information about local orientation. The controlled manipulation of the spin Hamiltonian by rf irradiation (continuous irradiation or discrete rf pulses) is referred to as a pulse sequence. Generally speaking, pulse sequences are classified into two types: *Decoupling sequences*, which aim to further remove anisotropic interactions in addition to magic-angle spinning to improve resolution and reduce spectral overlap, and *recoupling sequences*, which reintroduce a spin interaction of interest by interference with MAS in order to make it time

independent. A further classification is made based on the nuclei that are involved in the experiment. *Homonuclear* experiments refer to experiments that operate on the same type of spins while *heteronuclear* experiments involve two different types of nuclear spins.

The design and optimization of pulse sequences has always been of great interest for solid-state NMR method development. The ultimate goal is to make pulse sequences as experimentally robust and efficient as possible. This is crucial for multi-dimensional NMR experiments as they involve multiple recoupling and decoupling steps during which accumulated signal loss cannot be tolerated. Due to the complexity of the systems under study, experiments up to three-, four-, and sometimes even higher-dimensions are employed that require at least one magnetization transfer step per dimension. Efficient transfer through recoupling sequences reduces the experiment time drastically due to the enhanced signal-to-noise ratio.

Two theoretical concepts have proven to be useful tools for the design of pulse sequences, namely average Hamiltonian theory (AHT) [18, 19] and Floquet Theory [20–23]. The ability to calculate effective system Hamiltonians that govern spin dynamics allows for a better theoretical understanding of the underlying quantum mechanics. This understanding allows for further improvement of the robustness of pulse sequences. Pulse-sequence robustness ensures short experimental optimization time as well as a broad field of application for any given pulse sequence. A famous example of such an improvement is imposing certain symmetry constraints on pulse sequences by changing the phase of the applied rf pulses to remove error terms from the effective system Hamiltonian. This procedure is known as phase cycling and has been extensively described with AHT [24]. Further improvements to pulse sequences have been discovered utilizing a Floquet description of the system Hamiltonian, e.g. asynchronous implementation of sequences [25] or continuous phase modulations [26, 27].

Despite the theoretical analyses and improvements, many pulse sequences still suffer from performance degradation due to experimental imperfections. These imperfections can include rf-field inhomogeneity, pulse imperfections, an inhomogeneous static magnetic field, or sample inhomogeneity. The rf-field inhomogeneity is a problem inherent to the probe and is determined by the design of the solenoid coil that generates the rf field. Several studies of the rf-field inhomogeneity have been published and many have tried to overcome these inhomogeneities by e.g. the use of optimum-control approaches

in order to design robust sequences [28–30].

Further inhomogeneities over the sample volume are caused by an inhomogeneous static magnetic field B_0 which can be corrected by small locally induced fields from shimming coils with adjustable current. Apart from the imperfect shim of the probe, sample inhomogeneity is still a limiting factor for solid-state NMR and a lot of effort is put into sample preparation, especially for the expression of proteins and molecular assemblies [31].

The third experimental imperfection is pulse imperfections, also known as pulse transients [32, 33], and is the central topic of this thesis. Pulse imperfections in solid-state NMR arise from the spectrometer, which is an imperfect resonance circuit. Due to the finite rise time of the resonance circuit, the amplitude of the pulse builds up in an exponential fashion and not with infinitely steep edges as usually programmed. Additionally, an impedance mismatch in the circuit due to the many components can cause phase distortions and imperfect phases of the pulse.

In this thesis, a detailed analysis of pulse imperfections with regards to the experimental hardware of a solid-state NMR spectrometer and the impact on prominent pulse sequences will be presented. Chapter 3 focuses on a practical compensation of pulse transients that has been introduced in Ref [34] and an extension of previously developed compensation method. The theoretical model of pulse transients presented in the literature is applied to physically measured pulse shapes in order to find the source of pulse imperfections in the resonance circuit (the spectrometer). Additionally, small adjustments to the experimental setup are presented, improving the ease of implementation of pulse-transient compensation.

Chapters 4 to 7 are focused on the study of pulse sequences that are widely used in solid-state NMR. All presented sequences are analysed theoretically using Floquet theory and numerical simulations in order to understand the influence of imperfect pulses on the performance of the sequence. The removal of experimental errors by pulse-transient compensation allows additionally for the extraction of error terms that are inherent to the sequence and improved implementations for the sequence are suggested.

Chapter 4 focuses on homo- and heteronuclear recoupling sequences utilizing a single rotor-synchronized π pulse as the recoupling element. The two sequences, RFDR [35, 36] and REDOR [37, 38], respectively, are extensively studied in the literature. They are

especially important in distance determination of hetero- and homonuclear spin pairs, and their ease of experimental implementation makes them a widely used building block in standard experiments. Phase cycling is often applied to these sequences to make them more robust, and here the phase cycles are analysed in terms of their stability towards pulse imperfections using the concept of effective Floquet Hamiltonians and numerical simulations. The advantages and disadvantages of various phase cycles are discussed and the influence of pulse transients on RFDR and REDOR can be understood using the theoretical concepts developed.

Chapter 5 uses symmetry-based sequences known as C and R sequences as a recoupling element for homonuclear recoupling [39–41]. These types of sequences offer great flexibility in terms of application as they can serve either as decoupling or recoupling sequences. A Floquet description of the sequences examined in this chapter shows inherent flaws in the design of the sequence that are also demonstrated experimentally. The influence of pulse transients is investigated and surprising results are shown that are in stark contrast to the results found in Chapter 4. A phase cycle presented in the literature shows great robustness towards any kind of experimental imperfections, but calculation of the dipolar scaling coefficient shows a smaller recoupling efficiency than the basic sequence.

In Chapter 6, a very prominent sequence used for homonuclear decoupling is investigated: the frequency-switched Lee Goldburg (FSLG) [42] for the use of proton-detected spectra at low spinning speed. Conceptually, this sequence was developed 5 decades ago but still has not found broad experimental applications despite its possible potential. This work focuses on the root of the performance degradation of this sequence. Through the use of analytical calculations, numerical simulations, and experimental modifications the residual line broadening is analysed. A concise conclusion of the origin of the performance degradation is presented for the first time and it is understood why this sequence is still limited in use.

In Chapter 7, a basic sequence for heteronuclear spin decoupling is investigated. Heteronuclear decoupling sequences are an essential building block of every high-resolution solid-state NMR experiment, and have a detrimental influence on the spectral line shape and the signal-to-noise ratio (SNR). The optimization of these sequences must be straightforward and the implementation should be robust towards different conditions. Theoretical concepts to describe the simple two-pulse decoupling sequences with discrete phase modulations (TPPM [43]) presented previously are extended to understand the

influence of pulse transients. The difference between continuous phase modulation and discrete phase jumps as well as a commonly-used phase cycle of the basic two-pulse sequence [44] is investigated theoretically and experimentally.

2. Theoretical Background

2.1. Basic NMR Theory

Generally speaking, spin dynamics and certain NMR phenomena are described either classically or using a quantum-mechanical description. The approaches of the two theories are only equivalent for one-spin problems for which the classical approach uses Bloch equations. For multi-spin problems, the approaches are not equivalent and each offers advantages and disadvantages. The classical theory can be used to describe larger spin systems or phenomena like spin diffusion for which quantum mechanics is limited due to the size of the system [45]. Nevertheless, the classical theory that uses spin-temperature approaches and rate equations is unable to explain the echo phenomenon [46]. Therefore, it can be stated that classical theory is mainly used phenomenological and it is not exact. Quantum mechanics is used to describe the system under an exact Hamiltonian. This includes the treatment of the density operator, time-independent and time-dependent Hamiltonians, spin interactions, and many more. The advantage of quantum mechanics is the exact description of the system but is often limited by its complexity and high demand of computational power.

A brief introduction of the quantum mechanical approach is presented in the following since it is an important tool for the design and understanding of pulse sequences that is used throughout this work. Only nuclei with spin $I = {}^1\!/_2$ are treated in this work, and therefore, quadrupole interactions are not discussed further. This theoretical introduction is meant to give an overview and is not extensive. A more detailed and comprehensive treatment can be found in several NMR textbooks which are taken as a basis for the following relations [47–50].

The Density Operator

In principle, the state of an ensemble is described using the density-operator formalism. The state of a quantum system is defined by a wave function $|\Psi(t)\rangle$ which can always be written as a superposition of orthonormal basis functions $|\phi_i\rangle$

$$|\Psi(t)\rangle = \sum_i c_k(t)|\phi_i\rangle. \tag{2.1}$$

For a single $I = \frac{1}{2}$ spin, there are two basis functions $|\alpha\rangle$ and $|\beta\rangle$. They are the eigenfunctions of the Zeeman Hamiltonian and are often called 'spin-up' and 'spin-down' indicating a parallel or anti-parallel alignment of the z component of the spin-angular momentum with respect to the external B_0 field. This set of eigenfunctions is sensible since the Zeeman Hamiltonian is the dominant interaction in NMR.

However, state functions are rarely used in NMR since usually an ensemble of spins is considered. Therefore, the density operator represents a good choice for the description of the quantum system. It is defined as

$$\hat{\rho}(t) = \sum_{i,j} \overline{c_i(t)c_j(t)^*}|\phi_i\rangle\langle\phi_j| \tag{2.2}$$

with the expectation value of a certain operator $\hat{A}$ formulated as

$$\begin{aligned}
\langle\hat{A}\rangle(t) &= c_i(t)c_j(t)^*\langle\phi_j|\hat{A}|\phi_i\rangle \\
&= \langle\phi_i|\hat{\rho}(t)|\phi_j\rangle\langle\phi_j|\hat{A}|\phi_i\rangle \\
&= \langle\phi_i|\hat{\rho}(t)\hat{A}|\phi_i\rangle \\
&= \text{Tr}\{\hat{\rho}(t)\hat{A}\}.
\end{aligned} \tag{2.3}$$

Signal Intensity and Equilibrium Density Operator

The signal intensity in NMR is an important quantity since most experiments are signal-to-noise limited. The signal intensity is directly related to the equilibrium density opera-

tor $\hat{\rho}_0$ of a spin ensemble. Assuming the system is in thermal equilibrium, the occupancy probability is given by

$$\hat{\rho}_0 = \frac{\exp(-\hbar\hat{\mathscr{H}}_Z/k_B T)}{\mathrm{Tr}\{\exp(-\hbar\hat{\mathscr{H}}_Z/k_B T)\}} \tag{2.4}$$

$$\approx \frac{\hat{1}}{\mathrm{Tr}\{\hat{1}\}} - \frac{-\hbar\hat{\mathscr{H}}_Z}{k_B T \mathrm{Tr}\{\hat{1}\}} \tag{2.5}$$

$$\text{where} \quad \hat{\mathscr{H}}_Z = -\gamma \hat{I}_z B_0. \tag{2.6}$$

In order to obtain the second line in the equation above, the high-temperature approximation ($\hbar\gamma B_0 \ll k_B T$) is evoked. T is the spin temperature, k_B is the Boltzmann constant, and $\hat{\mathscr{H}}_Z$ the Zeeman Hamiltonian which is discussed in Chapter 2.2.1. The temperature is used often times to push the sensitivity as is moving to high-γ nuclei or even electrons. The amount of NMR signal, i.e. the sensitivity, is calculated as the population difference between the two states in the Zeeman Hamiltonian; spin-up ($(\hat{\rho}_0)_{11}$) and spin-down ($(\hat{\rho}_0)_{22}$). Calculation of the population difference for standard NMR conditions (B_0=20 T, T=303 K) leads to a value of $6.5 \cdot 10^{-5}$ of the spin ensemble which actually contributes to the effective NMR signal.

Time Evolution of the Density Operator

The time evolution of the density operator under an arbitrary Hamiltonian is given by the Liouville-von Neumann equation

$$\frac{d}{dt}\hat{\rho}(t) = -i\left[\hat{\mathscr{H}}, \hat{\rho}(t)\right]. \tag{2.7}$$

If the density operator commutes with the Hamiltonian at all times, the density operator does not evolve with time and it is stationary. Assuming a time-independent system Hamiltonian that does not commute with the density operator, the general solution is given by

$$\hat{\rho}(t) = \hat{U}(t)\hat{\rho}_0\hat{U}^{-1}(t) \tag{2.8}$$

with the term $U(t)$ being a so called propagator that has the functional form of

$$\hat{U}(t) = \exp\left(-i\hat{\mathscr{H}}t\right) \tag{2.9}$$

following the relation $\hat{U}^{-1}(t) = \hat{U}^{\dagger}(t)$ since it is a unitary operator due to the Hermitian property of the Hamiltonian.

The treatment of time-dependent Hamiltonians is presented in Chapter 2.5 in more detail since it is an integral part of this thesis.

2.2. Interactions in Solid-State NMR

The interactions in solid-state NMR can generally be divided into two groups. Firstly, the interactions of a nuclear spin with a magnetic field is considered and is expressed in the most general form as

$$\hat{\mathscr{H}}^{(i,B)} = \hat{\vec{I}}_i \underset{\sim}{A}^{(i,B)} \vec{B}. \tag{2.10}$$

Secondly, the interactions between two nuclear spins are considered which are given in the general form

$$\hat{\mathscr{H}}^{(i,j)} = \hat{\vec{I}}_i \underset{\sim}{A}^{(i,j)} \hat{\vec{I}}_j. \tag{2.11}$$

The strength and the spatial and angular dependency are in both cases described by the tensor $\underset{\sim}{A}$ which is a 3x3 matrix. The magnetic field vector is per definition aligned along the z axis and is hence reduced to $\vec{B} = (B_x, B_y, B_z) = (0, 0, B_0)$. The vector containing the spin operators is given by $\hat{\vec{I}} = (\hat{I}_x, \hat{I}_y, \hat{I}_z)$. For a spin with $I = 1/2$ these operators are represented by the Pauli matrices.

All Hamiltonians $\hat{\mathscr{H}}$ are given in angular frequency units throughout the whole thesis. All interactions and energy units are given in angular frequencies and are denoted by the symbol ω. Ordinary frequencies are specifically mentioned or labelled ν.

2.2.1. The Zeeman Hamiltonian

The Zeeman interaction is the most crucial for NMR since it is also the dominant one. It describes an interaction of an NMR-active spin with an external magnetic field B_0. This spin precesses around the external magnetic field clockwise or anti-clockwise depending

on the sign of the gyromagnetic ratio. The Zeeman Hamiltonian under a magnetic field along the z direction is defined as

$$\hat{\mathscr{H}}_Z^{(i)} = -\gamma_i \vec{B}_0 \cdot \hat{\vec{I}}_i = \omega_0^{(i)} \hat{I}_{iz} \tag{2.12}$$

where γ_i is the gyromagnetic ratio of spin i and ω_0 is the Larmor frequency. From a known Zeeman Hamiltonian, the population difference and hence the NMR signal intensity can be calculated according to the formalism outlined for the equilibrium density operator.

Considering a classical analogue of the Zeeman Hamiltonian is the torque experienced by a magnetic moment μ subjected to an external magnetic field. This torque aligns itself such that the potential energy $E = -\mu \cdot B_0$ is minimum.

2.2.2. The Chemical-Shift Hamiltonian

So far, only the interactions of a bare nucleus with the magnetic field have been described which is a case never encountered that would lead to indistinguishable signals for the same isotopes. Since the nucleus is surrounded by electrons, the local B_0 field is influenced. Consequently, currents are induced that produce a local magnetic field interacting with the nuclear spin. This local induced field $\vec{B}_{\text{ind}}$ depends on the charge distribution around the nucleus and can be non-uniform. In very good approximation, the induced field is directly proportional to the external magnetic field

$$\begin{aligned} \vec{B}_{\text{eff}} &= \vec{B}_0 + \vec{B}_{\text{ind}} \\ &= \vec{B}_0 + \underline{\sigma}\vec{B}_0 \end{aligned} \tag{2.13}$$

with $\underline{\sigma}$ being the chemical-shift tensor. Due to the possible non-uniform charge distribution, this interaction does not exhibit spherical symmetry and is therefore considered an anisotropic interaction. Using the chemical-shift tensor as the interaction of interest, the full chemical-shift Hamiltonian is written as

$$\hat{\mathscr{H}}_{\text{CS}}^{(i)} = -\gamma_i \cdot \underline{\sigma}^{(i)} \vec{B}_0 \cdot \hat{\vec{I}}_i. \tag{2.14}$$

Using the Cartesian coordinates the chemical-shift tensor is represented as a 3x3 matrix

$$\underline{\sigma} = \begin{pmatrix} \sigma_{xx} & \sigma_{xy} & \sigma_{xz} \\ \sigma_{yx} & \sigma_{yy} & \sigma_{yz} \\ \sigma_{zx} & \sigma_{zy} & \sigma_{zz} \end{pmatrix}. \tag{2.15}$$

As the external magnetic field is per convention aligned along the z axis, Equation 2.14 can be simplified using the definition in Equation 2.15 to

$$\hat{\mathscr{H}}_{\mathrm{CS}}^{(i)} = \omega_0^{(i)} \left(\sigma_{xz}^{(i)} \hat{I}_{ix} + \sigma_{yz}^{(i)} \hat{I}_{iy} + \sigma_{zz}^{(i)} \hat{I}_{iz} \right). \tag{2.16}$$

Since the magnitude of the chemical shift is much smaller (10^{-4} to 10^{-6} times) than the Zeeman Hamiltonian, it is convenient to go into a rotating frame around the z axis with the Larmor frequency ω_0. In the rotating frame, all terms proportional to $\hat{I}_x$ and $\hat{I}_y$ become time dependent and can be neglected; this is the high-field or secular approximation. Therefore, the chemical-shift Hamiltonian simplifies to

$$\hat{\mathscr{H}}_{\mathrm{CS}}^{(i)} = \omega_0^{(i)} \sigma_{zz}^{(i)} \hat{I}_{iz}. \tag{2.17}$$

The chemical-shift tensor can also be expressed in the principal-axis system (PAS) in which the off-diagonal elements vanish. Alternatively, the three principal components are defined by the isotropic chemical shift

$$\sigma_{\mathrm{iso}} = \frac{1}{3} \mathrm{Tr}\{\underline{\sigma}\} \tag{2.18}$$

the anisotropy of the tensor

$$\delta = \sigma_{zz} - \sigma_{\mathrm{iso}} \tag{2.19}$$

and its asymmetry

$$\eta = \frac{\sigma_{yy} - \sigma_{xx}}{\delta}. \tag{2.20}$$

The convention for the definition of the tensor elements follows $|\sigma_{zz} - \sigma_{\mathrm{iso}}| \geq |\sigma_{xx} - \sigma_{\mathrm{iso}}| \geq |\sigma_{yy} - \sigma_{\mathrm{iso}}|$.

The relation between the chemical-shift tensor in the laboratory frame and the PAS is given by three consecutive rotations: the Euler rotations. The Euler angles α and

β give the relative orientations; the third Euler angle γ does not play a role since the laboratory system is rotationally symmetric with respect to the z axis. The rotational matrices along the principal axes x, y, and z are given by

$$R_x = \begin{pmatrix} 1 & 0 & 0 \\ 0 & \cos\theta & -\sin\theta \\ 0 & \sin\theta & \cos\theta \end{pmatrix} \quad R_y = \begin{pmatrix} \cos\theta & 0 & \sin\theta \\ 0 & 1 & 0 \\ -\sin\theta & 0 & \cos\theta \end{pmatrix} \quad R_z = \begin{pmatrix} \cos\theta & -\sin\theta & 0 \\ \sin\theta & \cos\theta & 0 \\ 0 & 0 & 1 \end{pmatrix}$$
$$(2.21)$$

The net rotation matrix $\mathbf{R}(\alpha, \beta, \gamma)$ is constructed from three successive rotations defined as

$$\mathbf{R}(\alpha, \beta, \gamma) = R_{z''}(\gamma) R_{y'}(\beta) R_z(\alpha) \tag{2.22}$$

with the Cartesian tensor in the new coordinate system given by

$$\mathcal{A}^{(\text{new})} = \mathbf{R}(\alpha, \beta, \gamma) \mathcal{A}^{(\text{old})} \mathbf{R}^{-1}(\alpha, \beta, \gamma). \tag{2.23}$$

Note that this solution is not unique and follows the convention that the first rotation with angle α is around the z axis, the second rotation with β around the new y' axis, and the third rotation γ around the obtained z'' axis.

Following this procedure, the chemical-shift value at which a resonance frequency is observed can be expressed as

$$\omega_{\text{CS}} = \omega_0 \left[\sigma_{\text{iso}} + \frac{1}{2}\delta \left((3\cos^2\beta - 1) - \eta \sin^2\beta \cos 2\alpha \right) \right]. \tag{2.24}$$

Due to the sensitivity of the chemical shift and the electronic structure, measuring $\underset{\sim}{\sigma}$ allows the extraction of relative molecular orientations and torsion angles [51]. However, most solid-state NMR samples are not single crystals but randomly orientated powdered samples. Therefore, the static spectrum is given as the superposition of all different orientations which exhibit differing resonance frequencies depending on the Euler angles (Equation 2.24). This leads to characteristic powder patterns that depend on the parameters given in Equations 2.18-2.20. A characteristic powder pattern is shown in Figure 2.1A with differing asymmetry parameters.

2.2.3. The Dipolar-Coupling Hamiltonian

The dipolar-coupling Hamiltonian describes the interactions between two spins i and j. This interaction is analogous to the attraction or repulsion of two magnets in close proximity depending on the spatial orientation. As in the classical description, the strength of the dipole-dipole coupling depends on the distance, i.e. $\propto r_{i,j}^{-3}$. The corresponding Hamiltonian is a spin-spin interaction and can be written as

$$
\begin{aligned}
\hat{\mathscr{H}}_{\mathrm{D}} &= \hat{\vec{I}}_i \underset{\sim}{D}^{(i,j)} \hat{\vec{I}}_j \\
&= -\frac{\mu_0}{4\pi} \frac{\gamma_i \gamma_j \hbar}{r_{i,j}^3} \left(\frac{3(\hat{I}_i \cdot \vec{r}_{i,j})(\hat{I}_j \cdot \vec{r}_{i,j})}{r_{i,j}^2} \right)
\end{aligned}
\tag{2.25}
$$

with $\underset{\sim}{D}$ being a symmetric and traceless 3x3 matrix. The matrix form of this traceless dipolar tensor is given in the PAS by

$$
\underset{\sim}{D}^{(i,j)} = -2\frac{\mu_0}{4\pi} \frac{\gamma_i \gamma_j \hbar}{r_{i,j}^3} \begin{pmatrix} -\nicefrac{1}{2} & 0 & 0 \\ 0 & -\nicefrac{1}{2} & 0 \\ 0 & 0 & 1 \end{pmatrix}.
\tag{2.26}
$$
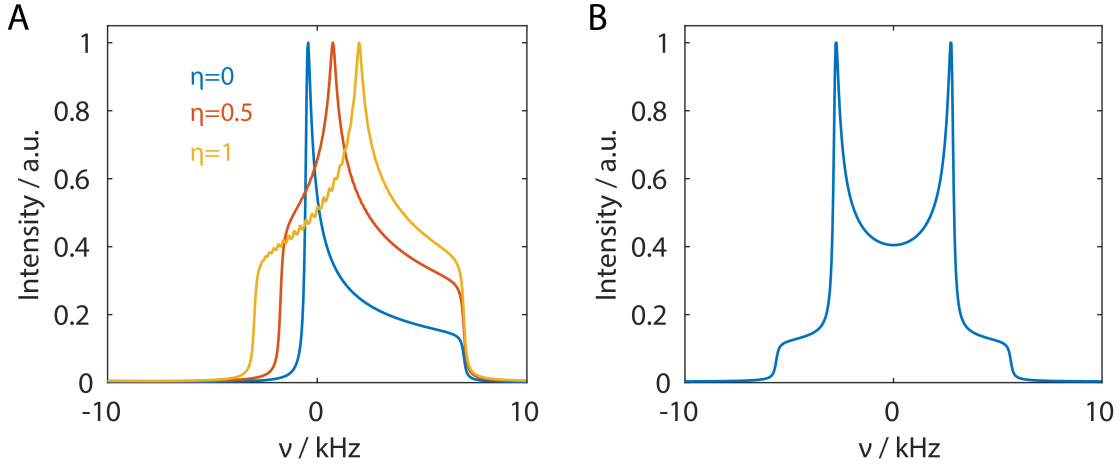
Figure 2.1. A) Representation of a characteristic CSA powder pattern observed in solid-state NMR with varying asymmetry parameter. The isotropic chemical-shift value was set to 2 kHz with an anisotropy of 5 kHz. B) The resulting spectrum of purely dipolar coupled spins assuming a homonuclear coupling with dipolar coupling of -7.5 kHz. The splitting of the Pake pattern is equal to $\frac{3}{4}\delta_{i,j}$ for the homonuclear case and $\frac{1}{2}\delta_{i,j}$ for a heteronuclear spin pair.

The factor with which the matrix is scaled is defined as the anisotropy of the dipolar coupling $\delta_{i,j}$. Often times it is convenient to expand the dipolar Hamiltonian in the so-called dipolar alphabet

$$\hat{\mathscr{H}}_{\mathrm{D}} = \frac{\delta_{i,j}}{2} \left[A + B + C + D + E + F \right] \tag{2.27}$$

with the individual terms defined as

$$
\begin{aligned}
A &= 2\hat{I}_{iz}\hat{I}_{jz}\frac{(3\cos^2\beta - 1)}{2} \\
B &= -\frac{1}{2}\left[\hat{I}_i^+\hat{I}_j^- + \hat{I}_i^-\hat{I}_j^+\right]\frac{(3\cos^2\beta - 1)}{2} \\
C &= \left[\hat{I}_{iz}\hat{I}_j^+ + \hat{I}_i^+\hat{I}_{jz}\right]\frac{3}{2}\sin\beta\cos\beta e^{-i\gamma} \\
D &= \left[\hat{I}_{iz}\hat{I}_j^- + \hat{I}_i^-\hat{I}_{jz}\right]\frac{3}{2}\sin\beta\cos\beta e^{+i\gamma} \\
E &= \frac{1}{2}\left[\hat{I}_i^+\hat{I}_j^+\right]\frac{3}{2}\sin^2\beta e^{-2i\gamma} \\
F &= \frac{1}{2}\left[\hat{I}_i^-\hat{I}_j^-\right]\frac{3}{2}\sin^2\beta e^{-2i\gamma}.
\end{aligned}
\tag{2.28}
$$

The angles β and γ define the orientation of the internuclear vector $\vec{r}_{i,j}$ with respect to the external magnetic field. In the secular approximation, a rotating coordinate system is assumed resulting in time dependency for terms that contain the factor $e^{in\gamma}$. This is due to the rotation around the z axis. Hence, A and B are the only terms to remain time invariant under such a transformation. This leads to a simplified dipolar Hamiltonian assuming two homonuclear spins

$$\hat{\mathscr{H}}_{\mathrm{D}}^{(\mathrm{homo})} = \frac{\delta_{i,j}}{2}\frac{(3\cos^2\beta - 1)}{2}\left(2\hat{I}_{iz}\hat{I}_{jz} - \frac{1}{2}\left(\hat{I}_i^+\hat{I}_j^- + \hat{I}_i^-\hat{I}_j^+\right)\right). \tag{2.29}$$

with β being the angle between the static B_0 field and the internuclear vector.
Assuming a heteronuclear-dipolar coupled spin pair, i.e. $\gamma_i \neq \gamma_j$, the Hamiltonian is transformed in a double rotating frame ($\hat{I}_z$ rotates with $\omega_{0,I}$ and $\hat{S}_z$ with $\omega_{0,S}$). This leads to a time dependence of the spin part in term B, also often referred to as the

flip-flop term. This term is additionally neglected in the high-field approximation and the heteronuclear dipole-dipole Hamiltonian simplifies further to

$$\hat{\mathcal{H}}_{\mathrm{D}}^{(\mathrm{het})} = \frac{\delta_{i,j}}{2} \frac{(3\cos^2\beta - 1)}{2} \left(2\hat{I}_{iz}\hat{S}_{jz}\right). \tag{2.30}$$

The spatial dependence of the dipolar Hamiltonian shows a zero crossing at the specific angle $\beta = 54.74°$. This angle has special relevance as it is known as the magic angle at which the dipolar-coupling contribution is non-existent in the full system Hamiltonian. This property is of utmost important for magic-angle spinning (MAS) experiments which are discussed in detail in Chapter 2.4.2.

In a static case, a characteristic pattern is observed which is termed Pake pattern. This contains the superposition of two symmetric powder patterns and is shown in Figure 2.1B.

2.2.4. The Scalar *J*-Coupling Hamiltonian

The J-coupling interaction belongs to the group of spin-spin couplings. The strength of the interaction is related to the probability to find the electron at the position of the nucleus. This is known as a Fermi contact interaction. The Hamiltonian is given in the most general form with the tensor $\underset{\sim}{J}^{(i,j)}$

$$\hat{\mathcal{H}}_{\mathrm{J}} = 2\pi \hat{\vec{I}}_i \underset{\sim}{J}^{(i,j)} \hat{\vec{I}}_j. \tag{2.31}$$

The matrix $\underset{\sim}{J}^{(i,j)}$ contains anisotropic contributions and is therefore a tensor. However, since the anisotropic contributions to the J-coupling are experimentally indistinguishable from the dipolar-coupling tensors, these contributions are conveniently included into the dipolar-coupling Hamiltonian.

Therefore, for light nuclei in which the anisotropy is small to begin with, the Hamiltonian is reduced to an isotropic interaction given by

$$\hat{\mathcal{H}}_{\mathrm{J}} = 2\pi J^{(i,j)} \hat{\vec{I}}_i \cdot \hat{\vec{I}}_j \tag{2.32}$$

with $J^{(i,j)}$ being a scalar quantity.

In full analogy to the dipolar-coupling Hamiltonian, a distinction between homo- and heteronuclear couplings is made using the secular approximation neglecting all transverse

terms due to their time dependency. For homonuclear couplings, the scalar product in Equation 2.32 remains unaffected and is expressed as

$$\hat{\mathscr{H}}_{\mathrm{J}}^{(\mathrm{homo})} = 2\pi J^{(i,j)} \hat{\vec{I}}_i \cdot \hat{\vec{I}}_j \tag{2.33}$$

and for the heteronuclear case

$$\hat{\mathscr{H}}_{\mathrm{J}}^{(\mathrm{het})} = 2\pi J^{(i,j)} \hat{I}_{iz} \hat{S}_{jz}. \tag{2.34}$$

2.2.5. The Radio-Frequency Hamiltonian

In principle, spin magnetization can be manipulated by the use of external rf pulses. The frequency of these pulses matches the Larmor frequency. The B_1 field, that is time dependent, is generated by a single coil as a linearly-polarized electromagnetic wave. The rf fields are applied perpendicular to the external magnetic field. This orthogonal direction is per convention defined to be the x axis and the B_1-field vector is given by

$$\vec{B}_1(t) = (B_{1x}(t), 0, 0). \tag{2.35}$$

Due to the linearity of the oscillation of the field, the time dependence is described by a cosine term and in principle, the amplitude and the phase can have an explicit time dependence. Therefore, the time-dependent rf field is given by

$$B_{1x}(t) = 2B_1(t) \cos\left(\omega_{\mathrm{rf}} t + \varphi(t)\right) \tag{2.36}$$

with $B_1(t)$ as the amplitude, $\varphi(t)$ the phase, and ω_{rf} as the frequency of the pulse known as the carrier frequency. The time dependency of the amplitude and the phase is on a much slower time scale than the carrier frequency.

Considering the manipulation of the spins by the rf field as a spin-field interaction, the rf Hamiltonian can be written as

$$\begin{aligned}
\hat{\mathscr{H}}_{\mathrm{rf}} &= \hat{\vec{I}}_i \cdot (-\gamma_i) \cdot \vec{B}_1(t) \\
&= -2\gamma_i B_1(t) \cos\left(\omega_{\mathrm{rf}} t + \varphi(t)\right) \hat{I}_{ix}.
\end{aligned} \tag{2.37}$$

After transformation into a rotating frame rotating around the z axis with the carrier frequency, the Hamiltonian is given by

$$\hat{\mathscr{H}}_{\mathrm{rf}} = -\gamma_i B_1(t) \left(\hat{I}_{ix} \cos\left(\varphi(t)\right) + \hat{I}_{iy} \sin\left(\varphi(t)\right) \right). \tag{2.38}$$

The amplitude $-\gamma_i B(t)$ is given in terms of resulting nutation frequencies $\omega_1(t)$. This rotating-frame transformation removes the Zeeman term from the total Hamiltonian if the carrier frequency matches the Larmor frequency, i.e. $\omega_{\mathrm{rf}} = \omega_0$. If the irradiation is not on-resonant, an additional term $\Omega \hat{I}_{iz}$ is added with Ω being the difference between the carrier and the Larmor frequency. This term is called an offset and offset effects are an important parameter to consider for a lot of experiments. Additionally, terms that oscillate with twice the carrier frequency $2\omega_{\mathrm{rf}}$ are neglected in the rotating-frame rf Hamiltonian. These terms can give rise to a shift of the resonance line which is known as the Bloch-Siegert shift [52]. This contribution is usually small and not important and therefore its neglect is a valid approximation for NMR experiments in this thesis.

2.3. Spherical-Tensor Notation

For now, all tensor components have been defined in the Cartesian coordinate system. However, certain interactions have been classified according to isotropic and anisotropic contributions and the properties under rotation have been mentioned. Adapting a concerted rotation symmetry for the spin and/or spatial part of the Hamiltonian simplifies the theoretical description by a great deal and rotations are readily calculated. The symmetry-adapted basis chosen for NMR interactions possesses the symmetry group $SO(3)$. Using irreducible spherical-tensor notation, the Hamiltonian can be written as a sum over all interactions i, the rank of the tensor ℓ, and sub components q [53]. The spatial and spin part ($A_{\ell,q}^{(i)}$ and $\hat{\mathscr{T}}_{\ell,q}^{(i)}$, respectively) can be manipulated independently and are combined as a product to form the total Hamiltonian

$$\hat{\mathscr{H}} = \sum_i \sum_{\ell=0}^{2} \sum_{q=-\ell}^{\ell} (-1)^q A_{\ell,q}^{(i)} \hat{\mathscr{T}}_{\ell,-q}^{(i)}. \tag{2.39}$$

A list of the spherical spin tensors can be found in Appendix A.
The rotation of spherical tensors is computed readily by the use of the Wigner rotation

matrix $\mathscr{D}^\ell$. The rotation is treated according to the symmetries of the spherical-tensor components and the advantage is that the ranks do not mix during rotation. The description is equivalent to the use of Euler rotation matrices. Using the three Euler angles, the rotations are given by

$$
\begin{aligned}
\mathscr{T}_{\ell,q}^{(\text{new})} &= \sum_{q'=-\ell}^{+\ell} \mathscr{D}_{q',q}^\ell(\alpha,\beta,\gamma)\mathscr{T}_{\ell,q'}^{(\text{old})} \\
&= \sum_{q'=-\ell}^{+\ell} e^{-i\alpha q'} d_{q',q}^\ell(\beta) e^{-i\gamma q}\mathscr{T}_{\ell,q'}^{(\text{old})}.
\end{aligned}
\tag{2.40}
$$

$d_{q',q}^\ell(\beta)$ are the reduced Wigner rotation elements and are tabulated functions that can be looked up.

2.4. Time-Dependent Hamiltonians

2.4.1. Introduction

A time-independent Hamiltonian $\hat{\mathscr{H}}$ can be analysed analytically and the dynamics of the spin operators fully understood. However, the analytical analysis of a Hamiltonian that is time dependent, $\hat{\mathscr{H}}(t)$, is non-trivial. A conceptually simpler approach is a numerical simulation of the system with a Hamiltonian that is assumed to be time independent over a short time and calculating the propagation of the density operator with this time-independent Hamiltonian. This concept of time slicing is introduced in more detail later in this Chapter for the interaction-frame transformation.

A time dependency is generally introduced if the system is perturbed in a continuous manner, e.g. by rf irradiation or physical spinning of the sample in a magic-angle spinning experiment. The induced time dependence by the external perturbations is indicated on the system Hamiltonian

$$
\hat{\mathscr{H}}(t) = \sum_i \sum_{\ell=0}^2 \sum_{q=-\ell}^\ell (-1)^q \underbrace{A_{\ell,q}^{(i)}(t)}_{\text{MAS}} \underbrace{\hat{\mathscr{T}}_{\ell,-q}^{(i)}(t)}_{\text{rf irradiation}}.
\tag{2.41}
$$

A change in the system Hamiltonian with respect to time leads to a temporal changes of the eigenvalues and in some cases to the system's eigenfunctions. The analytical solu-
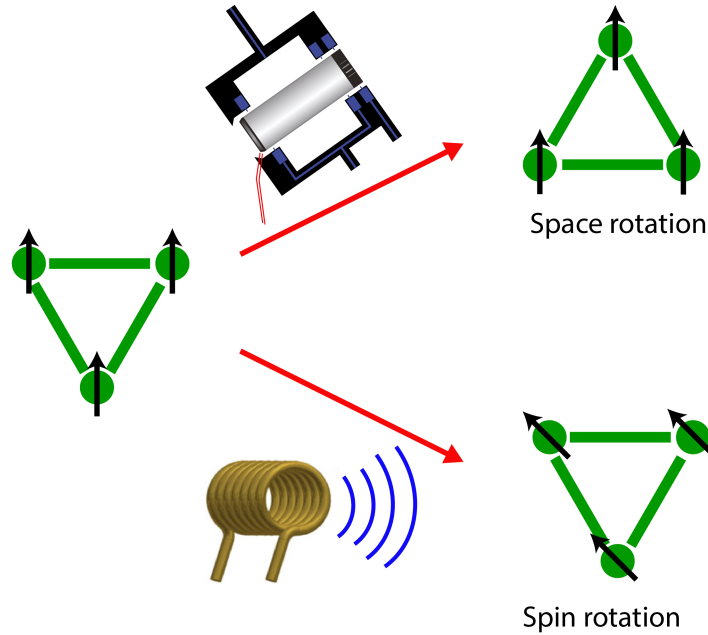
Figure 2.2. Schematic representation of external perturbations that introduce time dependence of the Hamiltonian. The spin part of the system Hamiltonian is perturbed by an external B_1 field. The spatial part is modulated by physical rotation around the rotor axis known as magic-angle spinning.

tion of the Liouville-Von Neumann equation is not always valid with a time-dependent Hamiltonian. Hence, a theory has to be applied from which time-independent effective Hamiltonians can be derived that govern the system throughout the perturbation. The resulting evolution of the density operator under these Hamiltonians allows conclusions about the spin dynamics and play an essential role in the theoretical description and understanding of the pulse sequences presented throughout this thesis. In principle, two main theories to finding effective time-independent Hamiltonians are applied, namely average Hamiltonian theory (AHT) [18, 19] and Floquet theory [20–23]. Both will be discussed in detail in this Chapter.

Additionally to the external perturbations to the system by experimental design there are stochastic modulations of the spin or spatial part of the Hamiltonian. These time-dependent modulations are induced by random molecular motion. A phenomenon of this time dependence is relaxation behaviour of the system which is classified either in longitudinal or transverse relaxation times ($T_1, T_2, T_{1\rho},...$). An analytical treatment of relaxation behaviour is beyond the scope of this work as it is only covered in a very

phenomenological way throughout this work. Further reading regarding relaxation can be found in [54, 55].

2.4.2. Modulation of the Spatial Tensors by MAS

The rotation of the sample around the rotor axis is a pre-requisite for the application of high-resolution solid-state NMR. The rapid rotation around the spinning axis inclined by 54.74° to the external magnetic field, known as magic-angle spinning, averages out anisotropic interactions [16, 17]. Despite the rich content of information of the anisotropic interactions about the spin environment, they render broad spectral lines that make the interpretation of spectra nearly impossible.

As already shown in Equation 2.41, magic-angle spinning modulates the spatial part of the Hamiltonian and introduces a time dependence. In order to analyse the effect of MAS on the Hamiltonian, the spatial part of the Hamiltonian is rotated sequentially from the PAS into the laboratory coordinate system. At first the interaction of interest has to be transformed from the principal-axis system into a coordinate system corresponding to a rotor-fixed frame using the reduced Wigner elements

$$A_{\ell,q'}^{(\text{rot})} = \sum_{q''=-\ell}^{\ell} \mathscr{D}_{q'',q'}^{\ell}(\alpha, \beta, \gamma) A_{\ell,q''}^{(\text{PAS})}. \tag{2.42}$$

Further, the tensor in the rotor-fixed frame is rotated in the laboratory frame assuming a rotation of $\omega_{\text{r}}t$ with ω_{r} being the rotation speed and an incline with respect to the external magnetic field θ_{r}. The interaction in the laboratory frame is given by

$$A_{\ell,q}^{(\text{lab})} = \sum_{q'=-\ell}^{\ell} \mathscr{D}_{q',q}^{\ell}(-\omega_{\text{r}}t, -\theta_{\text{r}}, 0) A_{\ell,q'}^{(\text{rot})}. \tag{2.43}$$

Invoking the high-field approximation, only the component $q = 0$ remains time independent and is considered. Combining the two rotations, the spatial tensor under MAS is derived as

$$A_{\ell,0}^{(\text{lab})} = \sum_{q'=-\ell}^{\ell} e^{-iq'\omega_{\text{r}}t} d_{q',0}^{\ell}(-\theta_{\text{r}}) A_{\ell,q'}^{(\text{rot})}. \tag{2.44}$$

The exponential terms containing $q' = \pm 1, \pm 2, \ldots$ vanish if the signal is sampled at multiples of the rotor periods, known as stroboscopic sampling. However, in real solid-

state NMR experiments stroboscopic sampling is not applied routinely because it is very restricting for the choice of dwell time. The result of non-stroboscopic sampling are spinning side bands which are signals that are spaced from the central line by the rotor frequency. At higher MAS frequencies, these side bands move further out and are reduced in intensity resulting in higher signal-to-noise of the central peak. The time-independent component ($q' = 0$) is scaled with the Wigner element $d_{0,0}^2 = \frac{3\cos^2\theta_r - 1}{2}$ which is 0 at the magic angle $\theta_r = \theta_m = 54.74°$.

The full Hamiltonian with the MAS time dependence and the high-field approximation is given by

$$\hat{\mathscr{H}}(t) = \sum_\ell A_{\ell,0}(t)\hat{\mathscr{T}}_{\ell,0}. \tag{2.45}$$

Substituting the spatial tensor with the explicit expressions derived in Equation 2.44, the Hamiltonian can be interpreted as a Fourier series

$$\begin{aligned}
\hat{\mathscr{H}}(t) &= \sum_{q=-\ell}^{\ell} \hat{\mathscr{H}}^{(q)} e^{-iq\omega_r t} \\
&= \sum_{q=-\ell}^{\ell} d_{q,0}^\ell(-\theta_r) A_{\ell,q}^{(\text{rot})} e^{-iq\omega_r t} \cdot \hat{\mathscr{T}}_{\ell,0} \\
&= \sum_q \sum_{q'} d_{q,0}^\ell(-\theta_r) e^{-iq'\alpha} d_{q',q}^\ell(\beta) e^{-iq\gamma} A_{\ell,q'}^{(\text{PAS})} e^{-iq\omega_r t} \cdot \hat{\mathscr{T}}_{\ell,0} \\
&= \sum_q \omega^{(q)} e^{-iq\omega_r t} \cdot \hat{\mathscr{T}}_{\ell,0} \tag{2.46}
\end{aligned}$$

where $\omega^{(q)}$ is the spatial tensor component of a spin interaction under MAS given by

$$\omega^{(q)} = \sum_{q'} d_{q,0}^\ell(-\theta_r) e^{-iq'\alpha} d_{q',q}^\ell(\beta) e^{-iq\gamma} A_{\ell,q'}^{(\text{PAS})}. \tag{2.47}$$

The sum over q is restricted to -2 to 2 because the tensors have rank 2. Oftentimes, the spatial tensor in the principal-axis system is represented by the symbol $\rho_{\ell,q}^{(\mathrm{PAS})}$ and is defined by

$$\rho_{0,0} = -\sqrt{3}\sigma_{\mathrm{iso}}$$
$$\rho_{2,0} = \sqrt{3/2}\delta$$
$$\rho_{2,\pm2} = -1/2(\delta\eta) \tag{2.48}$$

where σ_{iso}, δ, and η have been defined in Chapter 2.2.2. Note that the dipolar-coupling tensor does not contain asymmetric parts and therefore, only $\rho_{2,0}$ has to be considered for the dipole-dipole interaction.

2.4.3. Modulation of the Spin Tensors by RF Irradiation

If the perturbation of the Hamiltonian is of periodic nature, the time-dependent system Hamiltonian can be represented as a Fourier series with an infinite sum. The first example of such a Fourier series was shown for the time-dependent Hamiltonian under MAS with a restricted sum due to the rank of the spatial component. Generally, a periodic Hamiltonian can thus be expressed as

$$\hat{\mathscr{H}}(t) = \sum_{n=-\infty}^{\infty} \hat{\mathscr{H}}^{(n)} \cdot e^{in\omega_{\mathrm{c}}t}. \tag{2.49}$$

This implies that the Hamiltonian is cyclic in nature and the relation $\hat{\mathscr{H}}(t) = \hat{\mathscr{H}}(t+\tau_{\mathrm{c}})$ holds true where $\tau_{\mathrm{c}} = 2\pi/\omega_{\mathrm{c}}$ with τ_{c} being the cycle time. $\hat{\mathscr{H}}^{(n)}$ are the time-independent Fourier coefficients of the Hamiltonian and are not Hermitian. Theoretically, through simultaneous modulation of the spin and the spatial part, the Hamiltonian can gain multiple time dependencies which do not have to be commensurate. The resulting time-dependent Hamiltonian can consequently be written in terms of multiple characteristic frequencies with multiple Fourier expansions.

Interaction-Frame Transformation

A similar procedure to the transformation of the spatial part in a system that rotates with the MAS frequency (Chapter 2.4.2) can be applied to analyse the influence of a

time-dependent spin part of the Hamiltonian. This spin part can be manipulated by external rf irradiation with a Hamiltonian $\hat{\mathscr{H}}_{\text{rf}}(t)$ (Chapter 2.2.5). Transforming the spin part of the Hamiltonian into an interaction frame that rotates with the rf Hamiltonian leads to a modulation of the Hamiltonian with the pulse sequence. This transformation is mathematically written out by

$$\hat{\tilde{\mathscr{H}}}(t) = \hat{U}^{-1}(t)\hat{\mathscr{H}}(t)\hat{U}(t). \tag{2.50}$$

The propagator $U(t)$ contains the dominant interaction from the Hamiltonian $\hat{\mathscr{H}}_1(t)$ (usually containing the rf Hamiltonian, the offset Hamiltonian, or another dominant interaction) and is given by

$$\hat{U}(t) = \hat{T}\exp\left(-i\int_0^t \hat{\mathscr{H}}_1(t_1)dt_1\right). \tag{2.51}$$

where $\hat{T}$ is the Dyson time-ordering operator [56]. This operator ensures that the Hamiltonian at an earlier time acts on the density operator first, and hence, is written mathematically as

$$\hat{T}\{\hat{\mathscr{H}}(t_1)\hat{\mathscr{H}}(t_2)\} = \begin{cases} \hat{\mathscr{H}}(t_1)\hat{\mathscr{H}}(t_2) & \text{if } t_1 > t_2 \\ \hat{\mathscr{H}}(t_2)\hat{\mathscr{H}}(t_1) & \text{if } t_1 < t_2. \end{cases} \tag{2.52}$$

The density operator transforms in full analogy to the system Hamiltonian and is given in the interaction frame by

$$\hat{\rho}'(t) = \hat{U}^{-1}(t)\hat{\rho}(t)\hat{U}(t). \tag{2.53}$$

Substituting the transformed density operator into the Liouville-Von Neumann Equation (Eq. 2.7), a modified relation is obtained

$$\begin{aligned} \frac{d}{dt}\hat{\rho}' &= -i\left[\hat{\tilde{\mathscr{H}}} - \hat{\mathscr{H}}_1, \hat{\rho}'\right] \\ &= -i\left[\hat{\mathscr{H}}_0', \hat{\rho}'\right] \end{aligned} \tag{2.54}$$

with $\hat{\tilde{\mathscr{H}}}$ being the full Hamiltonian in the interaction frame and $\hat{\mathscr{H}}_0' = \hat{\tilde{\mathscr{H}}} - \hat{\mathscr{H}}_1$ the non-dominant part of the full Hamiltonian. This term, $\hat{\mathscr{H}}_0'$, is now the governing Hamiltonian in the interaction frame for the spin dynamics.

The influence of the new governing time-dependent Hamiltonian can be expressed again in a Fourier series as shown before. Considering an arbitrary rf-field Hamiltonian, two frequencies are characteristic for the description of the time dependence. The modulation frequency, ω_{m}, describing the basic rate at which the pulse sequence is repeated, and the effective field, ω_{eff}, giving the net flip angle over the basic modulation period. Therefore, the interaction-frame Hamiltonian can be written as

$$\hat{\tilde{\mathscr{H}}}(t) = \sum_{k=-\infty}^{\infty} \sum_{\ell=-\infty}^{\infty} \hat{\mathscr{H}}^{(k,\ell)} e^{ik\omega_{\mathrm{m}}t} e^{i\ell\omega_{\mathrm{eff}}t}. \tag{2.55}$$

The time-independent Fourier coefficients $\hat{\mathscr{H}}^{(k,\ell)}$ can be calculated analytically for certain irradiation schemes and pulse sequences with perfect rectangular pulses. Arbitrary shaped rf fields require a numerical calculation of the transformation. In order to calculate the density operator and the interaction-frame Hamiltonian numerically, a time slicing has to be employed and the propagator is given as the product of piece-wise time-independent propagators

$$\hat{U}(t) \approx \prod_{k} \exp\left(-i\hat{\mathscr{H}}_1(k\Delta t)\Delta t\right). \tag{2.56}$$

The time dependence of the interaction-frame transformation can either by expressed using Cartesian coordinates

$$\hat{\tilde{I}}_{\kappa}(t) = \sum_{\chi} a_{\kappa\chi}(t)\hat{I}_{\chi} \tag{2.57}$$

with κ and χ as the coordinates x, y, z, or using spherical tensor notation

$$\hat{\tilde{\mathscr{T}}}_{r,0}(t) = \sum_{s=-r}^{r} a_{r,s}(t)\hat{\tilde{\mathscr{T}}}_{r,s}. \tag{2.58}$$

The time-dependent coefficients $a_{ki}(t)$ respectively $a_{r,s}(t)$ map out the interaction-frame trajectory. A subsequent Fourier analysis of these coefficients allows the extraction of time-independent coefficients that allow the effective Hamiltonian to be directly determined from these coefficients. This procedure is the basis of a Floquet analysis which is presented in Chapter 2.5.2.

2.5. Analysis of Time-Dependent Hamiltonians

2.5.1. Average Hamiltonian Theory

A simple analysis of time-dependent Hamiltonians is given by the concept of average Hamiltonian theory (AHT). It requires the time-dependent Hamiltonian to be cyclic, i.e. $\hat{\mathscr{H}}(t) = \hat{\mathscr{H}}(t + \tau_c)$ and the sampling is stroboscopic. A time-independent Hamiltonian $\overline{\hat{\mathscr{H}}}$ is obtained by calculating the average of different time-dependent Hamiltonians acting on the system during the period τ_c. Assuming the simplest case of two different time-dependent Hamiltonian, e.g. two rf schemes applied for a certain time steps t_1 and t_2, an effective propagator over the whole period can be calculated according to

$$\hat{U}_{\text{eff}}(\tau_c) = \exp\left(-i\overline{\hat{\mathscr{H}}}\tau_c\right) = \exp\left(-i\hat{\mathscr{H}}_1 t_1\right)\exp\left(-i\hat{\mathscr{H}}_2 t_2\right). \tag{2.59}$$

This relation requires that $\hat{\mathscr{H}}_1$ and $\hat{\mathscr{H}}_2$ are constant during the time periods t_1 and t_2, respectively. In order to evaluate the product of the two exponent operators, the Baker-Campbell-Hausdorff (BCH) relation can be invoked and leads to the expansion

$$\begin{aligned}
\exp\left(-i\overline{\hat{\mathscr{H}}}\tau_c\right) &= \exp\left(-i\hat{\mathscr{H}}_1 t_1\right)\exp\left(-i\hat{\mathscr{H}}_2 t_2\right) \\
&= \exp\Big(-i(\hat{\mathscr{H}}_1 t_1 + \hat{\mathscr{H}}_2 t_2) - \frac{1}{2}\left[\hat{\mathscr{H}}_2 t_2, \hat{\mathscr{H}}_1 t_1\right] \\
&\quad + \frac{i}{12}\left(\left[\hat{\mathscr{H}}_2 t_2, \left[\hat{\mathscr{H}}_2 t_2, \hat{\mathscr{H}}_1 t_1\right]\right] + \left[\left[\hat{\mathscr{H}}_2 t_2, \hat{\mathscr{H}}_1 t_1\right], \hat{\mathscr{H}}_1 t_1\right]\right) + \dots\Big).
\end{aligned} \tag{2.60}$$

The average Hamiltonian is given by the first term of Equation 2.60 if the two Hamiltonians commute at all times. Otherwise, an infinite series is obtained from which the
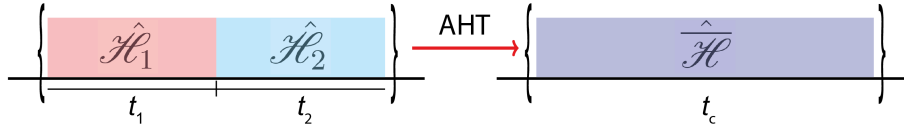

Figure 2.3. Schematic representation of the substitution of a time-dependent Hamiltonian comprising of two time-independent Hamiltonians $\hat{\mathscr{H}}_1$ and $\hat{\mathscr{H}}_2$ by an average Hamiltonian $\overline{\hat{\mathscr{H}}}$ forming the basis of average-Hamiltonian theory.

terms can be attributed to different orders which is usually truncated after second or third order. This series is then given by

$$\overline{\hat{\mathscr{H}}} = \overline{\hat{\mathscr{H}}}^{(1)} + \overline{\hat{\mathscr{H}}}^{(2)} + \overline{\hat{\mathscr{H}}}^{(3)} + \dots \tag{2.61}$$

where the contributions are given for the two-Hamiltonian case by

$$\overline{\hat{\mathscr{H}}}^{(1)} = \frac{1}{\tau_{\mathrm{c}}} (\hat{\mathscr{H}}_1 t_1 + \hat{\mathscr{H}}_2 t_2) \tag{2.62}$$

$$\overline{\hat{\mathscr{H}}}^{(2)} = \frac{-i}{2\tau_{\mathrm{c}}} [\hat{\mathscr{H}}_2 t_2, \hat{\mathscr{H}}_1 t_1] \tag{2.63}$$

$$\overline{\hat{\mathscr{H}}}^{(3)} = \frac{-1}{12\tau_{\mathrm{c}}} \left(\left[\hat{\mathscr{H}}_2 t_2, \left[\hat{\mathscr{H}}_2 t_2, \hat{\mathscr{H}}_1 t_1 \right] \right] + \left[\left[\hat{\mathscr{H}}_2 t_2, \hat{\mathscr{H}}_1 t_1 \right], \hat{\mathscr{H}}_1 t_1 \right] \right) \tag{2.64}$$

This concept can be generalized for continuously time-dependent Hamiltonians in the form of a Magnus expansion [57]. The first three contributions to this expansion are given by

$$\overline{\hat{\mathscr{H}}}^{(1)} = \frac{1}{\tau_{\mathrm{c}}} \int_0^{\tau_{\mathrm{c}}} dt_1 \hat{\mathscr{H}}(t_1) \tag{2.65}$$

$$\overline{\hat{\mathscr{H}}}^{(2)} = \frac{-i}{2\tau_{\mathrm{c}}} \int_0^{\tau_{\mathrm{c}}} dt_2 \int_0^{t_2} dt_1 \left[\hat{\mathscr{H}}(t_2), \hat{\mathscr{H}}(t_1) \right] \tag{2.66}$$

$$\overline{\hat{\mathscr{H}}}^{(3)} = \frac{-1}{6\tau_{\mathrm{c}}} \int_0^{\tau_{\mathrm{c}}} dt_3 \int_0^{t_3} dt_2 \int_0^{t_2} dt_1 \left[\hat{\mathscr{H}}(t_3), \left[\hat{\mathscr{H}}(t_2), \hat{\mathscr{H}}(t_1) \right] \right]$$
$$+ \left[\left[\hat{\mathscr{H}}(t_3), \hat{\mathscr{H}}(t_2) \right], \hat{\mathscr{H}}(t_1) \right]. \tag{2.67}$$

Note that the first-order average Hamiltonian does not have an explicit dependence on the cycle time τ_{c}. Therefore, the cycle time does not influence the first-order terms. However, the second-order term has an explicit time dependence in the divisor, and hence, is scaled down by shorter cycle times. This is the reason why coherent averaging is more efficient at higher MAS frequency. On the other hand, it is also the reason why pulse sequences relying on large second-order terms are less promising at high MAS frequencies. An additional property inferred from the Magnus expansion is the vanishing of all even-order terms if the Hamiltonian is symmetric with respect to the cycle time, i.e.

$$\hat{\mathscr{H}}(t) = \hat{\mathscr{H}}(\tau_{\mathrm{c}} - t). \tag{2.68}$$

Nevertheless, AHT has certain limitations as the description is only exact at multiples of the cycle time and the stroboscopic sampling is experimentally restricting. Furthermore, multiple time dependencies with basic frequencies that are not commensurate can only be treated for very long time steps which would not yield meaningful results. A viable alternative for the treatment of multiple non-commensurate frequencies is offered by Floquet theory.

2.5.2. Floquet Theory

Floquet theory overcomes the limitations of average Hamiltonian Theory as the treatment of multiple periodic time dependencies is possible. This is a powerful approach for solid-state NMR because experiments often comprise of multiple modulation frequencies (e.g. from the MAS and the rf-field irradiation).

The basic approach is based on a transformation from the Hamiltonian in a time-dependent Hilbert space into an infinite-dimensional time-independent Floquet space. The transformation turns a finite-dimensional, time-dependent problem into a infinite-dimensional, time-independent one. There are two fundamentally different ways to perform a Floquet analysis of the time-dependent problem. Firstly, the time evolution of the density operator can be calculated under an infinitely-dimensional Floquet Hamiltonian to obtain the spectrum. This approach is predominantly interesting for numerical simulations but they are computationally demanding and time slicing of the Hamiltonian in Hilbert space is more efficient.

A second, more useful, approach is the analytical transformation and subsequent perturbation theory on the Floquet Hamiltonian. This leads to an approximation of the analytical solution of the problem in Floquet space. Projecting the resulting effective Hamiltonian back onto the finite Hilbert space yields operators, mostly in a spin-operator approach, that can be interpreted physically.

The second approach is depicted in Figure 2.4 with the construction of the Floquet Hamiltonian and the Van Vleck perturbation treatment for the derivation of effective Hamiltonians.
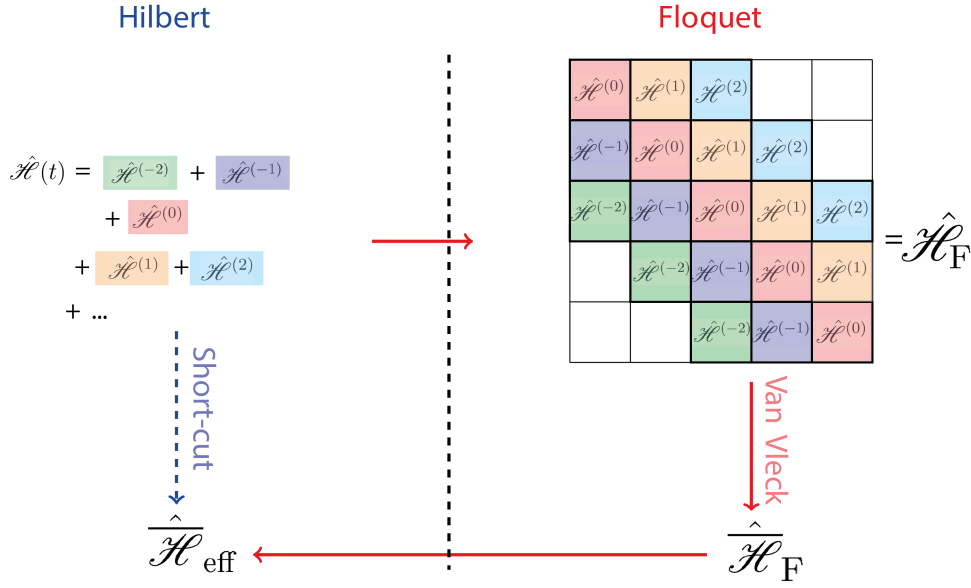
Figure 2.4. Schematic representation of the treatment of time-dependent Hamiltonians using Floquet theory.

Definition of Floquet Space

Transforming the operators and matrix representations from Hilbert space into Floquet space is done by a direct product with the Fourier space. The Fourier space is infinitely dimensional where the quantum numbers are all integer numbers. Hence, the full basis set of the Fourier space is given by

$$\Psi^{(\text{Fourier})} = \{|-\infty\rangle, \ldots, |-3\rangle, |-2\rangle, |-1\rangle, |0\rangle, |1\rangle, |2\rangle, |3\rangle, \ldots, |\infty\rangle\}. \qquad (2.69)$$

The Floquet space is therefore given by

$$\Psi^{(\text{Floquet})} = \Psi^{(\text{Hilbert})} \otimes \Psi^{(\text{Fourier})} \qquad (2.70)$$

with the Hilbert space spanned by the wave functions

$$\Psi^{(\text{Hilbert})} = \{|\phi_1\rangle, |\phi_2\rangle, \ldots, |\phi_N\rangle\}. \qquad (2.71)$$

In Floquet space, each of the wave functions is characterized by the wave function ϕ_i from Hilbert space and the Fourier number n.

Defining an operator $\hat{F}_m$ in Fourier space, often called the 'ladder' operator, follows the definition

$$\hat{F}_m|n\rangle = |n + m\rangle \tag{2.72}$$

and has a matrix representation that is infinite with a one at the mth side diagonal with F_0 being the identity operator. A further useful operator F_z, also known as the number operator, is defined by

$$\hat{F}_z|n\rangle = n|n\rangle. \tag{2.73}$$

Furthermore, the operators obey the following relations

$$\hat{F}_m\hat{F}_n = \hat{F}_{n+m}$$
$$\left[\hat{F}_m, \hat{F}_n\right] = 0$$
$$\left[\hat{F}_z, \hat{F}_m\right] = m\hat{F}_m. \tag{2.74}$$

Matrix representations of two examples of these operators are given by

$$\hat{F}_z = \begin{array}{c} \\ \end{array} \begin{array}{ccccc} \dots & |2\rangle & |1\rangle & |0\rangle & |-1\rangle & |-2\rangle & \dots \\ \left(\begin{array}{ccccc} +2 & 0 & 0 & 0 & 0 \\ 0 & +1 & 0 & 0 & 0 \\ 0 & 0 & 0 & 0 & 0 \\ 0 & 0 & 0 & -1 & 0 \\ 0 & 0 & 0 & 0 & -2 \end{array}\right) & \begin{array}{c} |2\rangle \\ |1\rangle \\ |0\rangle \\ |-1\rangle \\ |-2\rangle \end{array} \end{array} \tag{2.75}$$

for the number operator and

$$\hat{F}_2 = \begin{array}{c} \\ \end{array} \begin{array}{ccccc} \dots & |2\rangle & |1\rangle & |0\rangle & |-1\rangle & |-2\rangle & \dots \\ \left(\begin{array}{ccccc} 0 & 0 & 1 & 0 & 0 \\ 0 & 0 & 0 & 1 & 0 \\ 0 & 0 & 0 & 0 & 1 \\ 0 & 0 & 0 & 0 & 0 \\ 0 & 0 & 0 & 0 & 0 \end{array}\right) & \begin{array}{c} |2\rangle \\ |1\rangle \\ |0\rangle \\ |-1\rangle \\ |-2\rangle \end{array} \end{array} \tag{2.76}$$

for the ladder operator with $n = 2$. For multiple time dependencies that are not commensurate, the Floquet space is defined as the direct product between the Hilbert space and multiple Fourier spaces with the number of basis sets equal to the number of characteristic frequencies.

The Floquet Hamiltonian and Effective Hamiltonians

Deriving the Floquet Hamiltonian is done by starting from the general time-dependent expression as a Fourier series

$$\hat{\mathscr{H}}(t) = \sum_{n=-\infty}^{\infty} \hat{\mathscr{H}}^{(n)} \cdot e^{in\omega_{\mathrm{m}}t} \tag{2.77}$$

and expressing it in Floquet space as

$$\hat{\mathscr{H}}_{\mathrm{F}} = \sum_{n=-\infty}^{\infty} \hat{F}_n \otimes \hat{\mathscr{H}}^{(n)} + \omega_{\mathrm{m}} \hat{F}_z \otimes \hat{1}^{(\mathrm{s})}. \tag{2.78}$$

The additional term $\omega_{\mathrm{m}} \hat{F}_z \otimes \hat{1}^{(\mathrm{s})}$ can be attributed to the interaction-frame transformation and is analogous to a fictitious Coriolis force with $\hat{1}^{(\mathrm{s})}$ being the identity operator in the Hilbert space.

Extending the problem to multiple time dependencies, one obtains the time-dependent Hamiltonian as

$$\hat{\mathscr{H}}(t) = \sum_{\left[n^{(p)}\right]} \hat{\mathscr{H}}^{\left(\left[n^{(p)}\right]\right)} \prod_p e^{in^{(p)}\omega^{(p)}t}. \tag{2.79}$$

Applying the Van Vleck perturbation treatment allows the derivation of general effective Hamiltonians without a detailed knowledge of the spin parts since the treatment is only done in on the Fourier-space part. This leads to resonance conditions that are only dependent on degeneracies between the various Fourier frequencies. The resulting effective Hamiltonian can be obtained to different orders and is given by

$$\bar{\hat{\mathscr{H}}}_{\mathrm{eff}} = \bar{\hat{\mathscr{H}}}_{\mathrm{eff}}^{(1)} + \bar{\hat{\mathscr{H}}}_{\mathrm{eff}}^{(2)} + \bar{\hat{\mathscr{H}}}_{\mathrm{eff}}^{(3)} + \ldots \quad . \tag{2.80}$$

Once these Hamiltonians are derived, the expressions for them can be used as a 'shortcut' directly from $\hat{\mathscr{H}}(t)$. In the following the expressions up to third order will be discussed with two and three time dependencies, respectively.

Bimodal Floquet Theory

Assuming a Hamiltonian, which is modulated with two frequencies, ω_{r} and ω_{m}, it can be written in a general form as introduced in Equation 2.79 by

$$\hat{\mathscr{H}}(t) = \sum_{n=-\infty}^{\infty} \sum_{k=-\infty}^{\infty} \hat{\mathscr{H}}^{(n,k)} e^{in\omega_{\mathrm{r}}t} e^{ik\omega_{\mathrm{m}}t}. \tag{2.81}$$

At the resonance condition

$$n_0\omega_{\mathrm{r}} + k_0\omega_{\mathrm{m}} = 0 \tag{2.82}$$

the first-order Hamiltonian is given as the sum of the terms $\hat{\bar{\mathscr{H}}}^{(0,0)}$ that have the trivial solution $(n_0 = k_0 = 0)$ and are known as non-resonant terms, and the resonant terms $\hat{\bar{\mathscr{H}}}^{(n_0,k_0)}$, where n_0 and k_0 fulfil Equation 2.82, by

$$\overline{\hat{\mathscr{H}}}^{(1)} = \hat{\bar{\mathscr{H}}}^{(0,0)} + \sum_{n_0,k_0} \hat{\bar{\mathscr{H}}}^{(n_0,k_0)}. \tag{2.83}$$

The second-order effective Hamiltonian is given again as the sum over the resonant and non-resonant terms by

$$\overline{\hat{\mathscr{H}}}^{(2)} = \hat{\bar{\mathscr{H}}}_{(2)}^{(0,0)} + \sum_{n_0,k_0} \hat{\bar{\mathscr{H}}}_{(2)}^{(n_0,k_0)}. \tag{2.84}$$

with the resonant term containing commutators between the Fourier coefficients and defined as

$$\hat{\bar{\mathscr{H}}}_{(2)}^{(n_0,k_0)} = -\sum_{\nu,\kappa} \frac{1}{2} \frac{\left[\hat{\bar{\mathscr{H}}}^{(n_0-\nu,k_0-\kappa)}, \hat{\bar{\mathscr{H}}}^{(\nu,\kappa)} \right]}{\nu\omega_{\mathrm{r}} + \kappa\omega_{\mathrm{m}}}. \tag{2.85}$$

In Equation 2.85, the summations of ν and κ are restricted and must fulfil the inequality $\nu\omega_{\mathrm{r}} + \kappa\omega_{\mathrm{m}} \neq 0$ to avoid singularities.

The third-order effective Hamiltonian is given in full analogy to the second order by

$$\overline{\hat{\mathscr{H}}}^{(3)} = \hat{\bar{\mathscr{H}}}_{(3)}^{(0,0)} + \sum_{n_0,k_0} \hat{\bar{\mathscr{H}}}_{(3)}^{(n_0,k_0)}. \tag{2.86}$$

In the course of this thesis, only the non-resonant term in third order is considered which is given by

$$\hat{\bar{\mathscr{H}}}_{(3)}^{(0,0)} = \sum_{\nu,\kappa} \sum_{n_0',k_0'} \frac{1}{2} \frac{\left[\left[\hat{\bar{\mathscr{H}}}^{(\nu,\kappa)}, \hat{\bar{\mathscr{H}}}^{(n_0',k_0')}\right], \hat{\bar{\mathscr{H}}}^{(-\nu-n_0',-\kappa-k_0')}\right]}{\left(\nu\omega_\mathrm{r} + \kappa\omega_\mathrm{m}\right)^2}$$

$$+ \sum_{\nu,\kappa} \sum_{\nu',\kappa'} \frac{1}{3} \frac{\left[\hat{\bar{\mathscr{H}}}^{(\nu,\kappa)}, \left[\hat{\bar{\mathscr{H}}}^{(\nu',\kappa')}, \hat{\bar{\mathscr{H}}}^{(-\nu-\nu',-\kappa-\kappa')}\right]\right]}{\left(\nu\omega_\mathrm{r} + \kappa\omega_\mathrm{m}\right)\left(\nu'\omega_\mathrm{r} + \kappa'\omega_\mathrm{m}\right)} \quad (2.87)$$

Triple-mode Floquet Theory

In full analogy to the bimodal Floquet theory, problems with three non-commensurate time dependencies are treated. The time-dependent Hamiltonian is expanded in a Fourier series as

$$\hat{\bar{\mathscr{H}}}(t) = \sum_{n=-\infty}^{\infty} \sum_{k=-\infty}^{\infty} \sum_{\ell=-\infty}^{\infty} \hat{\bar{\mathscr{H}}}^{(n,k,\ell)} e^{in\omega_\mathrm{r}t} e^{ik\omega_\mathrm{m}t} e^{i\ell\omega_\mathrm{eff}t}. \quad (2.88)$$

At the trimodal resonance condition

$$n_0\omega_\mathrm{r} + k_0\omega_\mathrm{m} + \ell_0\omega_\mathrm{eff} = 0. \quad (2.89)$$

the first-order effective Hamiltonian is given by

$$\hat{\bar{\mathscr{H}}}^{(1)} = \hat{\bar{\mathscr{H}}}_{(1)}^{(0,0,0)} + \sum_{n_0,k_0,\ell_0} \hat{\bar{\mathscr{H}}}_{(1)}^{(n_0,k_0,\ell_0)} \quad (2.90)$$

with the second-order contribution to the full effective Hamiltonian given by

$$\hat{\bar{\mathscr{H}}}^{(2)} = \hat{\bar{\mathscr{H}}}_{(2)}^{(0,0,0)} + \sum_{n_0,k_0,\ell_0} \hat{\bar{\mathscr{H}}}_{(2)}^{(n_0,k_0,\ell_0)} \quad (2.91)$$

with

$$\hat{\bar{\mathscr{H}}}_{(2)}^{(n_0,k_0,\ell_0)} = -\sum_{\nu,\kappa,\lambda} \frac{1}{2} \frac{\left[\hat{\bar{\mathscr{H}}}^{(n_0-\nu,k_0-\kappa,\ell_0-\lambda)}, \hat{\bar{\mathscr{H}}}^{(\nu,\kappa,\lambda)}\right]}{\nu\omega_\mathrm{r} + \kappa\omega_\mathrm{m} + \lambda\omega_\mathrm{eff}}. \quad (2.92)$$

This summation has to be restricted again to $\nu\omega_\mathrm{r} + \kappa\omega_\mathrm{m} + \lambda\omega_\mathrm{eff} \neq 0$ to ensure that the second-order effective Hamiltonian does not become ∞. The third-order contribution for non-resonant terms of the effective Hamiltonians is given by

$$
\hat{\tilde{\mathscr{H}}}_{(3)}^{(0,0,0)} = \sum_{\nu,\kappa,\lambda} \sum_{n_0',k_0',l_0'} \frac{1}{2} \frac{\left[\left[\hat{\tilde{\mathscr{H}}}^{(\nu,\kappa,\lambda)}, \hat{\tilde{\mathscr{H}}}^{(n_0',k_0',l_0')}\right], \hat{\tilde{\mathscr{H}}}^{(-\nu-n_0',-\kappa-k_0',-\lambda-\ell_0')}\right]}{\left(\nu\omega_\mathrm{r} + \kappa\omega_\mathrm{m} + \lambda\omega_\mathrm{eff}\right)^2}
$$
$$
+ \sum_{\nu,\kappa,\lambda} \sum_{\nu',\kappa',\lambda'} \frac{1}{3} \frac{\left[\hat{\tilde{\mathscr{H}}}^{(\nu,\kappa,\lambda)}, \left[\hat{\tilde{\mathscr{H}}}^{(\nu',\kappa',\lambda')}, \hat{\tilde{\mathscr{H}}}^{(-\nu-\nu',-\kappa-\kappa',-\lambda-\lambda')}\right]\right]}{\left(\nu\omega_\mathrm{r} + \kappa\omega_\mathrm{m} + \lambda\omega_\mathrm{eff}\right)\left(\nu'\omega_\mathrm{r} + \kappa'\omega_\mathrm{m} + \lambda\omega_\mathrm{eff}\right)}. \quad (2.93)
$$

Note that the summations in the third-order term have to be restricted to values of $(\nu, \nu', \kappa, \kappa', \lambda, \lambda')$ that fulfil the inequalities $\nu\omega_\mathrm{r}+\kappa\omega_\mathrm{m}+\lambda\omega_\mathrm{eff} \neq 0$ and $\nu'\omega_\mathrm{r}+\kappa'\omega_\mathrm{m}+\lambda'\omega_\mathrm{eff} \neq 0$.

3. Pulse-Transient Compensation

3.1. Introduction

3.1.1. Basic Introduction

Many solid-state NMR experiments rely on the fact that the density operator is modulated with rf-irradiation. This modulation introduces a time dependency, as discussed in Chapter 2.4, in order to reintroduce or remove spin-spin or spin-field interactions of interest. The theoretical design of every pulse sequence is based on the assumption of perfect rotations and well-defined spin trajectories. However, in reality rectangular pulses leading to perfect rotations are impossible to realize due to the nature of the resonance circuit that is used in an NMR probe. The deviations from the 'perfect' pulses, which are conventionally programmed as rectangular pulses, and the actually generated pulses are called *pulse transients* [32, 33]. Pulse transients are inherent to every probe in solid-state NMR. This is on one hand due to the characteristics of a resonance circuit, such as the finite bandwidth and a potential detuning of the irradiation and the resonance frequency, and on the other hand due to potential impedance mismatches in the electrical components of the system. In literature, this phenomenon was realized very early and basic models have been developed and reported to describe pulse imperfections [32]. Assuming a single resonance circuit that is perfectly matched in impedance, the model uses the quantities of the pulse rise time τ_{rise} and the electronic offset frequency ω_{off}. The rise time, i.e. the time of the voltage build-up in the circuit, is directly proportional to the quality factor Q of the resonance circuit. The electronic offset frequency describes the detuning of the driving frequency, i.e. the rf frequency from its actual resonance frequency. The proposed model based on these two quantities describes the pulse transient as

$$p = p_{\mathrm{ideal}}(t) * \left(1 - e^{\frac{-t}{\tau_{\mathrm{rise}}}} \cdot e^{it\omega_{\mathrm{off}}} \right). \tag{3.1}$$

This inherent property of pulse imperfections to every solid-state probe has made the robustness of pulse sequences towards imperfect rotations a requirement. Several approaches to modifying the experimental setup have been reported. A common approach with a previous generation of NMR spectrometers was the use of 'tune-up' sequences. The tube amplifiers were used to minimize the anti-symmetric part of pulse transients by tuning and matching the amplifier [58–62]. However, the current generation of NMR spectrometers has an amplifier with a constant impedance that cannot be changed anymore. If one of the electrical components in the resonance circuit exhibits an impedance mismatch that creates a reflection, a similar result to minimize the anti-symmetric parts of the pulse transient can be achieved by changing the cable length. These modifications are always specific to the current configuration and must be re-optimized if the experimental setup is altered [63, 64]. Therefore, these procedures are not a suitable solution for the practical application of solid-state NMR experiments.

The effect of the pulse imperfections on the actual pulse sequence and its performance is hard to predict *a priori* without a full theoretical understanding of the theory behind it. Several reports in the literature discuss the influence of pulse transients on multi-pulse sequences for line narrowing in static samples and under slow MAS [32, 65]. A specific example of pulse imperfections that has been treated quite extensively in the literature is the homonuclear decoupling sequence phase-modulated Lee-Goldburg irradiation [64, 66–69]. Another type of sequence with performance heavily affected by pulse imperfections is symmetry-based sequences, which have been shown theoretically and in numerical simulations [70, 71]. Modifications to symmetry-based pulse sequences have been reported to compensate the pulse imperfections and make them more stable by either breaking the rotor synchronization [25] or phase-shifting one of the pulses [63]. An additional approach to improve the stability of pulse sequences are including optimum-control sequences where pulse transients are treated as input parameters [30, 72, 73]. As an alternative to using the pulse transients as input parameters, strategies of direct optimization on the spectrometer have also been reported [74, 75]. In these cases, the transfer function of the system is considered inherently in the optimization procedure. Determining the transfer function of the system and using it as an external optimization parameter is another way of increasing the robustness of the pulse sequence [76–78]. Nevertheless, the drawback of all of the approaches described above is the necessity to re-optimize the sequence for every setup. This is due to the fact that the transfer

function of the system changes with every alteration of the setup (filters, cable length, tuning/matching, dielectricity of the sample, etc.). This re-optimization can be time-consuming and rather cumbersome, especially when dealing with a low signal-to-noise ratio of the sample. A different approach for the compensation of pulse transients has been developed in the group of Takeda [79, 80] and implemented for symmetry-based sequences by Wittmann [34, 81]. This approach relies on the calculation and application of 'compensated' pulses based on the impulse-response function of the system measured directly in the probe with a pick-up coil. This approach is conceptually similar to actively compensating gradient pulses in magnetic resonance imaging, where this process is known as 'pre-emphasis' [82, 83]. This method of active compensation is used throughout this thesis and the influence of compensated pulses on resonant and non-resonant sequences is investigated.

3.1.2. Practical Pulse-Transient Compensation

Impulse-Response Function and Linear-Response Theory

The work-flow and practical considerations for the pulse-transient compensation is described in detail in the thesis of Wittmann [84] and is only sketched out roughly here. An elegant way to describe the transient response of a system is in the framework of linear-response theory [85, 86]. In this description, it is assumed that every output $y(t)$ of a linear system can be described as the convolution of the input $x(t)$ with the impulse-response function $h(t)$. The impulse-response function is the response of a system to a δ-pulse excitation. The assumption of the convolution is only valid if the system is i) linear, ii) causal, and iii) time invariant.

$$y(t) = x(t) \circledast h(t) = \int_0^\infty x(t')h(t-t')dt' \tag{3.2}$$

In the case of time-discrete signals, the output of the system is given by a discretized convolution

$$y[n] = \sum_0^\infty x[k]h[n-k]. \tag{3.3}$$

Deconvolution for the calculation of the required time-domain input is readily done in the frequency domain as a convolution in time domain corresponds to a multiplication
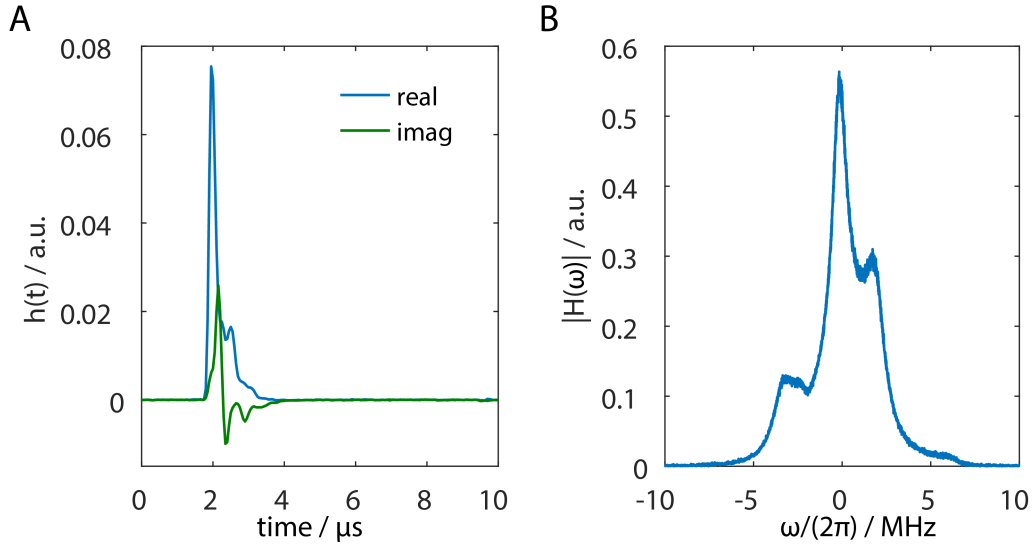
Figure 3.1. A) A characteristic example of a measured impulse-response function $h(t)$ in a solid-state NMR probe. B) The absolute value of the Fourier transform of the impulse-response function shown in A). The Fourier transform of the response to a δ-excitation is equal to the full excitation profile of the resonance circuit in the frequency domain.

in the frequency domain. Hence, Equation 3.2 can be re-written in terms of its Fourier transform

$$Y(\omega) = X(\omega) \cdot H(\omega) = \mathcal{F}(x(t)) \cdot \mathcal{F}(h(t)). \tag{3.4}$$

Only the shape files of time-domain signals will be shown here and discussed since the rf irradiation is of interest in the time domain. It will be assumed that the band width of the resonance circuit is always larger than the necessary basic frequencies. Applying linear-response theory and the concepts of time-domain signals to solid-state NMR, the input $x(t)$ corresponds to the single-pulse or multi-pulse sequences programmed in the computer and generated by the console. The system response $y(t)$ is the actual rf field that is seen by the spins in the sample. The system's output is measured with a small pick-up coil placed in close proximity to the stator. Consequently, the influence of all electronic components (cable, filter, amplifier, preamp, probe, etc.) is included in the impulse-response function. A characteristic example of a determined impulse-response function is shown in Figure 3.1.

Since the impulse-response function $h(t)$ is the output of the system to a Dirac δ-excitation, its Fourier transform $H(\omega)$ can be interpreted as the excitation profile of the complete resonance circuit in frequency space. A characteristic excitation profile is

shown in Figure 3.1B.

It has to be mentioned that two of the three criteria for linear-response theory are only approximations for real NMR systems. The linearity of the system is only valid for a certain range of pulse powers since it can be observed that the power amplifier from Bruker spectrometers exhibit non-linearities especially in the high-power regime. The second criterion of time invariance is also just an approximation as slight detuning or heating effects of the probe occurs in almost every experiment and the long-term stability is not perfectly provided. Lastly, the causality of the system is guaranteed since the response of the system never depends on future input signals but only on present and past values. The influence of non-linearities on actual NMR experiments is examined more closely in Chapter 3.3 using non-linear optimization.

Determining the Impulse-Response Function

In order to determine the impulse-response function, the output $y(t)$ of the system to an input $x(t)$ that is equal to a δ-excitation must be measured. Since it is physically impossible to generate a δ-pulse, any other input can be used, and from the measured output the transfer function can be determined by deconvolution in the frequency domain

$$H(\omega) = \frac{Y(\omega)}{X(\omega)}. \tag{3.5}$$

However, in practice the choice of input signal for the determination of the impulse-response function is critical. This is due to the fact that an input containing zeros leads to mathematical instabilities in the Fourier transform of the input and consequently the deconvolution becomes unstable. The most robust input function was found to be a maximum-length sequence (MLS) [87–89]. A maximum-length sequence is a pseudo-random noise sequence that is cyclic and made up of binary bits. The construction of a MLS is done recursively and the number of bits is $2^n - 1$. In practice, either the phase or the amplitude can be modulated and take the value $\{-1, +1\}$. The form of the exact sequence is not of crucial importance and is simply made up from a user-defined input seed. A great benefit of the MLS function is that its auto-correlation function is approximately equal to a δ-function. Therefore, the following relations hold true

$$\text{mls}(t) \circledast \text{mls}(t) \approx \delta(t) \tag{3.6}$$

and

$$\mathrm{mls}(t) \circledast h(t) = y^{\mathrm{mls}}(t). \tag{3.7}$$

Combining Equations 3.6 and 3.7 and adding a cyclic convolution with $\mathrm{mls}(t)$ to both sides of the equal sign leads to

$$\mathrm{mls}(t) \circledast y^{\mathrm{mls}}(t) = \mathrm{mls}(t) \circledast (\mathrm{mls}(t) \circledast h(t)) \tag{3.8}$$

$$= \delta(t) \circledast h(t) \tag{3.9}$$

$$= h(t). \tag{3.10}$$

In order to have meaningful measurements for the impulse-response function, certain requirements have to be fulfilled. The time during which the MLS is applied needs to be longer than the decay of the impulse-response function in order to avoid aliasing. Furthermore, the maximum amplitude of the MLS function should correspond to the one of the compensated pulses and it should be applied multiple times to mimic the cyclic character of the sequence as well as generate a steady-state condition in the probe.

Further Steps of Pulse-Transient Compensation

The determination of the impulse-response function is the most crucial and most sensitive step of the pulse-transient compensation procedure. Nevertheless, the choice of suitable pulse shapes to be compensated is also of great importance. One important requirement for the desired output shape is that the length of the pulse edge needs to be longer or in the order of the time constant of the whole resonance circuit. This can be approximated by determining the Q-factor of the probe, but usually a suitable edge time of the pulse is around 400 μs for typical solid-state NMR MAS probes. The influence of the detailed pulse shape will be discussed in more detail in Chapter 3.2.

After the correct setting of the pulse parameters, the time basis for the down mixing of the recorded pulses needs to be determined. The oscilloscope that is used for the measurement of the pulse shapes (Tektronix DPO 5204B) and the spectrometer are theoretically both clocked at 20 MHz but small deviations are still possible. In order to determine the correct time basis, a continuous wave irradiation is recorded, downsampled, and the slope of the phase is fitted. The difference in time bases is calculated based on the slope of the phase, which has to be 0 after the initial transient. In principle, it is also feasible to use an external clock from the spectrometer as a time basis for the
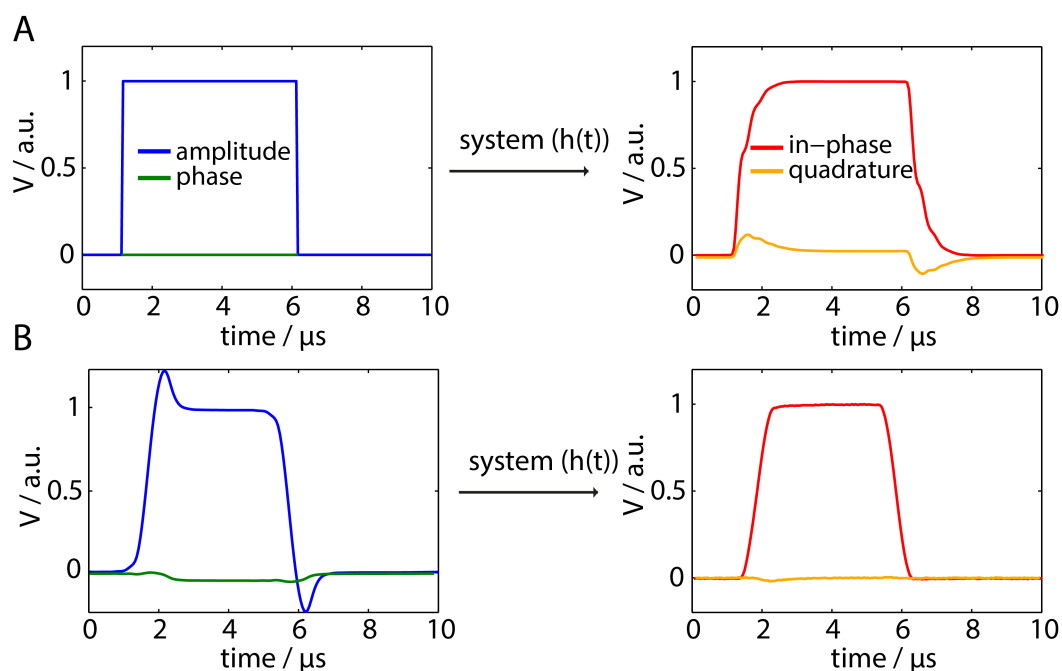
Figure 3.2. A) The input for a perfect rectangular pulse (blue, green) and its response at the probe (red, yellow). The transient is visible at the beginning and the end of the pulse as an exponential build-up respectively decay of the amplitude as well as the imperfect quadrature component. B) Compensated input file that yields a perfectly compensated pulse as an output.

oscilloscope. This was demonstrated to be a feasible approach and the step of frequency fitting can be omitted.

The impulse-response function is then determined based on the description above, and the compensated input files for the pulses are calculated. The shape files are then converted into standard Bruker shapes files with a time resolution of 50 ns and transferred to the spectrometer computer. A typical input file is shown in Figure 3.2B. Finally, the output of the compensated input file is measured and it is verified that the compensation was successful. In general, deviations of up to 1% are acceptable in the resulting B_1 field and are assumed to be negligible for the pulse sequence.

Experimental Setup of Pulse-Transient Compensation

A highly automated setup for the pulse-transient compensation has been developed before [84] and improved throughout the course of this thesis. The central piece of the experimental setup is an external computer with MATLAB (laukien.ethz.ch) that is connected to a fast, high-memory oscilloscope via a VXI-11 connection.

The oscilloscope settings are controlled and changed via MATLAB using the Simulink toolbox and modified instrument drivers. The shape files recorded with the oscilloscope are down-sampled and processed on laukien. At the same time, a home-written AU program is running on the spectrometer computer that executes a single-pulse experiment with variable shape files and parameters that are received from the laukien computer. The timing of the pulsing and the recording is done via trigger signals. One trigger dictates the timing of the pulsing in the AU program while the other trigger is for the oscilloscope to start the recording. In order to guarantee no aliasing, the recording speed of the oscilloscope is set to 5 GS/s for ^{13}C and to 10 GS/s for ^{1}H. In some instances, a sampling rate of 20 GS/s is required. The general work-flow and the connections of the experimental setup are shown in Figure 3.3. The relevant MATLAB scripts can be found in Appendix E.

The compensation procedure is nearly fully automated and the required user inputs are only the pulse parameters (pulse length, phase, and pulse-edge time) as well as the carrier frequency and the desired pulse power. In principle, the compensation can be
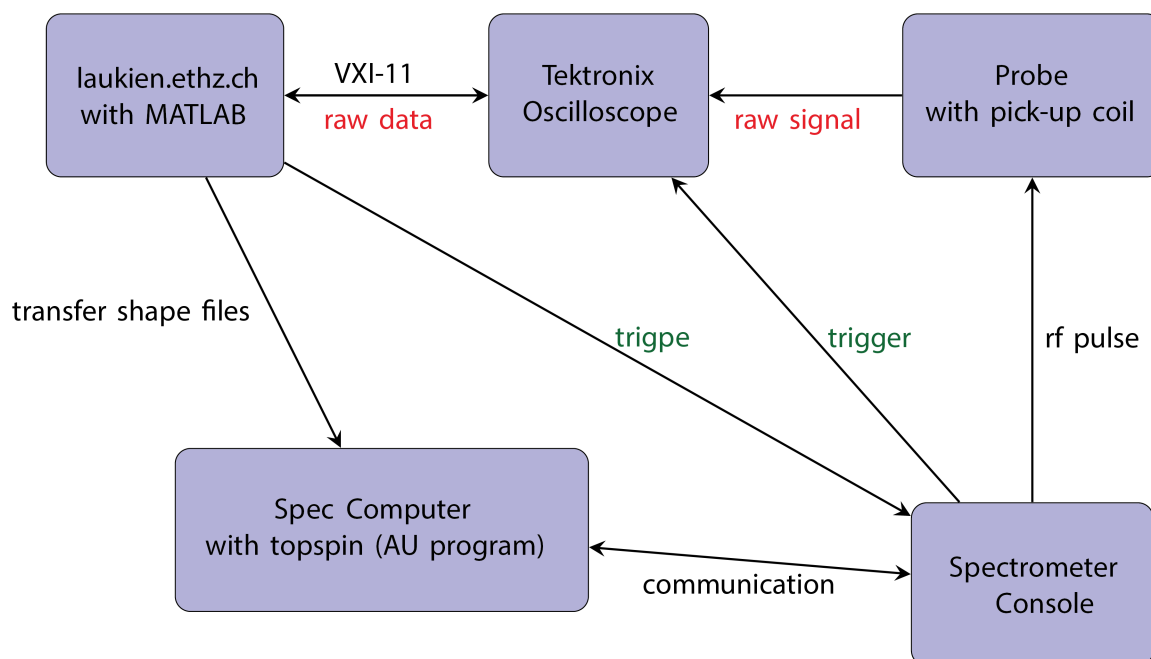

Figure 3.3. Schematic representation of the experimental setup used for pulse-transient compensation. The centre piece for the calculation of the shape files is an external computer (laukien.ethz.ch) using MATLAB and a VXI-11 connection to the high-speed oscilloscope with extended memory.

done fully on the spectrometer using the receiver with inverse gating as an oscilloscope but the current console generation (Avance HD III) is limited to time steps of 100 ns. The time step of 100 ns is too long for most resonance circuits of interest since it does not cover the full frequency range of interest. The covered frequency range is given by $\Delta\nu = \pm\frac{1}{2\Delta t}$ according to the Nyquist theorem. The required mathematical operations are fully implemented and automatized in TopSpin in order to calculate the desired input shape files.

3.2. Pulse-Shape Analysis

3.2.1. Pulse-Shape Fitting

In general, the pulse shapes are influenced most significantly by the quality of the resonance circuit, which changes with the observed nucleus. In the literature, only the pulse shapes of ^{13}C channel probes have been studied. In this thesis, a specific focus is placed on the pulse shapes of the ^{1}H channel due to the emergence of proton detection. Assuming the simple model for pulse transients given in Equation 3.1, a least-square fitting procedure with the two parameters τ_{rise} and ω_{off} is applied to measured pulse shapes. This model is only valid if all electrical components in the resonance circuit are matched to the same impedance. In practice, this assumption will never be truly fulfilled as many of the electrical components' impedance in the system is not matched to the required 50 Ω.

In Figure 3.4, three characteristic pulse shapes recorded on the ^{13}C channel on a 300 MHz spectrometer are shown. The best fitting result with the simple model is shown in blue and green. The difference in the pulse shapes results from three different cable lengths (A-C), which are representative setups throughout this work.

The fitting procedure of the pulse shapes is not always possible due to more complex pulse shapes. One example is shown in Figure 3.4A, where the fit does not resemble the measured pulse shape. This is due to the fact that the quadrature component of the pulse exhibits a small time delay in comparison to the amplitude build-up. This can be interpreted as a reflection of the pulse at a position that is not the rf coil and that leads to a delay in the anti-symmetric part of the pulse transient. However, theoretically modelling these transient behaviours is impossible as the time delay is not
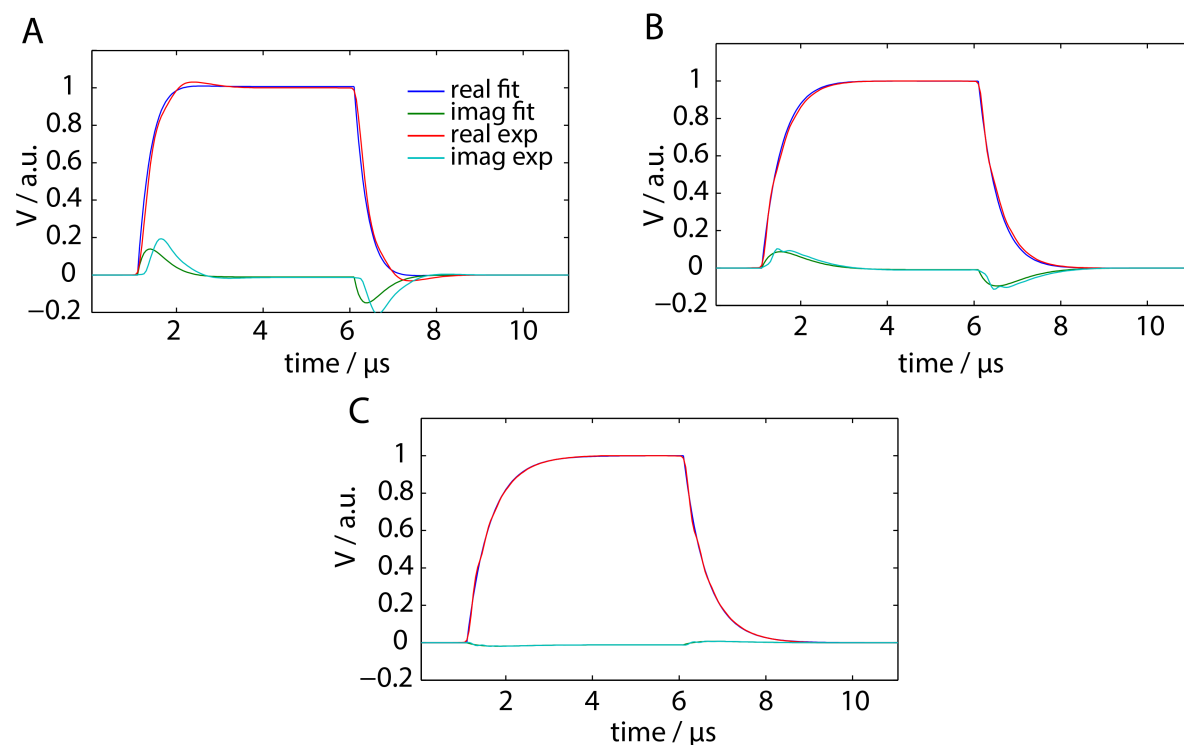
Figure 3.4. Characteristic pulse shapes for three different cable lengths (A-C) measured on the ^{13}C channel of a 300 MHz spectrometer. The experimental shapes are shown in red and turquoise and the fitted pulse shapes according to Equation 3.1 are shown in blue and green. The extracted fitting parameters are for A) τ_{rise}=0.31 μs, ω_{off}=206.6 kHz, for B) τ_{rise}=0.46 μs, ω_{off}=89.1 kHz and for C) τ_{rise}=0.53 μs, ω_{off}=-8.8 kHz.

readily determined. The other two pulse shapes shown in Figure 3.4B and C follow the single-exponential model and are fitted well. The build-up times are in the order of 500 ns, which is also the limiting factor for the pulse edges for the compensated shape files. Cable C presents a configuration in which the quadrature component is minimized and no out-of-phase rotational part is expected (assuming single pulse experiments).

The fitting parameters extracted from these pulse shapes can be used to back-calculate the impulse-response function of the system. The calculated impulse-response function is then convoluted with a multi-pulse input in order to model the transient behaviour for more complex sequences and back-to-back pulses.

3.2.2. Pulse-Shape Optimization

In order to generate suitable pulse shapes, discontinuities in the phase and amplitude have to be avoided. Any discontinuity causes a pulse transient, and these must be avoided for the compensated shape files. The best pulse sequence in terms of pulse imperfections is a implementation in which the phase for multi-pulses is switched continuously. However, only very few pulse sequences with continuous phase modulations exist. Therefore, suitable pulse shapes are generated with a finite edge and for every phase discontinuity the amplitude is ramped down to zero. As discussed previously, the edge time of the pulse is limited by the characteristic time constant of the resonance circuit.

A suitable solution for the form of the pulse is a shaped pulse with a sine-squared edge shape. Therefore, the pulse shape is defined as

$$
\omega_1(t) = \omega_1 \cdot
\begin{cases}
\sin^2\left(\frac{\pi t}{2\tau_{\text{edge}}}\right) & 0 < t \le \tau_{\text{edge}} \\
1 & \tau_{\text{edge}} < t < \tau_{\text{p}} - \tau_{\text{edge}} \\
\sin^2\left(\frac{\pi(\tau_{\text{p}} - t)}{2\tau_{\text{edge}}}\right) & \tau_{\text{p}} - \tau_{\text{edge}} \le t \le \tau_{\text{p}}.
\end{cases}
\tag{3.11}
$$

The total duration of the pulse τ_{p} needs to be the same as the rectangular or 'hard' pulse that the shape file is replacing but the maximum amplitude ω_1 has to be adjusted to compensate for the reduced amplitude during the rising and falling edge. This calibration of the flip angle is done by scaling the compensated pulse to the same integral as the hard pulse.

The shape of the edge is a parameter to be optimized for the best convergence of the compensation. The simplest shape is a linear edge, which results in a trapezoidal pulse form. However, this would lead to a discontinuity again in the pulse, which might lead to divergence in the compensation. In order to examine the quality of pulse shapes, several functional forms of edges (linear, sine^2, sine^4, Gaussian, Lorentzian) are tested towards the stability of signal generation. The desired pulse shape is approximated with a Fourier series that has a basic modulation frequency of $\frac{1}{\tau_{\text{p}}}$ and only symmetric sine terms

$$
f(t) = \sum_{n=1}^{\infty} b_n \sin\left(\frac{2\pi n}{\tau_{\text{p}}}\right).
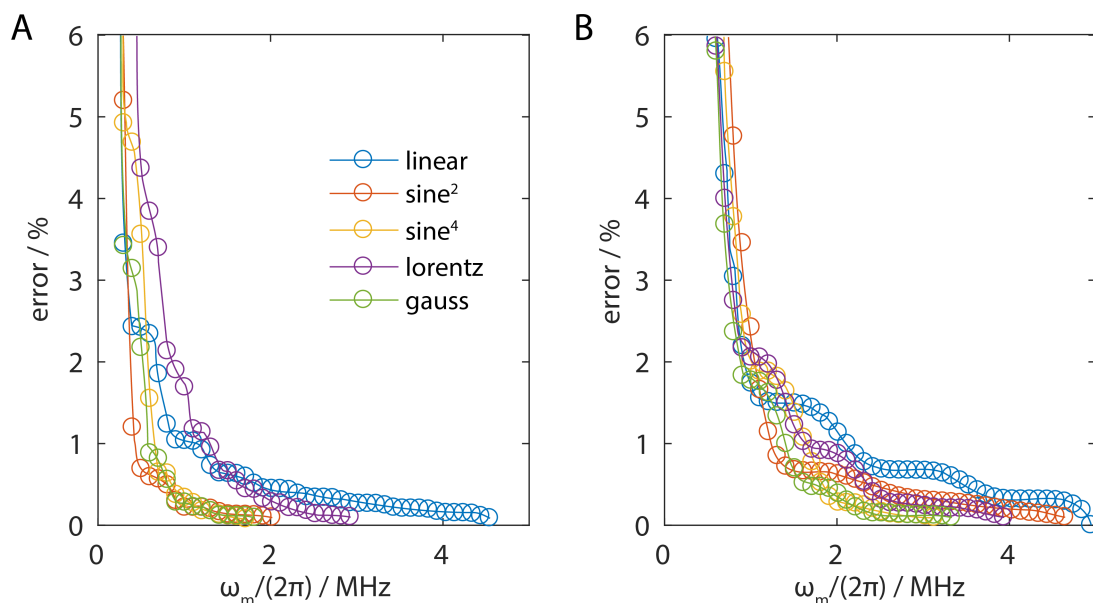\tag{3.12}
$$

Figure 3.5. Convergence of the signal generation of pulse shapes with various functional edges. The signal is approximated by a Fourier series with symmetric terms (sine terms) and a basic frequency of $\frac{1}{\tau_p}$ with a pulse length of 5 μs. A pulse shape with a 1 μs edge time (A) converges faster than a 0.4 μs edge time (B). The cut-off was chosen to be a 0.05% deviation from the desired target shape.

The series is stopped if the deviation of the target shape and the fit is less than 0.05%, and the maximum frequency needed to generate the shape is plotted in Figure 3.5. The fastest convergence is observed for the sine-squared function for long pulse-edge times (Fig. 3.5A), and the Gaussian function for short pulse-edge times (Fig. 3.5B). Despite the difference in convergence, the errors are fairly small for the different edge shapes already at low modulation frequencies. It is assumed that other sources of errors have a bigger influence on the compensation, as for the measured pulse shapes deviations up to 1% are observed.

3.3. Non-Linear Optimizer

The approximation of linear-response theory has certain weaknesses for the application to solid-state NMR and the pulse-transient compensation. The biggest problems are time-dependent instabilities in the tuning and matching, amplifier droops, and non-linear features of the amplifier. All of these problems can be circumvented if the pulse-transient compensation procedure is based on a non-linear optimization. This has to

be done via a feedback loop and can either be done with a PID controller [90] or a minimizer like the Levenberg-Marquardt algorithm [91–93]. The governing equation for the Levenberg-Marquardt algorithm (or any non-linear least square method) is

$$f(x) = \sum_{j=1}^{n} r_j^2(x) \tag{3.13}$$

with r_j being the residuals and $f(x)$ the function which needs to be minimized. The Jacobian matrix J in this case is taken to be the impulse-response function of the system. Therefore, the Hessian H is easily calculated in a near-linear approximation as

$$H = \nabla^2 f(x) \approx J^T J \tag{3.14}$$

and the first derivative of $f(x)$ as

$$\nabla f(x) = J \cdot r. \tag{3.15}$$

The starting value for the input x is chosen to be the calculated shape from linear-response theory. The further input values are calculated iteratively with the gradient descent method. The $(i + 1)$th input is given by

$$x_{i+1} = x_i - (H + \lambda I)^{-1} \cdot \nabla f(x_i) \tag{3.16}$$

with λ being the damping parameter and I the identity matrix. If the error is reduced in the iterative step, λ is decreased and otherwise augmented. The results of a simulated multi-pulse sequence using the minimizer are shown in Figure 3.6. The second derivate was added as an additional constraint to the minimization process to guarantee smoothness of the input shape.

Despite the promising simulated results, the minimizer does not work experimentally on a multi-pulse sequence. This is presumably due to numerical instabilities at the zero-amplitude points at which the phase discontinuity is present. The randomness of the measured phase value at zero amplitude introduces an illogically high error that pushes the minimizer in the wrong direction and convergence is not achieved. However, it is possible to compensate a single pulse using the non-linear optimization.
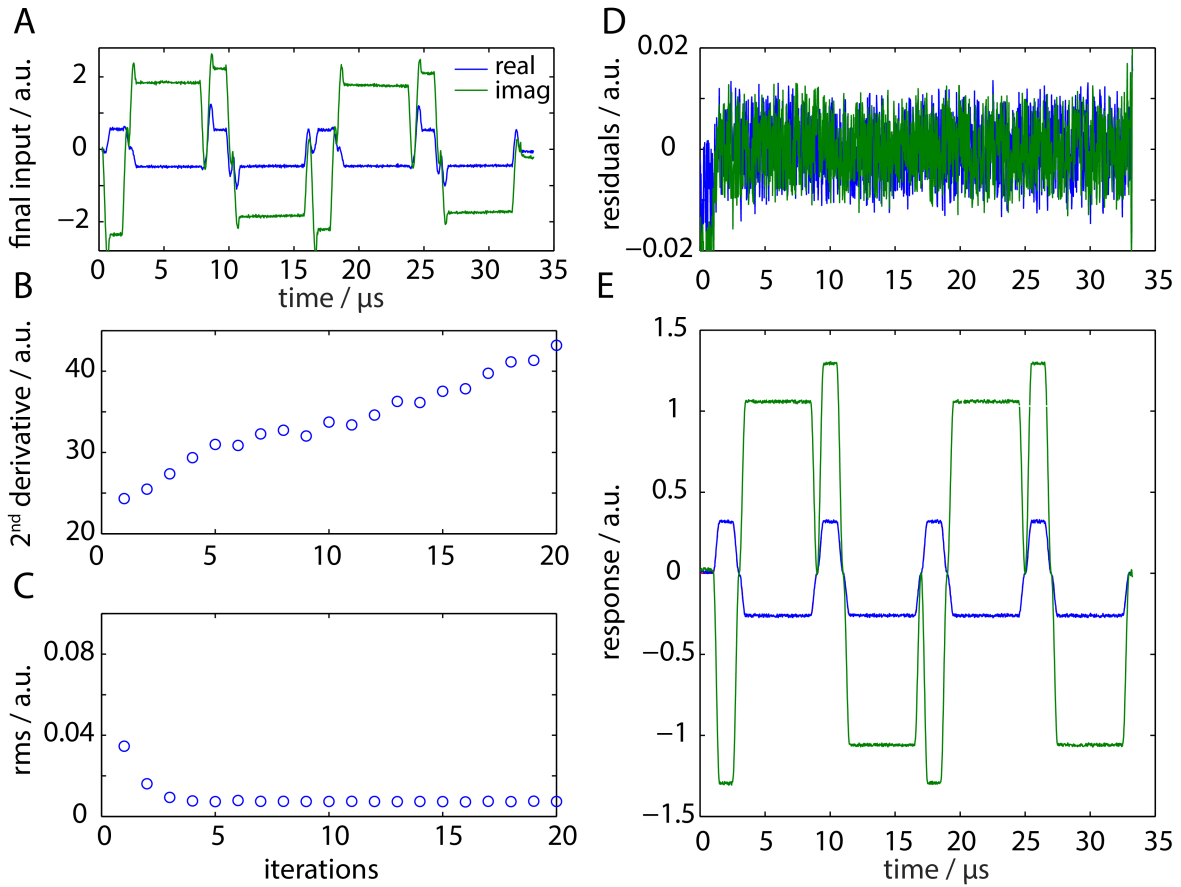
Figure 3.6. Simulated multi-pulse shapes using a Levenberg-Marquardt algorithm for the minimization of the residuals. Gaussian noise of 0.01 was added to mimic experimental conditions. The minimizer was stopped after the root-mean-squared was below 0.012 (panel C). The residuals are shown in panel D, the input and corresponding output of the last iteration step are shown in panel A and E, respectively. The second derivative of the residuals (B) was added as an additional constraint to guarantee smoothness of the input shape. The residuals of the output shape and the target shape (D) do not show unusual behaviour at the phase discontinuities proving that the minimizer works theoretically.

The simplest experiment to judge the quality of the pulse in terms of quadrature components is a nutation experiment. A perfect pulse will lead to a perfect zero crossing and absorptive line shapes. The nutation curves recorded with rectangular, linearly compensated, and non-linearly compensated pulses are shown in Figure 3.7. The improvement of the compensated pulses (Fig. 3.7D and E) versus the uncompensated pulse (Fig. 3.7F) is obvious. However, it is hard to judge whether there is an actual improvement going from the linear to the non-linear compensation. Furthermore, it is also unclear if this small improvement is visible and crucial in multi-pulse experiments.
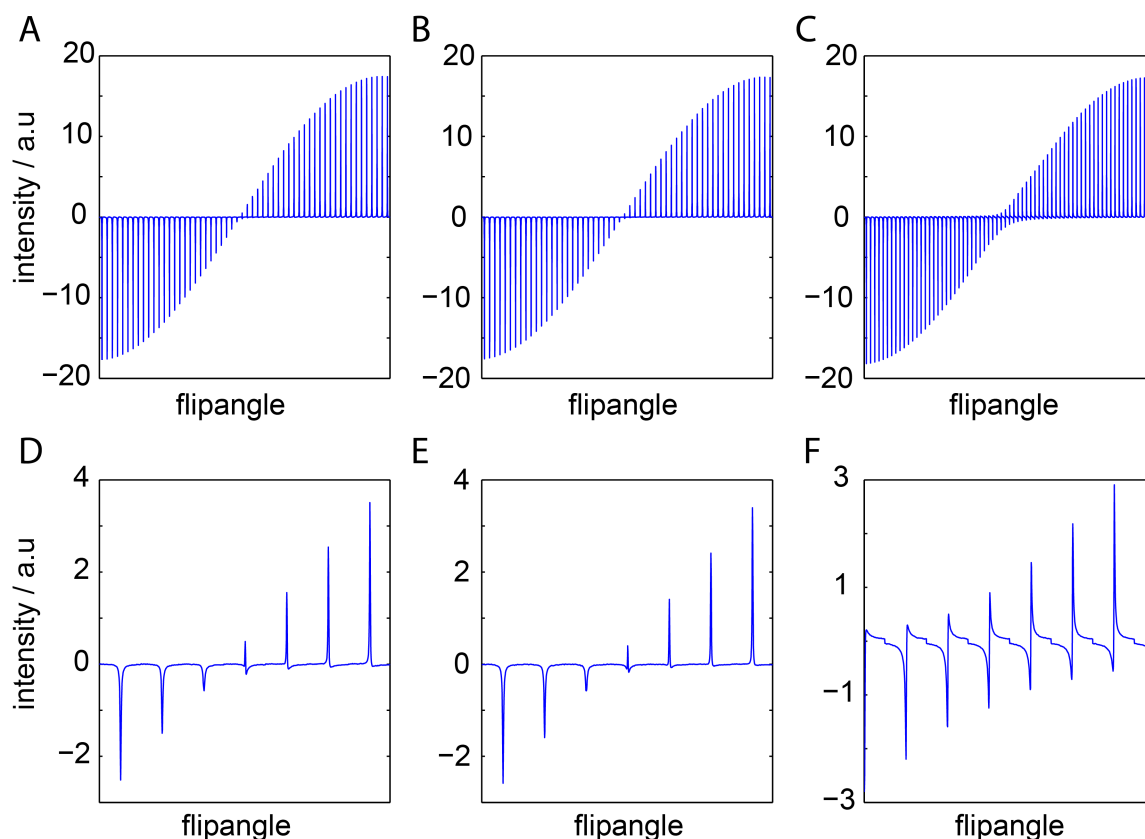
Figure 3.7. Experimentally measured nutation curves for a single pulse. The pulse was either programmed as a rectangular pulse (C) or a compensated pulse using linear-response theory (A) or a non-linear optimizer (B). The zoom of the zero crossing (D-F) shows the quality of the pulse. Due to the large quadrature components in the rectangular pulse, the zero crossing shows a dispersive line (F) while the compensated pulses generate an almost perfect absorptive line shape (D and E).

3.4. Bidirectional Coupler

The use of an externally installed pick-up coil in the probe to record the pulse shape places a big limitation on the wide applicability of the transient compensation. If this compensation method becomes routinely implemented in spectrometer technology, a small antenna near the sample can easily be implemented in the constructions of the probe. Up to this point, however, the recording of the pulse shape has to be done via a home-made device. In the course of this thesis, we have tried to find alternative routes to record the pulse shapes.

One solution for the recording of the pulse shape was developed and applied by Zdeněk Tošner [30]. In this approach, the signal transmitted by the dewar in the probe was

picked up via the heater input. We confirmed in experiments that the obtained impulse-response function from the pick-up coil and the transmission from the dewar was identical. A major drawback of this approach is the requirement of sufficient signal transmission through the dewar. This is not always guaranteed as multiple probes are constructed without strongly transmitting materials in order to avoid unwanted effects.

A different approach does not involve the manipulation of the probe itself but rather the detection of the signal before and after it enters the probe. In theory, the difference of these two signals corresponds to the power dissipated in the sample, i.e. the rf field that is seen by the spins. The time difference between the forward and the reflected power has to be considered as the travel time in the probe. The forward and reflected signal is recorded simultaneously with a bidirectional coupler. A schematic drawing of the setup is shown in Figure 3.8.

The most critical step in this procedure is the determination of the time difference between the forward and the reflected power. Several approaches are possible; the simplest one is the calculation of the difference of the first points in the pulse. The signal-to-noise of the measured voltages are high enough to readily determine the onset of the pulse.
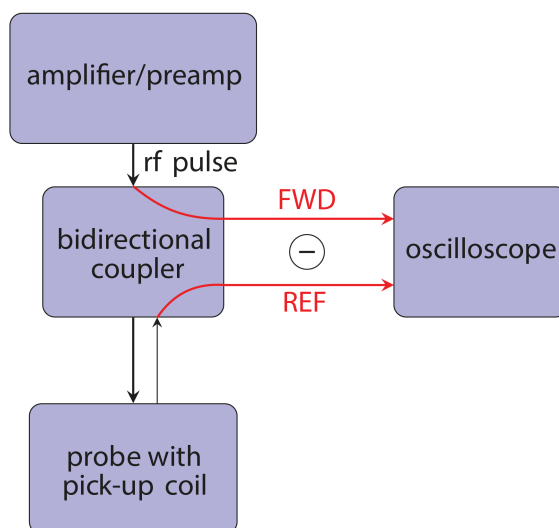

Figure 3.8. Experimental setup for the measurement of pulse shapes with a bidirectional coupler. In theory, the forward and reflected power subtracted yield the power dissipated in the sample. The time difference is approximated from the first point of the rising edge of the pulse with the same trigger signal on both channels of the oscilloscope.

A second approach is a linear fit of the time difference measured with various cable lengths between the bidirectional coupler and the probe. This linear fit has a higher tolerance towards errors than the time difference arising from the determination of a single point. The increment in time difference is known precisely, as the velocity of the signal in a coaxial cable is given by $2/3 \cdot c$, with c being the speed of light. Furthermore, the difference in cable length is an easily measurable quantity. This approach allows the extraction of the travel time of the signal in the probe and gives a reliable calibration for every channel on different probe.
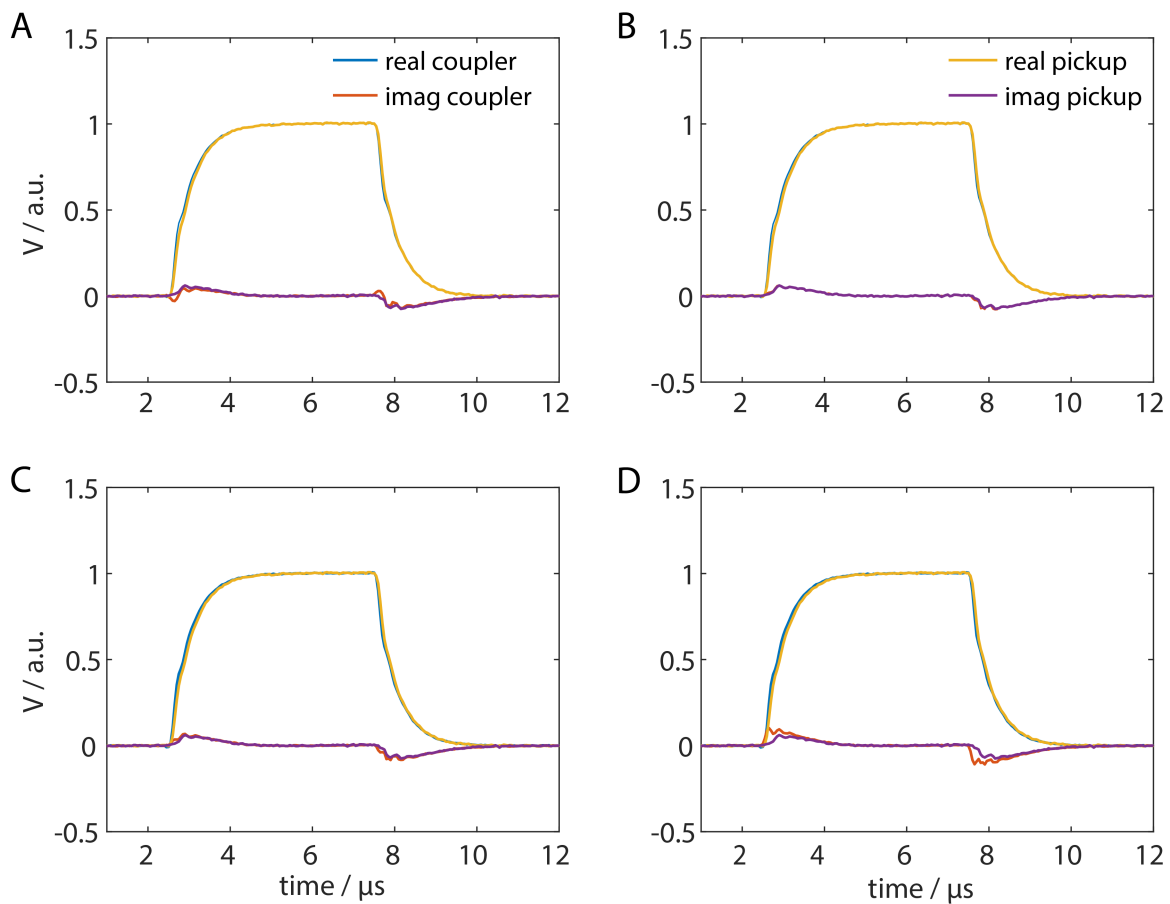

Figure 3.9. Comparison of pulse shapes recorded with the pick-up coil (yellow, purple) and shapes calculated as the difference from the bidirectional coupler (blue, red). The four different panels symbolize various time delays between the forward and the reflected power: A) 25.85 ns, B) 26.05 ns, C) 26.10 ns, D) 26.35 ns. Only the delay of B) yields the exact same pulse shape and even a time difference of 0.05 ns as seen in C) leads to small errors in the phase. Therefore, a high-speed oscilloscope (20 GS/s) is required to reliably determine the correct pulse shape.

Both approaches yield time differences that are in the correct range, although the determination of the exact pulse shape is still problematic. This is due to the fact that the exact timing is crucial and conventional oscilloscopes do not have the required time resolution. In order to have the highest time resolution possible, a special oscilloscope with 20 GS/s, corresponding to 0.05 ns per point, was used to prove the principle.

It is shown in Figure 3.9 that it is possible to determine the exact pulse shape using the bidirectional coupler. Furthermore, it is also shown that the exact timing between the forward and the reflected power is critical as a difference of 0.05 ns already introduces errors.

The biggest drawback of this approach is the assumption that the system is perfectly matched in impedance and the power is only reflected at the rf coil. For the example presented in Figure 3.9 this assumption is valid and good results are obtained. However, different setups have been tested in which this assumption of impedance matching is not valid and the pulse shape measured with the pick-up coil could not be reconstructed with the bidirectional coupler. These setups often coincide with pulse shapes that are not fit-able with the mono-exponential model for an imperfect resonance circuit given in Equation 3.1.

4. Isolated π-Pulse Sequences

- Parts of this chapter are published in:
  J. Hellwagner, ... , M. Ernst, *J. Magn. Reson.*, **2018**, *287*, 65-73

4.1. Introduction to RFDR and REDOR

Isolated π-pulse sequences are widely used in solid-state NMR because of their simplicity and they are, therefore, an essential building block in many experiments [35–38, 94]. The biggest advantage of such sequences is the ease of experimental implementation because the recoupling of the dipolar interaction is done with simple inversion pulses that are synchronized with the rotor period. The only constraints for the radio-frequency (rf) field amplitude are that the pulses must correspond to π rotations and two must fit in the rotor period. There are two π-pulse sequences in particular, Radio-Frequency Driven Recoupling (RFDR) [35] for homonuclear recoupling and Rotational Echo Double Resonance (REDOR) [37, 38] for heteronuclear recoupling, that are prominent sequences and are frequently used as building blocks for polarization transfer in multi-dimensional experiments. Additionally, REDOR has been used as a simple and effective way to characterize the amplitude of backbone motions and dynamics in proteins [95, 96].

While π-pulse sequences are very well-characterized theoretically under ideal conditions, i.e. either for ideal (infinitely short) or finite rectangular pulses [35–38, 97], the effects of pulse imperfections on the performance of such sequences are not very well studied. Other error parameters like offset effects or rf-field miscalibration are studied as a function of different phase cycles [98–100]. However, pulse imperfections like deviations from the desired rotation axis due to rf-field inhomogeneity or pulse transients can lead to deterioration of the performance of pulse sequences. In the picture of Floquet theory, these imperfections cause effective fields that deteriorate the resonance condition and destroy the transfer efficiency. The influence of such effective fields on pulse sequences
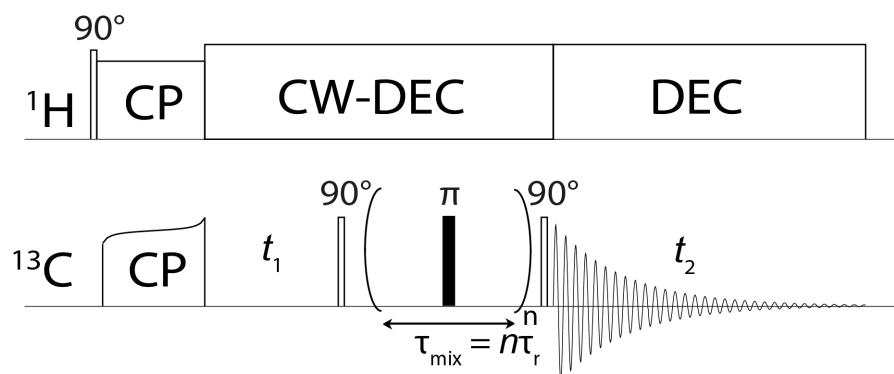
Figure 4.1. Pulse sequence for RFDR experiments. For measurements in two-spin systems and model compounds, the t_1 evolution period was omitted and a selective excitation before the z-filter was performed. The various phase cycles and the transient compensation was applied on the π pulses during the mixing period.

with isolated π pulses is studied in detail theoretically and experimentally in this chapter.

For periodic π-pulse sequences phase cycling is an essential requirement for good performance, as was discussed in the literature. The phase cycle is not only necessary to remove error terms like offset effects, pulse transients, or rf-field maladjustment, but also to remove unwanted terms in the average Hamiltonian. For REDOR, a XY4 phase cycle is needed for rectangular, finite pulses, in order to suppress contributions to the effective Hamiltonian other than the desired $2I_zS_z$ term [97, 98]. In theory, no phase cycle on the π-pulse train is needed for RFDR, but it was shown in the literature that for RFDR on ^{13}C nuclei a XY8$_4^1$ phase cycle is the most robust towards offset effects [99], and for RFDR on ^{1}H a XY4$_4^1$ performs best in the presence of rf-field inhomogeneity [100].

The basic pulse sequence for a 2D correlation experiment using RFDR is shown in Figure 4.1. The recoupling is implemented by rotor-synchronized π pulses on the X-channel. The mixing time has to be optimized experimentally and depends on the effective coupling determined by the strength of the dipolar coupling and the isotropic chemical-shift difference of the spin pair. An experimental modification is an adiabatic version of the RFDR recoupling. In this modified experiment, the position of the π pulse is varied with respect to the centre of the rotor period to create an adiabatic sweep through the recoupling condition [101]. To study the recoupling efficiency as a function of the mixing time and the rf-field amplitude, the experiment can be implemented as a pseudo-2D experiment setting the mixing time as a variable.

The most common phase cycles applied on the π-pulse train are XY4, XY8, and XY16, and supercycles thereof. In the theory section, we focus on three parameters, the small rf-field maladjustment, the isotropic chemical-shift offset, and the magnitude of the phase transients as a function of the various phase cycles.

The basic pulse sequence for a REDOR experiment bears close resemblance to the RFDR experiment (Figure 4.2). In the most simple experiment, the recoupling is done by two π pulses per rotor period that are spaced equally. A time shift of one of the pulses scales down the dipolar coupling and leads to a slower dephasing, but also induces a mixing of both Fourier components in the average Hamiltonian [38]. The mixing of the two Fourier components leads to a different functional form of the dephasing that has to be fitted with a grid search. A more practically applicable implementation was published by the group of P.K. Madhu and V. Agarwal. In their implementation, both π pulses are shifted and the spacing of $0.5\tau_{\mathrm{r}}$ is kept between the pulses. Additionally, the shift is symmetric around the refocusing pulse in the middle of the recoupling period. This introduces an additional phase in the Hamiltonian, which is compensated in the second half of the sequence. This introduces an effective scaling of the dipolar coupling and leads to slower dephasing curves. Through the constant spacing, the Fourier component $n = 2$ is still averaged out and the functional form of a simple REDOR curve is preserved [102].
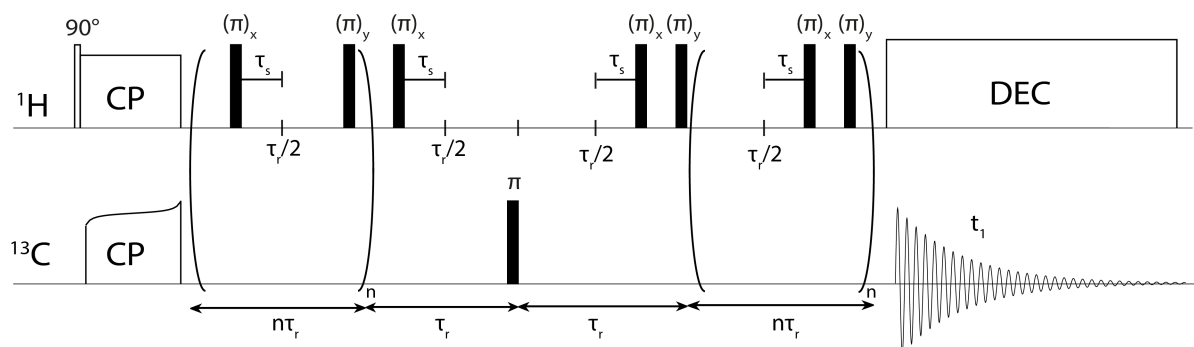

Figure 4.2. REDOR pulse sequence to measure the heteronuclear ^{1}H-^{13}C dipolar coupling. The π-pulse train is usually applied to the passive spin. The phase cycle and the transient compensation were applied to the π-pulse train on the passive spin. No compensation was added to the refocusing π pulse on the ^{13}C channel. The optional time shift τ_{s} is shown on the proton channel. For the implementation presented in [102], both π pulses are shifted.

The phase cycles used in REDOR are identical to the ones used in RFDR, although the literature is not as extensive as for RFDR. However, it was shown with average Hamiltonian theory that an XY4 phase cycle has to be applied to avoid unwanted $I_y S_z$ contributions to the Hamiltonian.

4.2. Simulations for RFDR

4.2.1. Theoretical Description of RFDR

Periodic and cyclic pulse sequences, like RFDR, can be described using average Hamiltonian theory if the modulation frequency of the pulse sequence is commensurate with the MAS frequency [103]. This is the case for all rotor-synchronized sequences given that the total radio-frequency (rf) propagator is a unity operator. A more general description can be based on Floquet theory which does not require rotor synchronization or a rf propagator that is a unity propagator. Average Hamiltonian theory and Floquet theory of recoupling pulse sequences are usually based on a transformation of the Hamiltonian into an appropriate interaction frame to make the series expansion converge faster [20–23]. For this, the spin-system Hamiltonian is transformed into an interaction frame with a Hamiltonian $\hat{\mathscr{H}}_1$, which typically contains the rf-field part of the Hamiltonian and may contain additional dominating terms. One such additional term that is sometimes required in the interaction-frame transformation is the chemical-shift offset. For example, Lee-Goldburg-type homonuclear decoupling sequences [42, 104] require such a description for a fast convergence of the average Hamiltonian. In another example, it was recently shown that the offset dependence of heteronuclear decoupling using a two-pulse sequence can also be described using such an approach [105]. For π-pulse sequences, including the isotropic chemical shift into the interaction-frame transformation is required for a correct description of RFDR [106]. In the most general case, the transformation for the interaction-frame Hamiltonian is given by

$$\hat{\tilde{\mathscr{H}}}(t) = \hat{U}^{-1}(t)\hat{\mathscr{H}}\hat{U}(t) \tag{4.1}$$

with the propagator

$$\hat{U}(t) = \hat{T} \exp\left(-i \int_0^t \hat{\mathscr{H}}_1(t') dt'\right) \tag{4.2}$$

where $\hat{T}$ is the Dyson time-ordering operator [56]. The combined rf and chemical-shift Hamiltonian in the rotating frame is given by

$$\hat{\mathscr{H}}_1(t) = \omega_1(t) \sum_p \left(\cos(\phi(t))\hat{S}_{px} + \sin(\phi(t))\hat{S}_{py}\right) + \sum_p \omega_p^{(0)} \hat{S}_{pz} \tag{4.3}$$

where $\omega_1(t)$ is an arbitrary time-dependent rf-field amplitude, $\omega_p^{(0)}$ the isotropic chemical shift, $\phi(t)$ the phase of the pulse, and p the index of the spin. Applying the propagator of Equation 4.2 to a single spin can be described in Liouville space as a rotation of the three Cartesian one-spin basis operators by a time-dependent rotation matrix $\mathbf{R}_p(t)$

$$\begin{pmatrix} \hat{\tilde{I}}_{px} \\ \hat{\tilde{I}}_{py} \\ \hat{\tilde{I}}_{pz} \end{pmatrix} = \mathbf{R}_p(t) \begin{pmatrix} \hat{I}_{px} \\ \hat{I}_{py} \\ \hat{I}_{pz} \end{pmatrix}. \tag{4.4}$$

The time-dependent elements of the rotation matrix, also sometimes called the interaction-frame trajectory of spin p, allow the calculation of important properties of the pulse sequence. The effective flip angle can be calculated by

$$\beta_{\text{eff}}^{(p)} = \arccos\left(\frac{\text{Tr}\{\mathbf{R}_p(\tau_{\text{m}})\} - 1}{2}\right) \tag{4.5}$$

where τ_{m} is the cycle time of the pulse sequence. For most ideal rotor-synchronized recoupling sequences, the flip angle will be zero or a multiple of 2π but in case of real, imperfect pulses, the flip angle can deviate from its theoretical value and generate an additional effective nutation frequency. The direction of this effective field is given by

$$\frac{\vec{\omega}_{\text{eff}}^{(p)}}{|\vec{\omega}_{\text{eff}}^{(p)}|} = \frac{1}{2\sin\left(\beta_{\text{eff}}^{(p)}\right)} \begin{pmatrix} R_{32} - R_{23} \\ R_{13} - R_{31} \\ R_{21} - R_{12} \end{pmatrix} \tag{4.6}$$

and its magnitude

$$|\vec{\omega}_{\text{eff}}^{(p)}| = \beta_{\text{eff}}^{(p)} \omega_{\text{m}} \tag{4.7}$$

where $\omega_{\text{m}} = 2\pi/\tau_{\text{m}}$ is the modulation frequency of the pulse sequence. Note that adding the chemical-shift offsets into the interaction-frame transformation makes the interaction-frame transformation and, therefore, also the flip angle and effective nutation frequency dependent on the spin considered. The matrix elements $\text{R}_{ij}(t)$ of the rotation matrix $\mathbf{R}_p(t)$ can be written as a Fourier series with the two basic frequencies ω_{m} and ω_{eff} as

$$\text{R}_{ij}(t) = \sum_{k=-\infty}^{\infty} \sum_{\ell=-1}^{1} a_{ij}^{(k,\ell)} e^{ik\omega_{\text{m}}t} e^{i\ell\omega_{\text{eff}}t}. \tag{4.8}$$

The time dependence of the two-spin terms in the Hamiltonian is described by the direct product of two one-spin rotation matrices, i.e., $\mathbf{R}_{p,q}(t) = \mathbf{R}_p(t) \otimes \mathbf{R}_q(t)$.

Therefore, the interaction-frame Hamiltonian has different effective fields for each of the spins. Since we are interested in dipolar recoupling of two coupled spins, we will limit the description to two spins and we obtain an interaction-frame Hamiltonian with four frequencies

$$\hat{\bar{\mathscr{H}}}(t) = \sum_{n=-2}^{2} \sum_{k=-\infty}^{\infty} \sum_{\ell=-1}^{1} \sum_{m=-1}^{1} \hat{\bar{\mathscr{H}}}^{(n,k,\ell,m)} e^{in\omega_{\text{r}}t} e^{ik\omega_{\text{m}}t} e^{i\ell\omega_{\text{eff}}^{(1)}t} e^{im\omega_{\text{eff}}^{(2)}t}. \tag{4.9}$$

In this case, the first-order effective Hamiltonian is given by

$$\overline{\hat{\mathscr{H}}}_{\text{eff}}^{(1)} = \hat{\bar{\mathscr{H}}}_{(1)}^{(0,0,0,0)} + \sum_{n_0,k_0,\ell_0,m_0} \hat{\bar{\mathscr{H}}}_{(1)}^{(n_0,k_0,\ell_0,m_0)} \tag{4.10}$$

at the four frequency resonance condition

$$n_0\omega_{\text{r}} + k_0\omega_{\text{m}} + \ell_0\omega_{\text{eff}}^{(1)} + m_0\omega_{\text{eff}}^{(2)} = 0. \tag{4.11}$$

If the effective fields of the two spins are the same ($\omega_{\text{eff}}^{(1)} = \omega_{\text{eff}}^{(2)}$), the description collapses to a tri-modal Floquet problem and in the case of vanishing effective fields ($\omega_{\text{eff}}^{(1)} = \omega_{\text{eff}}^{(2)} = 0$) to a bi-modal Floquet problem with the resonance condition $n_0 \omega_{\text{r}} + k_0 \omega_{\text{m}} = 0$. Here, we will only discuss the effects of the effective fields that lead to a detuning from the rotor-synchronization condition and not more subtle effects caused by changes in the Fourier coefficients of Equation 4.8.

For periodic π-pulse sequences with ideal, finite pulses it can be shown that the effective field is always zero if offset effects are neglected. In simple cases, e.g. for ideal rectangular pulses of finite length, the interaction-frame trajectory can be calculated analytically. More interesting is the case of imperfect pulses, i.e. the effect of pulse transients on the magnitude and the direction of the effective field. In general, a numerical calculation of the interaction-frame transformation can be performed by discretizing the cycle time of the pulse sequence assuming that the rf Hamiltonian is piece-wise constant for the chosen time step (50 ns). Using Equations 4.5-4.7, the magnitude and the direction of the effective field can be calculated for any given pulse sequence.

The interaction-frame transformation for the RFDR pulse sequence used in the following chapter includes the isotropic chemical-shift terms into the interaction-frame Hamiltonian. The calculated effective field and its direction will be used to make theoretical predictions about the recoupling efficiency. Further information, like second-order error terms, can also be predicted using Floquet theory. A detailed Floquet description of the RFDR sequence can be found in Ref. [101] and will not be given here. The interaction-frame transformation for the REDOR experiment requires only the rf-field Hamiltonian acting on a single spin. Therefore, we will only have a single effective field that can lead to a detuning from the rotor-synchronization condition.

4.2.2. The Influence of Chemical-Shift Difference

The magnitude and the direction of the effective field allow a good estimation of the performance of the sequence. A small effective field guarantees a bi-modal resonance condition that follows the ideal theoretical description of the sequence. Following the interaction-frame calculation outlined in Chapter 4.2.1, the effective field for the most common phase cycles (XY4, XY8, and XY16) were calculated numerically. A time
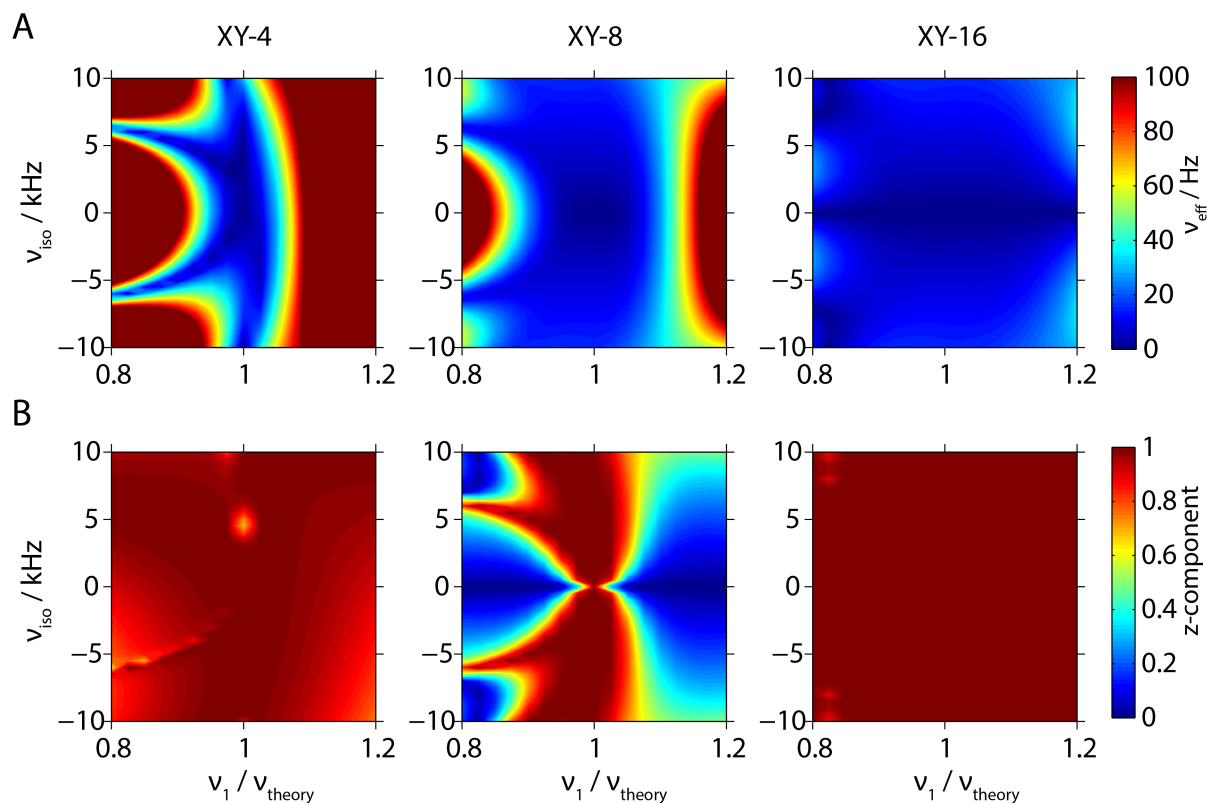
Figure 4.3. The magnitude of the effective field (A) and the normalized z-component (B) for three different phase cycles of an RFDR π-pulse train as a function of the isotropic chemical shift and the rf-field maladjustment. The MAS frequency was set to 30 kHz with a pulse length of 5 μs. Upon deviation from the theoretical values, the magnitude of the effective field increases rapidly for an XY4 phase cycle but its orientation remains parallel to the z-direction. The rf-field error is better compensated for XY8 and XY16 but the effective field direction is in the xy-plane for the XY8 phase cycle.

step of 50 ns was used over which the Hamiltonian was assumed to be constant. The isotropic chemical shift $\omega_p^{(0)}$ was included in the calculation as a variable according to Equation 4.3. The influence of the isotropic chemical shift and the deviation of the rf-field amplitude from the theoretical value on the magnitude of the effective field are depicted in Figure 4.3.

For rectangular pulses the effective field is symmetric for positive and negative isotropic chemical shifts. For small deviations (in the order of 5%) of the rf-field amplitude from the theoretical value, the magnitude of the effective field already becomes substantial for an XY4 phase cycle. The effective fields due to deviations of the rf-field amplitude from the theoretical value are better compensated by the XY8 and XY16 phase-cycling schemes. The direction of the effective field is primarily in the z-direction for XY4 and

XY16 as compared to XY8 where it is in the xy-plane even for small deviations of the rf field from the theoretical value. An effective field in the z-direction commutes with the ZQ RFDR Hamiltonian and is not detrimental to the transfer efficiency. It only has a small influence on the pulse sequence unless the magnitude of the effective field becomes significant and the resonance condition is no longer matched. However, an effective field orthogonal to the z axis does not commute with the ZQ Hamiltonian and deteriorates the total axis of rotation and alters the resonance condition for the RFDR transfer, as observed for the XY8 phase cycle.

4.2.3. The Influence of Phase Imperfections

The identical calculations of the interaction-frame trajectory using real pulses with phase transients lead to a less certain prediction of the effective field. The magnitude and the direction are not symmetric for positive and negative chemical-shift values and the compensation of the effective field towards higher phase imperfections becomes worse. In regards to phase transients, the XY4 phase cycle is performing worse than the XY8 and the XY16. However, the direction of the effective field is almost completely along the z-direction for XY4 and XY16 whereas for XY8 the z-component decreases slightly for high quadrature components.

Even for perfect rf-field calibration (as was used in Figure 4.4) the pulses with no quadrature components (ν_{off}=0 kHz) show residual effective fields for various chemical-shift offsets. It is assumed that for single, isolated pulses with amplitude transients the flip angle remains the same as for a rectangular pulse. This assumption is based on the fact that the exponential build-up and decay have the same time constant. Therefore, the amplitude transient only changes the 'centre-of-mass' of the pulse as well as the trajectory of the magnetization. This effect is negligible if the chemical-shift term is eliminated from the dominating Hamiltonian (Eq. 4.3). This is observable for all three phase cycles.

Repeating the calculations shown in Figure 4.3 with pulses including transients leads to effective fields that are not the same for chemical-shift values with opposing signs. Therefore, in an experiment with the carrier in the middle of the spins of interest, they will exhibit different effective fields and a quadruple-mode Floquet description has to be applied. The magnitude of the effective field is smaller for higher-order phase cycles, i.e.
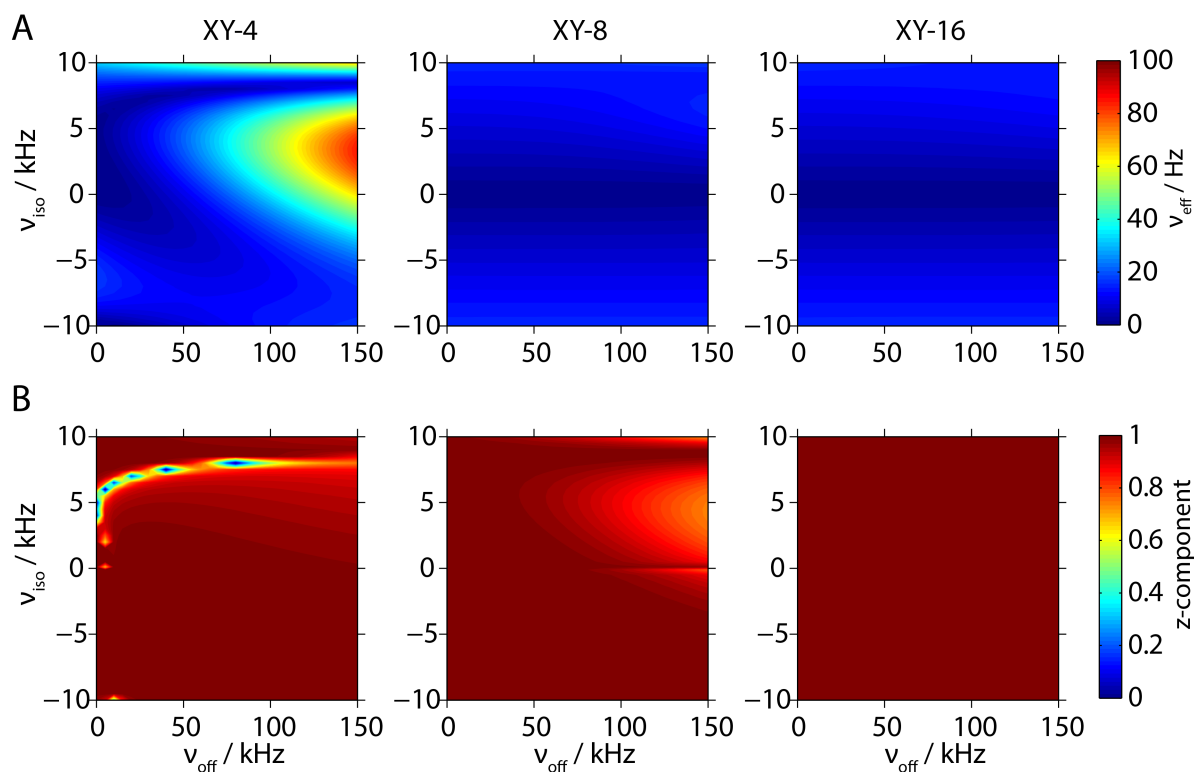
Figure 4.4. The magnitude of the effective field (A) and the normalized z-component (B) for three different phase cycles of an RFDR π-pulse train as a function of the isotropic chemical shift and the magnitude of the phase transient, assuming a time constant of the amplitude transient of τ_{rise} =0.5 μs. The pulse shapes were simulated according to Equation 3.1. The MAS frequency was set to 30 kHz with a pulse length of 5 μs and the theoretical rf-field amplitude of 100 kHz.

XY8 and XY16 perform better than XY4. In general, independently of perfect or imperfect pulses, the calculations of the effective field show that the XY4 and XY16 phase cycles generate effective fields along the z-direction, whereas XY8 generates a field in the xy-direction. Additionally, XY8 and XY16 compensate pulse imperfections better than XY4 in terms of absolute magnitude of the effective field.

In order to investigate the influence of the offset on the transfer efficiency of the recoupling sequence, numerical simulations using a ^{13}C 2-spin system were performed as a function of the two isotropic chemical shifts. A dipolar coupling of 1 kHz and a CSA tensor of 1 kHz was used with a π pulse of 5 μs length at a nominal rf-field amplitude of 100 kHz and a MAS frequency of 30 kHz. Different crystallite orientations were simulated according to the ZCW scheme for powder averaging with 1154 orientations [107]. The applied phase cycle during the recoupling period was XY4. The transfer efficiency
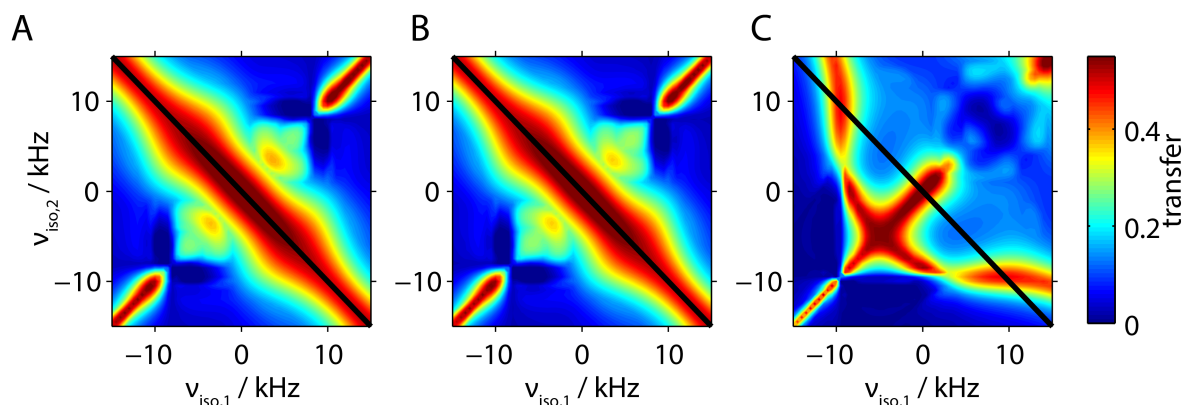
Figure 4.5. Carbon RFDR transfer efficiencies obtained from numerical situations for a two-spin system with a dipolar coupling of 1 kHz and a CSA tensor of 1 kHz. The chemical shift was varied to show the influence of the offset on the efficiency. The black line in the anti-diagonal shows the ideal situation in which the irradiation frequency is in the middle of the two spins. The π pulses had a length of 5 μs at a MAS frequency of 30 kHz and were phase cycled according to the XY4 scheme. A) Ideal rectangular pulse. B) Amplitude transient with a rise time of 0.5 μs. C) Phase transient pulse with a rise time of 0.5 μs and an offset frequency of 100 kHz.

was determined as the maximum of the first transient oscillation in the magnetization build-up curve. The simulations using ideal rectangular pulses (Figure 4.5A) are compared with amplitude transients with typically observed rise times of 0.5 μs (Figure 4.5B) and phase transients with $\nu_{\text{off}} = 100$ kHz (Figure 4.5C).

The differences between ideal pulses and pulses with amplitude transients are negligible since amplitude transients only change the shape of the pulse and not the net flip angle and thus do not generate large effective fields. However, phase transients change the expected resonance condition where the two spins are located symmetrically around the irradiation frequency. The reduction in transfer efficiency can be explained by the different axes of rotation of the two spins and, therefore, the sum or difference of the effective fields shifts the recoupling condition. The altered ideal carrier position caused by pulse transients is hard to predict for an experimental setup and optimization can be tedious especially for samples with low signal-to-noise ratio. Similar simulations for XY8 and XY16 phase cycles show a reduced offset dependence compared to the XY4 phase cycle, but also a slight reduction in overall transfer efficiency at large chemical-shift differences.

4.3. Experimental Results for RFDR

4.3.1. Ammoniumphthalate

Experimentally, the most challenging systems for dipolar recoupling experiments are homonuclear spin pairs with a large CSA tensor. In higher orders of the effective Hamiltonian, the CSA tensor can generate error terms in dipolar recoupling sequences. Additionally, RFDR spin systems with a small isotropic chemical-shift difference are challenging due to the low scaling factor and, therefore, long mixing times, leading to cumulative effects of pulse imperfections. A model compound to satisfy these criteria is doubly ^{13}C-labeled diammonium phthalate with ^{13}C-labels on the carbonyl groups. It has a large CSA tensor ($\delta = 77$ ppm and $\eta = 0.68$) with a medium-size dipolar coupling $\nu_{1,2} = $ -585 Hz [108].
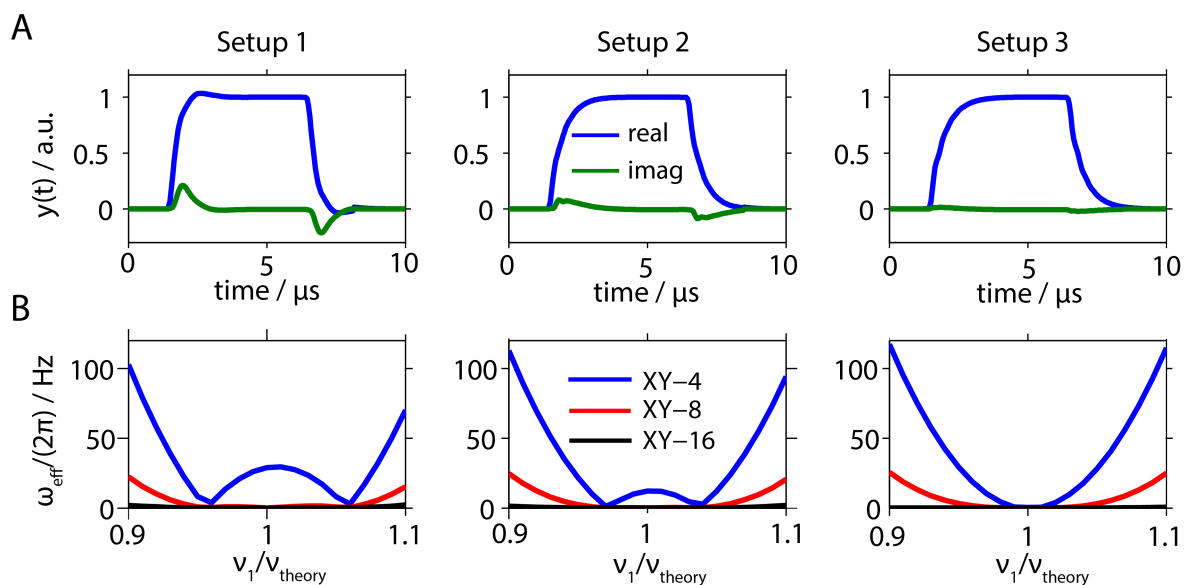

Figure 4.6. A) Experimentally determined pulse shape for the recoupling π pulse for three different setups (setup 1-3 differ in cable length between amplifier and probe). B) The effective field calculated from measured B_1 shapes over 16 rotor periods for RFDR assuming an MAS frequency of 30 kHz.

The recoupling efficiency for RFDR was investigated with three different experimental setups in which the cable length was varied. Therefore, the pulse transient looked different for every setup, which is shown in Figure 4.6A. Additionally, after a recoupling period of 16 rotor cycles, the effective field was calculated for the three basic phase cycles (XY4, XY8, and XY16). Using 16 rotor cycles for the calculation ensured a constant

modulation frequency for the calculations ($\omega_m = \omega_r/16$). Additionally, it guaranteed the full length of the phase cycle could be applied. The MAS frequency was set to 30 kHz with a π-pulse length of 5 μs, corresponding to theoretical rf-field amplitude of 100 kHz, assuming a time step of 50 ns for the calculation. The resulting effective fields are shown in Figure 4.6B.

Experimental RFDR build-up curves were recorded as pseudo-2D experiments for di-ammonium phthalate at a proton Larmor frequency of 300 MHz. The MAS frequency was set to 30 kHz with a π pulse length of 5 μs, corresponding to the theoretical rf field amplitude of 100 kHz to match the calculations from Figure 4.6. The experimental results clearly show that pulse transients heavily influence the polarization transfer under the XY4 phase cycle (Fig. 4.7A) with a reduction of the transfer efficiency from 48% to 25%. The transient compensation (Fig. 4.7B) yields a broad transfer condition that is fairly robust towards rf-field errors and independent of the experimental setup. Despite the fact that the effective fields are smaller in the case of the XY8 phase cycle, the resonance condition becomes narrow with respect to rf-field maladjustment (Fig. 4.7C and B). The overall transfer is slightly lower for XY8 (41%-43%), which is in agreement with the theoretical calculations. The XY16 phase cycle shows as expected only minor differences between compensated and uncompensated pulses, which is in agreement with the effective fields (Fig. 4.7E and F). With transient compensation the overall transfer efficiency (45%) is the same as for XY4 within experimental errors.

The same experiments as in Figure 4.7 were run for common supercycles in RFDR. These include $\mathrm{XY4}_4^1$, $\mathrm{XY4}_3^1$, and $\mathrm{XY8}_4^1$ which were applied with a basic repetition rate of 32, 24, and 32 rotor periods, respectively. This was to ensure that the full phase cycle was applied. The setups are identical as for the results shown in Figure 4.6. The results in Figure 4.8 show that the supercycles do not improve the robustness towards phase transients. In the uncompensated cases (Fig. 4.8A, C, and E) the setup with the largest quadrature component (Setup 1) performs the worst. The phase cycle derived from an XY8 phase cycle ($\mathrm{XY8}_4^1$, Fig. 4.8E and F) compensates the effective fields the best. The phase cycles derived from the most basic cycle XY4 ($\mathrm{XY4}_4^1$, Fig. 4.8A and B; $\mathrm{XY4}_3^1$, Fig. 4.8C and D) is very susceptible to phase transients. Especially interesting is the case for Setup 3 because it shows almost perfect recoupling for the basic cycles with uncompensated pulses, but the use of a supercycle worsens the recoupling efficiency.
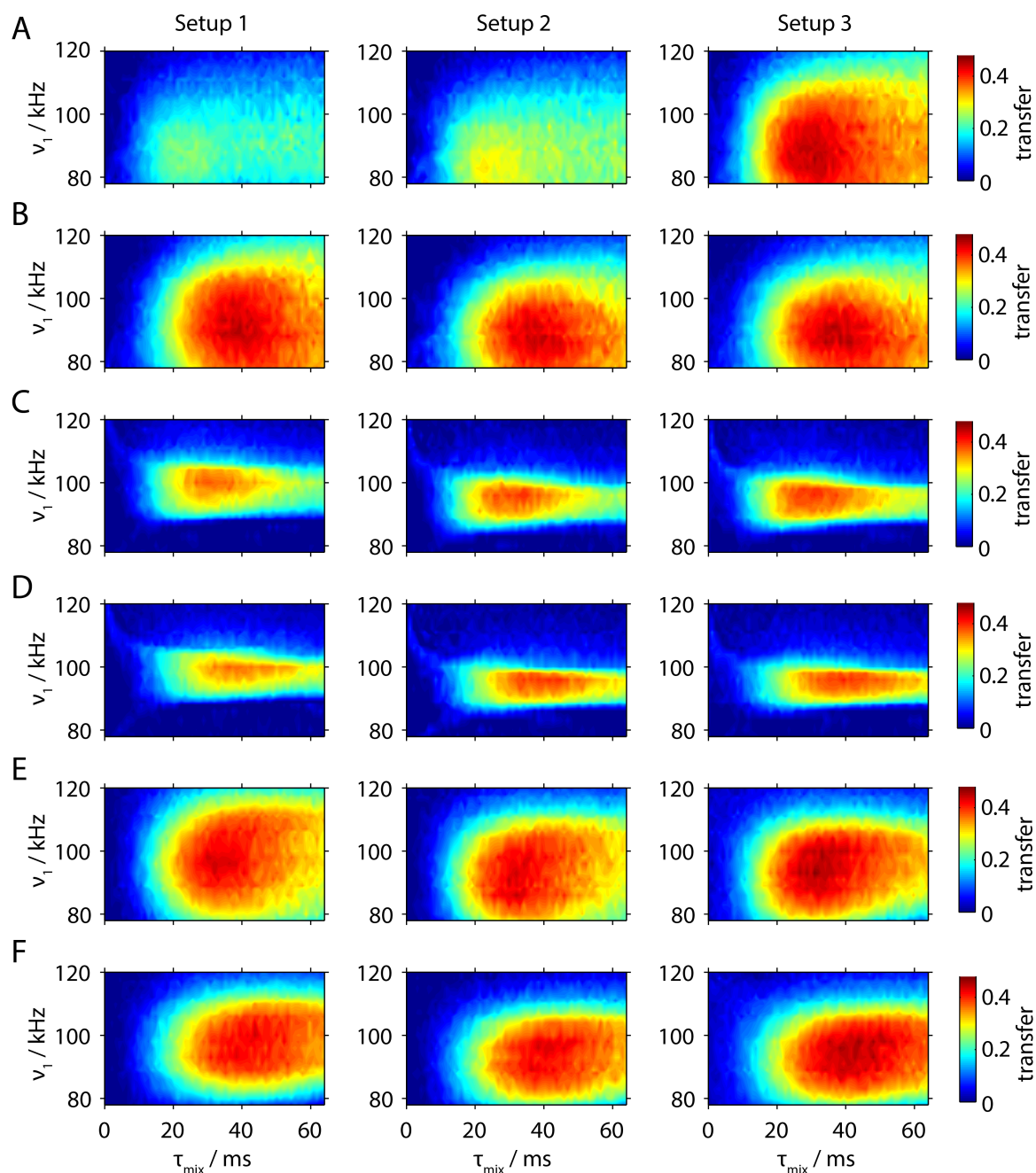
Figure 4.7. A)-F) Experimental pseudo 2D build-up curves for diammonium phthalate as a function of the rf-field amplitude and the mixing time for different phase cycles with compensated and uncompensated π pulses. The XY4 cycle shows strong improvement going from the uncompensated (A) to the compensated (B) implementation. Uncompensated XY8 (C) and compensated XY8 (D) show little difference but smaller tolerances towards rf-field errors. Compensated XY16 (F) and uncompensated XY16 (E) yield identical build-up curves and similar transfer efficiencies to the XY4 phase cycle. All experiments were performed on a 300 MHz spectrometer at a MAS frequency of 30 kHz with a π-pulse duration of 5 μs. Heteronuclear decoupling during the mixing period was achieved by cw irradiation on the protons with 120 kHz rf-field amplitude.
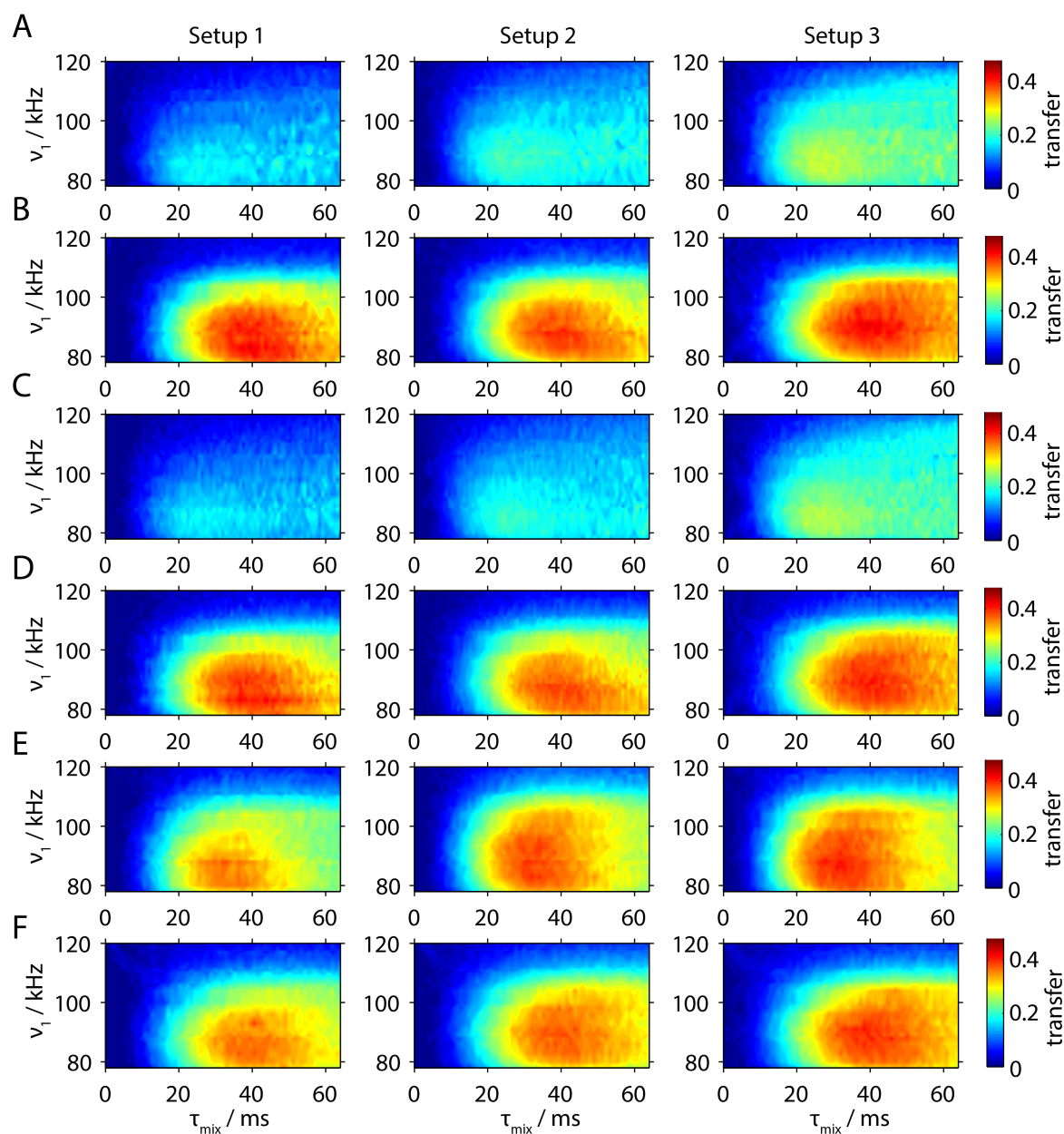
Figure 4.8. A)-F) Experimental pseudo 2D build-up curves for diammonium phthalate as a function of the rf-field amplitude and the mixing time for different phase cycles with compensated and uncompensated π pulses. The $XY4_4^1$ cycle shows strong improvement going from the uncompensated (A) to the compensated (B) implementation. This is true for all three setups even though Setup 3 does not show significant quadrature components in the pulse shape. The same situation is encountered for the $XY4_3^1$ phase cycle, which has bad recoupling efficiency for the uncompensated implementation (C) that improves drastically with pulse-transient compensation (D). Compensated $XY8_4^1$ (F) and uncompensated $XY8_4^1$ (E) yield identical build-up curves and similar transfer efficiencies to the compensated $XY4$ phase cycle or the $XY16$ in all implementations. All experimental conditions were identical to the results shown in Figure 4.7.

Generally speaking it can be stated that a supercycle does not improve the transfer efficiency or the robustness towards pulse imperfections in RFDR recoupling for the model substance ammonium phthalate. This is due to the fact that the phase cycles retain the properties of the basic cycles from which they are constructed. Therefore, the $XY4_4^1$ and the $XY4_3^1$ cycles are not robust towards pulse transients as the basic cycle XY4 is highly susceptible to pulse transients. Another factor that plays a role is the direction of the effective field as it is detrimental for the sequence if the effective field is pointed along the xy-plane after a modulation period.

4.3.2. Glycineethylester

RFDR experiments are generally easier on systems with large chemical shift differences due to the high effective coupling, which leads to a faster magnetization build-up. A model system to study these effects on is doubly ^{13}C labelled glycineethylester, which has a chemical shift difference of $\sim$120 ppm. It is assumed *a priori* that the influence of pulse transients is less due to the fast magnetization transfer. This is due to the low repetition number of recoupling periods needed. However, relaxation effects might play a bigger role compared to the phthalate since the transfer step has to be sufficiently fast to avoid relaxation losses. To avoid these effects, the ammonium phthalate sample was diluted with natural abundance substance (7:1). Nevertheless, the relaxation is an important parameter to consider as a factor for the practical application of this sequence. The basic phase cycles were applied to the RFDR sequence using either compensated or uncompensated pulses for the recoupling π pulse. The results for the recoupling efficiency are shown in Figure 4.9. The experimental setups are identical as for the results shown in Figure 4.7 and 4.8. The compensated XY4 phase cycle (Fig. 4.9A) shows good recoupling efficiency as well as high robustness towards rf-field maladjustments. As for the phthalate sample, Setup 3 performs equal to the compensated pulses when using uncompensated pulses (Fig. 4.9B). The results for the compensated and the uncompensated pulses for XY8 (Fig. 4.9C and D) show great resemblance to the results from the ammonium phthalate. The recoupling efficiency at the ideal condition is comparable to the XY4 phase cycle, but the breadth of the resonance condition with respect to rf-field missets is smaller. Additionally, the transfer efficiency at longer mixing times is worse than for the XY4 phase cycle.
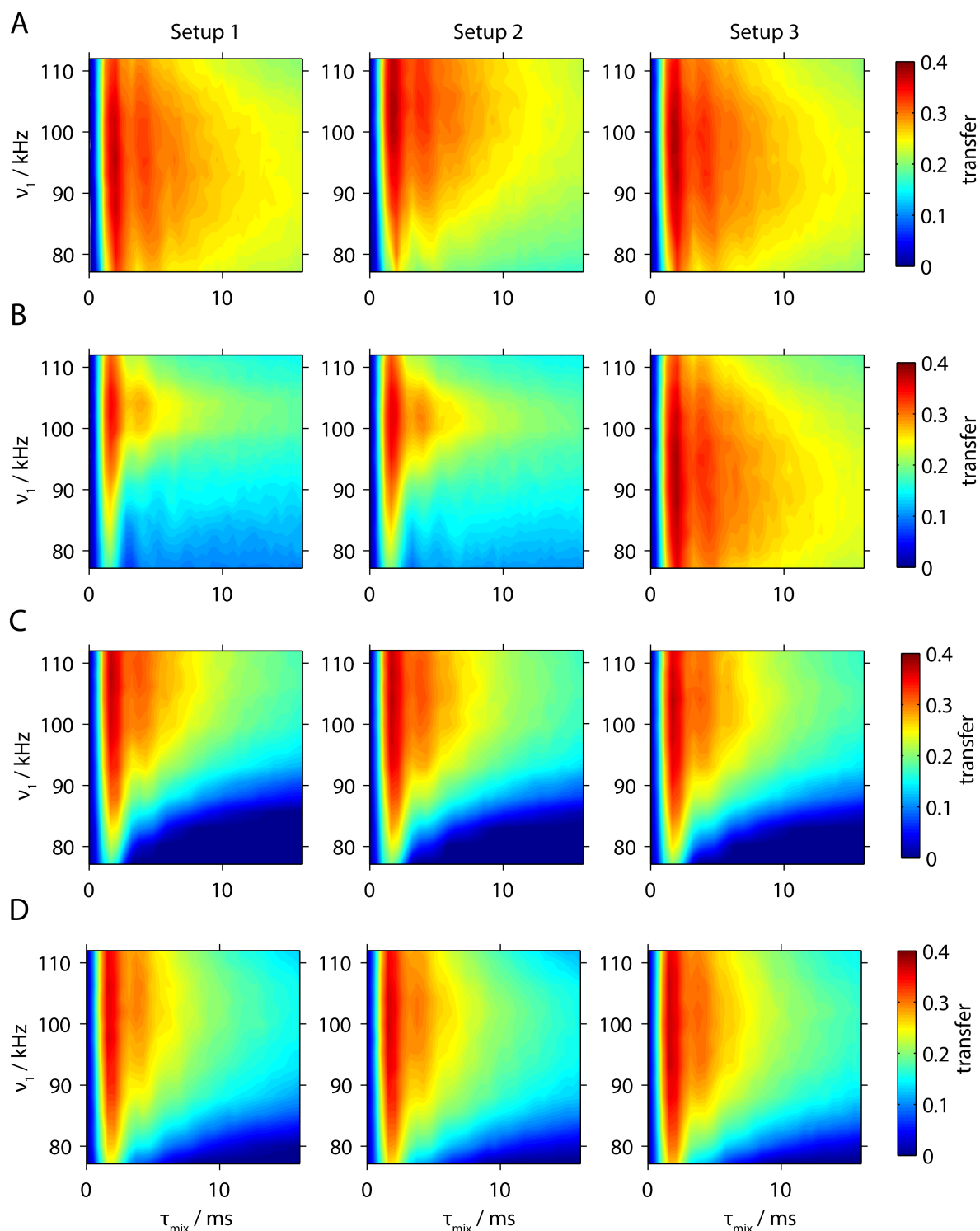
Figure 4.9. Transfer efficiency for RFDR experiments in glycineethylester at a MAS frequency of 15 kHz performed at an external magnetic field of 9.4 T. Three different setups shown in Figure 4.6, i.e. pulse shapes, were investigated with a pulse length of 5 μs. The XY4 phase cycle gives higher overall transfer with better stability towards rf-field miscalibration for compensated pulses (A), but suffers from loss in transfer efficiency for uncompensated implementation (B). The XY8 phase cycle is more robust towards pulse transients (compensated or uncompensated implementation in C and D, respectively) but the overall transfer efficiency is lower due to lesser robustness towards rf-field missets.

This is due to relaxation effects since the total magnetization also decreases faster for the XY8 phase cycle than the XY4. This is an important fact that speaks against the use of XY8 phase cycles for more complicated systems with large dispersion of chemical shift differences. Especially for small chemical-shift differences the loss of total magnetization is detrimental since it requires longer mixing times.

4.3.3. MLF

The concepts developed using the model compounds in Chapters 4.3.1 and 4.3.2 were then extended to multi-spin systems. 2D RFDR dipolar recoupling experiments were performed on the tri-peptide MLF (N-formyl-U-[^{13}C ^{15}N]-Met-Leu-Phe-OH), using compensated and rectangular pulses with the results shown in Figure 4.10. In order to show the influence of the compensation, a series of 2D spectra with different mixing times were recorded and the intensities of two representative cross-peaks are plotted as a function of the mixing time (Fig. 4.10B). Slices from the 2D spectra show that the compensation improves the transfer efficiency and accelerates the magnetization transfer. The decay of the sum magnetization is fairly independent of the compensation on the time scale of 10 ms. The experiments using hard pulses result in a higher source peak, i.e., the diagonal peak, while the experiments using compensated pulses result in higher cross-peak intensities. The decay of the cross-peak intensity, e.g., the CO-Cα peak of Leucine, is faster using compensated pulses since the magnetization is transferred further through relayed pathways. Figure 4.10B shows that the intensity of the Leucine CO-Cα cross-peak can be doubled using compensated pulses. The experiments were done at a 11.74 T magnet using a MAS frequency of 25 kHz. The carrier was placed in the centre of the spectrum at 90 ppm for all experiments. The carrier position has a big influence on the transfer efficiency since it introduces offset effects that generate additional effective fields. However, towards practical application of the sequence and the long range transfer in RFDR, the carrier in the centre of the spectrum is a justifiable choice.

A similar result was obtained for the XY8 phase cycle but the maximum transfer is not as high as in XY4 (Figure 4.11). The compensated pulses lead to slightly higher relayed transfer CO-Cβ for XY8 due to the robustness of the phase cycle towards offset effects. This is contrast to the experiments on the glycinethylester as the XY8 phase cycle resulted in shorter coherence life times.
The influence of offset effects has not been studied in detail, but according to the litera-
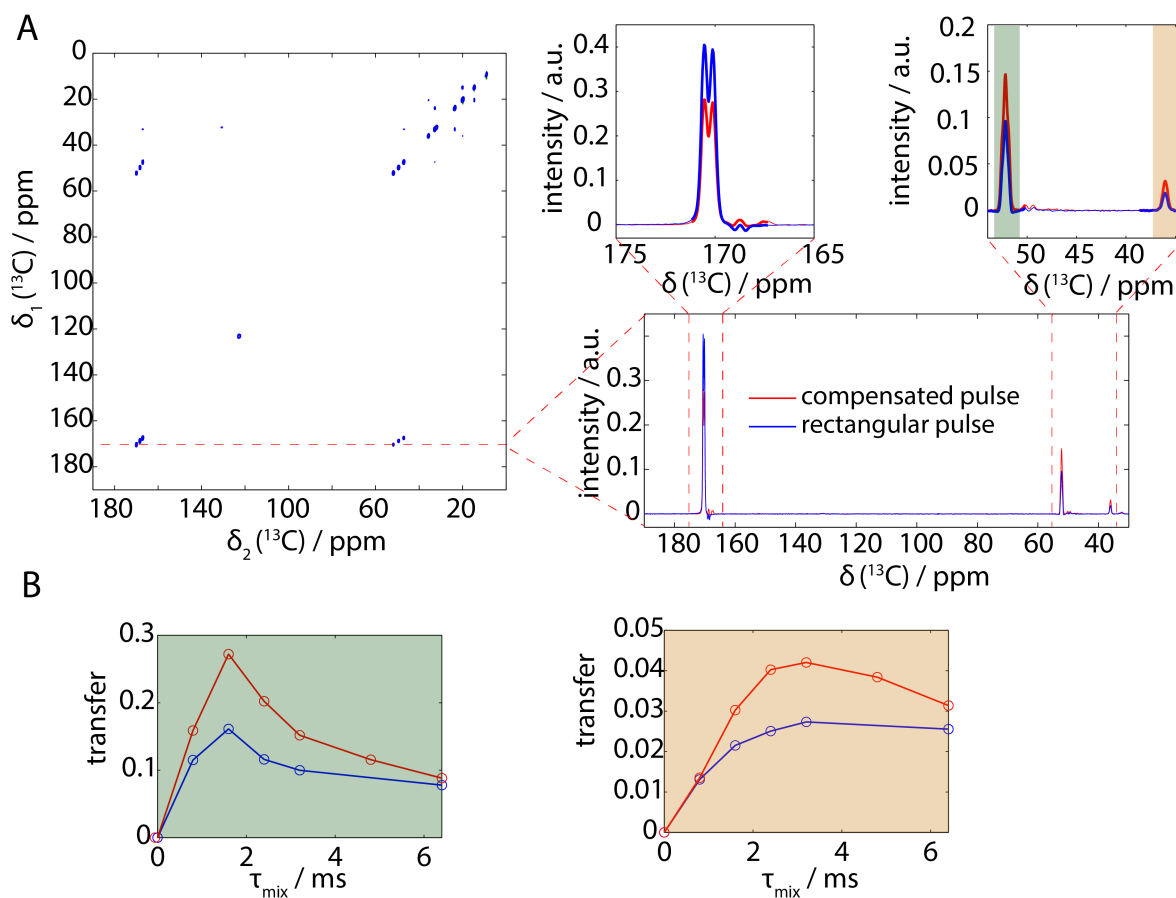
Figure 4.10. A) 2D ^{13}C-^{13}C homonuclear correlation spectrum of the tri-peptide MLF after 2.4 ms RFDR recoupling with an XY4 phase cycle. The slice at δ_1 = 171 ppm shows the comparison of the transfer efficiency between a compensated and an uncompensated pulse. B) Build-up curves for representative cross-peaks corresponding to the Leucine CO-Cα and a CO-Cβ correlation, respectively. The maximum transfer almost doubles for transient compensation. The experiments were performed at a MAS spinning frequency of 25 kHz using an rf-field amplitude of 100 kHz for the π pulses.

ture, any phase cycle derived from XY8 or XY16 has a higher stability. This is supported by the calculations of the effective field shown in Figure 4.4. The biggest drawback of XY16 phase cycles and supercycles is the long basic modulation period. Especially for CO-Cα transfer steps, the build-up is fast and the maximum is rather short-lived as is seen in Figure 4.10B. These maxima are easily undersampled when using long phase cycles and slow MAS frequencies.

In conclusion, multi-spin systems show slightly different behaviour compared to the two-spin model systems discussed before. However, the main conclusions still hold true;
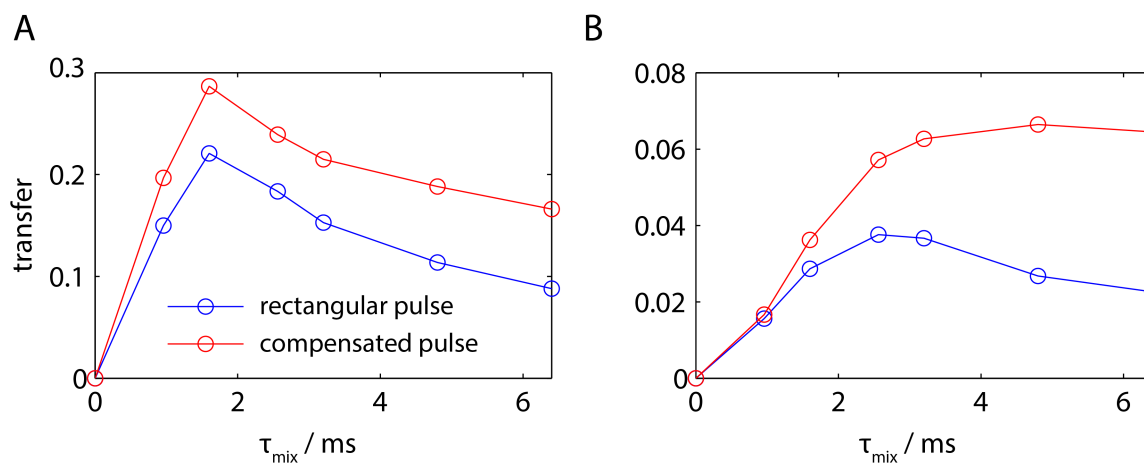
Figure 4.11. Build-up curves for the correlation peaks in a 2D ^{13}C-^{13}C homonuclear correlation experiment for a CO-Cα (A) and a CO-Cβ (B) cross peak using a XY8 RFDR mixing block. The MAS frequency was 25 kHz at a π-pulse duration of 5 μs. The overall transfer is slightly lower than for the XY4 phase cycle (Figure 4.10) but the longer-range transfer is higher. Furthermore, the influence of the compensation is higher than was expected from the theoretical calculations and numerical simulations. Note that the pulse compensation for XY4 and XY8 outperforms any phase cycle.

the XY4 phase cycle is susceptible to phase transients, but when compensated has a high stability towards rf-field maladjustments. The XY8 phase cycle compensates quadrature components well, but due to the generated effective field in the xy plane it has low breadth of the resonance condition in terms of rf-field amplitude. The XY16 compensates all pulse imperfections well but due to its long basic modulation frequency it might lead to an undersampling of the first transient oscillations. All supercycles perform very similar to their respective basic cycles and we did not find clear advantages of using them when transient compensation is available.

4.4. Numerical Simulations for REDOR

The effective fields can be calculated in full analogy to the RFDR sequence using the same phase cycles and pulse parameters (Figure 4.12). As is the case for RFDR, the XY8 phase cycle generates an effective field that is in the xy-plane. The XY4 and XY16 are hypothesized not to be influenced at all by quadrature components since the effective field only has a z-component. For the XY16, a few values of the z-component are 0 due to a vanishing effective field. The stability towards rf-field missets is not high for the XY4 phase cycle but as stated before, this is believed to not be detrimental.
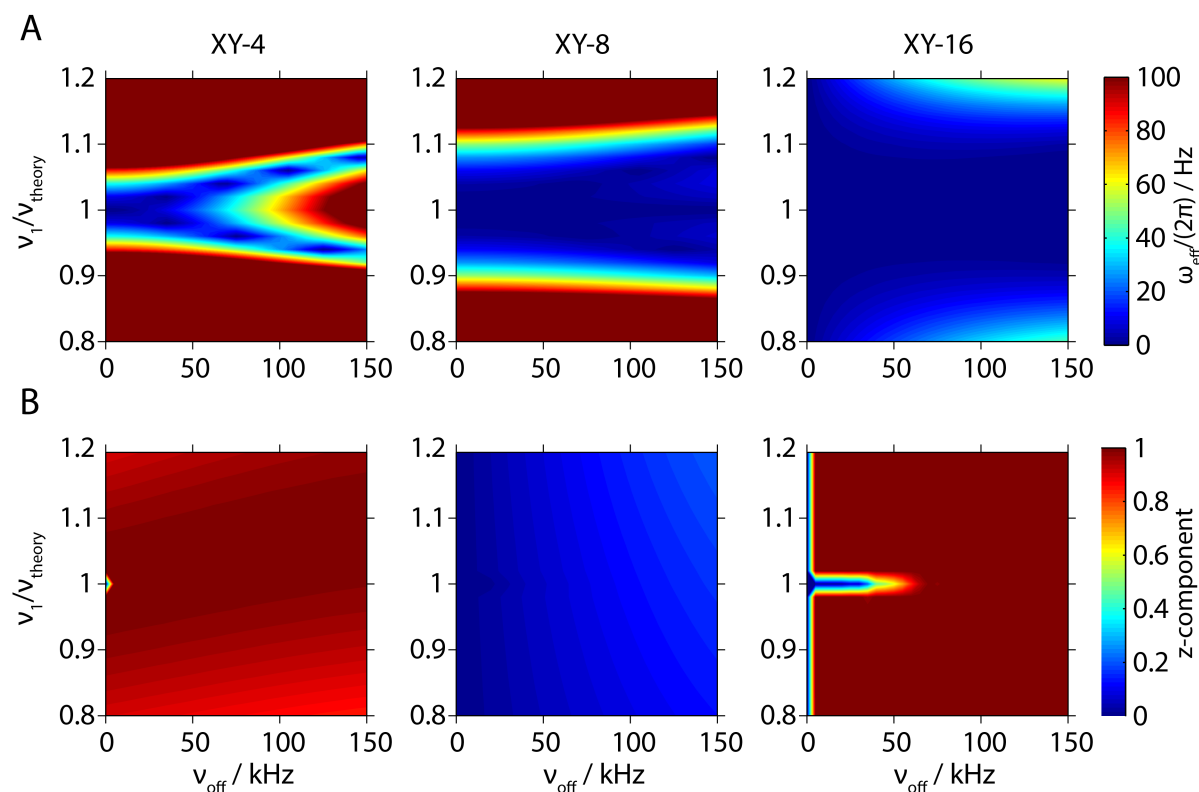
Figure 4.12. The magnitude of the effective field (A) and the normalized z-component (B) for the three different phase cycles of a REDOR π-pulse train as a function of the the rf-field misset and the magnitude of the phase transients. The rise time of the amplitude transient was assumed to be 500 ns. The MAS frequency was set to 30 kHz with a π-pulse length of 5 μs. The magnitude of the effective field increases rapidly for an XY4 phase cycle but remains in the z-direction. The rf-field misset is better compensated for XY8 and XY16 but the effective field direction is in the xy-plane for the XY8. It can be observed that for ideal rf-field amplitude, the XY8 phase cycle never generates an effective field independent of the phase transients.

The theoretical description for the REDOR sequence differs slightly from RFDR since the chemical-shift offsets can be excluded from the interaction-frame Hamiltonian calculation. In the REDOR sequence, a heteronuclear spin pair is considered but only one of the two spins is irradiated by the π-pulse train. The characteristics of the effective fields for a REDOR sequence show the same general trends as for the RFDR sequence. The main difference between the two sequences is the form of the effective Hamiltonian, which contains only an Ising-type $2I_zS_z$-term in the case of REDOR. This term commutes at all times with effective fields along the z-direction and also the density operator commutes at all times with the effective fields on the passive spin. Therefore, it is expected that pulse transients do not influence the REDOR transfer strongly.
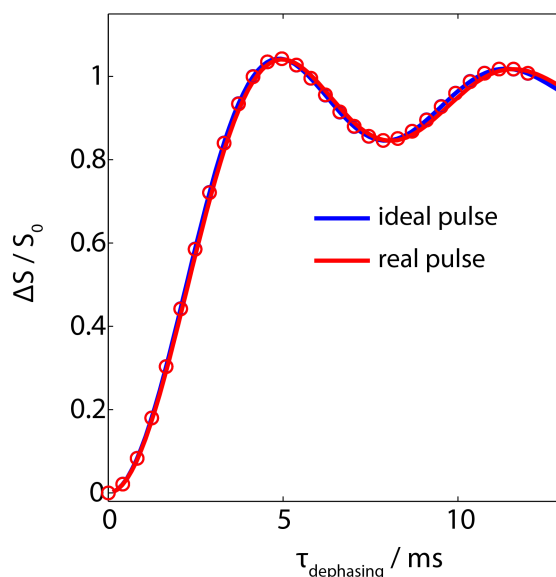
Figure 4.13. REDOR dephasing curve extracted from numerical simulations (line) and from Floquet calculations based on effective Hamiltonians (circles). The dephasing curves are virtually identical and the small deviations come from numerical inaccuracies in the simulations. Therefore, pulse transients are not expected to influence the dipolar recoupling efficiency during a REDOR experiment. The simulation parameters were set to a MAS frequency of 15 kHz with a dipolar coupling of 700 Hz and a rf-field amplitude of 50 kHz. The pulse transients were modelled with a rise time of 1 μs and an electronic offset frequency of 200 kHz.

The REDOR dephasing curve was calculated based on the effective first-order Hamiltonian obtained from Floquet theory. In order to investigate the influence of pulse transients on the REDOR sequence, a comparison of ideal and real pulses with numerical simulations was done. The resulting dephasing curves of the numerical and analytical calculations are shown in 4.13 and show virtually no differences. The anisotropy of the dipolar coupling was 700 Hz at a MAS frequency of 15 kHz with a π pulse length of 10 μs.

The numerical simulations and analytical calculations indicate that phase transients have very little influence on the dipolar-recoupling efficiency in REDOR. The effective field does not truncate the transfer because, under all experimental conditions, it is insignificantly small or along the z-direction (in analogy to the results shown in Figure 4.12). Small deviations in the dephasing curve might be introduced by amplitude tran-

sients since the centre of gravity of the pulse is shifted slightly and a time shift of the pulses scales the dipolar coupling by a well-defined factor.

4.5. Experimental Results for REDOR

The stability of the REDOR sequence against phase transients was also confirmed in experimental results. Figure 4.14 shows experimental REDOR recoupling curves for a C-N two-bond coupling at 15 kHz MAS frequency with and without transient-compensated pulses. In addition, a time-shifted REDOR was also acquired, which did not show any significant differences for transient compensation. This confirms the good compensation of effective fields in the REDOR sequence using an XY4 phase cycle found in the analytical and numerical simulations.
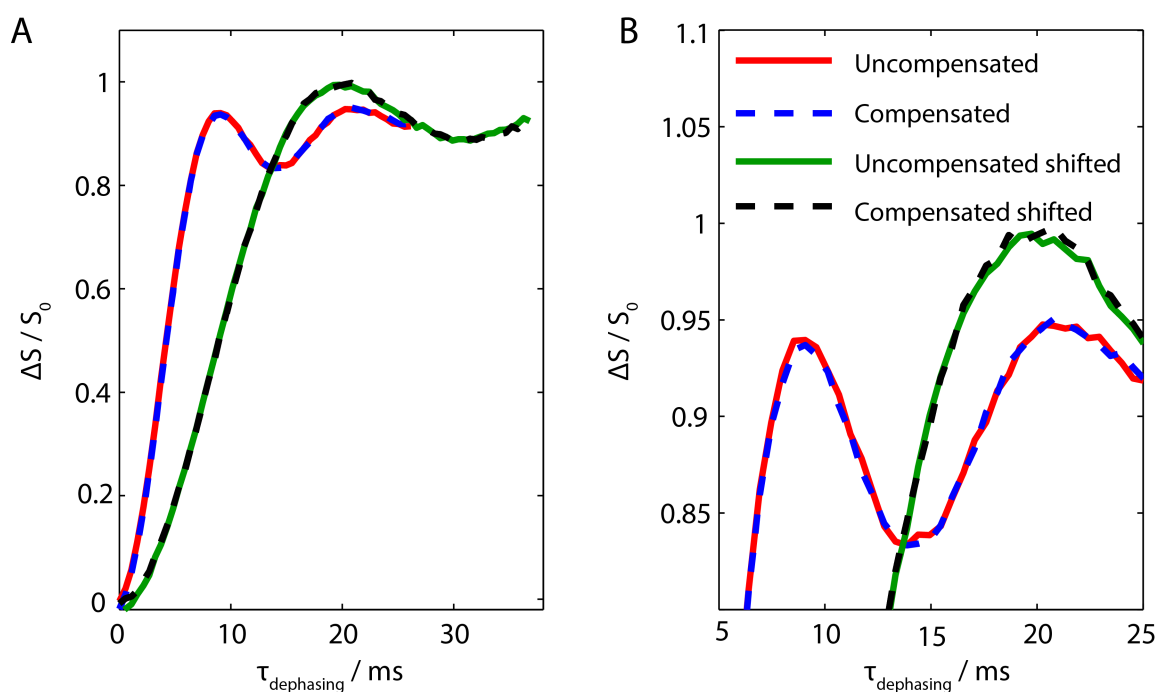
Figure 4.14. Experimental REDOR curves with compensated and uncompensated pulses to measure the CO-N coupling in selectively labelled $1\text{-}^{13}C_1\text{-}^{15}N$ glycine. Figure B is a zoom of the oscillations in the dephasing curve (A). The time shift (black and green) was 20 μs at a MAS frequency of 15 kHz. The difference between the compensated and uncompensated implementation is negligible and is well within the experimental uncertainty.

The experimental dephasing shown in Figure 4.14 corresponds to a rather challenging case. This is due to the fact that the dipolar coupling is small and thus the dephasing

period is long. This cumulates the error of phase transients and any pulse imperfections would become obvious in the dephasing curve. It was confirmed theoretically and experimentally that pulse imperfections do not have an impact on the sequence even over long dephasing times up to 25 ms.

4.6. Conclusion

In conclusion, it was shown from calculations and experiments that REDOR is a pulse sequence that is not susceptible to pulse imperfections. Despite the similar recoupling element of RFDR, the functional Hamiltonian has a different form that is not truncated by the effective fields generated, since they commute at all times. This fact makes REDOR one of the most widely used pulse sequences to-date in solid-state NMR. In RFDR, phase transients can lead to a significant reduction in the polarization-transfer efficiency. This is due to the fact that the two coupled spins experience effective fields of different magnitude and direction. The effective fields can either be compensated using transient-compensated pulses or using a more extensive phase cycle. Longer phase cycles have the disadvantage of a longer minimal recoupling period, which might lead to an undersampling of the polarization transfer curve. However, the stark differences between RFDR and REDOR with respect to pulse transients show the necessity of fully understanding the pulse sequences theoretically in order to predict the influence of pulse imperfections on the sequence.

5. Symmetry-Based Sequences

- Parts of this chapter are published in:
  J. Hellwagner, ... , M. Ernst, *J. Chem. Phys.*, **2017**, *146*, 244202

5.1. Introduction

Symmetry-based sequences (so called CN_n^ν and RN_n^ν sequences [39–41]) are a type of pulse sequences that allow for recoupling and decoupling experiments by carefully choosing the symmetry numbers N, n, and ν. The correct choice of symmetry numbers generates an interference between the MAS and the spin part of the Hamiltonian to either achieve decoupling or recoupling. In the literature, reports of homonuclear dipolar-recoupling [70, 109–111], homonuclear decoupling [112], scalar J-coupling [113–116], heteronuclear recoupling [117, 118], and heteronuclear decoupling [119] are found. The focus of this chapter is a homonuclear dipolar-recoupling sequence $R26_4^{11}$ and its supercycle, denoted as SR26 [111, 120]. Important properties of these types of sequences are γ encoding and robustness towards pulse-error terms and rf inhomogeneity. The property of γ encoding implies that the first-order effective Hamiltonian is only phase modulated by the third Euler angle with respect to the laboratory frame, γ. This leads to high double-quantum recoupling efficiencies with a theoretical maximum of 73% for the first transient. In practice, such a high efficiency is usually unachievable, due to higher-order error terms contributing to the Hamiltonian and experimental artefacts, including pulse imperfections due to pulse transients.

The basic design of R sequences involves a basic element R_ϕ that implements a π rotation about an axis in the xy-plane. The most widely used implementations are either a simple $(\pi)_\phi$ pulse or a composite pulse $(\pi/2)_\phi(3\pi/2)_{\phi+\pi}$, both corresponding to a net π rotation. For the complete sequence, $N/2$ $R_\phi R_{-\phi}$ elements are fit into n rotor periods

with the phase ϕ given as $\pi\nu/N$.

The C sequences are generated in a similar fashion with a net 2π rotation and an incrementing phase $\Delta\phi = \frac{2\pi\nu}{N}$. N of these basic elements are then fit into n rotor periods. A more robust implementation with respect to offset effects is the POST element. It comprises of a $(\pi/2)_\phi (2\pi)_{\phi+\pi} (3\pi/2)_\phi$ basic element and generates a net 2π flip angle.

5.1.1. Space-Spin Selection Rules

Since the symmetry-based R and C sequences are essentially phase-modulated sequences, the spin interactions are rotated around the z axis. It was shown from effective Hamiltonians both from AHT and Floquet theory that a spin interaction of rank s with spatial component m is recoupled if the following selection rules are fulfilled.

For RN_n^ν sequences

$$mn - s\nu = \frac{z_\lambda N}{2} \tag{5.1}$$

with $z_\lambda = 0, \pm2, \pm4, ...$ for homonuclear dipolar couplings and $z_\lambda = \pm1, \pm3, ...$ for CSA tensors, i.e. z_λ has to have the same parity as the spin tensor.

Similarly, the selection rule for CN_n^ν sequences is given by

$$mn - s\nu = zN \tag{5.2}$$

with z being any integer.

A space-spin selection diagram shows the interactions that are being recoupled according to Equation 5.1 or 5.2. Figure 5.1 shows the selection diagram for the double-quantum homonuclear recoupling sequence $R26_4^{11}$.

The selection diagrams are a graphical tool to visualize the selection rules in a first-order approximation. An opening in the black bars on the right hand side shows allowed interactions, which are spaced by the symmetry number N. Other terms that do not fulfil the selection rules are suppressed in the first-order Hamiltonian. One example using the chemical-shift anisotropy is shown in Figure 5.1B. It is noteworthy that the space-spin selection diagrams only give a qualitative analysis of whether the interaction is symmetry allowed or forbidden. This analysis only considers a first-order average Hamiltonian and higher-order symmetries can also be determined with a similar approach. These higher-order terms become especially relevant in decoupling sequences.

An important criterion for the performance of the sequence is the scaling factor of the
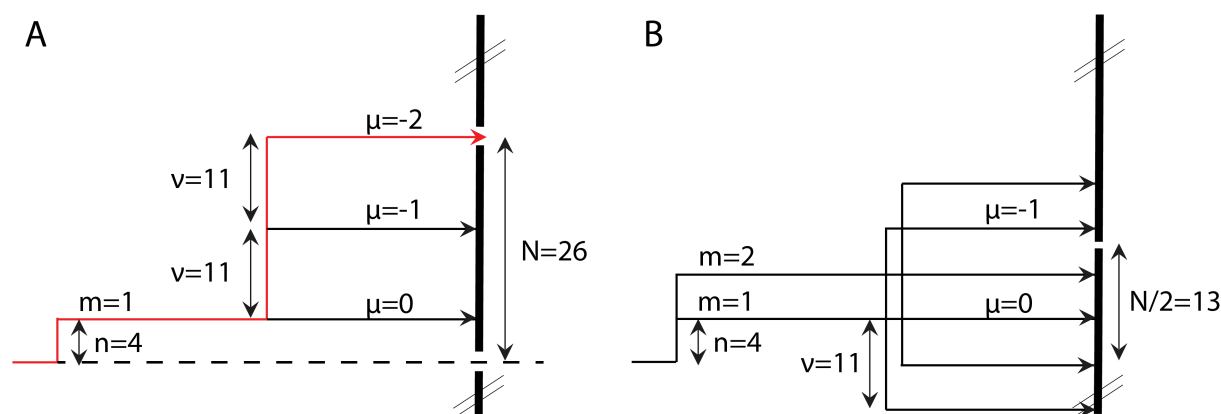
Figure 5.1. Spin-space selection diagram for the homonuclear recoupling sequence $R26_4^{11}$. The selection diagram follows the selection rule given in Equation 5.1 using $z_\lambda = 2$ in A) showing the symmetry for a homonuclear dipolar coupling because of its rank $\ell = 2$. The recoupled interaction is the tensor with the component $m = 1$ and $s = -2$. The CSA component is shown in B) using $z_\lambda = 1$ since the spin rank of the chemical-shift anisotropy is odd. None of the possible options fulfil the selection rule for the CSA component and thus it is symmetry forbidden.

interaction. This scaling factor can be calculated analytically for perfect rectangular pulses in the framework of Floquet theory or numerically for real pulses. Recoupling sequences perform best if the scaling factor for the time-independent interaction, i.e. the recoupled component, is as high as possible. Another example for the importance of the scaling factor is the isotropic chemical shift, as it is symmetry allowed in every C sequence and is often considered an error term in dipolar recoupling sequences. However, if a perfect POST element is used for the net 2π rotation, the scaling factor of the isotropic chemical shift is 0 and it is suppressed.

5.1.2. Resonance Conditions, Effective First- and Second-Order Hamiltonians

The theoretical description of these types of sequences is either based on symmetry arguments and Average-Hamiltonian theory [41], or bi-modal Floquet theory [20, 21, 23]. The relevant frequencies are the MAS frequency ω_r, and the modulation frequency of the pulse sequence ω_m. In the bi-modal Floquet description, we assume that the R element corresponds to an ideal inversion propagator. In reality, however, a more generalized description has to be applied, since pulse imperfections in the form of rf-field amplitude missetting or inhomogeneity, and phase transients can lead to a deviation from the

perfect inversion properties of the R element. As a consequence of this, the rf trajectory will no longer be cyclic and the Floquet description has to be extended with a third frequency, the effective field ω_{eff} [22]. For the theoretical description of RN_n^ν, we assume an ideal homonuclear-coupled two-spin system ($p = 1, 2$) with chemical-shift interactions. In spherical-tensor notation the rotating-frame Hamiltonian is given by

$$\hat{\mathscr{H}}(t) = \sum_{p=1}^{2} \omega_p(t) T_{1,0}^{(p)} + \omega_{1,2}(t) T_{2,0}^{(1,2)} + \hat{\mathscr{H}}_{\text{rf}}(t) \tag{5.3}$$

with an arbitrary amplitude and phase-modulated rf-field Hamiltonian

$$\hat{\mathscr{H}}_{\text{rf}}(t) = \omega_1(t) \sum_p \left(\cos(\phi(t)) S_{px} + \sin(\phi(t)) S_{py} \right). \tag{5.4}$$

In this case, $\omega_p(t)$ represents the time-dependent chemical shift of spin p, $\omega_{1,2}(t)$ the dipolar coupling, and $\omega_1(t)$ and $\phi(t)$ the amplitude and the phase of an arbitrary pulse sequence, respectively. The Floquet analysis is done in an interaction frame with the rf-field Hamiltonian, not including the chemical-shift offset. The interaction-frame transformation is calculated in full analogy to the treatment presented in Chapter 4.2.1 with the propagator

$$\hat{U}_{\text{rf}}(t) = \hat{T} \exp\left(-i \int_0^t \hat{\mathscr{H}}_{\text{rf}}(t') dt' \right) \tag{5.5}$$

with the interaction-frame Hamiltonian given by

$$\hat{\tilde{\mathscr{H}}}(t) = \hat{U}_{\text{rf}}^{-1}(t) \hat{\mathscr{H}}(t) \hat{U}_{\text{rf}}(t). \tag{5.6}$$

Here, $\hat{T}$ represents the Dyson time-ordering operator [56]. In the general case of a tri-modal Floquet description with $\omega_{\text{eff}} \neq 0$, the interaction-frame Hamiltonian can be written as a Fourier series

$$\hat{\tilde{\mathscr{H}}}(t) = \sum_{n=-2}^{2} \sum_{k=-\infty}^{\infty} \sum_{\ell=-1}^{1} \hat{\tilde{\mathscr{H}}}^{(n,k,\ell)} e^{in\omega_{\text{r}}t} e^{ik\omega_{\text{m}}t} e^{i\ell\omega_{\text{eff}}t}. \tag{5.7}$$

with the Fourier coefficients $\hat{\bar{\mathscr{H}}}^{(n,k,\ell)}$ given by

$$\hat{\bar{\mathscr{H}}}^{(0,k,\ell)} = \sum_{p=1}^{2} \omega_p^{(0)} \sum_{s=-1}^{1} a_{1,s}^{(k,\ell)} T_{1,s}^{(p)} \tag{5.8}$$

$$\hat{\bar{\mathscr{H}}}^{(n,k,\ell)} = \omega_{1,2}^{(n)} \sum_{s=-2}^{2} a_{2,s}^{(k,\ell)} T_{2,s}^{(1,2)} + \sum_{p=1}^{2} \omega_p^{(0)} \sum_{s=-1}^{1} a_{1,s}^{(k,\ell)} T_{1,s}^{(p)}. \tag{5.9}$$

The scaling factors $a_{r,s}^{(k,\ell)}$ are the Fourier coefficients of the interaction-frame trajectory of the $T_{r,0}$ spherical spin-tensor operators [121]

$$\tilde{T}_{r,0}(t) = \sum_{s=-r}^{r} a_{r,s}(t) T_{r,s} = \sum_{s=-r}^{r} T_{r,s} \sum_{k=-\infty}^{\infty} \sum_{\ell=-s}^{s} a_{r,s}^{(k,\ell)} e^{i(k\omega_{\mathrm{m}}+\ell\omega_{\mathrm{eff}})t} \tag{5.10}$$

and can be calculated analytically for the ideal π pulses [21]. In the case of real, non-ideal pulses, the Fourier coefficients have to be calculated numerically from the interaction-frame trajectory. The resulting first-order effective Hamiltonian $\overline{\hat{\mathscr{H}}}^{(1)}$ is given by

$$\overline{\hat{\mathscr{H}}}^{(1)} = \hat{\bar{\mathscr{H}}}_{(1)}^{(0,0,0)} + \sum_{n_0,k_0,\ell_0} \hat{\bar{\mathscr{H}}}_{(1)}^{(n_0,k_0,\ell_0)} \tag{5.11}$$

and the second-order effective Hamiltonian $\overline{\hat{\mathscr{H}}}^{(2)}$ by

$$\overline{\hat{\mathscr{H}}}^{(2)} = \hat{\bar{\mathscr{H}}}_{(2)}^{(0,0,0)} + \sum_{n_0,k_0,\ell_0} \hat{\bar{\mathscr{H}}}_{(2)}^{(n_0,k_0,\ell_0)} \tag{5.12}$$

with

$$\hat{\bar{\mathscr{H}}}_{(2)}^{(n_0,k_0,\ell_0)} = \sum_{\nu,\kappa,\lambda} -\frac{1}{2} \frac{\left[\hat{\bar{\mathscr{H}}}^{(n_0-\nu,k_0-\kappa,\ell_0-\lambda)}, \hat{\bar{\mathscr{H}}}^{(\nu,\kappa,\lambda)} \right]}{\nu\omega_{\mathrm{r}} + \kappa\omega_{\mathrm{m}} + \lambda\omega_{\mathrm{eff}}}$$

$$= \sum_{\nu,\kappa,\lambda} -\frac{1}{2} \frac{\omega_p^{(n_0-\nu)} \omega_p^{(\nu)}}{\nu\omega_{\mathrm{r}} + \kappa\omega_{\mathrm{m}} + \lambda\omega_{\mathrm{eff}}} A_{\kappa,\lambda}(k_0,\ell_0) \tag{5.13}$$

at the tri-modal resonance condition

$$n_0\omega_{\mathrm{r}} + k_0\omega_{\mathrm{m}} + \ell_0\omega_{\mathrm{eff}} = 0. \tag{5.14}$$

Here, $A_{\kappa,\lambda}(k_0,\ell_0)$ contains the spin part of the Hamiltonian (commutator terms) scaled with the Fourier coefficients $a_{r,s}^{(k_0-\kappa,\ell_0-\lambda)}$ and $a_{r,s}^{(\kappa,\lambda)}$. Note that the denominator in Equation 5.13 cannot be zero and resonant terms must be excluded.

In theory, n_0, k_0 and ℓ_0 can be any set of integer numbers that fulfils Equation 5.14 with the strength of the first-order recoupling condition given by the scaling factor $a_{r,s}^{(k,l)}$. For ideal pulses where the effective field is zero, one can describe the sequence in a bi-modal Floquet picture and the resonance condition of an RN_n^ν sequence is given by $k_0 = -nn_0$. It was shown in the selection rule in Equation 5.1, the coefficients $a_{r,s}^{(k_0,0)}$ are only non zero for $k_0 = (N/2)z - s\nu$ with z being an integer that has the same parity as r. This condition yields resonant first-order contributions to the Hamiltonian for RN_n^ν sequences in a bi-modal Floquet picture given by $\hat{\bar{\mathscr{H}}}^{(n_0,k_0)} = \hat{\bar{\mathscr{H}}}^{(n_0,-nn_0)}$ (see Eq. 5.9). For the R26_4^{11} sequence relevant non-zero terms are

$$\hat{\bar{\mathscr{H}}}^{(\mp 1,\pm 4)} = \omega_{1,2}^{(\mp 1)} \, a_{2,\pm 2}^{(\pm 4)} \, T_{2,\pm 2}^{(1,2)} \tag{5.15}$$

containing only double-quantum terms. If the pulses do not correspond to an ideal inversion, we have to use the full tri-modal picture including the effective field ω_{eff}. It can be shown that for an R-type sequence, the effective field axis lies close to the z axis and that the selection rules for the ideal sequence $k_0 = (N/2)z - s\nu$ are still valid and $\ell_0 = -s$ has to be fulfilled simultaneously, resulting in resonant first-order contributions to the effective Hamiltonian given by $\hat{\bar{\mathscr{H}}}^{(n_0,k_0,\ell_0)} = \hat{\bar{\mathscr{H}}}^{(n_0,-nn_0,\ell_0)}$, where $\ell_0 = \pm 2$ for double-quantum recoupling or $\ell_0 = 0$ for zero-quantum recoupling. For the R26_4^{11} sequence that selectively recouples the double-quantum terms, the relevant terms are

$$\hat{\bar{\mathscr{H}}}^{(\mp 1,\pm 4,\mp 2)} = \omega_{1,2}^{(\mp 1)} \, a_{2,\pm 2}^{(\pm 4,\mp 2)} \, T_{2,\pm 2}^{(1,2)}. \tag{5.16}$$

In the presence of an effective field, the resonance condition (Eq. 5.14) is slightly shifted compared to the ideal case, leading to the recoupling Hamiltonian as given in Equation 5.16. Besides the desired resonant contributions, we also have to discuss the non-resonant error terms that can lead to a truncation of the resonant part of the Hamiltonian. In

first order, the error terms originate from a term directly proportional to the isotropic chemical-shift Hamiltonian, given by

$$\hat{\bar{\mathscr{H}}}^{(0,0,0)} = \sum_{p=1}^{2} \omega_p^{(0)} \sum_{s=-1}^{2} a_{1,s}^{(0,0)} T_{1,s}^{(p)}. \tag{5.17}$$

Evaluation of the non-resonant second-order error terms (Eq. 5.13) shows that the biggest contributions often come from the CSA-CSA crossterms. They are obtained by evaluating the commutators in Equation 5.13.

$$
\begin{aligned}
A_{\kappa,\lambda}(k_0, \ell_0) = {} & \left(a_{1,-1}^{(k_0-\kappa,\ell_0-\lambda)} a_{1,1}^{(\kappa,\lambda)} - a_{1,1}^{(k_0-\kappa,\ell_0-\lambda)} a_{1,-1}^{(\kappa,\lambda)} \right) T_{1,0} \\
& + \left(a_{1,0}^{(k_0-\kappa,\ell_0-\lambda)} a_{1,1}^{(\kappa,\lambda)} - a_{1,1}^{(k_0-\kappa,\ell_0-\lambda)} a_{1,0}^{(\kappa,\lambda)} \right) T_{1,1} \\
& + \left(a_{1,-1}^{(k_0-\kappa,\ell_0-\lambda)} a_{1,0}^{(\kappa,\lambda)} - a_{1,0}^{(k_0-\kappa,\ell_0-\lambda)} a_{1,-1}^{(\kappa,\lambda)} \right) T_{1,-1}.
\end{aligned}
\tag{5.18}
$$

For the term $\hat{\bar{\mathscr{H}}}_{(2)}^{(0,0,0)}$ it can be shown using symmetry arguments for the Fourier coefficients $a_{1,s}^{(\kappa,\lambda)}$ that $A_{\kappa,\lambda}(0,0)$ only has contributions for the $T_{1,0}$ tensor components and Equation 5.18 reduces to

$$A_{\kappa,\lambda}(0,0) = \left(a_{1,-1}^{(-\kappa,-\lambda)} a_{1,1}^{(\kappa,\lambda)} - a_{1,1}^{(-\kappa,-\lambda)} a_{1,-1}^{(\kappa,\lambda)} \right) T_{1,0}. \tag{5.19}$$

In order to obtain the most efficient recoupling by an RN_n^ν sequence, the triple-mode resonance condition (Eq. 5.14) has to be fulfilled and the first-order dipolar scaling factor given in Equation 5.16 has to be maximized while simultaneously minimizing the first- and second-order error terms. A similar theoretical descriptions holds true for C sequences and can be found in detail in Ref. [63] and [25].

5.2. Analytical and Numerical Calculations

As discussed above, the R sequences are implemented by fitting the basic RR' element $N/2$ times into n rotor periods with an R element corresponding to a net π rotation. The phase of the pulse for the R26$_4^{11}$ sequence is given by $\phi = {}^{11}\!/_{26} \cdot \pi$. The pulses can be either implemented as hard rectangular pulses (Fig. 5.2B) or as amplitude-shaped pulses with finite edges that allow for the compensation (Fig. 5.2C).
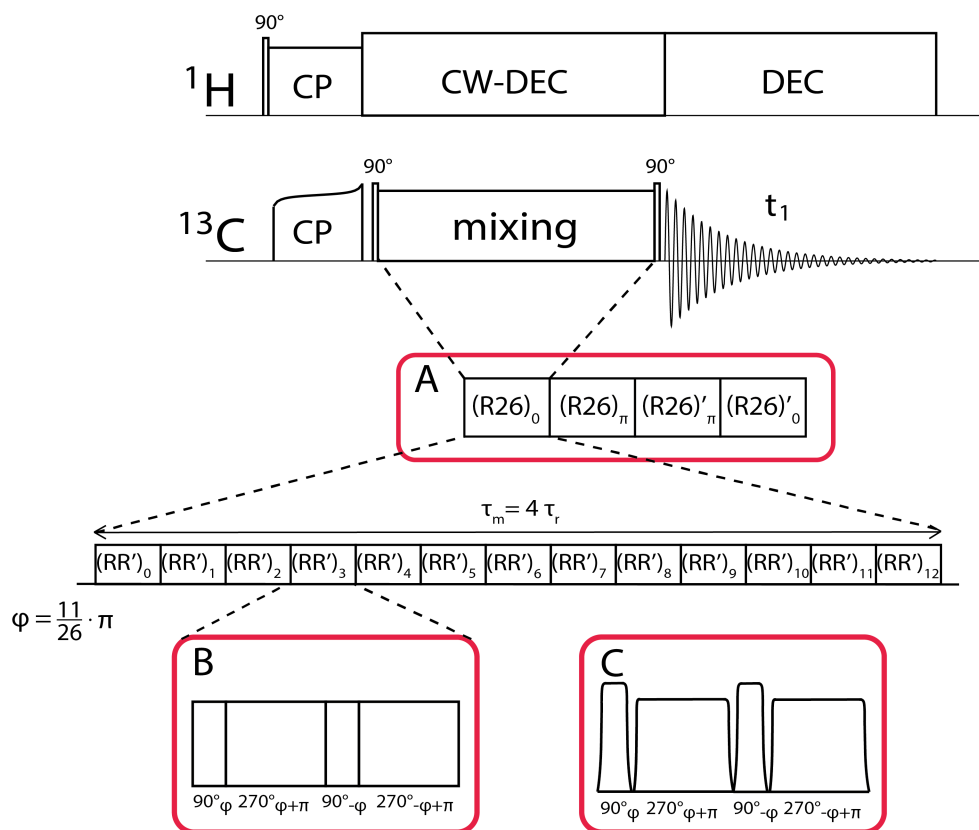
Figure 5.2. Schematic representation of the dipolar double quantum R26 recoupling sequence in a 1D experiment. Various implementations are shown with one example as a supercycle SR26 (A) with permutation and π phase shift of the R26 mixing block. The dash symbolizes a phase permutation. Different basic R elements are used to make up the R26 mixing block: (B) R element consisting of ideal rectangular pulses with composition $(\pi/2)_\phi(3\pi/2)_{\phi+\pi}$. (C) Transient-compensated R element consisting of amplitude-shaped pulses with sine-shaped edges.

The sequence can be stabilized towards different error terms using a supercycled implementation. A detailed theoretical analysis of the effect of supercycles on symmetry-based sequences is given in Ref. [40]. In the case of R26$_4^{11}$ a supercycle has been presented in the literature using π shifts and inversions of the R sequence as a means to achieve better compensation for error terms [120]. The detailed implementation is presented in Figure 5.2A. However, the supercycle comes at the cost of a loss of γ encoding for the sequence. This corresponds to a reduction in theoretical transfer efficiency from 73% for the basic R sequence to 52% for the supercylced implementation.

A good measure of the stability of the supercycle towards pulse errors, such as imperfect

rotations due to missets in rf-field amplitude, or tilted rotation axes due to quadrature components in the pulses, is the magnitude of the effective field. This effective field alters the resonance condition for the recoupling (Eq. 5.14) and thus reduces the transfer efficiency.

5.2.1. Effective Fields from Imperfect Rotations

The effective fields for misset of the rf-field amplitude and the size of the quadrature components were calculated following the interaction-frame transformation outlined in Chapter 5.1.2. The magnitude of the effective field is shown in Figure 5.3. The supercycle denoted as SR26 shows high stability towards the rf-field maladjustments, whereas the basic R sequence is heavily influenced (Fig. 5.3A). The behaviour exhibited by the sequences towards pulse transients is different as the effective field is reduced at higher quadrature components (given by the parameter ν_{off} from Equation 3.1 (Fig. 5.3B)). In the case of pure in-phase pulse transients (amplitude transients, $\nu_{\text{off}} = 0$ kHz), an effective field is present for R26, as the amplitude transients induced by the time constant of the pulse leads to an altered flip angle.
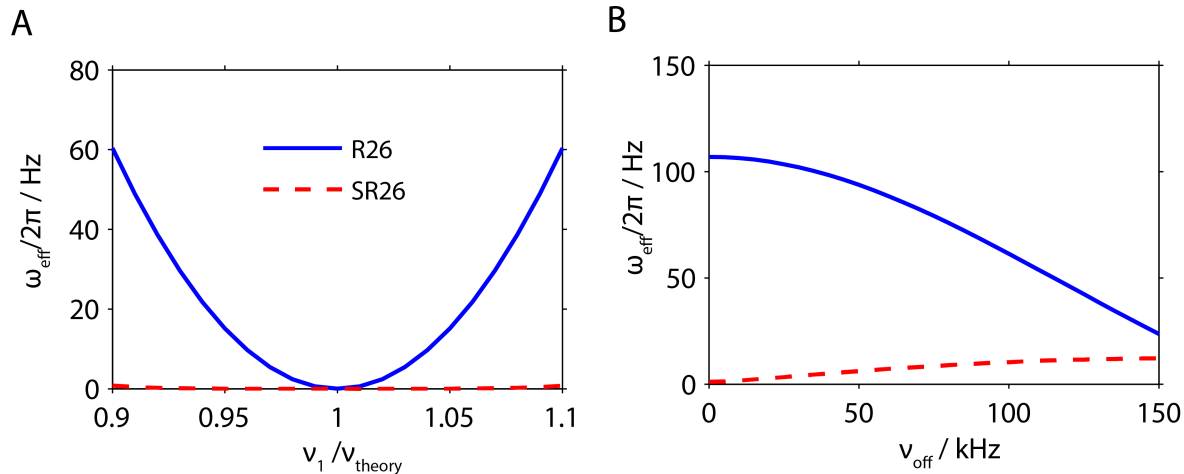
Figure 5.3. The effective fields after a full RN block for R26 (solid blue) and after a full supercycle SR26 (dashed red) as a function of the rf-field amplitude (A), and the magnitude of phase transients (B). The pulse transients were modelled with a constant rise time of 500 ns and variable electronic offset frequency (Eq.3.1).

The amplitude transients lead to a reduced effective nutation frequency due to the finite rise time of the pulse. The reduction in the effective flip angle is partially compensated

by the introduction of quadrature phase transients, as they also modify the effective pulse amplitude. Nevertheless, pure in-phase amplitude transients do not generate an effective field for SR26, as the stability towards rf-field amplitude misset is fairly high for the supercycled version and also quadrature phase transients generate only small effective fields (Fig. 5.3B).

There are three possible ways to optimize the transfer efficiency of the pulse sequence by counteracting the detuning caused by the effective fields: (i) asynchronous implementation of the R sequence, (ii) the use of supercycled sequences, and (iii) implementation of pulse-transient compensated pulses. All three possible approaches to optimize the pulse sequence were explored in the numerical simulations shown in Figure 5.4. An experimentally straightforward way to compensate the impact of effective fields in symmetry-based recoupling sequences is breaking the rotor synchronization of the pulse sequence to match the modified resonance condition of Equation 5.14. Experimentally the simplest way to achieve this is by a change of the MAS frequency, resulting in an asynchronous sequence. Numerical simulations of the transfer efficiency as a function of the MAS frequency and the rf-field amplitude are shown in Figure 5.4A for R26 and Figure 5.4B for SR26. The simulations were performed for parameters similar to the model compound of doubly ^{13}C labelled diammonium phthalate with the ^{13}C labels at the two carbonyl groups, which was also used for the RFDR experiments presented in Chapter 4.3.1.

Figure 5.4A shows that even for a perfect inversion propagator, corresponding to an rf-field strength of 62.5 kHz, there is an effective field for the R26 sequence of 32 Hz that originates from the second-order contributions of the CSA tensor. This effective field is called the fictitious field and is inherent to the pulse sequence. A detailed analysis of these fictitious fields will be discussed in detail in Chapter 5.2.2. The total value of the effective field is determined by a superposition of the contributions by the fictitious fields and by the altered effective flip angle of the pulses. The simulations show that despite the increasing magnitude of the effective field, almost maximum polarization transfer can be achieved over the whole range of rf-field amplitudes by compensating the effective field through a change in the MAS frequency.

A second approach is the application of a supercycled version of the R sequence. The sequence SR26 represents such an implementation that successfully mitigates the impact of an effective field by removing fictitious fields (Fig. 5.4B). This can be seen from the
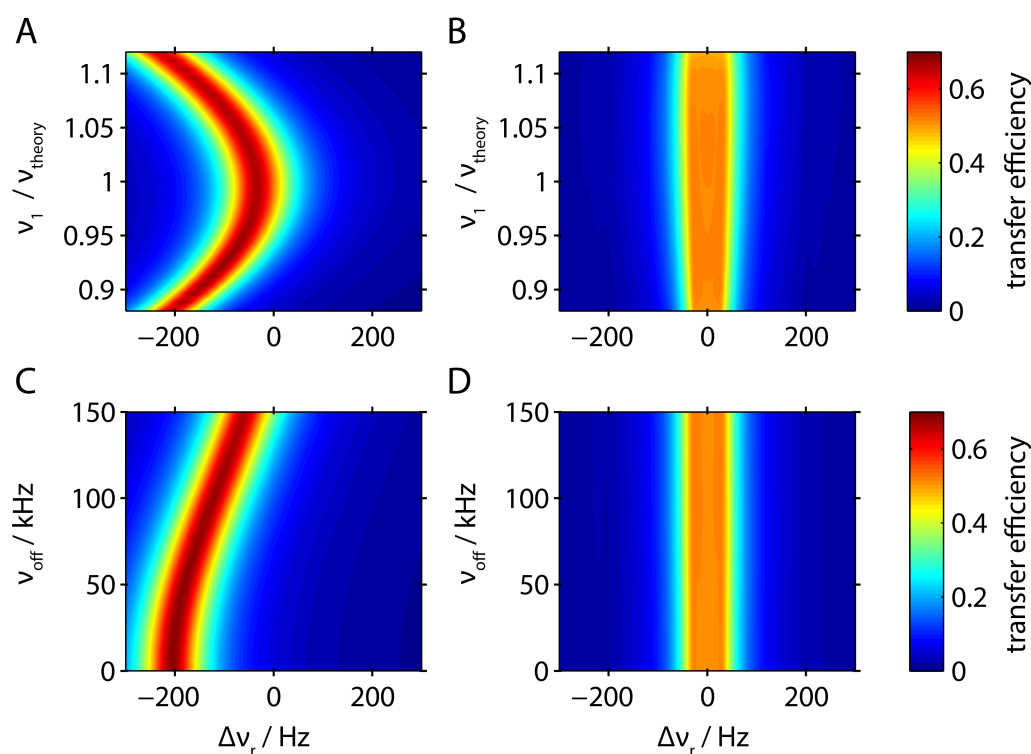
Figure 5.4. Numerical simulation of double-quantum transfer efficiency as a function of the change of the MAS frequency. The effect of a change rf amplitude and the magnitude of the phase transients were analysed in A and B, and C and D, respectively. The simulations were performed with a dipolar coupling of 585 Hz and a chemical-shift anisotropy of 8.75 kHz. The ideal rf-amplitude ν_1 corresponds to a value of 62.5 kHz at a MAS frequency of 9.615 kHz. A) Transfer efficiency for R26 with ideal rectangular pulses, B) SR26 with ideal rectangular pulses, C) R26 with pulse transients (τ_{rise} = 500 ns, variable ν_{off}) at the ideal rf-amplitude ν_1 = 62.5 kHz. D) SR26 using the same parameters for the pulse transients.

maximum of the transfer efficiency for perfect inversion pulses at an rf-field strength of 62.5 kHz, which is the theoretical value for the applied MAS frequency. The supercycled SR26 sequence also compensates rf-field amplitude missetting (Fig. 5.4B), but at the cost of losing the γ encoding of the sequence under MAS. Therefore, the maximum transfer efficiency for SR26 is 52%, whereas the maximum transfer for R26 is 73%.

Adding analytically modelled pulse transients to the simulations (Fig. 5.4C and 5.4D) results in a further shift from the theoretical recoupling condition for the R26 sequence. The pulse transients were simulated according to the model given in Equation 3.1. A time constant of τ_{rise} = 500 ns and a variable offset frequency ν_{off}, corresponding to experimentally observed pulse parameters, were used for the simulations. An additional effective field due to the quadrature component of the pulse transients is superimposed

on the effective field observed using ideal rectangular pulses. The best result is observed for high phase transients as the amplitude transient deteriorates the effective flip angle, which is partially compensated by the introduction of phase transients. Analogous calculations for the supercycle SR26 show that pulse transients are compensated almost perfectly (Fig. 5.4D).

The influence of the pulse errors shown in numerical simulations can be controlled by the experimentalist. A careful setup of the experiments and the use of transient compensation can negate these effects. However, the change of the resonance conditions due fictitious fields is inherent to the sequence and their magnitude is dependent on the spin system.

5.2.2. Fictitious Effective Fields

The effective field observed for perfect inversion pulses in the numerical simulations in Figure 5.4A can be attributed to CSA crossterms and are termed fictitious fields. Fictitious fields were first discussed in the literature arising from dipole-dipole crossterms [122] and for CSA-CSA crossterms in proton assisted recoupling (PAR) experiments [123].

This contribution of 32 Hz scales roughly quadratically with the CSA tensor and thus confirms the second-order nature of CSA-CSA crossterms (Fig. 5.5). The effective field is determined as the change in the synchronous MAS frequency needed to obtain the maximum transfer efficiency. The effective field shown in Figure 5.5 is a superposition of the imperfect inversion and the fictitious field of roughly 32 Hz for a CSA tensor of 8.75 kHz.

As shown in Figure 5.4, CSA-CSA crossterms are the main source of such effective fields. Their magnitude is shown in Figure 5.6A as a function of the applied rf field and the detuning of the MAS frequency. The crossterms were calculated according to Equations 5.13 and 5.18. The magnitude of the terms is virtually unaffected by the MAS frequency, but scales nearly linearly with increasing rf-field amplitude. Note that the Fourier coefficients in Equation 5.18 are almost independent of the MAS frequency. For a given rf field the MAS frequency changes the second-order Hamiltonian only through the denominator in Equation 5.13. The magnitude of the effective fields caused by CSA crossterms and the rf-field amplitude missetting matches the detuning of the MAS fre-
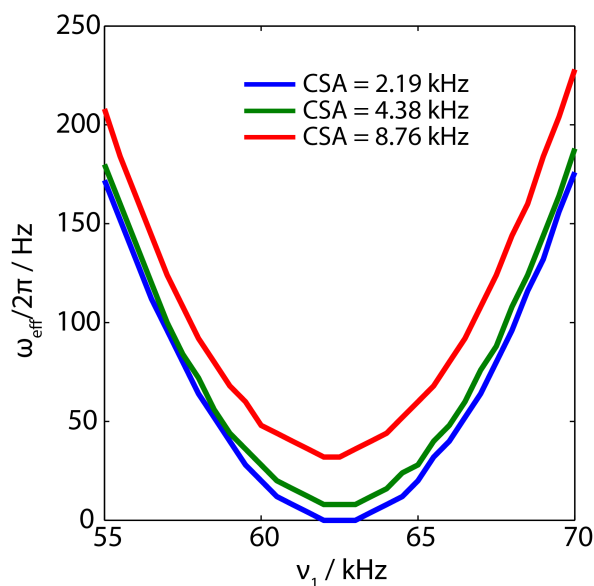
Figure 5.5. Simulation of the effective-field dependence on the CSA tensor. The effective field is taken as the MAS detuning needed for maximum transfer efficiency. The simulation input is the same as shown in Figure 5.4A. The MAS resolution was 4 Hz. The synchronous MAS frequency was set to 9.615 kHz, corresponding to a theoretical rf amplitude of 62.5 kHz. The effective field scales quadratically with the CSA tensor, proving that the fictitious field is due to CSA-CSA crossterms.

quency obtained by numerical simulations very well (Fig. 5.6B). Analogous calculations for the supercycle SR26 yield crossterms that are five orders of magnitude smaller, and the effective field due to these crossterms can be neglected to very good approximation.

There are many more potential error terms that have been neglected in this description based on the assumption that the CSA terms are dominating in our case. There are, for example, also heteronuclear dipole-dipole crossterms if the recoupling is done without decoupling. They can be significant for protonated carbons due to the large magnitude of the heteronuclear dipolar coupling of directly bound spin pairs. Identical numerical simulations of the results shown in Figure 5.4 with different spin systems yield additional effective fields generated by heteronuclear dipolar couplings. Under cw proton decoupling, these effective fields still exist but are significantly reduced in magnitude, and thus the description solely based on the CSA-CSA crossterms is valid in this case.

In conclusion, numerical simulations and a triple-mode Floquet description of the R26 sequence give insight into the contributions to the effective field after one modulation period. The most important contributions are the rf-amplitude misset that results in
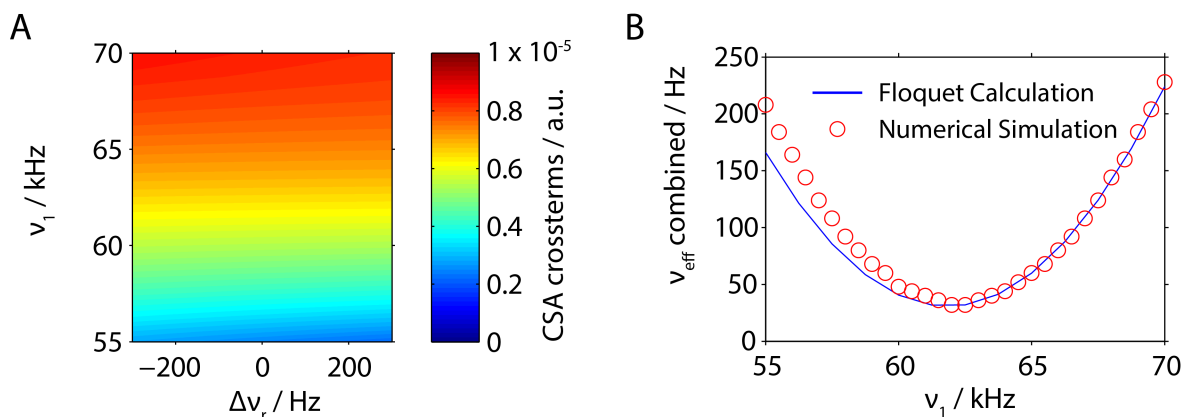
Figure 5.6. A) The magnitude of the second-order CSA-CSA scaling coefficients for R26 recoupling calculated with ideal rectangular pulses as a function of the MAS detuning and the rf amplitude ν_1 at an MAS frequency of 9.615 kHz. For the fictitious effective fields, these terms are scaled with the coefficients $\omega_p^{(\nu)}$ and $\omega_p^{(n_0-\nu)}$ to match the detuning of 32 Hz at an ideal rf-field amplitude. B) The fictitious fields from error terms added to the effective field caused by the altered flip angle calculated by interaction-frame transformation (blue line). The combined effective field agrees with the MAS detuning obtained from numerical simulations (red dots, taken from Figure 5.4A).

effective fields of up to 60 Hz for a misset of 10% and pulse transients that add an additional field between 20 and 100 Hz depending on the magnitude of the amplitude and phase transients. A third contribution observed in the numerical simulations is due to the second-order CSA-CSA crossterms. The magnitude of the generated fictitious field depends mainly on the spin system. It was calculated to be 32 Hz for a CSA tensor of 8.75 kHz.

5.3. Experimental Results

In order to verify the results from numerical simulations, we have experimentally optimized the polarization transfer using the three discussed approaches. Diammonium phthalate selectively labelled at the carbonyl groups and diluted 1:7 in natural abundance served as a model compound with its small chemical-shift difference and a medium CSA tensor. Polarization-transfer curves were measured at a static magnetic field of B_0 = 7.1 T, corresponding to a situation with a relatively small CSA tensor (5.25 kHz). In addition, measurements at a static magnetic field of 16.6 T were carried out, in which the influence of the CSA tensor is much more important.
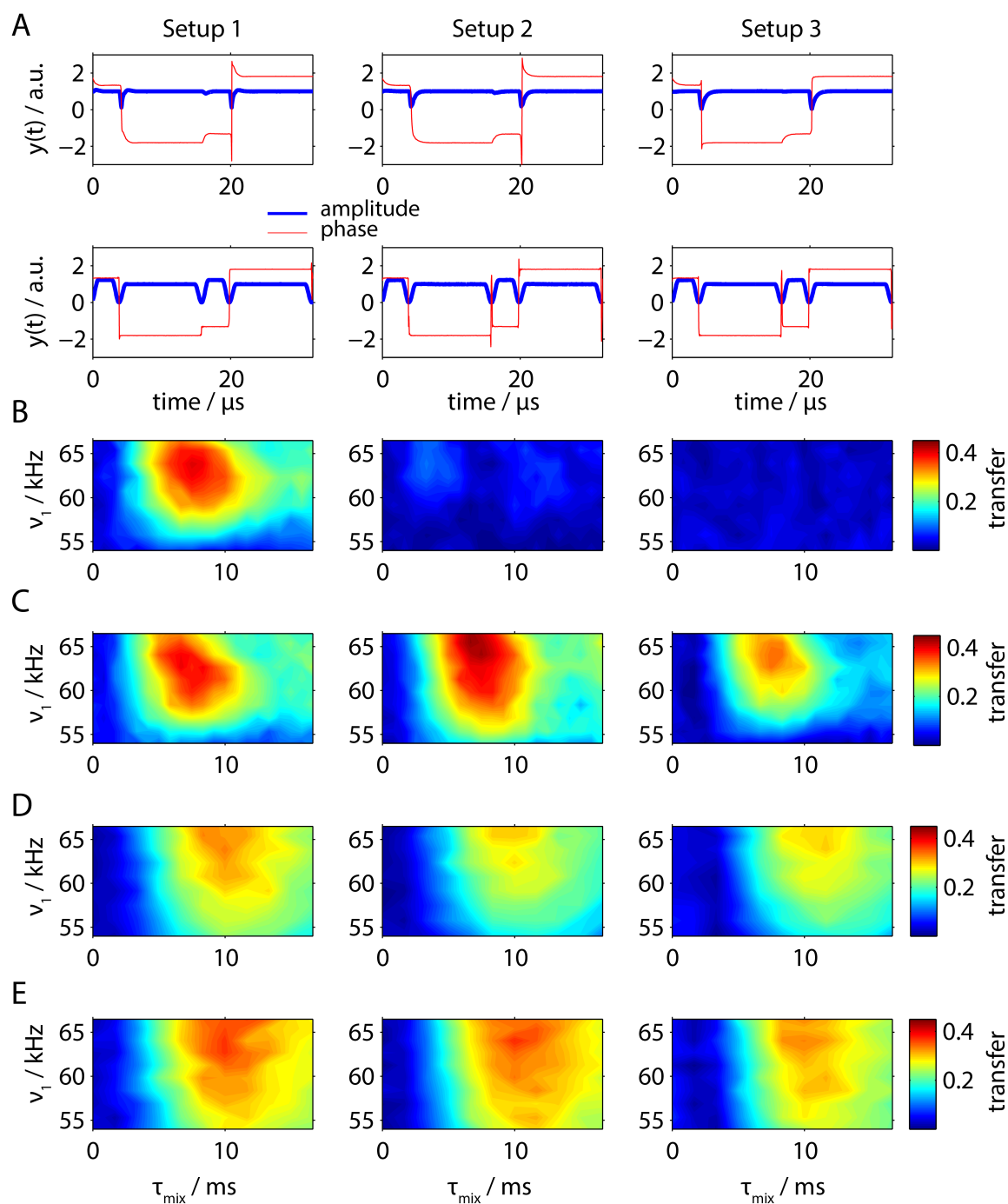
Figure 5.7. Experimental double-quantum transfer efficiency for R26 recoupling at 9.615 kHz MAS in doubly ^{13}C labelled phthalate. The external magnetic field was 7.1 T, with a basic R element $(\pi/2)_\phi(3\pi/2)_{\phi+\pi}$. Decoupling during the R sequence was implemented using cw irradiation with a rf-field amplitude of 105 kHz. A) Measured B_1 shapes for conventional hard pulses (top row) and the compensated pulses (bottom row). The transfer efficiency for three different setups for rectangular pulses (B) and compensated, amplitude shaped pulses with flip-angle correction (C) is shown for the basic R26 implementation. D) and E) are the analogous measurements as in B) and C), respectively, using the supercycle SR26.

To simulate different experimental conditions, we ran the experiments with three different cable lengths between the preamplifier and the probe (setup 1-3, 125 cm, 155 cm, and 170 cm cable length) corresponding to the setups shown in Chapter 4.3. The cable length influences the shape of the pulse transient if the impedance of the resonance circuit is not perfectly matched. The change of cable results therefore in an alteration of the pulse amplitude and phase. These differences can be seen in Figure 5.7A where the B_1-field shapes measured in the probe by the pickup coil are plotted for a basic $R_\phi R_{-\phi}$ element. The top row in Figure 5.7A shows the resulting pulse shape for rectangular pulses and the bottom row shows the compensated pulses. The B_1 shapes for the rectangular pulses experienced by the sample differ from each other at the pulse discontinuities, strongly affecting the transfer efficiency as can be seen in Figure 5.7B, where the transfer efficiency is plotted as a function of the mixing time and the rf-field amplitude for the simple R26 implementation. Significant polarization transfer could only be achieved in setup 1 (38%). In both setups 2 and 3, less than 12% efficiency was measured. Use of compensated pulses (Fig. 5.7C) results in a high reproducibility of the polarization-transfer condition and also higher polarization-transfer efficiencies of 36-42%. The recoupling condition for transient-compensated pulses becomes predictable because the effective fields caused by pulse transients are suppressed. The compensation of pulses leads to an almost perfect recovery of an inversion propagator for the basic R element without residual effective fields after the rotation.

It is interesting to observe that setup 3, which has the smallest quadrature component, shows the worst recoupling performance, which agrees with the calculations shown in Figure 5.4B. It is nearly impossible to predict the recoupling performance *a priori* solely based on the shape of the pulse transients. It is by chance that setup 1 showed favourable recoupling conditions. The maximum transfer could potentially be further optimized by higher decoupling power and a reduction of the B_1-field inhomogeneity (restricted sample). Decoupling efficiency becomes more important for carbons with directly bound protons.

The second possible approach is the use of the supercycled SR26 sequence, which partially compensates effective fields at the cost of a lower theoretical transfer efficiency. Figure 5.7D and E show the transfer efficiency for the SR26 pulse sequence using rectangular pulses and transient-compensated pulses. One can clearly see a significant im-

provement compared to the transfer efficiency under the uncompensated R26 sequence (Fig. 5.7B) and transfer efficiencies around 29% are achieved. However, the transfer efficiency of SR26 can still be improved to roughly 34% using transient-compensated pulses as can be seen in Figure 5.7E. The transfer of the SR26 sequence clearly shows a weaker dependence on the rf-field amplitude, but the transfer efficiencies are significantly lower than in the transient-compensated R26 sequence. This is due to the loss of γ encoding in the SR26 sequence, which leads to a reduction in the theoretical transfer efficiency. For the highest transfer efficiency, transient-compensated pulses are clearly the better solution even if they currently require specialized equipment.

If transient compensation is not possible, asynchronous sequences for compensating the effective field or supercycled sequences are an alternative that can be used. The asynchronous implementation of the R26 sequence was first investigated at low static field (7.1 T), and thus for a small magnitude of the second-order CSA crossterms. The asynchronous implementation can be done in different ways. Two possible implementations are discussed in detail: (i) the change of the MAS frequency to compensate any effective field that is generated by pulse errors and fictitious fields (Eq. 5.14) (ii) the change of the amplitude of the first ($\pi/2$) pulse in the R element to generate additional rotation that negates effective fields.
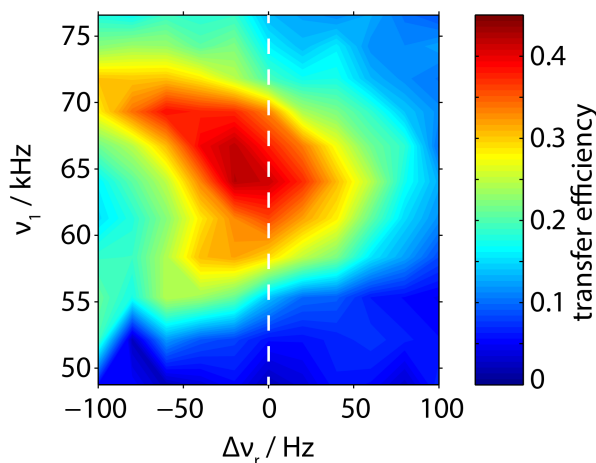
Figure 5.8. The experimental double-quantum transfer efficiency for ammonium phthalate as a function of the MAS frequency detuning and the rf-field amplitude. The theoretical rf-field amplitude is 62.5 kHz with a synchronous MAS frequency of 9.615 kHz. The experiments were performed on a 7.1 T magnet with setup 1 used in Figure 5.7. The superposition of the effective field generated by the CSA crossterms is obvious as the optimal MAS frequency at the recoupling condition is shifted by -20 Hz from the one determined from the symmetry condition.

In order to implement asynchronous conditions for the sequence, the MAS frequency was varied in steps of 10 Hz from +100 to -100 Hz with respect to the synchronous spinning frequency of 9.615 kHz. In addition, the rf-field amplitude was varied independently in order to show the effect of an altered effective flip angle. Even for setup 1 (Fig. 5.7) with favourable pulse transients, the transfer efficiency can be improved by 6% to 44% by satisfying the asynchronous condition, as shown in Figure 5.8.

In actual NMR applications, measurements are usually performed at high fields for optimum sensitivity and spectral resolution. We therefore compare the performance of each implementation at a higher static field (16.6 T) with larger second-order CSA contributions and without prior knowledge of the actual B_1 shapes, i.e., the pulse transients. Asynchronous implementation was tested by changing the MAS frequency in order to compensate for the combined effective fields from the CSA-CSA crossterms and the pulse transients. The MAS frequency was varied from 9.615 (synchronous), to 9.565, and to 9.515 kHz, while keeping the mixing time fixed at the experimentally optimized value. The highest observed transfer efficiency of 48% for R26 was found at a MAS detuning of -100 Hz (Fig. 5.9A) compared to an efficiency of 24% for the synchronous version. For SR26 the highest transfer efficiency of 38% was found for the synchronous implementation (Fig. 5.9B) and detuning resulted in significantly lower polarization transfer. The supercycled sequence suppresses the effective fields very efficiently and can be implemented without experimental optimization. This is achieved, however, at the price of a lower transfer efficiency. Without the knowledge of the pulse transients and the magnitude of the CSA tensor, estimation of the required MAS detuning is not feasible. The optimization of the asynchronous recoupling condition by changing the MAS frequency has to be done experimentally and can be tedious especially for samples with low signal-to-noise ratio. As demonstrated in Figure 5.9, however even a quick scan of the MAS frequency can restore transfer efficiencies for R26 to a value that is higher than the ones obtained for synchronous SR26 if the sample yields decent signal intensities.

Changing of the MAS frequency can be a tedious parameter to optimize on the spectrometer. Another approach to compensate the combined effective field was presented in Ref. [25] for C sequences by changing the amplitude ratio of the POST recoupling
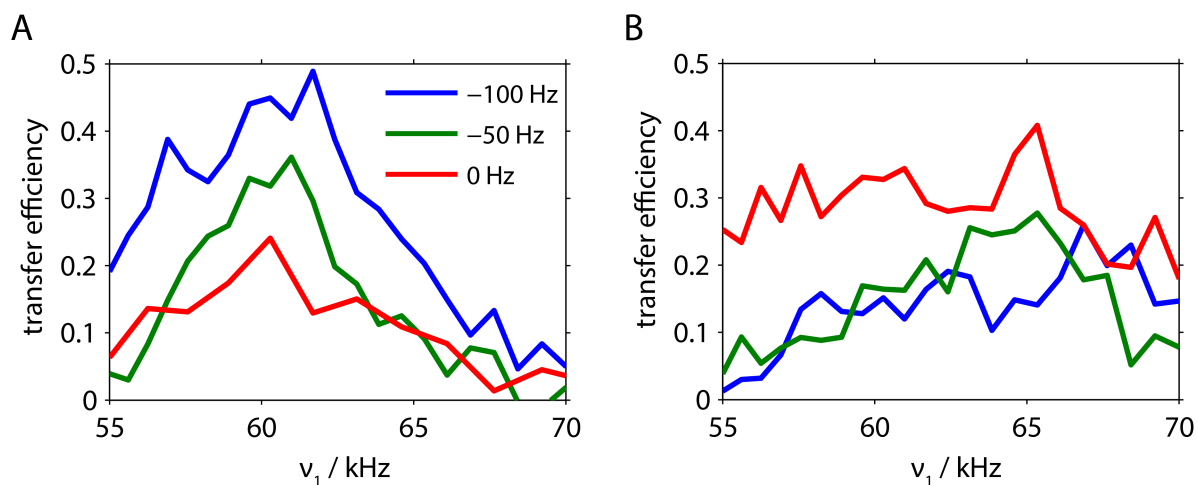
Figure 5.9. Experimental transfer for synchronous and asynchronous implementation of R26 (A) and SR26 (B) using conventional rectangular pulses at a static magnetic field of 16.6 T. The advantages of the R26 sequence are the higher transfer efficiency for the asynchronous implementation as compared to SR26 due to γ encoding. The advantages of SR26 are the robustness towards second-order error terms and rf-field missetting, making an asynchronous implementation obsolete. The maximum transfer for R26 is 48%, whereas the maximum of SR26 corresponds to 38%, as reported in the literature [111].

element. This induces an additional rotation that can counteract the effective field generated by pulse imperfections and second-order CSA contributions. The same effect is achieved when altering one of the pulse lengths, which is essentially the same as a change in amplitude, as the net flip angle of the pulse is changed.

The experimental implementation of this concept is investigated for the R26 sequence and the experimental results are supported with analytical calculations (Fig. 5.10). The two optimization parameters are the ratio of the first $(\pi/2)$ pulse with respect to the $(3\pi/2)$ pulse and the applied rf-field amplitude. The experiments were run at a MAS frequency of 12.821 kHz corresponding to a theoretical rf-field amplitude of 83.33 kHz at an external magnetic field of 11.8 T. From the experimental results in Figure 5.10A it is clear that the maximum transfer efficiency is a function of both experimental parameters and there is a linear relationship between the rf-field amplitude and the ratio. The transfer efficiency for higher ratios of the $(\pi/2)$ to the $(3\pi/2)$ element at the best rf-field amplitude is higher than for lower ratios with the matching rf-field. This observation can be understood when calculating the magnitude of the DQ dipolar scaling factor $a_{2,\pm2}^{(\pm4,\mp2)}$ (Eq. 5.16), which is directly proportional to the efficiency of the recoupling (Fig. 5.10B). The combination of the pulse ratio and the rf-field amplitude for best experimental
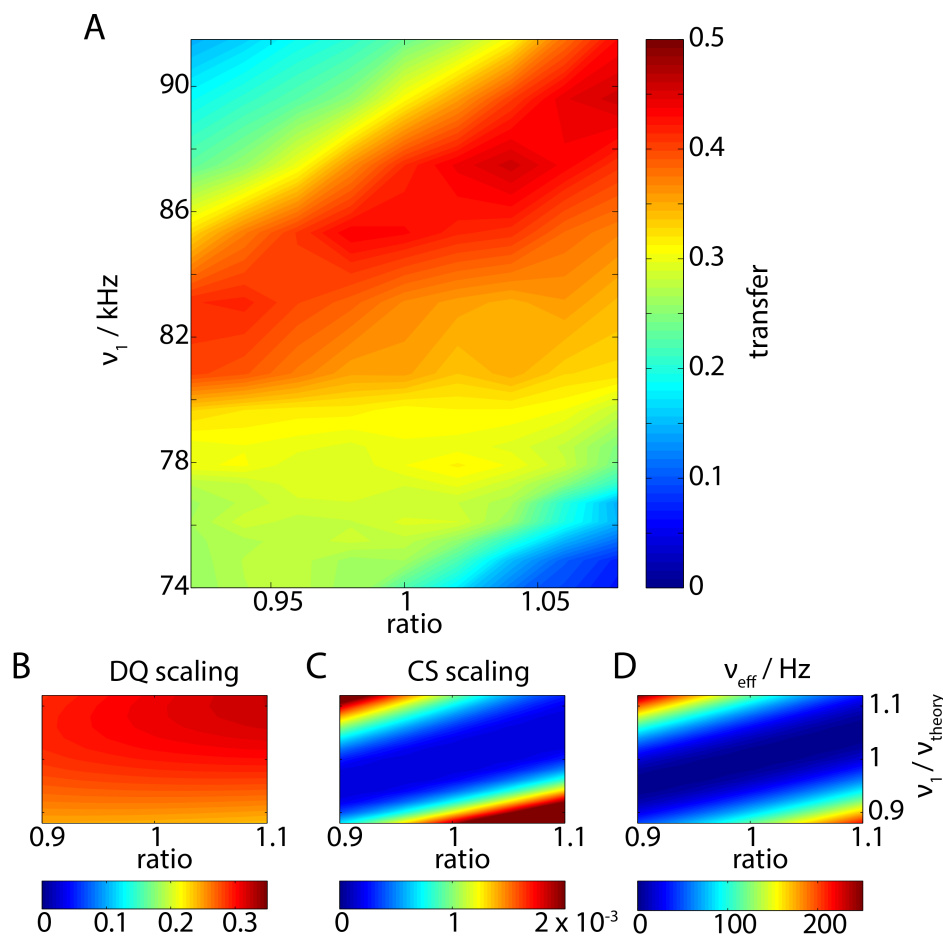
Figure 5.10. A) Experimental transfer efficiency for the basic R26 sequence as a function of the rf-field amplitude ($\nu_{1,\text{theory}}$=83.33 kHz for the synchronous implementation) and the ratio between the $(\pi/2)$ and the $(3\pi/2)$ pulse of the basic R element. The sequence was implemented using transient-compensated pulses. The transfer efficiency for every ratio can be restored by changing the rf-field amplitude, and at higher ratios and corresponding rf-field, the transfer efficiency is even higher than for the synchronous implementation. B) Analytical calculation of the DQ scaling factor $a_{2,\pm 2}^{(\pm 4,\mp 2)}$ as a function of the pulse ratio and the rf-field amplitude. C) Calculation of the isotropic chemical-shift scaling factor $a_{1,0}^{(0,0)}$, which is considered an error term in first order. D) Calculation of the effective field of the asynchronous implementation.

transfer efficiency can be explained theoretically by considering the effective field as an error term (Eq. 5.14). The isotropic chemical-shift scaling factor $a_{1,0}^{(0,0)}$ is considered an additional error term in first order in these types of sequences. Both parameters show the same behaviour that is mimicked in the experimental results (Fig. 5.10C and D). Note that the theoretical description shown in Figure 5.10B-D only considers first-

order terms, and second-order CSA contributions are not shown. However, as discussed
in Chapter 5.2.2, these contributions add a term to the effective field that is roughly
constant. This additional effective field can be observed in the experimental results
of Figure 5.10 since the best recoupling condition is shifted slightly to higher rf-field
amplitudes than predicted from a first-order calculation.

5.4. Conclusion

In conclusion, in symmetry-based R sequences unwanted effective fields are important
sources of decreased transfer efficiency when measuring intermediate or small couplings
because they lead to a mismatch of the two-frequency resonance condition. The sources
of the effective fields can be second-order CSA-CSA crossterms, pulse transients, or a
radio-frequency field that does not generate the required flip angle. The latter can be
due to a missetting of the rf-field amplitude or due to rf-field inhomogeneity. There
are three strategies to compensate the effective fields and restore efficient polarization
transfer: (i) asynchronous recoupling by detuning the spinning frequency or chang-
ing the relative pulse amplitudes, (ii) supercycled R sequences (e.g. SR26), and (iii)
transient-compensated pulses. Each of the three methods has different advantages and
disadvantages. The asynchronous recoupling by a change of the MAS frequency can
compensate all three of the sources of effective fields and leads to the highest transfer
efficiencies, but requires experimental optimization. The supercycled sequences have
generally lower efficiencies due to the lack of γ encoding, but they compensate for all
three sources and do not need any optimization. Transient compensation can be imple-
mented without experimental optimization and makes the performance of the sequences
very reproducible, but compensates only effective fields originating from pulse transients.
The choice of method or combination of methods to optimize the transfer efficiency de-
pends on the capabilities of the spectrometer and the relative magnitude of the three
different contributions. On spectrometers with the capability of phase-transient compen-
sation, transient-compensated pulses in combination with an asynchronous implementa-
tion to compensate for the second-order terms leads to the best results. On spectrometers
without the possibility to do transient compensations, an asynchronous implementation
is optimal if the S/N allows optimization of the spinning frequency. Otherwise super-

cycled sequences offer the best chance to obtain reasonable transfer efficiencies without the need for experimental optimization.

6. Homonuclear Decoupling

6.1. Introduction to FSLG

[1]H spins are present in most materials of interest and serve as an important nucleus in NMR for the study of materials in the solution state. Other than the advantage of the high sensitivity of protons, they also allow insights into molecular packing in solids, as direct observations of hydrogen bonding, C-H-π, and π-π interactions are possible [124–127]. [1]H detection has not been routinely implemented in solid-state NMR due to the large proton-proton dipolar couplings that are homogenous and are only partially averaged out by MAS at slow to medium spinning frequencies. The technical advances of probes with very fast spinning frequencies (up to 150 kHz) has been significant in recent years, however, the obtained resolution is still not sufficient for several systems [12, 128–131]. The residual linewidth in a typical fully protonated protein sample is still 100-200 Hz, making *de-novo* resonance assignment from proton-detected spectra challenging. Additionally, the small diameter of fast-spinning rotors reduces the amount of sample resulting in a significant signal-to-noise ratio loss.

An approach to improve spectral quality is the use of deuterated samples. The reduction of the density of the proton network leads to fewer spectral resonances, and thus more isolated peaks that can be assigned and used for structure calculations [132–134]. Deuteration in combination with fast spinning is, at the current stage, the method of choice for proton-detected spectra of large protein assemblies. However, the sample preparation can be difficult due to incomplete deuteration and larger systems will still suffer from spectral overlap. In order to circumvent these problems, strategies for the removal of homonuclear couplings using pulse sequences have been developed.

The first strategy using discrete rf pulses to average out homonuclear proton-proton interactions was suggested by Lee and Goldburg [42]. Further sequences that are used to

achieve homonuclear decoupling include single-pulse sequences (WAHUHA [135], MREV [59, 136], BR-24 [137, 138]), C- and R-symmetry based sequences [40, 112, 139], and DUMBO [140]. The single-pulse and symmetry-based sequences have been derived from theoretical concepts whereas DUMBO is a purely empirically developed sequence. After the development of DUMBO, it was shown that FSLG and DUMBO have the same underlying decoupling mechanism, and thus are rather similar in performance [141]. Each of these sequences has their own advantages and disadvantages in terms of robustness towards different MAS spinning regimes and requirements for the rf-field strength. Several examples of these types of sequences can be found in Ref. [142] and will not be discussed in detail.

The theoretical basis of the Lee-Goldburg sequence relies on the manipulation of the spin interactions by an off-resonance irradiation such that the quantization axis is aligned along the magic angle in a rotating frame [42]. This leads to the complete removal of the dipolar coupling in a purely homonuclear coupled system, assuming no interference from magic-angle spinning. The Lee-Goldburg pulse sequence has undergone many modifications to be more robust and to accommodate the technical deficits of spectrometer hardware. Famous alterations of the pulse sequence include the frequency-switched Lee-Goldburg (FSLG) [143–145] and the phase-modulated Lee-Goldburg (PMLG) [66]. Various supercycles have been developed to possibly compensate higher-order terms and pulse errors. The most commonly used supercycles or alterations include an inversion of the phase ramp (PMLG$_{x\bar{x}}$) [146, 147] and a relative phase shift between two PMLG cycles with an inversion of the second cycle (LG-4) [69, 148]. These supercycles have the disadvantage of lower scaling factors of the chemical shifts leading to worse spectra, assuming similar decoupling efficiency. The theoretical description of Lee-Goldburg sequences can be done within the framework of AHT or Floquet theory [22, 23, 149]. This description predicts first-order resonance conditions between the MAS frequency and the modulation frequency of the pulse sequence as well as the magnitude of second-order dipole-dipole crossterms. These crossterms were, to this point, believed to be the cause of the residual linewidth that is still observed after homonuclear decoupling in correspondence to heteronuclear decoupling. They should be minimized as well as possible to ensure spectral narrowing [105]. One theoretical description presented in the literature included the discussion of third-order heteronuclear terms that are not averaged out under simultaneous rf irradiation and MAS [150]. These terms were shown to cause a

shift in resonance frequency. A further factor for the performance degradation in FSLG sequences is believed to be experimental imperfections caused by pulse transients, which in certain cases were also used for the improvement of the pulse sequence [67]. It was also shown that the removal of phase transients leads to an improvement of the spectral quality obtained by S2-DUMBO sequences [64].

6.1.1. Theoretical Considerations of FSLG

The Lee-Goldburg scheme is based on minimizing the spin component of a homonuclear dipolar Hamiltonian by aligning the quantization axis along the magic angle since it is a rank 2 tensor. This averaging is similar to the removal of the spatial tensor of the Hamiltonian by MAS. The magic-angle irradiation is achieved by applying an rf-Hamiltonian of the general form given in Equation 5.4. In the rotating frame, the total Hamiltonian becomes time independent and is comprised of the offset Zeeman term and the rf terms. It is given by

$$\hat{\mathscr{H}} = \Delta\omega I_z + \omega_1 \left(I_x \cos(\phi(t)) + I_y \sin(\phi(t)) \right) \tag{6.1}$$

and the second term in the sum can be treated as a rotation around the z-axis by an angle ϕ. The off-resonance term $\Delta\omega$ is defined as $\omega^0 - \omega_{\text{rf}}$, where ω^0 denotes the Larmor frequency of the spin of interest. The combination of the offset and the rf irradiation along the x-axis can be interpreted as a rotation around the y-axis at an angle θ

$$\begin{aligned}
\hat{\mathscr{H}} &= R_z(\phi)\{\Delta\omega I_z + \omega_1 I_x\}R_z(-\phi) \\
&= R_z(\phi)R_y(\theta)\{\omega_{\text{eff}} I_z\}R_y(-\theta)R_z(-\phi),
\end{aligned} \tag{6.2}$$

which is defined as

$$\theta = \tan^{-1}\left(\frac{\omega_1}{\Delta\omega}\right) = \tan^{-1}\left(\frac{\nu_1}{\Delta\nu}\right) \tag{6.3}$$

and it can be shown that in first-order average Hamiltonian theory the homonuclear dipole-dipole interactions vanish if θ is adjusted to the magic angle. As a consequence, the chemical-shift Hamiltonian as a rank one tensor is also scaled down by a factor $d_{0,0}^{(1)}(-\theta) = \cos(\theta)$, which takes a value of around 0.577 at θ=54.7°. These arguments only hold true in a static regime and to get a full understanding of the sequence the

interference with the MAS has to be considered. The analysis of the Hamiltonian with multiple time dependencies that are not commensurate is done best using Floquet theory. The Floquet analysis is done in an interaction frame and the procedure was outlined in the previous Chapters (e.g. in the theory section 2.4.3 or in Equations 5.5-5.12).

Since decoupling sequences are mostly dominated by residual couplings, we will only focus on non-resonant terms, where the effective Hamiltonian is given by

$$
\bar{\hat{\mathscr{H}}} = \hat{\bar{\mathscr{H}}}_{(1)}^{(0,0,0)} + \hat{\bar{\mathscr{H}}}_{(2)}^{(0,0,0)} + \hat{\bar{\mathscr{H}}}_{(3)}^{(0,0,0)} + \ldots \tag{6.4}
$$

with the second-order Hamiltonian defined by

$$
\hat{\bar{\mathscr{H}}}_{(2)}^{(0,0,0)} = \sum_{\nu,\kappa,\lambda} -\frac{1}{2} \frac{\left[\hat{\bar{\mathscr{H}}}^{(-\nu,-\kappa,-\lambda)}, \hat{\bar{\mathscr{H}}}^{(\nu,\kappa,\lambda)} \right]}{\nu\omega_{\mathrm{r}} + \kappa\omega_{\mathrm{m}} + \ell\omega_{\mathrm{eff}}} \tag{6.5}
$$

and the third-order component given by

$$
\hat{\bar{\mathscr{H}}}_{(3)}^{(0,0,0)} = \sum_{\nu,\kappa,\lambda} \sum_{n_0',k_0',l_0'} \frac{1}{2} \frac{\left[\left[\hat{\bar{\mathscr{H}}}^{(\nu,\kappa,\lambda)}, \hat{\bar{\mathscr{H}}}^{(n_0',k_0',l_0')} \right], \hat{\bar{\mathscr{H}}}^{(-\nu-n_0',-\kappa-k_0',-\lambda-\ell_0')} \right]}{\left(\nu\omega_{\mathrm{r}} + \kappa\omega_{\mathrm{m}} + \lambda\omega_{\mathrm{eff}} \right)^2}
$$
$$
+ \sum_{\nu,\kappa,\lambda} \sum_{\nu',\kappa',\lambda'} \frac{1}{3} \frac{\left[\hat{\bar{\mathscr{H}}}^{(\nu,\kappa,\lambda)}, \left[\hat{\bar{\mathscr{H}}}^{(\nu',\kappa',\lambda')}, \hat{\bar{\mathscr{H}}}^{(-\nu-\nu',-\kappa-\kappa',-\lambda-\lambda')} \right] \right]}{\left(\nu\omega_{\mathrm{r}} + \kappa\omega_{\mathrm{m}} + \lambda\omega_{\mathrm{eff}} \right) \left(\nu'\omega_{\mathrm{r}} + \kappa'\omega_{\mathrm{m}} + \lambda\omega_{\mathrm{eff}} \right)} \tag{6.6}
$$

Note that the summations in the third-order term have to be restricted to values of $(\nu, \nu', \kappa, \kappa', \lambda, \lambda')$, which fulfil the inequalities $\nu\omega_{\mathrm{r}} + \kappa\omega_{\mathrm{m}} + \lambda\omega_{\mathrm{eff}} \neq 0$ and $\nu'\omega_{\mathrm{r}} + \kappa'\omega_{\mathrm{m}} + \lambda'\omega_{\mathrm{eff}} \neq 0$.

Evaluation of these expressions for homonuclear dipolar coupled Hamiltonians under FSLG irradiation provides insight into terms that are not averaged out and can contribute to the residual linewidth of the spectrum.

Pulse-Sequence Design

Apart from non-resonant error terms that are not averaged out, pulse imperfections in the phase ramp can lead to imperfect removal of dipolar coupling terms. In order to

remove pulse transients from the FSLG pulse sequence, slight modifications have to be made to the implementation to allow for the compensation. In theory, the sequence can be implemented either by setting the carrier to match the offset $\Delta\omega$ and switching the carrier after one LG pulse, by using rectangular pulses with discrete phase steps (e.g. PMLG-5), or by using a constant irradiation with an infinitely fast phase sweep. The new spectrometer hardware can generate shape files with time resolution up to 50 ns and an almost perfect phase ramp can be realized in order to generate a constant offset irradiation. Nevertheless, due to the finite bandwidth of the resonator, a finite rise time of the pulse is observed, as are phase transients at the 180° phase jump. To compensate for these pulse transients, a finite edge of the pulse has to be introduced. As a consequence of this pulse edge, the flip angle has to be corrected, and assuming a constant offset irradiation, an effective-field angle is generated that is not constant throughout the sequence. Therefore, the phase ramp has to be calculated explicitly by numerical integration of the offset irradiation that is needed in combination with the rf-field amplitude in order to generate a constant effective-field angle and a 2π net rotation about the effective field.

The phase of the shaped pulse is defined as

$$\phi(t) = \int_0^t \Delta\nu(t')dt' \tag{6.7}$$

with the offset frequency defined as

$$\Delta\nu = \sqrt{\nu_{\text{eff}}^2 - \nu_1^2}. \tag{6.8}$$

The rf-field amplitude ν_1 for shaped pulses is defined by setting the effective-field strength as well as the effective-field angle θ to a constant value and defining the rise time of the pulse.

The implementation of the pulse sequence for shaped and rectangular pulses is shown in Figure 6.1. The shape of the phase ramp can be understood by considering the functional form of the pulse edge which corresponds to a sine edge as discussed in Chapter 3.2.1. Therefore, the phase ramp during the pulse edges must correspond to a cosine function and the slope in the constant part is steeper compared to rectangular pulses in order to compensate for the reduced effective rotation during the finite edge.
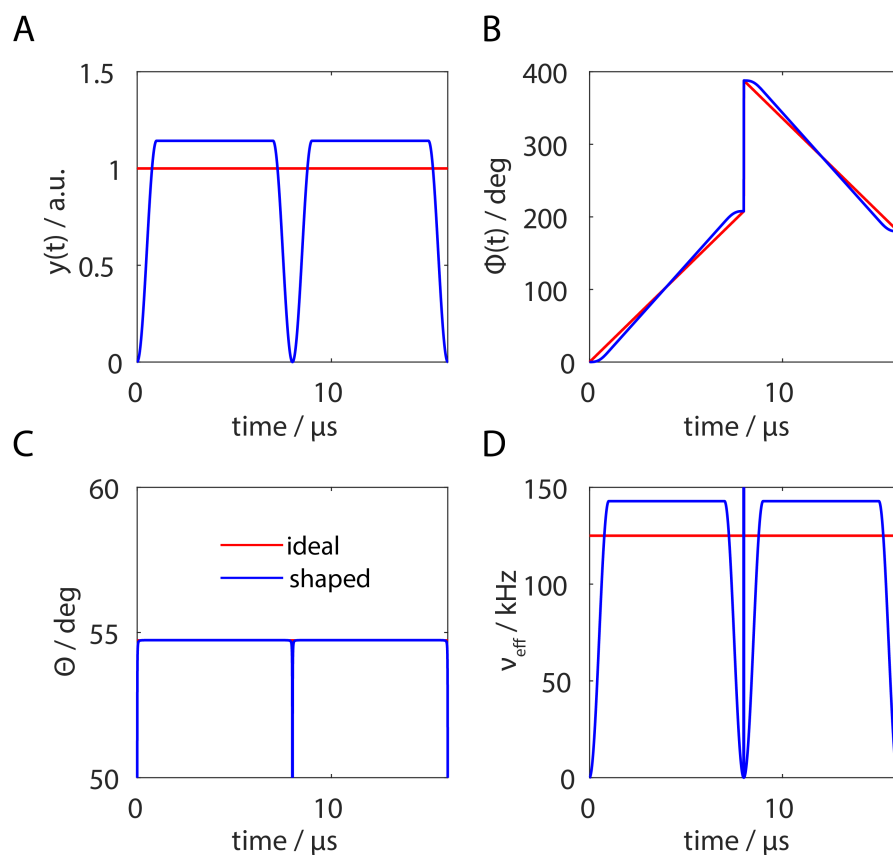
Figure 6.1. Representation of possible implementations for FSLG decoupling with shaped pulses guaranteeing a constant effective-field angle. In red, the ideal FSLG pulse sequence is shown assuming rectangular pulses and in blue, the implementation of shaped pulses. A) Flip-angle corrected amplitude with finite pulse edges of 0.4 μs. B) Time-dependent phase ramp with a 180° phase jump for the second pulse. C) Resulting effective-field angle which is kept constant at the magic angle for both implementations. D) Resulting effective field which corresponds to a net rotation of 2π at 125 kHz.

6.2. Analytical Calculations of Error Terms

Using the formalism introduced in Chapter 6.1, theoretical non-resonant error terms are calculated for a FSLG sequence assuming perfect pulses. Calculation of second-order crossterms of a homonuclear coupled spin systems with two couplings $\delta_{1,2}$ and $\delta_{1,3}$ yields lengthy expressions that depend on the powder angles α and β, the relative orientation of the two dipoles ϕ, and the angle of the effective field θ with respect to the external magnetic field. The effective-field angle is given by the magic angle for a standard FSLG sequence. All of these terms scale linearly with the product of the dipolar coupling constants $\delta_{1,2} \cdot \delta_{1,3}$. In order to illustrate the symmetry of the remaining

terms, the Hamilton operator is projected on the three-spin tensor operators. The three-spin operators are defined according to reference [151], in which they were first derived, and can be found in the Appendix A. The projections are derived for powder angles $\alpha = \beta = 45°$ and a relative dipole orientation $\phi = 45°$ since most expressions have a local maximum at these sets of angles. The modulation frequency of the pulse sequence was set to be 10 times larger than the MAS frequency to avoid any possible resonance conditions in the calculations and will be termed $z = \omega_{\mathrm{m}}/\omega_{\mathrm{r}}$. Figure 6.2 shows the dependence of the residual three-spin crossterms on the effective-field angle of the FSLG irradiation. The dominant terms are the $T_{0,0}(\tau_4)$ and the $T_{2,0}(\tau_2)$ and $T_{2,0}(\tau_3)$ tensors. The analytical expressions for the terms are given in Appendix B. The dependence on the effective-field angle can be fit with a combination of Legendre polynomial zeroth, second, and fourth order, indicating that the origin of the terms is indeed second order. In order to verify the analytical calculations, numerical simulations were run and decomposition of the obtained effective Hamiltonian led to the same values for the tensor operators.

In Figure 6.2, all existing terms from numerical calculations are shown, but analytical calculations only result in $T_{0,0}$ and $T_{2,m}$ terms. This discrepancy can be attributed to higher-order contributions that are not considered in the analytical calculations. It is obvious from the presented results that second-order three-spin terms are minimized around the magic angle which corresponds to the standard FSLG sequence. This minimum appears to be very broad and therefore, it is expected that the sequence is fairly robust towards missets in the rf-field amplitude or the phase ramp which would both result in a change of the effective field angle.

In order to investigate other possible contributions to the residual linewidth that are not averaged out by combination of MAS and the FSLG based pulse sequence, third-order autoterms are analytically calculated for a two-spin system with a single dipolar coupling. These terms are expected to scale with $\delta_{1,2}^3$ due to the third-order origin of these terms. Evaluating the double commutators for all non-resonant terms and analysing the resulting effective Hamiltonian, only terms with the tensor symmetry $T_{2,m}$ remain. The magnitude and dependence on the effective-field angle are shown in Figure 6.3. It can be deduced from this data that the terms are not averaged out by a FSLG irradiation where the angle of the effective field is set to the magic angle, but rather around 60° for the $T_{2,0}$ term and around 40° for the $T_{2,\pm2}$ term. The $T_{2,\pm1}$ does not show a local minimum
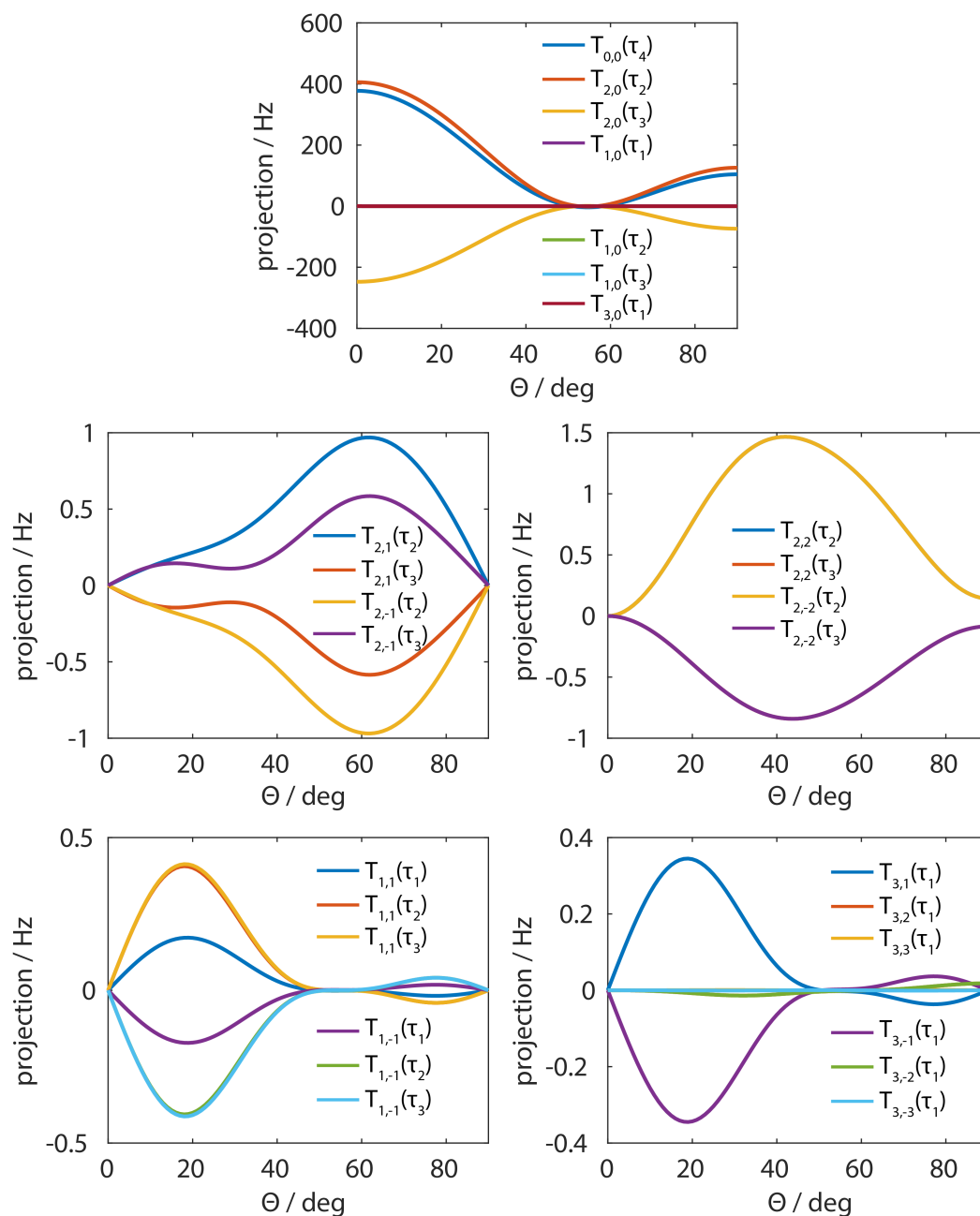
Figure 6.2. Projection of the magnitude of the three-spin tensor operators of the second-order effective Hamiltonian. The effective Hamiltonian was calculated for a Lee-Goldburg type irradiation scheme with a $(2\pi)(-2\pi)$ rotation about the effective-field angle θ. For the analytical calculations a Hamiltonian with two homonuclear dipolar couplings was assumed and the powder angles were set to $\alpha = \beta = 45°$ and the relative orientation of the dipoles to $\phi = 45°$ with the dipolar couplings set to $\delta_{1,2}=10$ kHz and $\delta_{1,3}=20$ kHz. The ratio of the modulation frequency of the pulse sequence and the MAS frequency was assumed to be 10 in order to avoid higher-order contributions to the numerical simulations. It is obvious from the magnitude of the tensor components that only the $T_{0,0}(\tau_4)$ and the $T_{2,0}(\tau_2)$ and $T_{2,0}(\tau_3)$ terms are relevant but they exhibit a broad minimum centred around the magic angle.

around sensible effective-field angles, but calculations of the propagation of the starting density operator under such a term show that it does not result in an effective splitting leading to line broadening, but rather in a shift of the resonance frequency. This fact does not hold true for the $T_{2,0}$ and the $T_{2,\pm 2}$ terms, which ultimately contribute to the linewidth under FSLG due to the additional effective field in the Hamiltonian. The magnitude of these tensors is shown in Figure 6.3 and they were calculated with the powder angles $\alpha = \beta = 45°$ and z of 10. The dipolar coupling was set to 45 kHz, which is representative of a CH_2-group that is one of the biggest challenges for homonuclear decoupling. The effective-field strength was set to 125 kHz and it can be shown that the magnitude of the third-order terms scale down quadratically with the effective field, assuming the same ratio z. However, rf-field amplitudes higher than 100 kHz are not feasible for practical applications.

It is obvious from Figure 6.3 that the third-order terms do not vanish under FSLG irradiation and they are significant in size assuming that the $T_{2,0}$ and the $T_{2,\pm 2}$ contribute directly to the linebroadening. However, these terms scale with the dipolar coupling cubed, and thus are only significant for very strong couplings. The results shown in 6.3 are calculated for a dipolar coupling of 45 kHz and are most likely overestimating the effect of a CH_2-group. However, the fact that a 'conventional' FSLG sequence does not average out the third-order terms and that their size is significant is a result that has not been discussed before in the literature.

Other than the third-order homonuclear autoterms, heteronuclear autoterms for a single ^{13}C-^1H coupling and crossterms between two homonuclear coupling contribute to third-order calculations. The crossterms between two dipoles scale in third order either with the pre-factor $\delta_{1,2}^2 \cdot \delta_{1,3}$ or with $\delta_{1,2} \cdot \delta_{1,3}^2$. Calculation of these terms show that their behaviour towards the effective-field angle is very similar to the second-order three-spin terms, as they are minimized around the magic angle or are negligible over the whole range of sensible effective-field angles.

The third-order heteronuclear terms show similar spatial behaviour as the homonuclear autoterm $T_{2,\pm 1}$ for the symmetry components $T_{0,0}$ and $T_{2,0}$. The results are shown in Figure 6.4, assuming a dipolar coupling of 40 kHz corresponding roughly to a directly bound ^{13}C-^1H spin pair. The maximum of both components is observed at $\theta=54.7°$, which corresponds to the conventional FSLG sequence. The $T_{0,0}$ and $T_{2,0}$ contribute
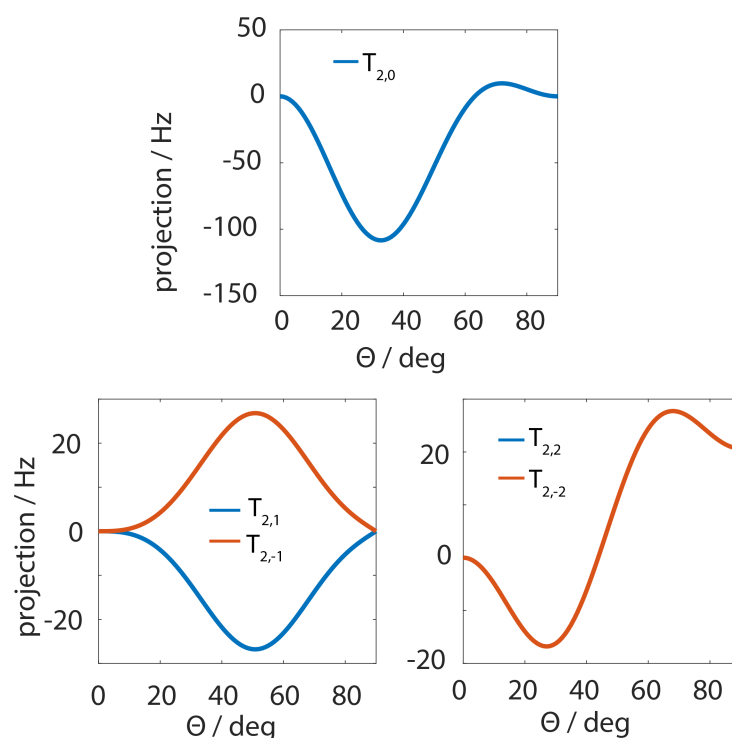
Figure 6.3. Projection of the magnitude of the third-order spin tensors resulting after FSLG irradiation only assuming a single homonuclear dipolar coupling of $\delta_{1,2}$=45 kHz. The simulation parameters for the powder orientations and the MAS to modulation frequency ratio are the same as shown in Figure 6.2. The remaining terms vanish either around 60° for the $T_{2,0}$ and around 40° for the $T_{2,\pm2}$ term. It is interesting to note that with the traditional FSLG scheme none of the third-order terms vanish.

directly to the linewidth, and thus a linebroadening of around 60 to 100 Hz is assumed when using fully ^{13}C- and ^{15}N-labelled substances instead of natural abundance. This fact is found to be true in experiments by comparison of spectra using FSLG decoupling of fully labelled and unlabelled glycine. Due to this fact, only natural abundance samples are considered for numerical calculations as well as experiments unless stated otherwise. The second-order heteronuclear terms are not of concern because they correspond to an inhomogeneous interaction and are therefore averaged out fully by magic-angle spinning since the interactions commute at any point in time.

6.3. Numerical Calculations of Effective Hamiltonians

To validate the theoretical consideration of the pulse sequence using shaped pulses presented in Chapter 6.1.1, numerical simulations were performed with both implemen-
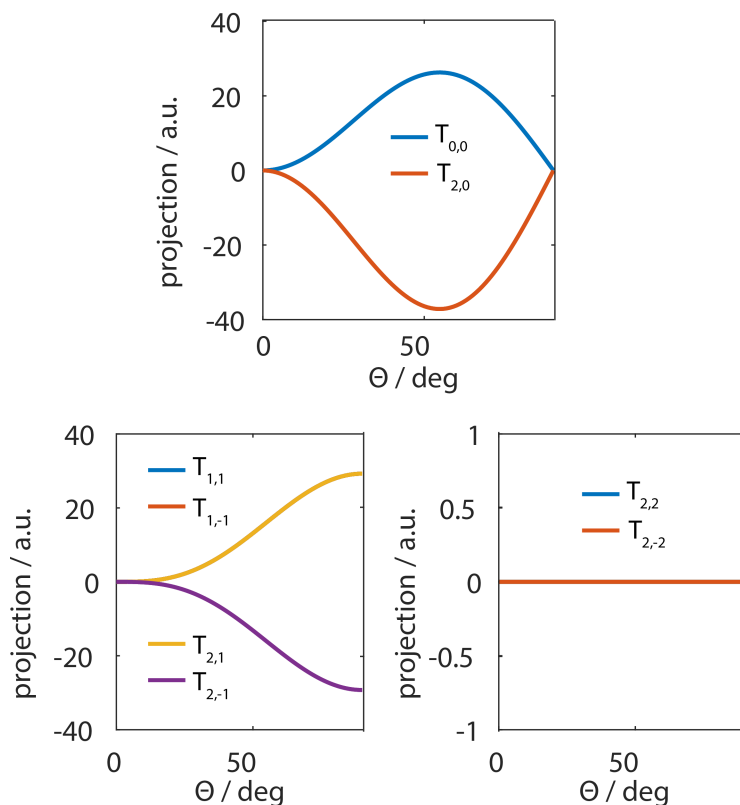
Figure 6.4. Projection of the magnitude of the third-order spin tensors resulting after FSLG irradiation assuming one heteronuclear dipolar coupling. The simulation parameters for the powder orientations and the MAS to modulation frequency ratio are the same as shown in Figure 6.3. The remaining autoterms $T_{0,0}$ and $T_{2,0}$ are maximal around the magic angle and contribute directly to the residual linewidth. Here, a dipolar coupling of 40 kHz was assumed, which corresponds to a direct C-H bond.

tations shown in Figure 6.1. The simulations were performed in the GAMMA spin-simulations environment [152]. To validate the contributions of second- and third-order terms discussed in the theory section, simulations using one and two dipolar couplings, respectively, were run. The effective field was set to be 125 kHz, corresponding to a LG pulse length of 8 μs. The MAS frequency was assumed to be 6.25 kHz leading to a ratio z of 10. Powder averaging as well as single crystal orientations of $\alpha = \beta = 45°$ with relative dipole orientations of $\phi=45°$ were used.

Only the results from powder averaging are presented, but it was additionally validated that the single crystal simulations lead to the same functional form of the linewidth. The maximum splitting of the lines is shown in Figure 6.5 without chemical-shift correction, which depends on the effective-field angle. Therefore, these splittings represent the
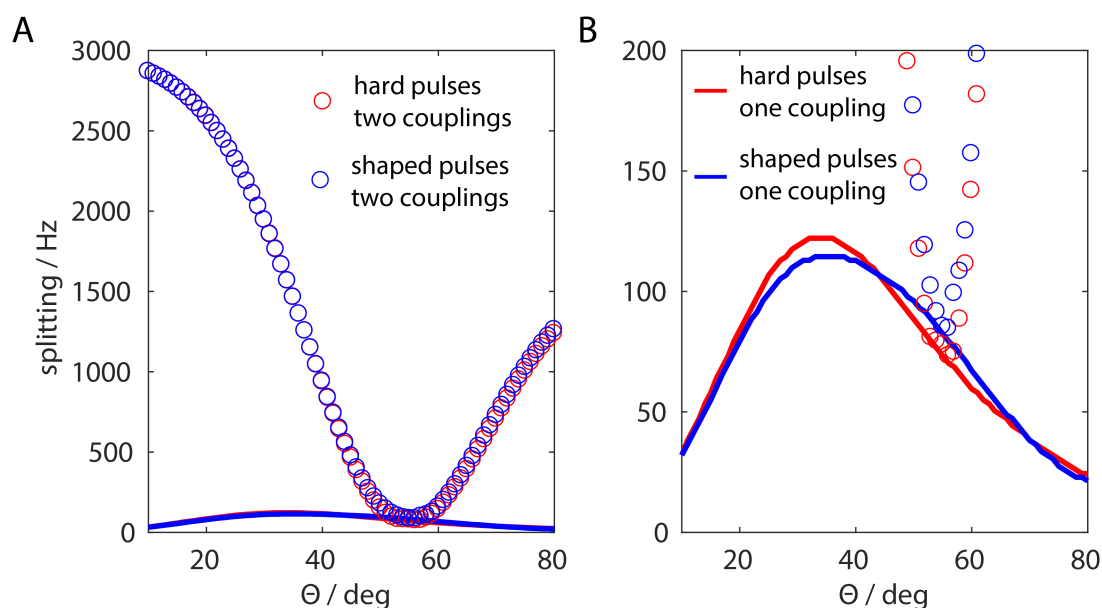
Figure 6.5. Simulations of FSLG sequence as a dependence of the effective-field angle, and implementations using rectangular pulses (red) and shaped pulses (blue). The splitting of the effective Hamiltonian corresponding to residual linewidth is presented without chemical-shift correction. The second-order crossterms are minimized around the magic angle (circles) but the third-order terms resulting from a single dipolar coupling are never fully removed (solid line). A) Full scale of linewidths as a function of the effective-field angle. B) Zoom on the residual linewidth contributions up to 200 Hz. The MAS frequency was set to 6.25 kHz, the effective field to 125 kHz, the relative dipole orientation to 45°, the dipolar couplings to 40 kHz for the single coupling and to 10 kHz for the second coupling, and powder averaging was applied.

residual effective fields in the Hamiltonian. It is obvious that the shaped-pulse implementation and the rectangular pulses lead to very similar linewidths and dependences on the effective-field angle θ. Furthermore, these results demonstrate that the second-order three-spin terms are averaged out fairly well around the magic angle, but that there are still significant contributions from third-order terms. These third-order terms are a combination of the functional forms shown in Figure 6.3 for the $T_{2,0}$ and the $T_{2,\pm2}$.

The numerical simulations and subsequent extraction of the effective Hamiltonians is a method to readily investigate the influence of various parameters on the performance of the sequence. An important parameter is the misset of the rf-field amplitude, to which the sequence is also susceptible even if pulse-transient compensation is applied. The influence of imperfect rf-field amplitude is shown in Figure 6.6.
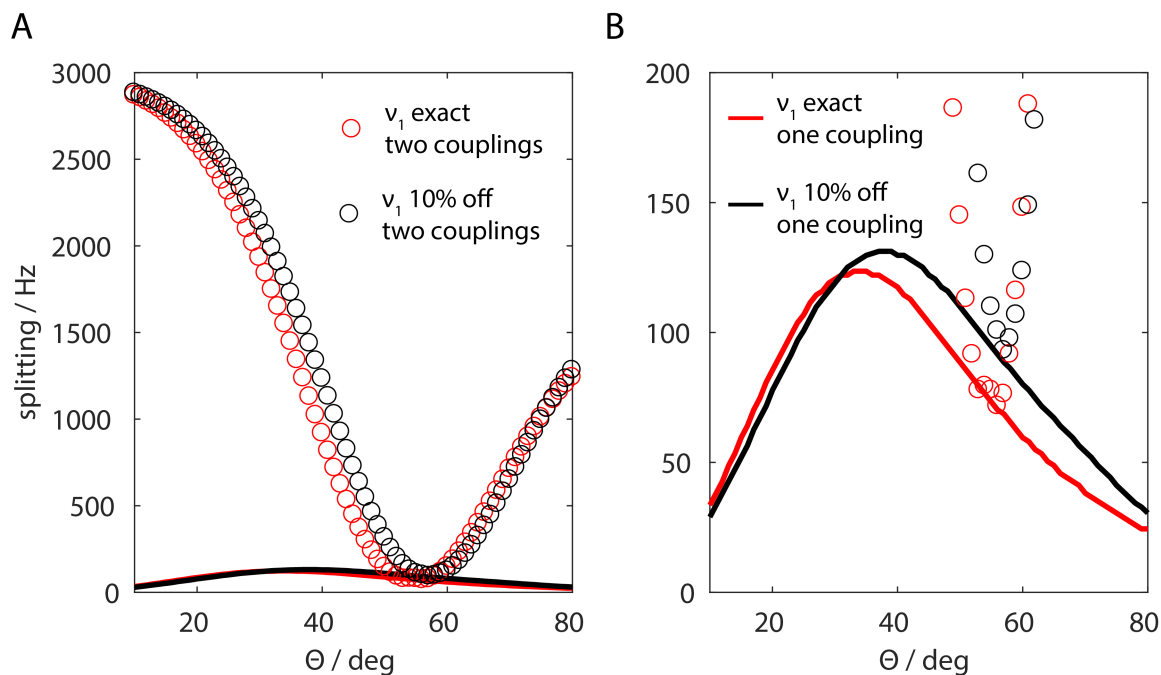
Figure 6.6. Simulations of FSLG sequence as a dependence of the effective-field angle and implementations using rectangular pulses with ideal ν_1 field strength (red) and 10% miscalibration (black). The simulation parameters are identical to the results presented in Figure 6.5.

The degradation of the decoupling efficiency is quantified by the additional splitting in the effective Hamiltonian, corresponding to 18 Hz for an effective field angle $\theta=54.7°$. However, when considering rf-field maladjustments, the decrease in performance efficiency does not seem detrimental for the sequence, but rather for the altered chemical-shift scaling. As discussed in the theory section (Chapter 6.1.1), the chemical shift scales with $\cos(\theta)$, which deviates from the set value in case of rf-field maladjustment. Therefore, a distribution of different rf-fields over the sample leads to chemical-shift scaling factors that differ for parts of the rotor. A superposition of these lines induces a broadening that cannot be removed by perfect pulses. The influence of rf-field inhomogeneities will be discussed in more detail in the experimental section in Chapter 6.4.3.

A further parameter that can potentially have a detrimental impact on the performance of the decoupling sequence is the misset of the magic angle. This parameter is investigated in numerical simulations, but the splitting of the effective Hamiltonian for sensible values up to a misset of 0.1° is nearly identical to the ideal implementation. However, these simulations only consider homonuclear couplings and a misset in the magic an-

gle could lead to potential linebroadening through imperfectly averaged heteronuclear dipolar coupling.

6.4. Experimental Results

6.4.1. θ-FSLG

Experiments were performed on various glycine derivates designed to illustrate the different contributions to the residual linewidth under FSLG decoupling. In order to avoid unexpected effects due to detection windows during the decoupling period, the experiments were implemented as 2D experiments with the FSLG decoupling in the indirect dimension followed by a long CP for direct carbon detection. The CP time was chosen to be 3 ms to ensure transfer from all protons in natural abundance glycine and negate the effects of heteronuclear dipolar couplings in unlabelled samples. This is believed to be a valid approach because spin diffusion is very efficient at the low MAS speed applied. Additionally, no supercycle was used for the FSLG sequence to benefit from the maximum possible chemical-shift scaling. Therefore, quadrature images and axial peaks were observed in the indirect dimension, which were discarded for the analysis. A full 2D spectrum obtained from the measurements including all artefacts is shown in Figure 6.7A with a magnification of the relevant slices of the CO and the Cα peak shown in B and C, respectively. In order to illustrate the effect of the compensation and the change in effective-field angle, 1D spectra are presented for the uncompensated and compensated implementation at $\theta = \theta_{\mathrm{m}}$ and $\theta = 60°$ (Fig. 6.7D and E).

Figure 6.8 shows a quantitative comparison of the decoupling efficiency using transient-compensated pulses as well as conventional rectangular pulses. The dependence on the effective-field angle is investigated in the range from $40°$ to $65°$. The pulse sequence is denoted as θ-FSLG due to the variation of the effective-field angle. The experiments were performed on a uniformly labelled ^{13}C-^{15}N-glycine at an external magnetic field of 14.1 T using a constant effective field of 125 kHz and MAS spinning speed of 14 kHz. The quantity that was used to judge the decoupling efficiency was the separation of the two proton signals of the CH$_2$-group. A value of 0 corresponds to baseline separation, whereas a value of 1 represents indistinguishable spectral lines. Figure 6.8A shows this splitting as a function of the effective-field angle and it can be appreciated that the
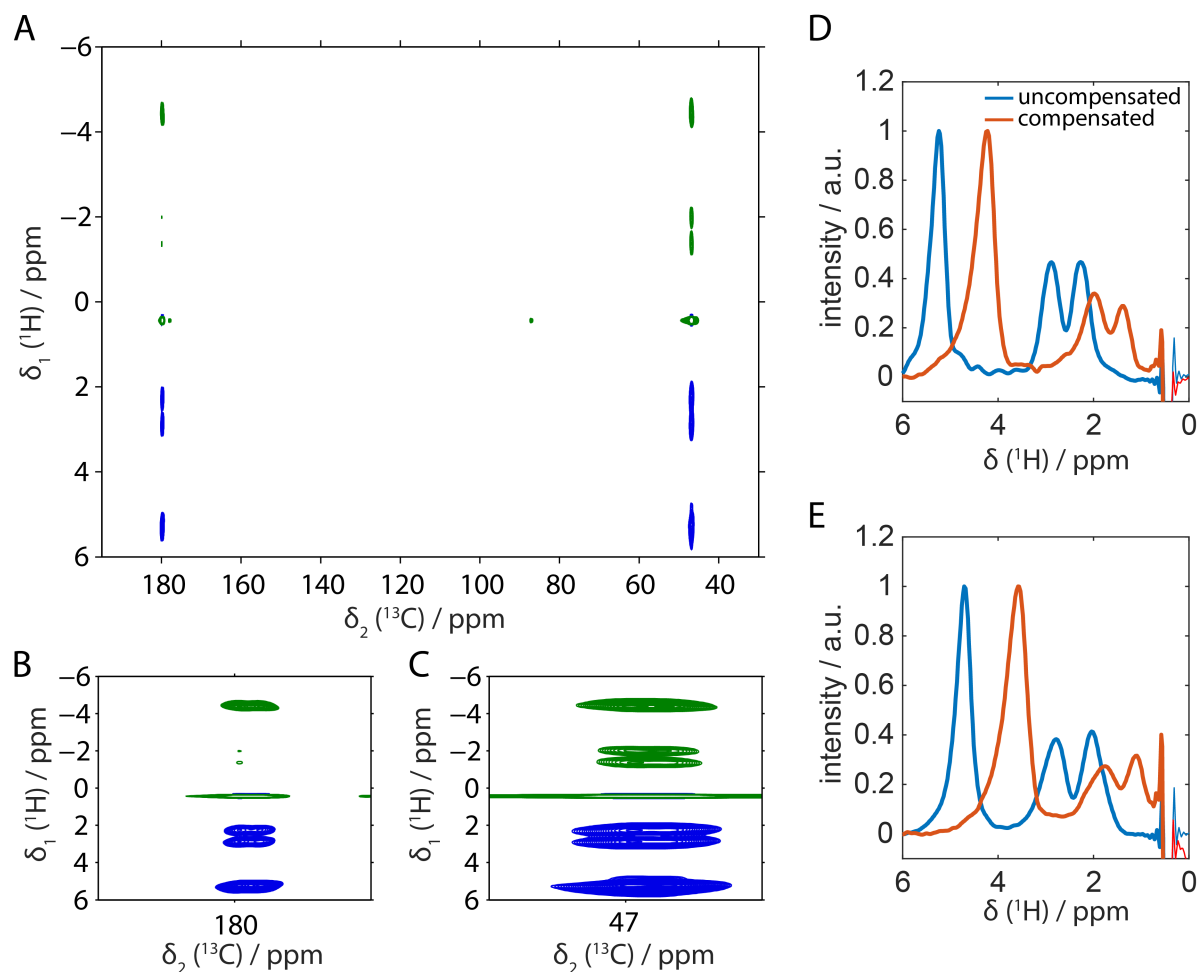
Figure 6.7. A) Experimental spectra obtained after FSLG based decoupling in the indirect dimension followed by a long CP on U-^{13}C-^{15}N-glycine. The quadrature images and axial peaks can been seen in the zooms of the CO peak (B) and the Cα peak (C). The obtained 1D spectra used for the analysis are shown for uncompensated (blue) and compensated (red) implementation at an effective-field angle of $\theta = \theta_\mathrm{m}$ (D) and $\theta = 60°$ (E). In both experiments, the compensated implementation performed slightly worse. For all experiments, the MAS frequency was set to 14 kHz with an effective field of 125 kHz at an external magnetic field of 14.1 T.

compensated pulses perform slightly worse than the conventional rectangular pulses, but the deviation lies within the experimental uncertainty. Furthermore, it is shown in the figure that the optimum decoupling efficiency is not at the magic angle but rather around 58°. This is in agreement with the theoretical predictions that the third-order terms, which are believed to be dominant in a CH$_2$-group, are minimized around this angle. The slight shift towards lower effective-field angles from the predicted 60° angle is due to additional three-spin terms that are best averaged out at the magic angle. A

Figure 6.8. Experimental results of FSLG based decoupling on U-^{13}C-^{15}N-glycine as a function of the effective-field angle. The decoupling performance is analysed in terms of t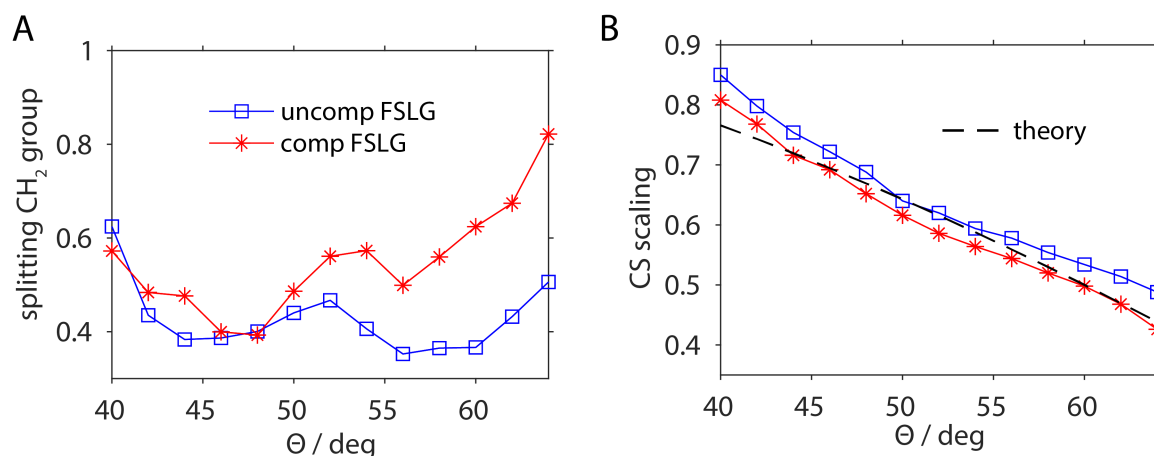he splitting between the two resonance lines of the CH$_2$-group (A), where 0 corresponds to baseline separation and the chemical-shift scaling factor (B). The MAS frequency was set to 14 kHz with an effective field of 125 kHz at an external magnetic field of 14.1 T.

further observation of these experiments is the behaviour of the chemical-shift scaling. The use of compensated pulses leads to chemical-shift scaling factors that agree very well with the theoretical prediction of $\cos\theta$, whereas rectangular pulses lead to higher chemical-shift scaling (Fig. 6.8B).

It can be seen from Figure 6.8 that pulse transients are not the main source of performance degradation in FSLG decoupling. It was shown that the behaviour of the pulse sequence becomes more predictable according to theory, but the decoupling performance is not significantly improved.

A further contribution to the residual linewidth is the heteronuclear dipolar coupling, which can be avoided by moving towards natural abundance samples. The influence of the heteronuclear decoupling was investigated by recording the spectra of natural abundance glycine using compensated and rectangular pulses and comparing the results to the ones obtained on a ^{13}C- and ^{15}N-labelled sample. The resulting spectra of the unlabelled compound for an effective-field angle of $\theta = \theta_m = 54.7°$ and $60°$ are shown in Figure 6.9A and B, respectively. These experiments can be directly compared to the spectra of the fully-labelled compound shown in Figure 6.7D and E. The improvement is dramatical, when compared to the labelled compound since in every implementation the separation of the CH$_2$-group is almost at the baseline. Quantifying the linewidth

(without chemical-shift scaling), an improvement of $\sim$60 Hz is observed going from fully labelled to unlabelled samples, which is in very good agreement with the theoretical calculations shown in Figure 6.4.
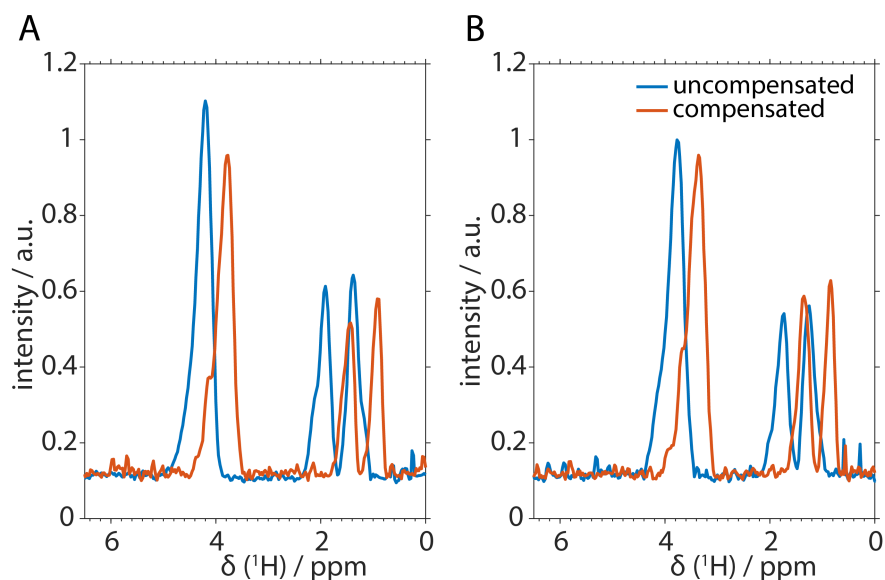
Figure 6.9. Experimental spectra of FSLG based decoupling on natural abundance glycine. The spectra are not processed in terms of chemical-shift scaling and referencing to illustrate the effect of implementing compensated pulses. The effective-field angle was either set to the magic angle (A) or 60° (B). The shift in resonance frequencies between the uncompensated pulses (blue) and the compensated (red) can be attributed to additional effective fields caused by pulse transients. The MAS frequency was set to 14 kHz with an effective field of 125 kHz at an external magnetic field of 14.1 T.

It can be argued from the spectra shown in Figure 6.9 that the pulse-transient compensation leads to slightly narrower CH_2-resonances which is in contrast to the effect observed for the fully-labelled glycine. However, this improvement is still within the range of experimental uncertainties. Note that the spectra are shown without post-processing, i.e. chemical-shift scaling and relative referencing. It is interesting to observe that the whole spectrum shifts to lower *ppm*-values for the compensated implementation. This is hypothesized to be due to the additional removal of effective fields by applying transient compensation. The effect of changing the effective-field angle from the magic angle to 60° is very small and is hard to judge from the directly-detected spectra.

6.4.2. Selectively Labelled Glycine

Quantification of the relative size of the second- and third-order terms was achieved by designing and synthesizing glycine derivates that contain an isolated two-spin system as well as a multi-spin system. A deuterated 2-^{13}C-^{15}N-glycineethylester with an isolated CH_2-group was synthesized to represent an isolated ^{1}H-^{1}H spin system. For a full analogy, a deuterated 2-^{13}C-^{15}N-glycineethylester with a CH_2- and a NH_3^+-group was used as a multi-spin system. Hahn-Echo sequences with FSLG-based decoupling during the echo time were recorded and the T_2' times were extracted. The oscillations in the decay curves have been observed before and, according to the literature, could be removed by a double-echo sequence [153].
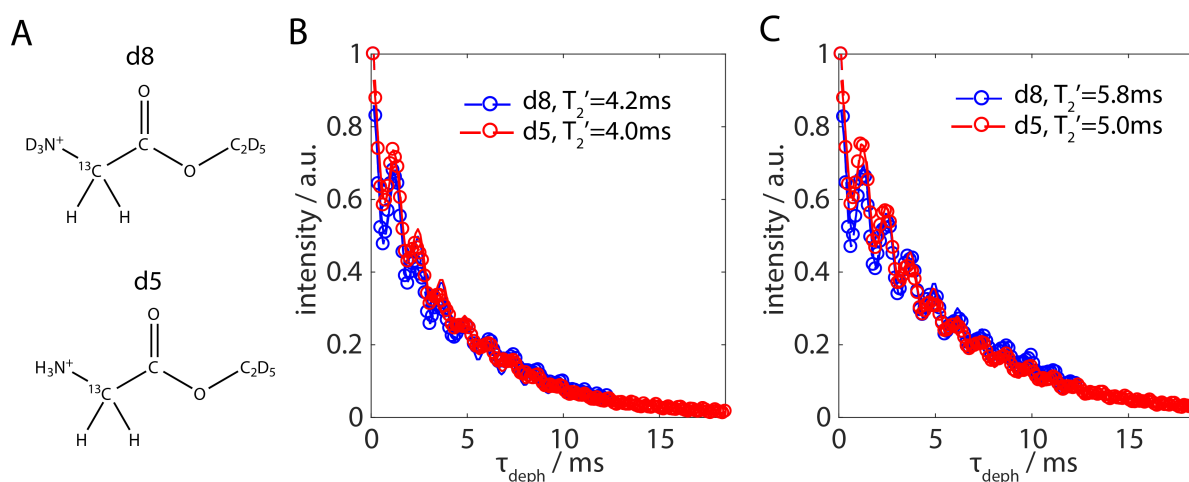
Figure 6.10. Quantification of the second- and third-order error terms in the FSLG pulse sequence. A) Model compounds of glycineethylester with an isolated CH_2-spin system (d8) and protonated NH_3^+-group representing a multi-spin system (d5). B) T_2' decay curves of the CH_2-signal using FSLG decoupling during the echo time with rectangular pulses during the echo period and an effective-field angle equal to the magic angle. C) The same curves as to B) but using compensated pulses. The MAS frequency was set to 14 kHz with an effective field of 125 kHz at an external magnetic field of 14.1 T.

It can be observed from Figure 6.10 that the influence of the second-order terms is very small and only contributes to about 5-10% of the effective T_2' times. The dominating terms are identified to be the third-order autoterms since they make up most of the residual linewidth when comparing a two-spin to a multi-spin system. Furthermore, the quantification of the decoupling performance leads to the conclusion that the pulse-transient compensation does improve the decoupling efficiency by 20-30%. As shown before, this effect is barely visible in the directly detected spectra, but pulse-transient

compensation leads to higher predictability of the sequence in terms of chemical-shift scaling and absolute frequency calibration.

The influence of transients can be divided into two contributions: i) the shift in resonance frequency and ii) the decrease in decoupling efficiency. The shift in resonance frequency is due to the fact that the amplitude of a phase ramp is different for the two directions of the phase sweeps if pulse imperfections are considered. This leads to an additional effective rotation that induces a shift in the resonance frequency. The decrease in decoupling efficiency is quantified to be 20-30% of the inherent lifetime of the sequence (Fig. 6.10). Converting this into observed linewidth, a contribution of 10-15 Hz is obtained, which corresponds solely to at most 5% of the total experimental linewidth.

The measured T_2' times can presumably be increased significantly by using unlabelled compounds in order to remove the residual heteronuclear coupling autoterms.

6.4.3. RF-Field Inhomogeneity

The effect of rf-field inhomogeneity on FSLG-based sequences has been investigated theoretically and used as input parameter for numerical simulations in the literature [67]. However, reduction or improvement of the rf inhomogeneity is routinely done in most homonuclear decoupling experiments by reducing the sample volume with spacer. The influence of this B_1-field inhomogeneity can be elucidated by comparing the rf profiles for different parts of the rotor and the influence on the decoupling efficiency. A similar approach was chosen to optimize a CP-based experiment with an optimum control algorithm, when considering the rf-field inhomogeneity as a variable [29, 30]. The contributions to the rf-field inhomogeneity can be split into an axial and a radial component. The axial component is the spatial distribution along the rotor axis and is time independent. This component can be mapped by the use of a B_0 gradient, although solid-state probe heads are usually not equipped with a gradient coil. The radial component along the rotor diameter is modulated by the MAS frequency, and is therefore time dependent. This time dependence could lead to possible resonance conditions between the pulse sequence and the rf-field modulation [28, 154].

In order to study the effect of the axial rf-field inhomogeneity, a variety of 2.5 mm

rotors for a standard Bruker probe were packed by filling different parts of the rotor with sample. Similar studies have been shown for the REDOR sequence [155, 156]. Five rotors each of adamantane and natural abundance glycine were packed using either a full rotor, the upper third (*up*), the bottom third (*low*), the middle third (*mid*), and a very small part in the middle of the rotor (*centre*). The remaining rotor volume was filled with Teflon spacer. The distribution of the rf field over the active sample volume is extracted by the measurement of nutation curves of the adamantane sample with direct detection of the signal. Subsequent Fourier transform of the nutation curves yields a distribution profile of the rf fields within the probe. These profiles are depicted in Figure 6.11.
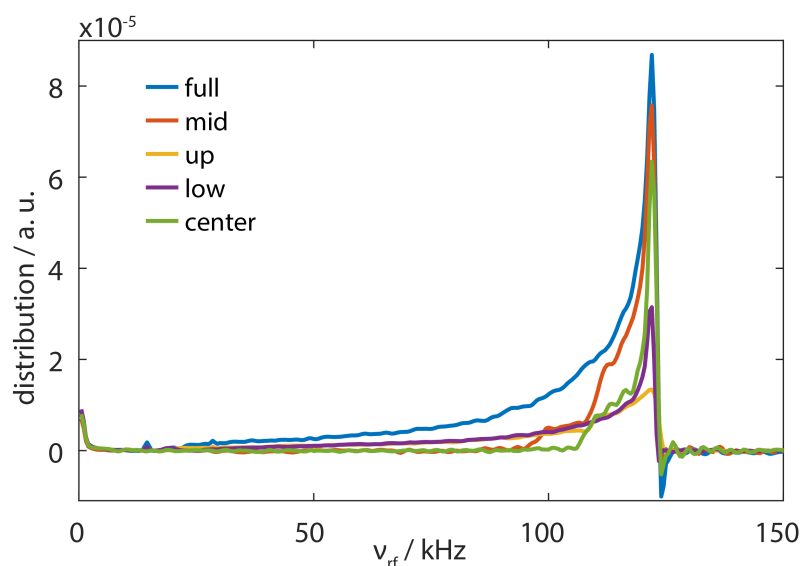
Figure 6.11. Rf-field distribution measured on an adamantane sample for different parts of a 2.5 mm rotor in a standard Bruker probehead. The sum of the lower, middle and upper third equals roughly to 1.1 times the signal of the full rotor. The applied B_1 field was calibrated using the full rotor and the first zero crossing of a π pulse. The highly restricted sample (*centre*) shows the narrowest distribution but still spans a range of several kHz. The radial component of the rf-field inhomogeneity can be observed at integer multiples of the MAS frequency which was set to 14 kHz in the nutation experiments.

The radial components can be seen in Figure 6.11 as small peaks at integer multiples of the MAS frequency, which was set to 14 kHz. Upon closer inspection of the intensity of the radial sidebands, it is observed that most of the radial contributions are observed for the upper and the lower third and not in the central part of the rotor.

Additionally, the maxima of the profile are consistently higher than the calibrated rf-field strength of 100 kHz. The calibration has been done on a full rotor with the first

zero crossing of a π pulse. These shifted maxima are due to the very broad distribution of rf-field strengths in the full rotor (blue trace in Figure 6.11) and the large drawn out foot towards low rf fields. The other profiles show that this foot is mostly observed in the outer thirds of the rotor, whereas the middle as well as the centre part is narrowed down around the maximum. The sum of the middle, upper, and lower part of the rotor compares very well to the profile of the full rotor. However, the integral of the distribution is slightly higher by a factor of 1.1, which is due to spacers that do not cover exactly a third of the rotor, or looser packing in the full sample.

These rf profiles have been used in further studies to investigate the influence of the distribution on the decoupling efficiency. Numerical simulations were performed using an 8-spin system with characteristic couplings and shifts for glycine (spin system details can be found in the Appendix C) with FSLG decoupling at the range of experimentally observed rf-field strengths. In order to validate and compare the simulations, FSLG experiments were performed on differently restricted natural abundance glycine samples. The comparison of the numerical and experimental results are shown in Figure 6.12.

The simulated and experimental spectra shown in Figure 6.12 agree well in certain regards. The detailed values for the simulations and experiments are listed in Table 6.1. The full width at half maximum (FWHM) obtained from the simulations compare well with the experiments. There are a few outliers but the overall trend can be reproduced. The relative intensities of the NH_3^+-peaks for different packing is also reproduced fairly well with small discrepancies for the centre packed and the middle third rotor. A problem that arises from the experimental spectra is the phase correction as well as the baseline correction. Due to the very broad and drawn out rf profile, the simulated peak is also very smeared out with a large foot. In conventional experiments, this asymmetry in the peak is corrected by a zeroth-order phase correction to obtain a symmetric and full absorption peak. This phase correction can lead to a distortion of the relative intensity as well as the extracted linewidth. This problem is especially eminent when comparing the glycine spectra of the full rotor (not shown here) with the middle third because the relative intensity of the middle third is higher than the full rotor, which is physically impossible. Additionally, the baseline correction as well as the baseline subtraction make the relative intensities hard to compare.
The linewidth of the CH_2-group from the simulation is comparable with the experiment
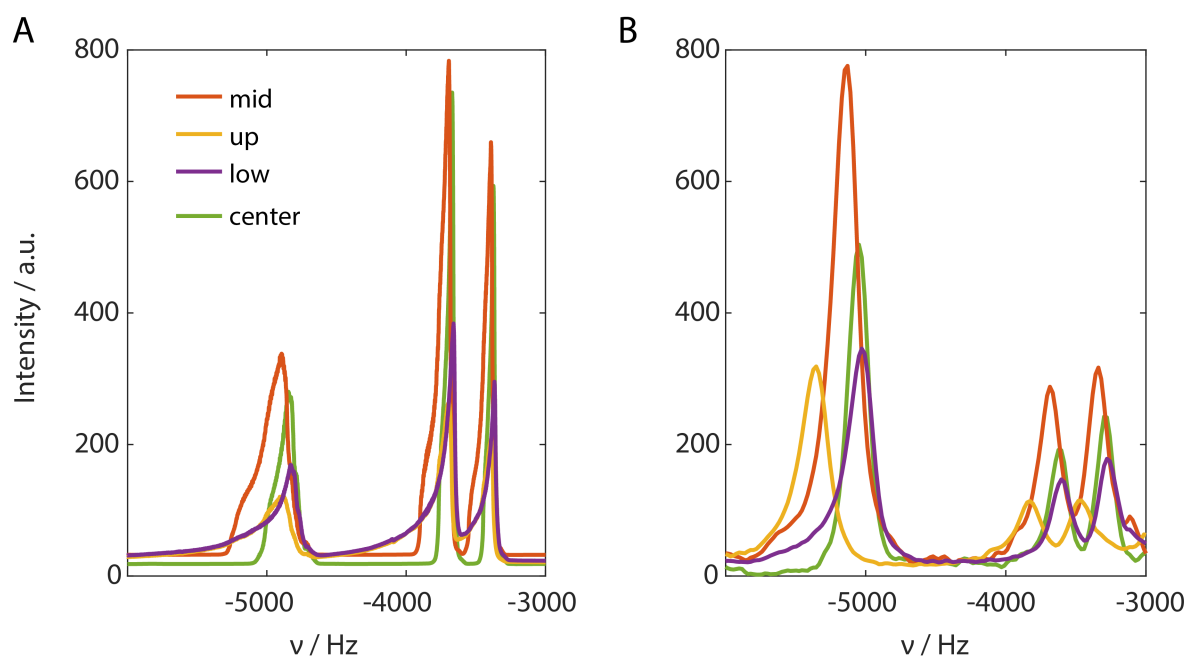
Figure 6.12. A) Simulated proton spectra of natural abundance glycine using an 8-spin system as input. The different contributions of the rotor to the total spectra are shown in different colours that match Figure 6.11. The rf-field resolution was 500 Hz using the rf profiles measured on adamantane. The frequency axis is not an absolute axis and only the spacing between the peaks is correct. B) Experimental spectra of natural abundance glycine using FSLG decoupling in the indirect dimension. The packing schemes correspond to the adamantane samples. The linewidth and relative intensities of the NH_3^+-peaks are comparable. The single outlier is the relative intensity of the middle third compared to the centre packed rotor. However, this might be due to slightly different packing in the adamantane and the glycine.

but the relative intensities are not. The discrepancy in relative intensities is due to the input of numerical simulation in which 3 N-H spins and 5 C-H$_2$ spins were considered to mimic the strong couplings of the CH$_2$ groups.

Further data that can be extracted from the simulations is the inherent linewidth that remains due to insufficient decoupling at various rf fields. This can be interpreted and compared with an experimentally determined T_2'. The inherent linewidth is extracted by correcting for the chemical-shift scaling of the different rf-field strengths and super-imposing the lines onto each other. The FWHM of this collapsed line corresponds to the inherent linewidth of FSLG, which was shown analytically to be due to third-order error terms (Chapter 6.2). The obtained coherence lifetime of the simulation is around 10 ms, which corresponds to a width of about 35 Hz. Analytical calculations and experiments

yield higher linewidths (both around 60 Hz), although it is obvious from the magnitude of this inherent linewidth that it is not the limiting factor of the FSLG sequence as compared to the rf-field inhomogeneity.

Table 6.1. Tabulated values of the linewidths at half maximum of the simulated and experimental spectra of natural abundance glycine. The values are extracted from the spectra shown in Figure 6.12 and are without chemical-shift correction. In order to obtain the real value, they have to be divided by a factor of 0.57.

	middle	centre	upper	lower
Δ_{sim} / Hz	196	168	365	226
Δ_{exp} / Hz	220	174	225	252

6.5. Conclusion

In conclusion, we examined the contributions that cause the linebroadening in the widely used FSLG pulse sequence and tried to quantify their influence. The most important factor was found to be the rf-field inhomogeneity that still contributes to about 75% of the linewidth even if the sample is restricted in the centre. The outer parts of the rotor do not contribute heavily to the observed spectrum and are oftentimes observed as a foot in the peak due to the low rf fields at the edges of the coil. A further confirmation that the rf-field inhomogeneity is the main source of the residual linewidth is the fact that the use of higher effective fields does not result in better signal resolution. It was expected that error terms scale down linearly or quadratically with the effective-field strength but this was not the experimental observation. The relative rf-field distribution is always the same independently of the calibrated rf-field. Therefore, the chemical-shift scaling and the resulting spectra are all the same. The only changing behaviour is in the spectrum of a single rf-field value, but they are all superimposed by the varying rf-field strength. Since this inhomogeneity is the major contribution to the linewidth, a drastic improvement in the sequence is only expected if the probe design is improved so that the rf profile is very homogeneous over the whole sample.

Additionally, it was shown that pulse transients do not have a big influence on the linewidth, but rather on the shift of the spectrum, which makes it more difficult to interpret the results and achieve a reliable frequency calibration. Removal of phase transients and adaption of the pulse sequence led to more predictable results in terms of chemical-shift scaling and absolute frequency axis. However, the impact of pulse

transients on the linewidth is negligible.

Furthermore, it was shown theoretically that third-order terms contribute to the residual linewidth with a factor that is highly dependent on the dipolar coupling and can be estimated to about 60 Hz for a CH_2-group. Selectively labelling the sample improves the coherence lifetime by removal of multi-spin terms but as theoretically predicted, the two-spin terms are still dominant. These terms cannot be removed by altering the sequence, e.g. changing the angle of the effective field, as they do not exhibit the same spatial behaviour as three-spin terms. Small improvements were found by changing the effective-field angle to slightly higher values of around 60°, which is understood theoretically, but the spectral quality still remains too bad to be useful for practical applications.

7. Heteronuclear Decoupling

7.1. Introduction to Two-Pulse Decoupling

Heteronuclear spin decoupling is essential in standard MAS experiments in order to obtain high-resolution spectra [157–159]. In general, heteronuclear decoupling is divided into two regimes; high-power and low-power decoupling. High-power decoupling [43, 44, 160–163] requires the nutation frequency to be much higher than the spinning frequency ($\nu_1 \gg \nu_r$) and vice versa for low-power [164–168]. The focus of this chapter is placed on high-power decoupling. Considering the high-power regime, pulsed decoupling strategies become more important at higher spinning frequencies as compared to CW decoupling [169, 170], due to the reduction of "self-decoupling" [171, 172]. This line narrowing effect is due to spin diffusion, which is slower at high MAS frequencies. In order to stay in the high-power regime, higher nutation frequencies have to be applied to match the condition $\nu_1 \gg \nu_r$. In pulsed strategies, higher ν_1 frequencies correspond to higher modulation frequencies ω_m, which contribute to the divisor of second-order terms in the effective Hamiltonian that cause residual linebroadening. Therefore, the decoupling efficiency is expected to be better. However, high nutation frequencies correspond to short pulses which are potentially more susceptible to pulse imperfections. This fact has been discovered experimentally, but it remains unclear if worse decoupling efficiency at very high rf fields is solely due to pulse transients [173].

Despite considerable progress in the last few years, numerical simulations and accurate *a priori* prediction of decoupling efficiency remain a challenge [174]. An elegant way of estimating good decoupling regimes for generalized decoupling schemes was developed by Tan, *et.al.* based on a second-order Floquet treatment [105] derived from the theoretical framework of two-pulse decoupling schemes [121]. A different approach using numerical simulations was presented by Equbal, *et.al.* to find a unified solution

for two-pulse decoupling sequences [175]. The two most commonly employed two-pulse strategies for heteronuclear decoupling are two-pulse phase modulation (TPPM) [43] and X-inverse-X (XiX) [176]. TPPM comprises two pulses with the same duration, τ_{p} and phase, ϕ and $-\phi$. This basic element is repeated during the whole detection period, which makes it a cyclic pulse sequence with the modulation frequency $\omega_{\mathrm{m}} = 2\pi/(2\tau_{\mathrm{p}})$. This implementation can be altered by changing the phase continuously with a cosine function, which is known as CM sequence [26, 27]. The basic implementation of the pulse sequence requires a two-parameter optimization, but there are many variations that make the pulse sequence more stable and more broadband. These modifications are small phase incremental alternation (SPINAL) [44], an amplitude-modulated (AM-TPPM) scheme [177], and the swept-frequency (SW$_f$-TPPM) decoupling scheme [162]. All of these sequences aim to be easily optimizable and have a large parameter range of good decoupling performance. Most of these modifications can be considered supercycles of the basic TPPM sequence and have, therefore, a high robustness towards pulse imperfections. The continuous-modulation sequence is essentially identical to TPPM in the sense that it has a basic element of two pulses with the same length but the phase is a continuous sine modulation during the two pulses. It is shown later from analytical calculations that the two implementations are interchangeable.

The XiX sequence will not be studied in detail with respect to pulse imperfections because it was shown that the optimal pulse length for XiX is $2.83\tau_{\mathrm{r}}$. This long pulse length renders the imperfections at the beginning and the end of the pulse unimportant. Small deviations for pulse-transient compensation are expected due to a small change in flipangle but this is routinely compensated by optimizing the pulse duration which is the only free parameter for XiX.

The quality of a heteronuclear decoupling sequence can be judged by many quantities. Two easy parameters that can be optimized are the FWHM or the amplitude of the spectral line. There is no simple analytical relationship between those two measures, but the maxima coincide in many cases. Additionally, the refocusable linewidth in spin-echo experiments (T_2') is an important quantity for the discussion of the efficiency of decoupling sequences. As already shown in Chapter 6.4.2, the coherence lifetime can be used to estimate the smallest possible linewidth, since additional linebroadening contributions like chemical-shift effects, imperfect shim, and sample inhomogeneities are refocused. In the experimental section of this Chapter, the different quantities will be

discussed and similarities and differences in optimization based on these criteria will be outlined.

7.2. Analytical Calculations of TPPM/CM

For a general Floquet description of decoupling sequences, a general spin system is considered that consists of N I-spins coupled to a single S-spin. Expressing the full Hamiltonian in the usual rotating frame, one obtains

$$
\hat{\mathscr{H}}(t) = \sum_{n=-2}^{2} \omega_S^{(n)} e^{in\omega_r t} S_z + \sum_{k=1}^{N} \sum_{n=-2}^{2} \omega_k^{(n)} e^{in\omega_r t} I_{kz} + \sum_{k=1}^{N} \sum_{n=-2}^{2} \omega_{Sk}^{(n)} e^{in\omega_r t} 2 S_z I_{kz}
$$
$$
+ \sum_{k<\ell} \sum_{n=-2}^{2} \omega_{k\ell}^{(n)} e^{in\omega_r t} \left(3 I_{kz} I_{\ell z} - \vec{I}_k \cdot \vec{I}_\ell \right) + \hat{\mathscr{H}}_{\mathrm{rf}}(t) \qquad (7.1)
$$

where $\omega_S^{(n)}$ and $\omega_k^{(n)}$ are the nth spatial components of the chemical-shift tensors for spin S and I, respectively. $\omega_{Sk}^{(n)}$ and $\omega_{k\ell}^{(n)}$ symbolize the hetero- and homonuclear dipolar couplings. Using an arbitrary wave form for the rf Hamiltonian $\hat{\mathscr{H}}_{\mathrm{rf}}(t)$ one obtains the expression given in Equation 5.4, substituting S with I spins since the irradiation is on the protons. The total Hamiltonian is then transformed into an interaction frame (according to Equation 5.5 and 5.6) making the I-spin terms time dependent. They transform separately according to

$$
\tilde{I}_z = \sum_{\chi=x,y,z} a_\chi(t) I_\chi = \sum_{k=-\infty}^{\infty} \sum_{\ell=-\infty}^{\infty} \sum_{\chi=x,y,z} a_\chi^{(k,\ell)} e^{ik\omega_m t} e^{i\ell\omega_{\mathrm{eff}} t} I_\chi \qquad (7.2)
$$

where k and ℓ are integer numbers and $a_\chi^{(k,\ell)}$ represent the Fourier coefficients characterizing the interaction-frame trajectory of the I_z operator in full analogy to Equation 5.10. The modulation frequency is given as the basic frequency of the repeating element and for TPPM this is given by $\omega_m = 2\pi/\tau_m = 2\pi/(2\tau_p)$. The effective field is defined through the net flipangle over a basic element $\omega_{\mathrm{eff}} = \beta_{\mathrm{eff}}/\tau_m$ that can be determined either using Euler rotations or quaternions [178]. The time-dependent interaction-frame Hamiltonian can therefore be derived as given in Equation 5.7. In decoupling sequences,

residual couplings are of specific interest and thus the relevant terms are given by the non-resonant second-order terms. The general expressions for second-order terms are given in Equation 5.12 and 5.13 and can be decomposed for a general Hamiltonian in six crossterms. These terms are given by

$$\overline{\hat{\mathscr{H}}}^{(2)} = \overline{\hat{\mathscr{H}}}_{IS\otimes I} + \overline{\hat{\mathscr{H}}}_{IS\otimes II} + \overline{\hat{\mathscr{H}}}_{I\otimes II} + \overline{\hat{\mathscr{H}}}_{II\otimes II} + \overline{\hat{\mathscr{H}}}_{I\otimes I} + \overline{\hat{\mathscr{H}}}_{IS\otimes IS} \tag{7.3}$$

for which detailed expressions can be found in Ref. [105]. The two relevant terms for the residual linewidth on the S spin are the heteronuclear dipolar-CSA crossterm $\overline{\hat{\mathscr{H}}}_{IS\otimes I}$ and the heteronuclear-homonuclear dipolar crossterm $\overline{\hat{\mathscr{H}}}_{IS\otimes II}$. The terms are given by

$$\overline{\hat{\mathscr{H}}}_{IS\otimes I} = \sum_k \sum_{\nu=-2}^{2} \sum_{\chi=x,y,z} iS_z I_{k\chi} q_\chi^{(\nu)} \left(\omega_{kS}^{(-\nu)}\omega_k^{(\nu)} + \omega_{kS}^{(\nu)}\omega_k^{(-\nu)} \right) \tag{7.4}$$

for the dipole-CSA term and

$$\overline{\hat{\mathscr{H}}}_{IS\otimes II} = \sum_{k\neq\ell} \sum_{\nu=-2}^{2} \sum_{\mu,\chi=x,y,z} -3iS_z I_{k\mu} I_{\ell\chi} \left(q_{\mu\chi}^{(\nu)}\omega_{kS}^{(-\nu)}\omega_{k\ell}^{(\nu)} - \left(q_{\mu\chi}^{(\nu)}\right)^* \omega_{kS}^{(\nu)}\omega_{k\ell}^{(-\nu)} \right) \tag{7.5}$$

for the dipole-dipole term. The important quantities are the scaling coefficients $q_\chi^{(\nu)}$ and $q_{\mu\chi}^{(\nu)}$ for the corresponding crossterms, which are independent of the spin system (this is encoded in the spatial Fourier coefficients ω_k, ω_{kS}, and $\omega_{k\ell}$). The scaling coefficients for the two relevant crossterms are given by

$$q_\chi^{(\nu)} = \sum_k \sum_{\lambda=-1}^{1} \frac{\varepsilon_{\chi ij} a_j^{(-\kappa,-\lambda)} a_i^{(\kappa,\lambda)}}{\nu\omega_r + \kappa\omega_m + \lambda\omega_{eff}} \tag{7.6}$$

and

$$q_{\mu\chi}^{(\nu)} = \sum_k \sum_{\lambda=-1}^{1} \frac{\varepsilon_{\mu ij} a_j^{(-\kappa,-\lambda)} a_{\chi i}^{(\kappa,\lambda)}}{\nu\omega_r + \kappa\omega_m + \lambda\omega_{eff}}. \tag{7.7}$$

$\varepsilon_{\chi ij}$ is the Levi-Civita symbol and $a_{\mu\chi}^{(\kappa,\lambda)}$ are the Fourier coefficients from the rank-two spin tensors that can be calculated by a convolution of the rank-one Fourier coefficients $a_{\mu}^{(\kappa,\lambda)}$

$$a_{\mu\chi}^{(\kappa,\lambda)} = \sum_{k=-\infty}^{\infty} \sum_{\ell=-1}^{1} a_{\mu}^{(k,\ell)} a_{\chi}^{(\kappa-k,\lambda-\ell)}. \tag{7.8}$$

The rank-one Fourier coefficients can be calculated analytically for ideal TPPM, but have to be extracted numerically through interaction-frame transformation with a piecewise time-independent rf Hamiltonian otherwise. This is especially the case for real pulses that include pulse transients. In principle, offset irradiation can be considered by including an offset term in the rf Hamiltonian used for the interaction-frame transformation but will not be considered here in detail.

7.2.1. Comparison of TPPM and CM

It has been shown in previous work [121] that the experimental decoupling efficiency using either CM or TPPM is almost indistinguishable. This can be understood by considering the phase modulation of the TPPM sequence as a square wave function with the values $+\phi$ and $-\phi$. A square wave can be represented by an infinite Fourier series containing only sine terms with a frequency that is an odd integer multiple of the modulation frequency. The phase of a TPPM sequence is therefore given by

$$\phi(t) = \frac{4}{\pi}\phi \sum_{k=1}^{\infty} \frac{\sin\left((2k-1)\omega_{\mathrm{m}}t\right)}{2k-1}. \tag{7.9}$$

Therefore, the continuous phase modulation of the sequence is very similar to the TPPM scheme if only the first term of Equation 7.9 is considered and the phase value scaled with a factor of $4/\pi$.

Calculation of the rank-one Fourier coefficients prove that the TPPM and CM are indeed also very similar from a theoretical point of view. The Fourier coefficients for the TPPM sequence are calculated analytically but the CM sequence has to be calculated by numerical interaction-frame transformation due to the continuous modulation of the

phase. The results for the one-spin coefficients for the two implementations are shown in Figure 7.1 for CM (A) and TPPM (B). The notation is according to Equation 7.2, in which the first index represents the spatial component of the spin operator in the interaction frame and the second index the one in the static frame. Only the coefficients for the $\tilde{I}_z(t)$ operator are shown, since only those are relevant. The coefficients are virtually identical except for very small contributions in the TPPM scheme at higher k values. This is due to the high-frequency sine components that appear in the square phase modulation, but not in the CM sequence.
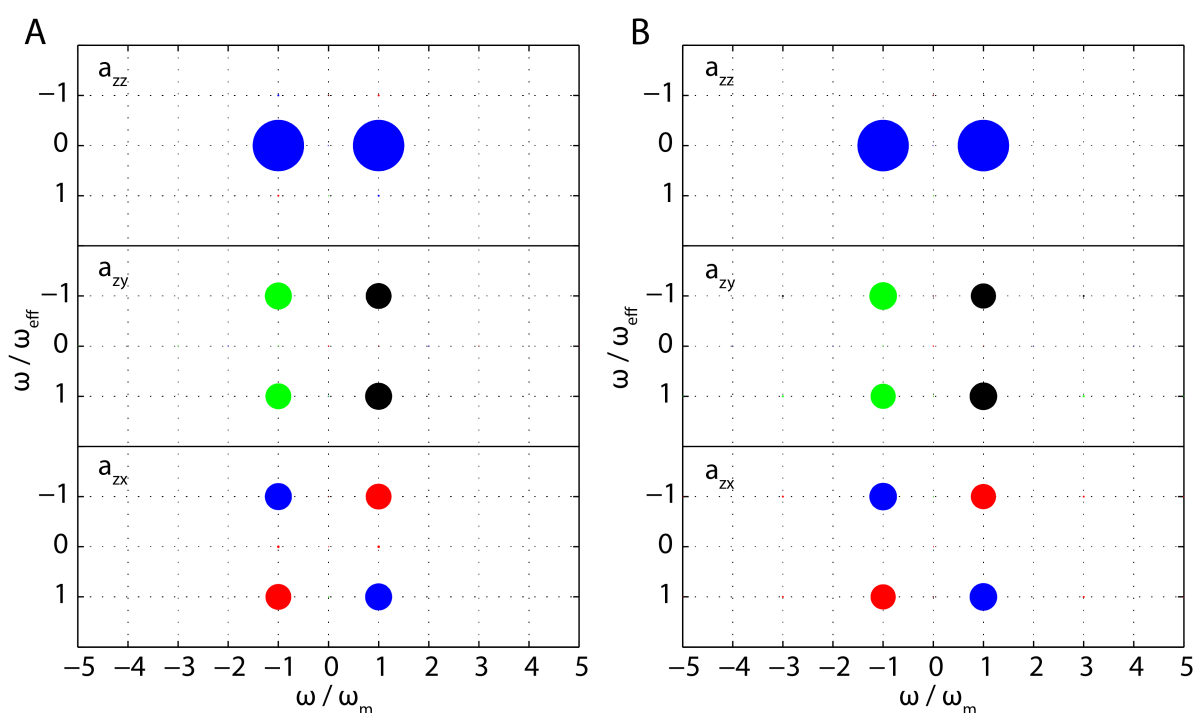
Figure 7.1. The rank-one time-dependent Fourier coefficients of the CM (A) and the TPPM (B) sequence. The parameters used for the implementation are a pulse length of 2 μs at a rf-field strength of 250 kHz and a phase (for TPPM) of 8.5°. The coefficients are virtually identical with small contributions at high k values for the TPPM sequence that are not observed in the CM implementation. This is due to the high-frequency sine components that are neglected for CM. The blue circles represent positive and real values, red is negative and real, and black and green are imaginary components with positive or negative sign, respectively. The diameter of the circles corresponds to the size of the coefficients. Note that the solution is not unique and depending on the implementation of the calculation the combination of indices (k and ℓ) can differ.

In the range of typical TPPM parameters $(\tau_\mathrm{p} \leqslant \tau_{2\pi}$ and $\phi < 40°)$, the coefficients and the scaling for the second-order crossterms given in Equations 7.6 and 7.7 are identical to a precision of 0.2%. Advantages and disadvantages of the experimental implementation of

the CM sequence over TPPM will be discussed in detail in Chapter 7.3. From a practical point of view, the TPPM sequence is a lot easier and faster to optimize because every data point in the CM optimization requires a new shape file, whereas for TPPM a pulse-length scan is readily implemented.

7.2.2. Influence of Pulse Transients on TPPM and CM

The influence of pulse transients on the general two-pulse decoupling scheme is investigated by analytically calculating the size of the scaling factors for the second-order crossterms (Equations 7.6 and 7.7). Two considerations have to be taken into account when implementing pulse-transient compensation for TPPM. On one hand, the removal of phase imperfections is expected to have a beneficial effect for the decoupling efficiency. Pulse imperfections might reintroduce error terms that would be averaged out by perfect pulses. On the other hand, the practical implementation of transient compensation requires shaped pulses. From theory and experiments it is known that TPPM works best if the phase is around $15°$ and the pulse has a flipangle slightly higher than π. Assuming very high ν_1-fields ($\sim$250 kHz), the pulses for optimal decoupling are very short and the finite edge time required for the compensation becomes relatively long compared to the total pulse length.

Theoretical calculations show that the implementation with rectangular pulses and ideal shaped pulses are indistinguishable. Calculation of the scaling factors for high rf fields and moderate MAS frequencies are shown in Figure 7.2 for rectangular pulses. The rf-field amplitude was set to 250 kHz at a MAS frequency of 40 kHz. The phase was altered in steps of $0.25°$ and the step size for the pulse length was chosen to be 0.1 μs. The simulations show the normalization of the dipole-CSA crossterms defined as

$$\bar{q}_{\mathrm{CSA}}^{(\nu)} = \sqrt{\sum_{\chi} |q_{\chi}^{(\nu)}|^2} \tag{7.10}$$

and the dipole-dipole scaling factor is defined as

$$\bar{q}_{\mathrm{DD}}^{(\nu)} = \sqrt{\sum_{\mu\chi} |q_{\mu\chi}^{(\nu)}|^2}. \tag{7.11}$$
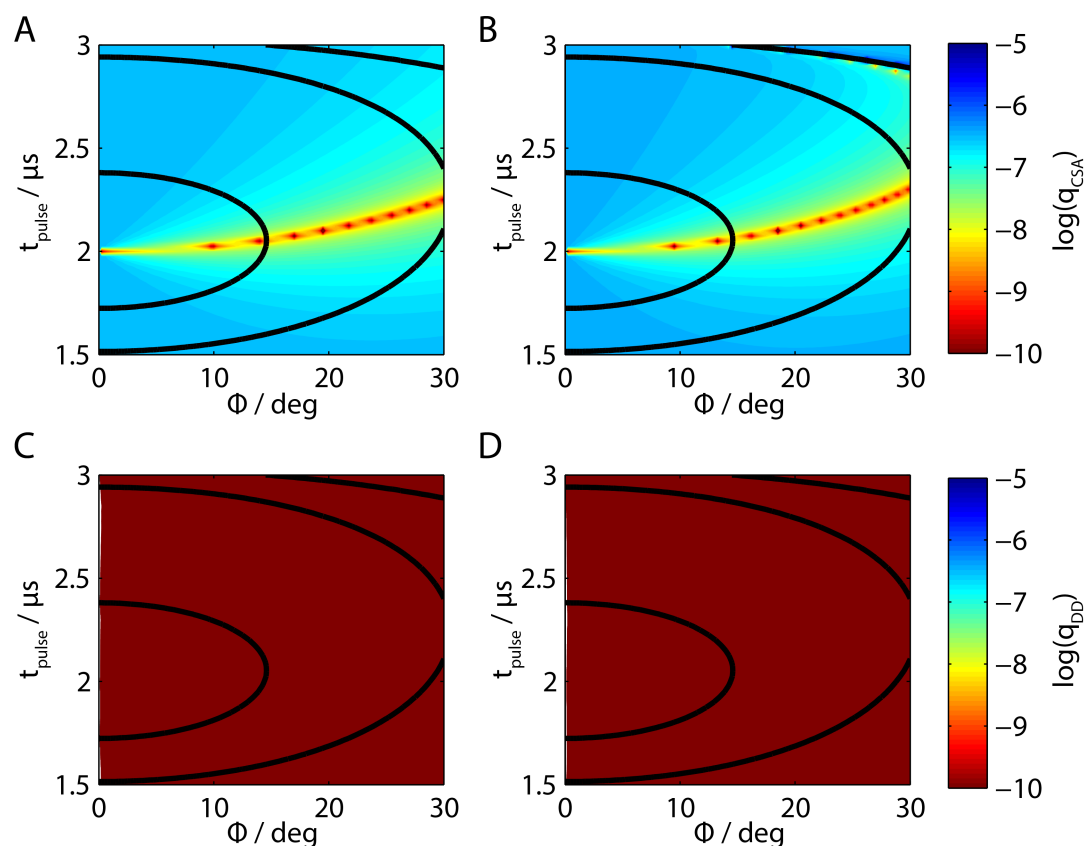
Figure 7.2. The scaling coefficients for dipole-CSA crossterms for $\nu = 1$ and $\nu = 2$ (A and B) as defined in Equation 7.10 and the dipole-dipole coefficients for $\nu = 1$ and $\nu = 2$ (C and D) as defined in Equation 7.11 of a basic TPPM sequence. The decadic logarithm of the scaling terms is plotted and the colourbar is set in a way that red corresponds to favourable decoupling regions. The set parameters were ν_1=250 kHz and ν_r=40 kHz. The black lines represent resonance conditions at which multiple of the characteristic frequencies are commensurate.

The scaling factor for dipole-dipole interactions are zero for any combination of pulse length and phase value. The dipole-CSA scaling factor shows a very favourable decoupling region which is at a theoretical pulse length defined by $\tau_p = \tau_\pi / \cos\phi$. Despite the better decoupling efficiency at high rf fields, the breadths of the resonance conditions become smaller. This can be seen in Figure 7.2 A and B which show the dipole-CSA scaling factors that exhibit a very narrow decoupling condition. The black lines correspond to resonance conditions at which the three characteristic frequencies, namely the MAS frequency ν_r, the modulation frequency ν_m, and the effective field ν_{eff}, are multiple integers of each other. These conditions describe a possible recoupling condition and are detrimental for decoupling sequences.

The calculation for the CM implementation of the sequence yields identical plots as shown in Figure 7.2 if the correction factor of $4/\pi$ is included for the phase value. This supports the experimental results, shown in previous work [121], that the two sequences are virtually the same. Furthermore, the same characteristic plots are obtained if the interaction-frame trajectory is calculated with shaped pulses using a finite sine edge. In this case, the maximum amplitude has to be adjusted in order to generate the same net flipangle but if this is done correctly, the results are indistinguishable to the rectangular pulses. Theoretically, there is no advantage of either application (TPPM or CM), independently of using rectangular or shaped pulses, if perfect rotations are assumed.

The addition of pulse transients alters the functional form of the scaling coefficients. The modelled transients were assumed to have a rise time of 0.4 μs and an electronic
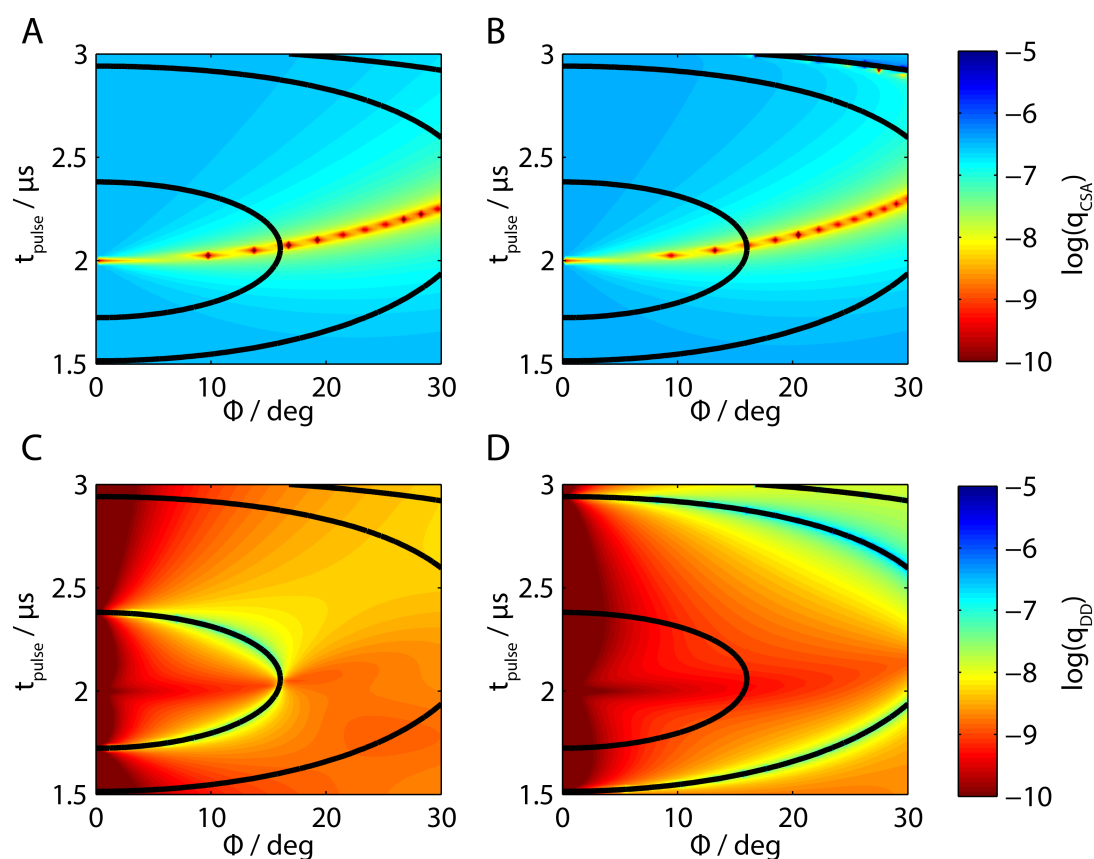

Figure 7.3. The same scaling coefficients for TPPM as shown in Figure 7.2, but assuming real pulses with a rise time of 0.4 μs and an electronic offset frequency of 20 kHz.

offset frequency of 20 kHz. The CSA-dipole coefficients are not influenced by pulse imperfections, but the dipole-dipole coefficients become non-zero. The regions in the dipole-dipole coefficients that have large contributions coincide with the resonance conditions. Therefore, inherently bad decoupling is assumed in this region. However, from a practical point of view, these regions will show poor decoupling efficiency due to the large CSA-dipole crossterm and the impact of the dipole-dipole term might be negligible.

In conclusion, the theoretical calculations show that the difference between TPPM with rectangular or shaped pulses and the CM scheme is not visible in the relevant scaling coefficients and therefore, the experiments are assumed to be indistinguishable. Furthermore, the influence of pulse transients appears to solely be relevant in parameter areas that experience inherently bad decoupling efficiency. Thus, the influence of pulse transients on the best decoupling performance is assumed to be small and it is hypothesized that TPPM or CM implementations do not suffer from pulse imperfections even with very short pulses and corresponding high rf fields.

7.3. Experimental Results of TPPM and CM

As discussed in the introduction to this Chapter (7.1), there are several parameters that can be used to judge the decoupling efficiency. The two that will be used throughout this work are the height of the line, since this coincides in very many cases with the narrowest line for samples with good SNR, and the coherence lifetime T_2' using a refocusing pulse on the carbon channel. The set of experiments recorded for the evaluation of decoupling efficiency are shown in Figure 7.4. The simplest experiment is the direct detection of the carbon spectrum after an initial CP step (A) from which either the linewidth or the line height is determined. The second quantity, T_2', is extracted by measuring dephasing curves of the carbon magnetization under heteronuclear decoupling with a π pulse centred in the middle of the decoupling block (B). The resulting curve can then be fit by a mono-exponential decay, and depending on the spin system, an additional cosine oscillation. This cosine oscillation is due to the homonuclear J-couplings, which are not being refocused by the π pulse. The decoupling scheme during the detection is either optimized to give the best possible resolution or it is matched to the decoupling during the dephasing period. The argument for using the same decoupling during both

periods is the varying decoupling efficiency for different crystallite orientations, which is not consistent in XiX and TPPM decoupling schemes or even in the same decoupling scheme with different parameters.

Additionally, experiments are implemented in which the dephasing time is kept constant and the integral of the spectral line is evaluated as a function of the parameters of the decoupling scheme. This implementation is shown with optimized XiX decoupling (D) or with 'matched' decoupling (C) where the decoupling during the detection matches the decoupling during the dephasing. One practical concern for matched decoupling is the ability of the probe head to take the applied rf fields for a long time ($\sim$100 ms) if high ν_1 fields are being studied. Additionally, the memory of the spectrometer to save the shape files needed for shaped pulses or CM poses a limitation.
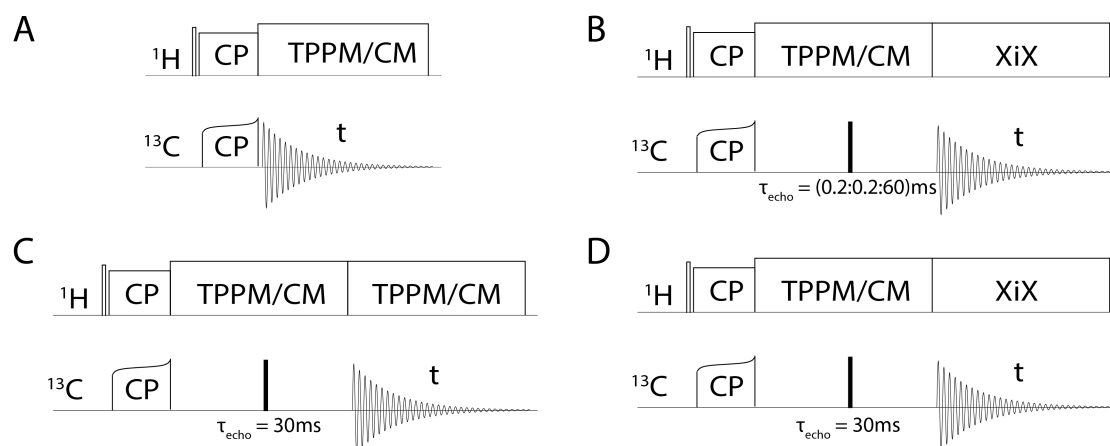
Figure 7.4. Different pulse sequences used to optimize and analyse decoupling sequences of interest. A) Direct detection with varying decoupling used to determine total linewidths. B) T_2' dephasing curves for a mono-exponential fitting procedure. C) and D) Experiments with constant dephasing time that are used to determine the decay of the spectral line under the T_2' relaxation. The decoupling during the detection can either be matched (C) to the dephasing time or optimized (D) to give maximum spectral intensity.

The experiments shown in Figure 7.4B-D are prone to errors in the data analysis because the assumption of a mono-exponential decay is only valid in very simple spin systems. Additionally, the evolution of the magnetization under the homonuclear J-coupling must be included in the fit. The determination of the coupling is only readily possible if the 1D spectra show a splitting that can be determined. Therefore, the experiments were used as a comparison to the direct detection and a reference for whether the best decoupling parameters for the total linewidth (Fig. 7.4A) coincide with the longest
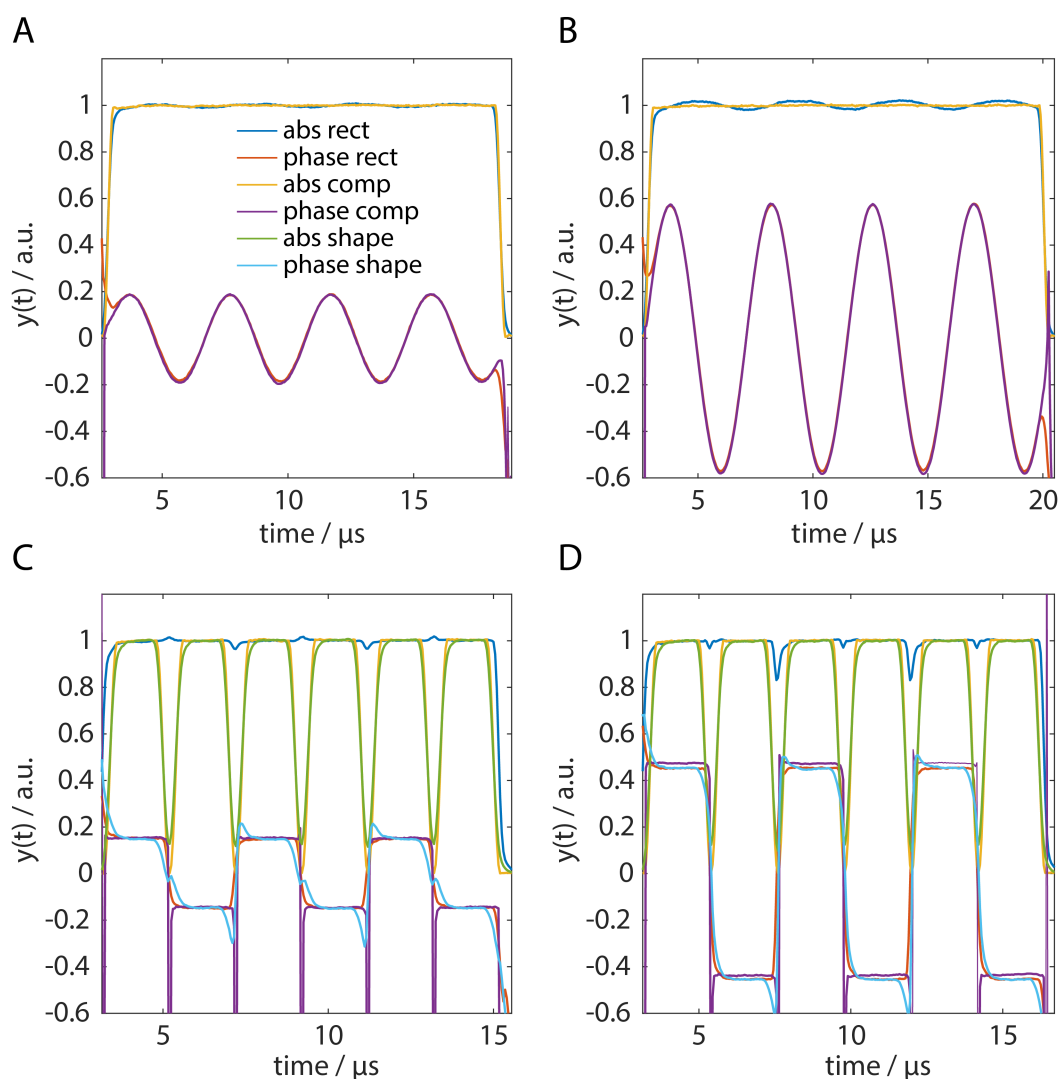
Figure 7.5. Recorded B_1 fields for different implementations of two-pulse decoupling. A) and B) are CM with a continuous phase modulation that are either compensated (yellow and purple) or uncompensated rectangular pulses (blue and red). The pulse parameters are τ_p=2 μs and 8.5° for A) and τ_p=2.2 μs and 26° for B). The uncompensated pulses show a very similar behaviour for the phase but higher phase values lead to an oscillation in the amplitude that is removed with the compensation. C) and D) are the identical implementation with discrete phase changes and additionally to the rectangular and compensated pulses, uncompensated shaped pulses are shown (green and light blue). The shaped pulses show the slowest transition for the phase values and are therefore expected to show the worst decoupling efficiency.

coherence lifetimes. For exact quantitative results, the experiment shown in B is used, as the high quantity of data points allows for a reliable fit of the decay curve.

The implementation of the pulse sequence is done by generating the basic element of the pulse sequence (TPPM or CM two-pulse element) and repeating it n times to fit into the required time step. The big advantage of the CM modulation for pulse-transient compensation is the continuity of the phase modulation. Therefore, the beginning and the end of the total segment are required to have a shaped edge and the rest of the pulse train does not need to be ramped down in amplitude. The TPPM implementation has discrete phase jumps, and thus discontinuities in the pulses for which the amplitude needs to be ramped down if compensation is applied. Basic pulse elements for both implementations are shown in Figure 7.5 with and without compensation. The elements presented consist always of three or four basic repetitions including the beginning and the end of the pulse sequence.

The phase modulation of the CM for the uncompensated and compensated implementation look nearly identical, but the amplitude shows small modulations that increase with increasing phase differences. This amplitude modulation is believed to be irrelevant for the decoupling efficiency because it does not change the net flip angle. The discrete phase jumps for TPPM exhibit strong influence from pulse transients, and especially the uncompensated pulses using shaped edges show large phase transients. An interesting fact that has been observed before is the behaviour of the amplitude for different phase values. At the discontinuity points, the amplitude overshoots for certain phase changes and for others it undershoots depending on the sign and the magnitude of the phase switching. A further problem visible in the pulse shapes is the significant edge time of the compensated implementation. For a 2 μs pulse, a 0.4 μs edge time is required to ensure good compensation. Thus, around a third of the pulse duration is not a flat amplitude. Nevertheless, theoretical calculations of the scaling factors have predicted that the results with shaped pulses are indistinguishable from the ones with rectangular pulses if the flipangle is corrected.

Experiments have been run on U-^{13}C-^{15}N-glycineethylester in a 1.8 mm probe head built by Ago Samoson at a MAS frequency of 40 kHz and an external magnetic field of 11.7 T. The rf field was calibrated at 250 kHz leading to a good decoupling parameter for TPPM at a pulse length of 2 μs or slightly higher. The parameter space for TPPM and CM decoupling was scanned from a pulse length of 1.5 to 3 μs at a pulse increment of 0.1 μs and phase values from 0 to 30° at a step size of 0.25°. Figure 7.6 shows the results using the direct detection implementation shown in Figure 7.4A. The contour plot
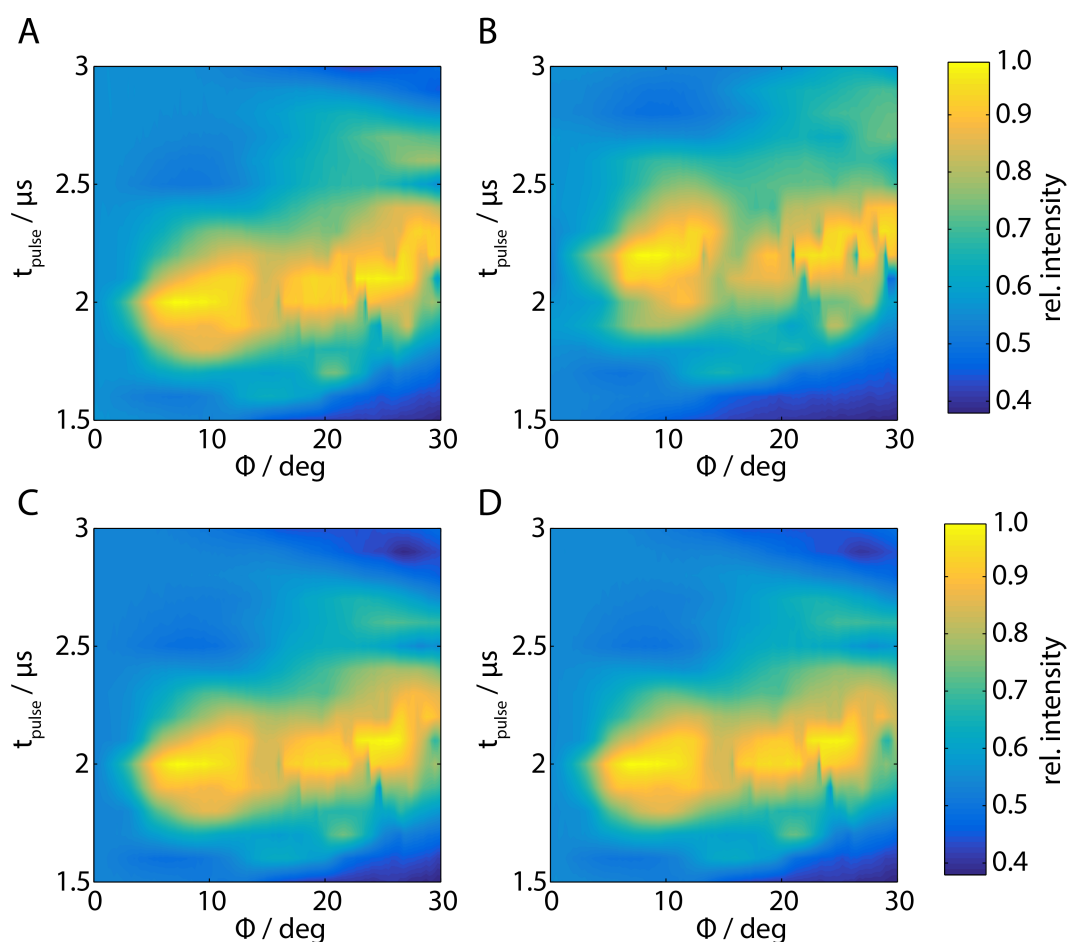
Figure 7.6. Experimental peak height of the Cα peak of U-^{13}C-^{15}N-glycineethylester using TPPM and CM decoupling for direct observation of the carbon signal. The peak height is normalized to the absolute maximum of the 4 implementations. The MAS frequency was set to be 40 kHz with a decoupling rf-field strength of 250 kHz. The step size for the pulse length was 0.1 μs and the phase step was 0.25°. A) Uncompensated TPPM implementation, B) compensated TPPM, C) uncompensated CM, and D) compensated CM.

represents the line height of the Cα line with the absolute global maximum normalized to 1.

The decoupling maps shown in Figure 7.6 follow to great extent the maps of the scaling factors for the crossterms shown in Figure 7.2. The theoretical prediction that the pulse transients do not influence the area of best decoupling has been confirmed experimentally. The maxima of experimental decoupling efficiency compare well to the minima of the theoretically calculated CSA-dipole crossterms. It was shown in Figure 7.2 and 7.3 that those terms are unaffected by pulse imperfections. The scaling coefficients which

are affected by pulse transients are dipole-dipole terms, but the experimental results show that they do not play a significant role in this spin system. Thus, results for the uncompensated and the compensated implementations look identical and the TPPM and CM schemes are also proven experimentally to give indistinguishable results. Small differences can be observed for the compensated implementation of TPPM (Fig. 7.6B). The decoupling maxima are shifted slightly to longer pulse durations and the breadth of the resonance condition is not as large as for the other results. This is hypothesized to be due to small errors in the compensation due to the short pulses and finite edges.
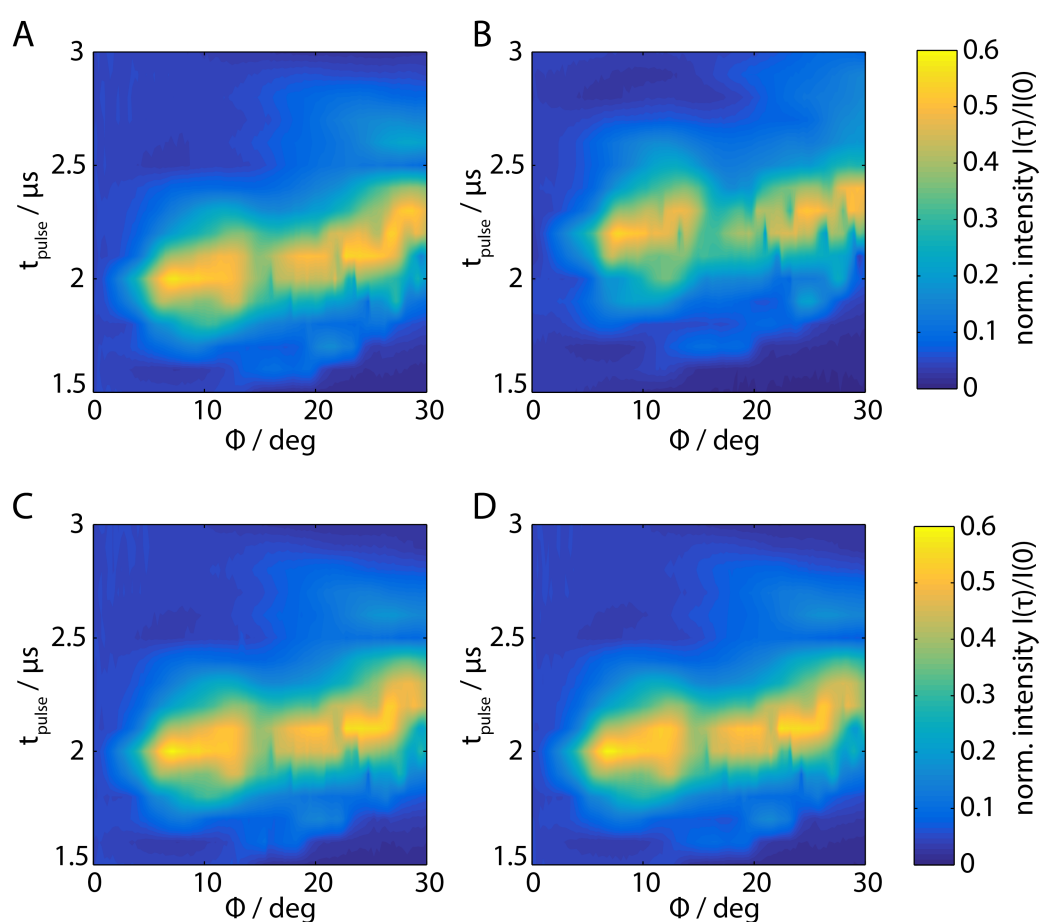
Figure 7.7. Experimental peak height of the Cα peak of U-^{13}C-^{15}N-glycineethylester using TPPM and CM decoupling for a constant dephasing time of 30 ms with a refocusing pulse on the carbon channel (compare Figure 7.4D). The peak height is referenced to the signal at 0 ms dephasing time. The detection period was XiX at 200 kHz and a pulse length of 71.25 μs. The step size for the pulse length was 0.1 μs and the phase step was 0.25°. A) Uncompensated TPPM implementation, B) compensated TPPM, C) uncompensated CM, and D) compensated CM.

Experiments with constant dephasing time and refocusing of chemical shift have been run with identical pulse and acquisition parameters as in Figure 7.6. The maps and the location of the intensity maxima are very similar to the results for direct detection as can been seen in Figure 7.7.

Additionally, these maps were recorded with 'matched' decoupling with nearly identical results. The matched decoupling map differs a little bit in the sense that the breadth of good decoupling is slightly larger than for the direct observation or the optimized decoupling. For optimized decoupling, XiX was used at a rf field of 200 kHz with a pulse length of 71.25 μs. XiX was used as a decoupling scheme because it was shown to be marginally more efficient at faster spinning speed than TPPM or supercycles thereof.

In order to get a quantitative measure of the decoupling efficiency, dephasing curves were measured at favourable decoupling points. The linewidth determined in Figure 7.6 is largely dominated by refocusable interactions like chemical-shift dispersion and shim. Therefore, obtaining quantitative information on the inherent linewidth under the decoupling sequence needs to be done by Hahn-Echo sequences. Two favourable decoupling points were chosen for the detailed analysis of the refocusable interactions. Figure 7.8 shows the results for dephasing curves using the two favourable decoupling points for TPPM and CM, respectively. One point was chosen with pulse parameters $\tau_p=2$ μs and 8.5° and the other point with $\tau_p=2.2$ μs and 26°. Despite very similar linewidths and peak heights, the first decoupling point yields coherence lifetimes that are at least 10 ms longer than the second one. Additionally, the CM implementation yields longer T_2' times than the discrete phase modulation. At the slightly worse decoupling point (based on the coherence lifetime shown in Figure 7.8), the compensation is beneficial for CM, whereas at the good decoupling efficiency, the transient compensation does not improve the transverse relaxation time. The compensation for TPPM appears to be hindering, as the coherence lifetimes decrease when using compensated pulses. This fact was observed qualitatively in the maps using direct detection and are confirmed in the dephasing curves. Shaped uncompensated pulses perform better, but TPPM is best implemented with rectangular pulses at very short pulse durations. This is believed to be due to the ramping down of the amplitude between the phase jumps. As discussed before, optimized CM is easier to realize in terms of signal generation, as the amplitude can remain flat throughout.
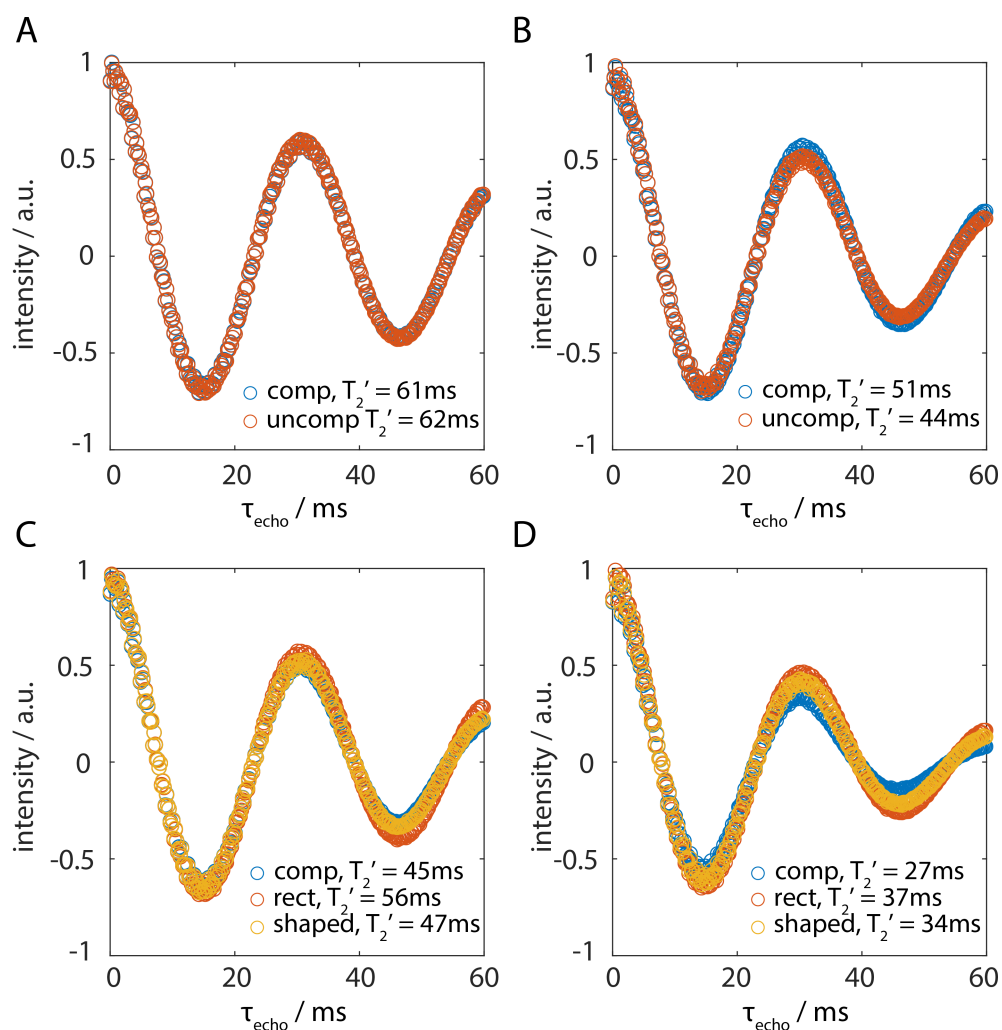
Figure 7.8. Experimental dephasing curves of the intensity of the Cα peak in U-^{13}C-^{15}N-glycineethylester. From the maps shown in Figure 7.6, two local maxima were chosen for the decoupling parameters, τ_p=2 μs and 8.5° for A and C, and τ_p=2.2 μs and 26° for B and D. CM implementation was used for A and B, and TPPM scheme for C and D. The other experimental parameters were kept identical to the results shown in Figure 7.6. The oscillations of the curves are due to the homonuclear J-coupling between the CO and the Cα which was determined to be 63 Hz. The fitted value for the coherence lifetime is given in the legend for the various implementations.

The decoupling efficiency can be further improved by restricting the sample to limit the rf-field inhomogeneity. Experiments of a centre-packed rotor show coherence lifetimes of up to 85 ms for the same decoupling points as in Figure 7.8. The trend observed for the full sample is amplified if the sample is restricted. At the best decoupling point for CM (Fig. 7.8A), the compensation is not beneficial, but the difference to the worse decoupling point is bigger and the impact of the compensation is also higher. For TPPM the

implementation with rectangular pulses performs best, but is not quite comparable with the CM scheme. Shaped pulses and compensated pulses exhibit coherence lifetimes that are around 25% shorter than the rectangular pulse. The influence of rf inhomogeneity and pulse imperfections can potentially be removed by a supercycle of the two-pulse decoupling.

7.4. Experimental Results of SPINAL

An extension of the two-pulse decoupling scheme is the small phase incremental alteration (SPINAL) [44]. The basic building block of two pulses with the same duration and opposite phases is kept consistent. As an alteration, the following pulses have a phase value that is increased by a value α, and the subsequent phases are increased by β. The eight phases of the basic SPINAL sequence are given by

$$Q = \phi,\ -\phi,\ \phi + \alpha,\ -(\phi + \alpha),\ \phi + \beta,\ -(\phi + \beta),\ \phi + \alpha,\ -(\phi + \alpha) \tag{7.12}$$

with the same pulse length τ_p. Depending on the implementation of SPINAL, different inversions and number of repetitions of the basic Q block of Equation 7.12 are applied. The most widely used scheme is SPINAL-64, consisting of 64 pulses, and thus eight Q blocks. The combined supercycle is given by

$$\text{SPINAL-64} = Q\bar{Q}\bar{Q}Q\ \bar{Q}QQ\bar{Q} \tag{7.13}$$

where $\bar{Q}$ is the inversion of the basic Q block.
The advantage of SPINAL is the broad conditions for the combination of parameters for good decoupling efficiency. This is due to the long modulation frequency and the different side bands in the Fourier coefficients that are generated by the large number of frequencies. This advantage outweighs the disadvantage of the large space of free parameters of SPINAL. In principle, the optimization requires a 4-dimensional grid search: the pulse duration τ_p, the basic phase ϕ, and the two phase increments α, and β. Often, the two phase increments are combined to a single value θ, defined as $\theta = \alpha = \beta/2$, and in good approximation set to 5°. This reduces the problem to a two-parameter

optimization. Instead of using a discrete phase modulation given in Equation 7.12 the scheme can also be implemented with continuous phase modulation. As was shown before, the results for two pulse decoupling using either discrete or continuous phase changes are indistinguishable (Chapter 7.3) and the same holds true for the different phase schemes in the case of SPINAL decoupling.
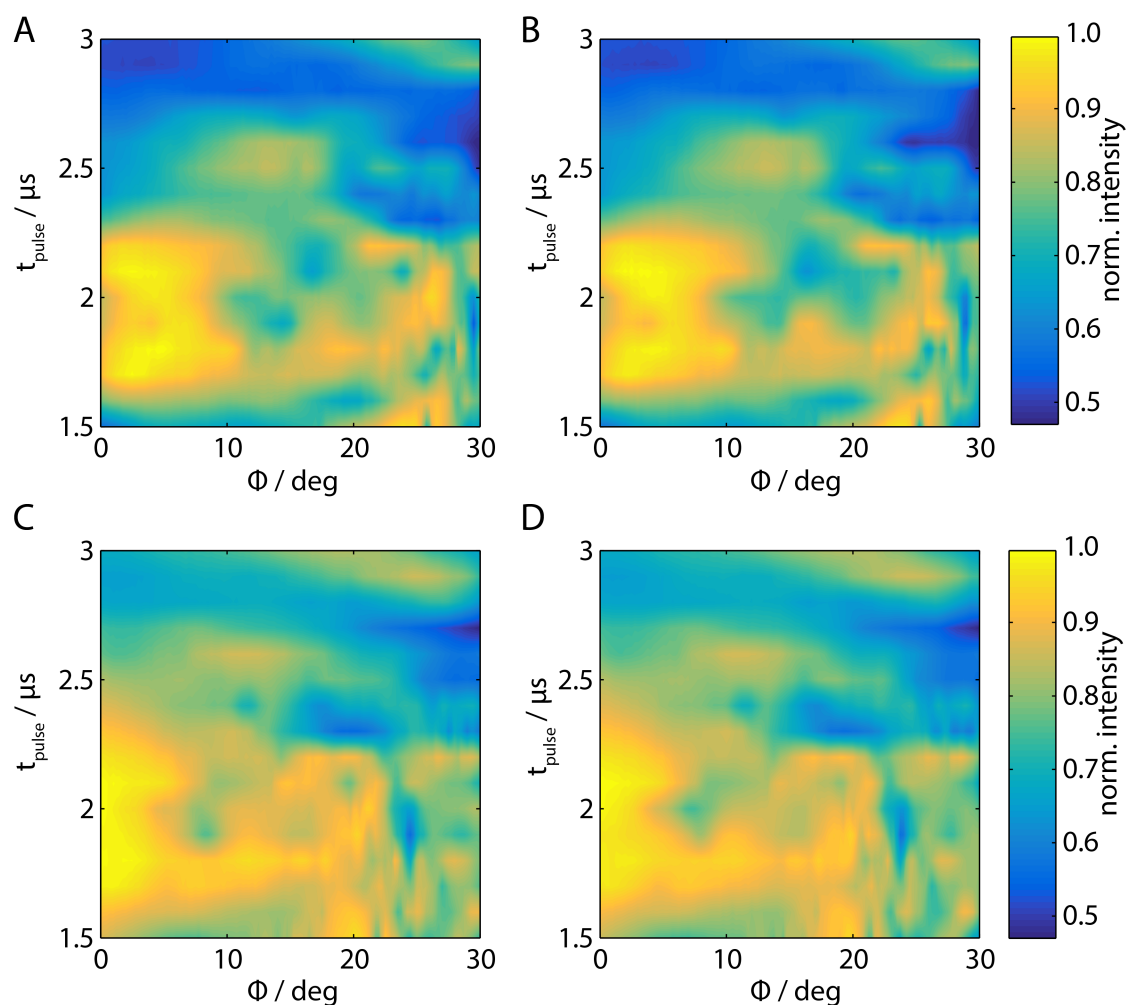
Figure 7.9. Experimental peak height of the Cα peak in U-^{13}C-^{15}N-glycineethylester using SPINAL-64 decoupling with continuous phase modulation. The phase increment $\theta = \alpha = \beta/2$ was set to 5° (A and B) or 10° (C and D). The phase and the pulse length were varied according to Figure 7.6, keeping the experimental parameters identical. The use of compensated pulses (B and D) does not improve the decoupling efficiency as compared to uncompensated pulses (A and C).

Experiments were run with the SPINAL-64 as decoupling scheme using the same parameter space as shown in Figure 7.6 with direct detection of the carbon line. Due to the similarity of the discrete and continuous phase implementation, only results for the CM decoupling are shown. The phase increment θ was fixed to 5 and 10°, respectively, while the phase ϕ and the pulse length were varied. The results are shown in Figure 7.9 for both compensated and uncompensated pulses. The difference between the compensated and the uncompensated pulses is not visible from these maps, which are to a certain extent qualitative. As expected, the best decoupling regions are shifted to lower phase values of ϕ depending on the size of θ, but the optimal pulse duration is still around a π pulse of ~ 2 μs. The recoupling conditions are significantly broader than for conventional two-pulse decoupling schemes. Even the bad decoupling regions show relative line intensities that are around 0.6 of the maximum, whereas TPPM is around 0.4 in the worst case in the examined parameter space. The absolute intensity of the maxima for TPPM/CM and SPINAL-64 are comparable and the linewidth is around 15 Hz in both implementations. Therefore, even the first qualitative maps renders SPINAL a more suitable option for a decoupling scheme due to the robustness towards small parameter missets and pulse transients.

In order to quantify the decoupling efficiency, T_2' dephasing curves have been recorded at favourable decoupling points, as observed in Figure 7.9. The decoupling efficiencies at $\theta = 5°$ are marginally better than at 10° as determined from coherence lifetimes. The decoupling points chosen for $\theta = 5°$ are τ_{p}=1.8 μs and 2.1 μs with the phase value of $\phi = 4.75°$ for both pulse durations. The dephasing curves with the corresponding transverse relaxation times are shown in Figure 7.10 for CM and for discrete phase implementation. It is interesting to observe that the use of discrete phase changes leads to better decoupling efficiency, since the opposite was shown for simple TPPM or CM. Additionally, for SPINAL the implementation with compensated pulses is not worse than the use of rectangular pulses. This is also opposite to the discoveries for TPPM. It is hypothesized that this is due to the addition of multiple frequencies introduced by the small phase increments. These additional Fourier coefficients are combined in a way that does not follow the predictable pattern of the two-pulse sequence and leads to broader resonance conditions. Another difference to the two-pulse CM scheme is the effect of the compensation, because even at slightly worse decoupling points, the compensated pulses do not improve the coherence lifetimes. Lack of such improvement was observed
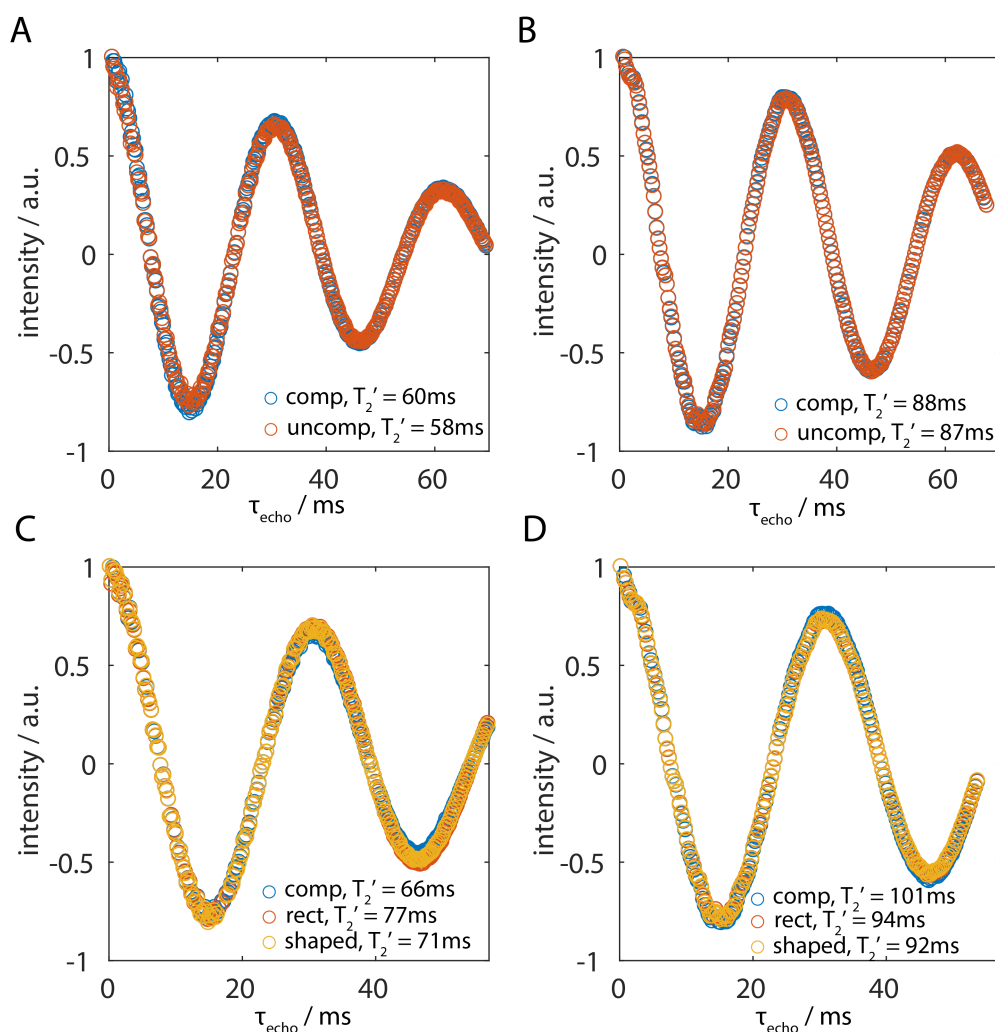
Figure 7.10. Experimental dephasing curve of the Cα line in U-^{13}C-^{15}N-glycineethylester under SPINAL-64 decoupling using a phase increment of $\theta = 5°$. The decoupling parameters were determined from Figure 7.9 using pulse lengths of either 1.8 (A and C) or 2.1 μs (B and D) at a phase value of 4.75 °. As opposed to the basic TPPM and CM, the discrete phase modulation (C and D) shows better decoupling efficiency than the continuous sine phase (A and B). The observed coherence lifetimes are generally longer than for two-pulse implementations.

for good decoupling points for two-pulse CM, but at worse decoupling, the compensation led to longer transverse relaxation times with CM.

Despite all the differences between two-pulse implementation and SPINAL, which are not fully understood, it has to be stated that the SPINAL scheme leads to overall better decoupling efficiency. The longest coherence lifetime under SPINAL decoupling (101 ms) can only be obtained by TPPM/CM by restricting the sample size, which leads to 85 ms.

7.5. Conclusion

The results for the best decoupling points and different schemes are summarized in Table 7.1 for all implementations presented in this chapter.

Table 7.1. Tabulated values of the coherence lifetimes under various decoupling schemes. The decoupling parameters are given in the left column as well as the implementation of the phase change (discrete or continuous) and the packing of the sample. For SPINAL, only full samples were measured due to the robustness towards the rf-field inhomogeneity

	T_2' (rect.)	T_2' (shaped)	T_2' (comp.)
TPPM (τ_p=2 μs, ϕ=8.5°), full	56 ms	47 ms	45 ms
CM (τ_p=2 μs, ϕ=8.5°), full	62 ms	-	61 ms
TPPM (τ_p=2 μs, ϕ=8.5°), restr.	87 ms	66 ms	61 ms
CM (τ_p=2 μs, ϕ=8.5°), restr.	87 ms	-	85 ms
SPINAL (τ_p=2.1 μs, ϕ=4.75°, θ=5°)	94 ms	92 ms	101 ms
SPINAL-CM (τ_p=2.1 μs, ϕ=4.75°, θ=5°)	97 ms	-	88 ms
SPINAL (τ_p=2.1 μs, ϕ=1.5°, θ=10°)	67 ms	75 ms	92 ms
SPINAL-CM (τ_p=2.1 μs, ϕ=1.5°, θ=10°)	75 ms	-	72 ms

In conclusion, it has been shown that pulse-transient compensation is not always beneficial for heteronuclear decoupling sequences at very high rf fields and short pulses. The compensation becomes even less important if longer pulses are applied like TPPM at low rf fields, or XiX. The results reported in Ref. [173] have not been confirmed but the rf-field strengths reported in this study could not be achieved with the available probes.

8. Conclusion and Outlook

In this thesis, a general problem of solid-state NMR was investigated by characterizing and quantifying the influence of pulse imperfections on a wide variety of pulse sequences. The theoretical concepts of Floquet theory were applied to obtain a deeper understanding of the influence of pulse transients on these sequences. The application of an experimental compensation gave more reproducible results in solid-state NMR experiments and furthered the understanding of inherent mis-designs in pulse sequences.

In **Chapter 3**, a more methodical approach to the characterization of pulse transients was presented. The measured shapes of the pulses were fitted by a model presented in the literature to characterize the rise time and electronic offset frequencies of the system. Based on the fitting procedure and the results, conclusions were drawn based on the reflection of the signal and impedance mismatch that is observed in the resonance circuit (the NMR spectrometer). Additionally, a previously used compensation method was investigated further by changing the shaped edge of the pulse. A Fourier analysis of the pulse shape based on required terms showed that the sine edge is indeed the best shape for the pulse. Non-linearities and other effects, like amplifier droop and heating effects, were excluded as error terms since the compensation was done using non-linear optimization and the result of nutation experiments were indistinguishable. In order to make the compensation more user-friendly and easily applicable, different alternatives to using the pick-up coil as a receiver for the generated B_1 fields were investigated. The most promising approach was the implementation of a bidirectional coupler to couple out a small fraction of the signal before and after it entered the probe head. Some of the pulse shapes obtained using the coupler were in good agreement with the signal of the pick-up coil. However, there was no reliable method to determine the time difference between the forward and the backward signal and the time resolution of a standard oscilloscope is not sufficient to obtain accurate results.

In **Chapter 4**, a theoretical analysis, supported with experimental results, was presented for the recoupling sequences RFDR and REDOR, which use an isolated, rotor-synchronized π pulse as recoupling element. It was shown that REDOR is a pulse sequence that is very robust against pulse imperfections. The effective Hamiltonian during REDOR has a different form than for RFDR and thus is not truncated by the effective fields generated, since they commute at all times. For RFDR, phase transients can lead to a significant reduction of the polarization-transfer efficiency. This is due to the fact that the two coupled spins experience effective fields of different magnitudes and directions. The effective fields can either be compensated using transient-compensated pulses or using a longer phase cycle. Longer phase cycles have the disadvantage of a longer minimal recoupling period, which might lead to an undersampling of the polarization-transfer curve.

In **Chapter 5**, an example of symmetry-based recoupling sequence was investigated in terms of pulse transients and further error terms were studied, which turned out to result from fictitious effective fields caused by second-order CSA-CSA crossterms. The unwanted effective fields are important sources of decreased transfer efficiency when measuring intermediate or small couplings because they lead to a mismatch of the two-frequency resonance condition dictated by the design of the sequence. Therefore, three strategies to compensate the effective fields and restore efficient polarization transfer were presented: (i) asynchronous recoupling by detuning the spinning frequency or changing the relative pulse amplitudes, (ii) super cycled sequences, and (iii) transient-compensated pulses. The advantages and disadvantages of each approach were discussed extensively based on the theoretical and experimental results. Ultimately, the choice of method or combination of methods to optimize the transfer efficiency depends on the capabilities of the spectrometer and the relative magnitude of the three different contributions.

In **Chapter 6**, the contributions that cause the line broadening in the widely used FSLG pulse sequence were examined and their influence was quantified. The most important factor was found to be the rf-field inhomogeneity, which still contributes to about 75% of the linewidth even if the sample is restricted in the centre. It was shown that the theoretically calculated error terms scale down linearly or quadratically with the effective-field strength but this was not the experimental observation. The relative rf-field distribution is always the same independently of the calibrated rf field. Therefore, the chemical-shift scaling and the resulting spectra remained almost identical. The only changing behaviour is in the individual spectra, but through the distribution of the rf

field the spectra are all superimposed by the varying chemical-shift scaling. Additional performance degradation was shown to result from pulse transients that do not have a big influence on the linewidth but rather on the shift of the spectrum, making it more difficult to interpret the results and achieve a reliable frequency calibration. Removal of phase transients and adaption of the pulse sequence led to more predictable results in terms of chemical-shift scaling and absolute frequency axis. However, the impact of pulse transients on the linewidth is negligible. Furthermore, it was shown theoretically that third-order terms contribute to the residual linewidth with a factor that is highly dependent on the dipolar coupling and can be estimated at about 60 Hz for a CH_2-group. Selectively labelling the sample improved the coherence lifetime by removal of multi-spin terms but as theoretically predicted, the two-spin terms were still dominant. These terms cannot be removed by altering the sequence, e.g. changing the angle of the effective field as they do not exhibit the same spatial behaviour as three-spin terms. Small improvements were found by changing the effective-field angle to slightly higher values of around 60°, which are understood theoretically, but the spectral quality still remained too bad to be useful for practical use. This leaves fast MAS as the method of choice for practical application of proton spectroscopy especially for large and compelx systems.

In **Chapter 7**, the heteronuclear decoupling sequence two-pulse phase modulation (TPPM) was investigated. The theoretical calculations showed that the difference between TPPM with rectangular or shaped pulses and an implementation with continuous sine phase modulation scheme is not visible in the relevant scaling coefficients, and therefore, the performance of the experiments should be indistinguishable. Furthermore, the influence of pulse transients is solely relevant in parameter areas that experience inherently bad decoupling efficiency. As a consequence, the influence of pulse transients on the best decoupling performance was determined to be small. The experimental coherence life time was slightly improved by implementing the decoupling with a continuous phase modulation independent of pulse imperfections. The supercycled implementation of TPPM, SPINAL-64, was demonstrated to be experimentally more efficient due to the high number of different modulation frequencies and thus the blurring out of the relevant Fourier coefficients. There was no clear distinction found between the discrete phase and the continuous phase implementation and the sequence was only slightly improved with pulse-transient compensation.

Overall, the results presented in this thesis provide a solid foundation for the application of pulse-transient compensation to different kinds of sequences. A wide variety of different recoupling and decoupling schemes have been presented with special focus on the theoretical understanding behind the performance degradation in the experimental results that are associated with pulse imperfections. It was shown in a general way how the removal of experimental uncertainties allows for a deeper understanding of the spin physics behind experiments. This deeper knowledge of the pulse sequence enables the experimentalists to have a better understanding of the pitfalls of the sequence and use the simple modifications proposed throughout this work to circumvent them.

In the future, more effort should be put into making the application of pulse-transient compensation more user friendly. The required programs and hardware components can be easily implemented in a standard spectrometer as the signal of the generated B_1 field can be readily picked up with the receiver instead of an oscilloscope. The deconvolution in the Fourier space and back-calculation of the required input shape is possible with the current software. The results in this thesis have conclusively shown that the effort of pulse-transient compensation is worth the gain in reproducibility, ease of experimental optimization, and overall performance enhancement of the sequences. Pulse-transient compensation could be avoided in the future with better design of pulse sequences. However, at the current stage, the improvements through pulse-sequence design is negated by drawbacks that certain supercycles or modifications have. From the current point of view, using compensated pulses for certain standard experiments is more beneficial than investing more time into the design of tailored sequences.

Further concerns about the compensation, including non-linearities, temporal instabilities, and heating effects, have proven to be negligible in the investigated experiments. Therefore, it is hypothesized that no further effort needs to be put into the basic procedure and the linear-response theory is a valid approximation for the system.

An important future use for pulse-transient compensation is the application to pulse sequences used at very fast MAS frequencies. This is due to the fact that the smaller diameter rotors allow for a reduction of the solenoid coil that generates the rf pulses, which results in higher achievable rf fields. This goes hand-in-hand with a reduction in pulse lengths used and thus the transient part of the pulse becomes longer compared to the total pulse length and gains in significance. It is believed that pulse-transient compensation will be an invaluable tool for the development of new generations of pulse sequences specifically designed to use high rf fields combined with very fast MAS fre-

quencies.

Finally, the biggest field for pulse-transient compensation in the future will be the application to specifically designed pulse sequences. At the current stage, method development in solid-state NMR is very far advanced in taking advantage of basic pulse sequences and modifying them slightly. Ground-breaking achievements in method development will go hand-in-hand with high computational power that enables the scan of huge parameter spaces for possible rf-field sequences designed for specific re- or decoupling. This approach will require highly controlled rf-field amplitudes and phases in the experimental realisation that can only be achieved with pulse-transient compensation. This control will further the agreement between experiments and theory and will lead to more control of the spin dynamics resulting in more efficient and more selective experiments. Furthermore, it will bridge the gap between method development and applications to more complex systems in order to tackle important biological questions.

Bibliography

[1] A. Ilari and C. Savino, in *Bioinformatics: Data, Sequence Analysis and Evolution*, ed. J. M. Keith, Humana Press, Totowa, NJ, 2008, pp. 63–87.

[2] J. Cavanagh, W. J. Fairbrother, A. G. Palmer III and N. J. Skelton, *Protein NMR spectroscopy: principles and practice*, Elsevier, 2007.

[3] R. Henderson and P. Unwin, Three-dimensional model of purple membrane obtained by electron microscopy, *Nature*, 1975, **257**, 28–32.

[4] J. Frank, Advances in the field of single-particle cryo-electron microscopy over the last decade, *Nature Protocols*, 2017, **12**, 209–212.

[5] J. Hardy and G. Higgins, Alzheimer's disease: the amyloid cascade hypothesis, *Science*, 1992, **256**, 184–185.

[6] J. Hardy and D. J. Selkoe, The Amyloid Hypothesis of Alzheimer's Disease: Progress and Problems on the Road to Therapeutics, *Science*, 2002, **297**, 353–356.

[7] L. Gremer, D. Schölzel, C. Schenk, E. Reinartz, J. Labahn, R. B. G. Ravelli, M. Tusche, C. Lopez-Iglesias, W. Hoyer, H. Heise, D. Willbold and G. F. Schröder, Fibril structure of amyloid-β(1–42) by cryo–electron microscopy, *Science*, 2017, **358**, 116–119.

[8] K. Pervushin, R. Riek, G. Wider and K. Wüthrich, Attenuated T2 relaxation by mutual cancellation of dipole–dipole coupling and chemical shift anisotropy indicates an avenue to NMR structures of very large biological macromolecules in solution, *Proceedings of the National Academy of Sciences*, 1997, **94**, 12366–12371.

[9] V. Tugarinov, P. M. Hwang, J. E. Ollerenshaw and L. E. Kay, Cross-correlated relaxation enhanced 1H-13C NMR spectroscopy of methyl groups in very high molecular weight proteins and protein complexes, *Journal of the American Chemical Society*, 2003, **125**, 10420–10428.

[10] C. Wasmer, A. Lange, H. Van Melckebeke, A. B. Siemer, R. Riek and B. H. Meier, Amyloid Fibrils of the HET-s(218–289) Prion Form a β Solenoid with a Triangular Hydrophobic Core, *Science*, 2008, **319**, 1523–1526.

[11] R. Tycko, Solid-State NMR Studies of Amyloid Fibril Structure, *Annual Review of Physical Chemistry*, 2011, **62**, 279–299.

[12] V. Agarwal, S. Penzel, K. Szekely, R. Cadalbert, E. Testori, A. Oss, J. Past, A. Samoson, M. Ernst, A. Böckmann and B. H. Meier, DeNovo 3D Structure Determination from Sub-milligram Protein Samples by Solid-State 100kHz MAS NMR Spectroscopy, *Angewandte Chemie - International Edition*, 2014, **53**, 12253–12256.

[13] M. T. Colvin, R. Silvers, Q. Z. Ni, T. V. Can, I. Sergeyev, M. Rosay, K. J. Donovan, B. Michael, J. Wall, S. Linse and R. G. Griffin, Atomic Resolution Structure of Monomorphic Aβ42 Amyloid Fibrils, *Journal of the American Chemical Society*, 2016, **138**, 9663–9674.

[14] V. S. Mandala, J. K. Williams and M. Hong, Structure and Dynamics of Membrane Proteins from Solid-State NMR, *Annual Review of Biophysics*, 2018, **47**, 201–222.

[15] I. Bertini, C. Luchinat, G. Parigi, E. Ravera, B. Reif and P. Turano, Solid-state NMR of proteins sedimented by ultracentrifugation, *Proceedings of the National Academy of Sciences*, 2011, **108**, 10396–10399.

[16] E. Andrew, A. Bradbury and R. Eades, Nuclear Magnetic Resonance Spectra from a Crystal rotated at High Speed, *Nature*, 1958, **182**, 1659–1659.

[17] I. J. Lowe, Free Induction Decays of Rotating Solids, *Phys. Rev. Lett.*, 1959, **2**, 285–287.

[18] U. Haeberlen and J. S. Waugh, Coherent Averaging Effects in Magnetic Resonance, *Physical Chemistry Chemical Physics*, 1968, **175**, 453–467.

[19] M. M. Maricq, Application of average hamiltonian theory to the NMR of solids, *Physical Review B*, 1982, **25**, 6622–6632.

[20] J. H. Shirley, Solution of the schrödinger equation with a hamiltonian periodic in time, *Physical Review*, 1965, **138**, 979–987.

[21] E. Vinogradov, P. K. Madhu and S. Vega, Strategies for high-resolution proton spectroscopy in solid-state NMR, *Topics in current chemistry*, 2004, **246**, 33–90.

[22] I. Scholz, B. H. Meier and M. Ernst, Operator-based triple-mode Floquet theory in solid-state NMR, *Journal of Chemical Physics*, 2007, **127**, 204504.

[23] I. Scholz, J. D. Van Beek and M. Ernst, Operator-based Floquet theory in solid-state NMR, *Solid State Nuclear Magnetic Resonance*, 2010, **37**, 39–59.

[24] J. Keeler, in *Understanding NMR Spectroscopy*, ed. John Wiley & Sons, Wiley, 2nd edn., 2010, ch. 11, pp. 381–441.

[25] K. O. Tan, M. Rajeswari, P. K. Madhu and M. Ernst, Asynchronous symmetry-based sequences for homonuclear dipolar recoupling in solid-state nuclear magnetic resonance, *Journal of Chemical Physics*, 2015, **142**, 065101.

[26] A. Khitrin and B. M. Fung, Design of heteronuclear decoupling sequences for solids, *Journal of Chemical Physics*, 2000, **112**, 2392–2398.

[27] G. De Paëpe, B. Eléna and L. Emsley, Characterization of heteronuclear decoupling through proton spin dynamics in solid-state nuclear magnetic resonance spectroscopy, *Journal of Chemical Physics*, 2004, **121**, 3165–3180.

[28] P. Tekely and M. Goldman, Radial-field sidebands in MAS, *Journal of Magnetic Resonance*, 2001, **148**, 135–141.

[29] Z. Tošner, A. Purea, J. O. Struppe, S. Wegner, F. Engelke, S. J. Glaser and B. Reif, Radiofrequency fields in MAS solid state NMR probes, *Journal of Magnetic Resonance*, 2017, **284**, 20–32.

[30] Z. Tošner, R. Sarkar, J. Becker-Baldus, C. Glaubitz, S. Wegner, F. Engelke, S. J. Glaser and B. Reif, Overcoming volume selectivity of dipolar recoupling in bi-

ological solid-state NMR, *Angewandte Chemie - International Edition*, 2018, **2**, 14514–14518.

[31] D. Lacabanne, M. L. Fogeron, T. Wiegand, R. Cadalbert, B. H. Meier and A. Böckmann, Protein sample preparation for solid-state NMR investigations, *Progress in Nuclear Magnetic Resonance Spectroscopy*, 2019, **110**, 20–33.

[32] M. Mehring and J. S. Waugh, Phase transients in pulsed NMR spectrometers, *Review of Scientific Instruments*, 1972, **43**, 649–653.

[33] T. M. Barbara, J. F. Martin and J. G. Wurl, Phase transients in NMR probe circuits, *Journal of Magnetic Resonance*, 1991, **93**, 497–508.

[34] J. J. Wittmann, K. Takeda, B. H. Meier and M. Ernst, Compensating pulse imperfections in solid-state NMR spectroscopy: A key to better reproducibility and performance, *Angewandte Chemie - International Edition*, 2015, **54**, 12592–12596.

[35] A. E. Bennett, R. G. Griffin, J. H. Ok and S. Vega, Chemical shift correlation spectroscopy in rotating solids: Radio frequency-driven dipolar recoupling and longitudinal exchange, *Journal of Chemical Physics*, 1992, **96**, 8624.

[36] Y. Ishii, 13C-13C dipolar recoupling under very fast magic angle spinning in solid-state nuclear magnetic resonance: Applications to distance measurements, spectral assignments, and high-throughput secondary-structure determination, *Journal of Chemical Physics*, 2001, **114**, 8473–8483.

[37] T. Gullion and J. Schaefer, Rotational-echo double-resonance NMR, *Journal of Magnetic Resonance*, 1989, **81**, 196–200.

[38] T. Gullion and J. Schaefer, in *Adv. Magn. Reson.*, Academic Press, Inc., 1989, vol. 13, pp. 57–83.

[39] M. Carravetta, M. Edén, X. Zhao, A. Brinkmann and M. H. Levitt, Symmetry principles for the design of radiofrequency pulse sequences in the nuclear magnetic resonance of rotating solids, *Chem. Phys. Lett.*, 2000, **321**, 205–215.

[40] M. H. Levitt, in *Encyclopedia of Magnetic Resonance*, Wiley Online Library, 2007, vol. 9, pp. 165–196.

[41] M. H. Levitt, Symmetry in the design of NMR multiple-pulse sequences, *Journal of Chemical Physics*, 2008, **128**, 052205.

[42] M. Lee and W. I. Goldburg, Nuclear-magnetic-resonance line narrowing by a rotating rf field, *Physical Review*, 1965, **140**, 1261–1271.

[43] A. E. Bennett, C. M. Rienstra, M. Auger, K. V. Lakshmi and R. G. Griffin, Heteronuclear decoupling in rotating solids, *Journal of Chemical Physics*, 1995, **103**, 6951–6958.

[44] B. M. Fung, A. K. Khitrin and K. Ermolaev, An Improved Broadband Decoupling Sequence for Liquid Crystals and Solids, *Journal of Magnetic Resonance*, 2000, **142**, 97–101.

[45] M. Ernst and B. H. Meier, in *Studies in Physical and Theoretical Chemistry*, Elsevier B.V., 1998, vol. 84, pp. 83–121.

[46] S. Zhang, B. H. Meier and R. Ernst, Polarization Echoes in NMR, *Physical Review Letters*, 1992, **69**, 2149–2151.

[47] A. Abragam, *The Principles of Nuclear Magnetism*, Oxford University Press, 1961.

[48] R. R. Ernst, G. Bodenhausen and A. Wokaun, *Principles of Nuclear Magnetic Resonance in One and Two Dimensions*, Oxford University Press, New York, 1987.

[49] M. H. Levitt, *Spin dynamics: basics of nuclear magnetic resonance*, Wiley, Chichester, 2008.

[50] M. Duer, *Introduction to Solid-State NMR Spectroscopy*, Wiley, 2005.

[51] M. Hong, Determination of Multiple ϕ-Torsion Angles in Proteins by Selective and Extensive 13C Labeling and Two-Dimensional Solid-State NMR, *Journal of Magnetic Resonance*, 1999, **139**, 389–401.

[52] F. Bloch and A. Siegert, Magnetic resonance for nonrotating fields, *Physical Review*, 1940, **57**, 522–527.

[53] M. Mehring, *Principles of High Resolution NMR in Solids*, Springer, Berlin, 1983.

[54] J. McConnell, *The Theory of Nuclear Magnetic Relaxation in Liquids*, Cambridge University Press, 2009.

[55] J. Kowalewski and L. Mäler, *Nuclear Spin Relaxation in Liquids: Theory, Experiments, and Applications*, CRC Press, 2nd edn., 2017.

[56] F. J. Dyson, The radiation theories of Tomonaga, Schwinger, and Feynman, *Physical Review*, 1949, **75**, 486–502.

[57] W. Magnus, On the exponential solution of differential equations for a linear operator, *Communications on Pure and Applied Mathematics*, 1954, **7**, 649–673.

[58] R. W. Vaughan, D. D. Elleman, L. M. Stacey, W. K. Rhim and J. W. Lee, A simple, low power, multiple pulse NMR spectrometer, *Review of Scientific Instruments*, 1972, **43**, 1356–1364.

[59] W. K. Rhim, D. D. Elleman and R. W. Vaughan, Analysis of multiple pulse NMR in solids, *Journal of Chemical Physics*, 1973, **59**, 3740–3749.

[60] W. K. Rhim, D. D. Elleman, L. B. Schreiber and R. W. Vaughan, Analysis of multiple pulse NMR in solids. II, *Journal of Chemical Physics*, 1974, **60**, 4595–4604.

[61] D. P. Burum, M. Under and R. R. Ernst, A new "tune-up" NMR pulse cycle for minimizing and characterizing phase transients, *Journal of Magnetic Resonance*, 1981, **43**, 463–471.

[62] M. H. Levitt, Composite pulses, *Progress in Nuclear Magnetic Resonance Spectroscopy*, 1986, **18**, 61–122.

[63] J. Weber, M. Seemann and J. Schmedt Auf Der Günne, Pulse-transient adapted C-symmetry pulse sequences, *Solid State Nuclear Magnetic Resonance*, 2012, **43-44**, 42–50.

[64] D. H. Brouwer and M. Horvath, Minimizing the effects of RF inhomogeneity and phase transients allows resolution of two peaks in the 1H CRAMPS NMR spectrum of adamantane, *Solid State Nuclear Magnetic Resonance*, 2015, **71**, 30–40.

[65] U. Haeberlen, in *High Resolution NMR in Solids: Selective Averaging*, Academic Press, 1976, pp. 183–186.

[66] E. Vinogradov, P. Madhu and S. Vega, High-resolution proton solid-state NMR spectroscopy by phase-modulated Lee-Goldburg experiment, *Chemical Physics Letters*, 1999, **314**, 443–450.

[67] A. J. Vega, Controlling the effects of pulse transients and RF inhomogeneity in phase-modulated multiple-pulse sequences for homonuclear decoupling in solid-state proton NMR, *Journal of Magnetic Resonance*, 2004, **170**, 22–41.

[68] L. Bosman, P. K. Madhu, S. Vega and E. Vinogradov, Improvement of homonuclear dipolar decoupling sequences in solid-state nuclear magnetic resonance utilising radiofrequency imperfections, *Journal of Magnetic Resonance*, 2004, **169**, 39–48.

[69] M. E. Halse, J. Schlagnitweit and L. Emsley, High-resolution 1H solid-state NMR spectroscopy using windowed LG4 homonuclear dipolar decoupling, *Israel Journal of Chemistry*, 2014, **54**, 136–146.

[70] M. Carravetta, M. Edén, O. G. Johannessen, H. Luthman, P. J. Verdegem, J. Lugtenburg, A. Sebald and M. H. Levitt, Estimation of carbon-carbon bond lengths and medium-range internuclear distances by solid-state nuclear magnetic resonance., *Journal of the American Chemical Society*, 2001, **123**, 10628–10638.

[71] J. Schmedt auf der Günne, Distance measurements in spin-1/2 systems by 13C and 31P solid-state NMR in dense dipolar networks, *Journal of Magnetic Resonance*, 2003, **165**, 18–32.

[72] N. C. Nielsen, C. Kehlet, S. J. Glaser and N. Khaneja, Optimal Control Methods in NMR Spectroscopy, *Encyclopedia of Magnetic Resonance*, 2010, 1–30.

[73] M. Bechmann, J. Clark and A. Sebald, Genetic algorithms and solid state NMR pulse sequences, *Journal of Magnetic Resonance*, 2013, **228**, 66–75.

[74] B. Elena, G. de Paëpe and L. Emsley, Direct spectral optimisation of proton-proton homonuclear dipolar decoupling in solid-state NMR, *Chemical Physics Letters*, 2004, **398**, 532–538.

[75] D. L. A. G. Grimminck, S. K. Vasa, W. L. Meerts, A. P. M. Kentgens and A. Brinkmann, EASY-GOING DUMBO on-spectrometer optimisation of phase modulated homonuclear decoupling sequences in solid-state NMR, *Chemical Physics Letters*, 2011, **509**, 186–191.

[76] T. W. Borneman and D. G. Cory, Bandwidth-limited control and ringdown suppression in high-Q resonators, *Journal of Magnetic Resonance*, 2012, **225**, 120–129.

[77] P. E. Spindler, Y. Zhang, B. Endeward, N. Gershernzon, T. E. Skinner, S. J. Glaser and T. F. Prisner, Shaped optimal control pulses for increased excitation bandwidth in EPR, *Journal of Magnetic Resonance*, 2012, **218**, 49–58.

[78] A. Doll and G. Jeschke, Wideband frequency-swept excitation in pulsed EPR spectroscopy, *Journal of Magnetic Resonance*, 2017, **280**, 46–62.

[79] K. Takeda, Y. Tabuchi, M. Negoro and M. Kitagawa, Active compensation of rf-pulse transients, *Journal of Magnetic Resonance*, 2009, **197**, 242–244.

[80] Y. Tabuchi, M. Negoro, K. Takeda and M. Kitagawa, Total compensation of pulse transients inside a resonator, *Journal of Magnetic Resonance*, 2010, **204**, 327–332.

[81] J. J. Wittmann, V. Mertens, K. Takeda, B. H. Meier and M. Ernst, Quantification and compensation of the influence of pulse transients on symmetry-based recoupling sequences, *Journal of Magnetic Resonance*, 2016, **263**, 7–18.

[82] D. J. Jensen, W. W. Brey, J. L. Delayre and P. A. Narayana, Reduction of pulsed gradient settling time in the superconducting magnet of a magnetic resonance instrument, *Medical Physics*, 1987, **14**, 859–862.

[83] M. A. Morich, D. A. Lampman, W. R. Dannels and F. T. Goldie, Exact Temporal Eddy Current Compensation in Magnetic Resonance Imaging Systems, *IEEE Transactions on Medical Imaging*, 1988, **7**, 247–254.

[84] J. J. Wittmann, Development of Tailored and Robust Experiments in Solid-State NMR, *PhD Thesis*, 2016.

[85] C. L. Phillips, J. Parr and E. Riskin, *Signals, Systems, and Transforms*, Prentice Hall Press, Upper Saddle River, NJ, USA, 4th edn., 2007.

[86] J. P. Hespanha, *Linear Systems Theory: Second Edition*, Princeton University Press, NED - New edition, 2 edn., 2009.

[87] J. Borish and J. B. Angell, An Efficient Algorithm for Measuring the Impulse Response Using Pseudorandom Noise, *Journal of the Audio Engineering Society*, 1983, **31**, 478–489.

[88] D. D. Rife and J. Vanderkooy, Transfer-Function Measurement with Maximum-Length Sequences, *Journal of the Audio Engineering Society*, 1989, **37**, 419–444.

[89] G.-B. Stan, J.-J. Embrechts and D. Archambeau, Comparison of Different Impulse Response Measurement Techniques, *Journal of the Audio Engineering Society*, 2002, **50**, 249–262.

[90] H. B. Patel and S. N. Chaphekar, Developments in PID Controllers: Literature Survey, *International Journal of Engineering Innovation and Research*, 2012, **1**, 425–430.

[91] K. Levenberg, A Method for the Solution of Certain Non-Linear Problems in Least Squares, *Quarterly of Applied MathematicsJournal of the Audio Engineering Society*, 1944, **2**, 164–168.

[92] D. W. Marquardt, An Algorithm for Least-Squared Estimation of Nonlinear Parameters, *Journal of the Society for Industrial and Applied Mathematics*, 1963, **11**, 431–441.

[93] C. Kanzow, N. Yamashita and M. Fukushima, Levenberg-Marquardt methods with strong local convergence properties for solving nonlinear equations with convex constraints, *Journal of Computational and Applied Mathematics*, 2005, **173**, 321–343.

[94] T. Gullion, Introduction to rotational-echo, double-resonance NMR, *Concepts in Magnetic Resonance*, 1998, **10**, 277–289.

[95] P. Schanda, B. H. Meier and M. Ernst, Quantitative analysis of protein backbone dynamics in microcrystalline ubiquitin by solid-state NMR spectroscopy, *Journal of the American Chemical Society*, 2010, **132**, 15957–15967.

[96] P. Schanda, B. H. Meier and M. Ernst, Accurate measurement of one-bond H-X heteronuclear dipolar couplings in MAS solid-state NMR, *Journal of Magnetic Resonance*, 2011, **210**, 246–259.

[97] C. P. Jaroniec, B. A. Tounge, C. M. Rienstra, J. Herzfeld and R. G. Griffin, Recoupling of heteronuclear dipolar interactions with rotational-echo double-resonance at high magic-angle spinning frequencies, *Journal of Magnetic Resonance*, 2000, **146**, 132–139.

[98] Y. Li and J. N. S. Evans, The Importance of XY-8 Phase Cycling in the Rotational-Echo Double-Resonance Experiment with Total Sideband Suppression, *Journal of Magnetic Resonance*, 1995, **116**, 150–155.

[99] M. Shen, B. Hu, O. Lafon, J. Trébosc, Q. Chen and J.-P. Amoureux, Broadband finite-pulse radio-frequency-driven recoupling (fp-RFDR) with (XY8)41 supercycling for homo-nuclear correlations in very high magnetic fields at fast and ultra-fast MAS frequencies, *Journal of Magnetic Resonance*, 2012, **223**, 107–119.

[100] R. Zhang, Y. Nishiyama, P. Sun and A. Ramamoorthy, Phase cycling schemes for finite-pulse-RFDR MAS solid state NMR experiments, *Journal of Magnetic Resonance*, 2015, **252**, 55–66.

[101] L. A. Straasø, R. Shankar, K. O. Tan, J. Hellwagner, B. H. Meier, M. R. Hansen, N. C. Nielsen, T. Vosegaard, M. Ernst and A. B. Nielsen, Improved transfer efficiencies in radio-frequency-driven recoupling solid-state NMR by adiabatic sweep through the dipolar recoupling condition, *Journal of Chemical Physics*, 2016, **145**, 034201.

[102] M. G. Jain, K. R. Mote, J. Hellwagner, G. Rajalakshmi, M. Ernst, P. K. Madhu and V. Agarwal, Measuring strong one-bond dipolar couplings using REDOR in magic-angle spinning solid-state NMR, *Journal of Chemical Physics*, 2019, **150**, 134201.

[103] J. S. Waugh, Average Hamiltonian Theory, *Encyclopedia of NMR*, 1996, **2**, 849–854.

[104] W. I. Goldburg and M. Lee, Nuclear magnetic resonance line narrowing by a rotating rf field, *Physical Review Letters*, 1963, **11**, 255–258.

[105] K. O. Tan, V. Agarwal, B. H. Meier and M. Ernst, A generalized theoretical framework for the description of spin decoupling in solid-state MAS NMR: Offset effect on decoupling performance, *Journal of Chemical Physics*, 2016, **145**, 094201.

[106] A. E. Bennett, C. M. Rienstra, J. M. Griffiths, W. Zhen, P. T. Lansbury and R. G. Griffin, Homonuclear radio frequency-driven recoupling in rotating solids, *Journal of Chemical Physics*, 1998, **108**, 9463.

[107] V. B. Cheng, H. H. Suzukawa and M. Wolfsberg, Investigations of a nonrandom numerical method for multidimensional integration, *Journal of Chemical Physics*, 1973, **59**, 3992–3999.

[108] R. A. Smith, The crystal structures of a series of salts of phthalic acid. Diammonium phthalate (NH4)2(OOC.C6H4.COO), *Acta Crystallographica Section B Structural Crystallography and Crystal Chemistry*, 1975, **31**, 1773–1775.

[109] Y. K. Lee, N. D. Kurur, M. Helmle, O. G. Johannessen, N. C. Nielsen and M. H. Levitt, Efficient dipolar recoupling in the NMR of rotating solids. A sevenfold symmetric radiofrequency pulse sequence, *Chemical Physics Letters*, 1995, **242**, 304–309.

[110] M. Hohwy, H. J. Jakobsen, M. Edén, M. H. Levitt and N. C. Nielsen, Broadband dipolar recoupling in the nuclear magnetic resonance of rotating solids: A compensated C7 pulse sequence, *Journal of Chemical Physics*, 1998, **108**, 2686.

[111] P. E. Kristiansen, M. Carravetta, W. C. Lai and M. H. Levitt, A robust pulse sequence for the determination of small homonuclear dipolar couplings in magic-angle spinning NMR, *Chemical Physics Letters*, 2004, **390**, 1–7.

[112] P. K. Madhu, X. Zhao and M. H. Levitt, High-resolution 1H NMR in the solid state using symmetry-based pulse sequences, *Chemical Physics Letters*, 2001, **346**, 142–148.

[113] E. H. Hardy, R. Verel and B. H. Meier, Fast MAS total through-bond correlation spectroscopy, *Journal of Magnetic Resonance*, 2001, **148**, 459–464.

[114] E. H. Hardy, A. Detken and B. H. Meier, Fast-MAS total through-bond correlation spectroscopy using adiabatic pulses, *Journal of Magnetic Resonance*, 2003, **165**, 208–218.

[115] K. O. Tan, I. Scholz, J. D. Van Beek, B. H. Meier and M. Ernst, Improved decoupling during symmetry-based C9-TOBSY sequences, *Journal of Magnetic Resonance*, 2014, **239**, 61–68.

[116] K. O. Tan, V. Agarwal, N. A. Lakomek, S. Penzel, B. H. Meier and M. Ernst, Efficient low-power TOBSY sequences for fast MAS, *Solid State Nuclear Magnetic Resonance*, 2018, **89**, 27–34.

[117] A. Brinkmann and M. H. Levitt, Symmetry principles in the nuclear magnetic resonance of spinning solids: Heteronuclear recoupling by generalized Hartmann-Hahn sequences, *Journal of Chemical Physics*, 2001, **115**, 357–384.

[118] X. Zhao, W. Hoffbauer, J. Schmedt Auf Der Günne and M. H. Levitt, Heteronuclear polarization transfer by symmetry-based recoupling sequences in solid-state NMR, *Solid State Nuclear Magnetic Resonance*, 2004, **26**, 57–64.

[119] M. Edén and M. H. Levitt, Pulse sequence symmetries in the nuclear magnetic resonance of spinning solids: Application to heteronuclear decoupling, *Journal of Chemical Physics*, 1999, **111**, 1511–1519.

[120] P. E. Kristiansen, M. Carravetta, J. D. van Beek, W. C. Lai and M. H. Levitt, Theory and applications of supercycled symmetry-based recoupling sequences in solid-state nuclear magnetic resonance, *Journal of Chemical Physics*, 2006, **124**, 234510.

[121] I. Scholz, P. Hodgkinson, B. H. Meier and M. Ernst, Understanding two-pulse phase-modulated decoupling in solid-state NMR, *Journal of Chemical Physics*, 2009, **130**, 114510.

[122] M. Ernst, A. Samoson and B. H. Meier, Decoupling and recoupling using continuous-wave irradiation in magic-angle-spinning solid-state NMR: A unified description using bimodal Floquet theory, *Journal of Chemical Physics*, 2005, **123**, 064102.

[123] G. De Paëpe, J. R. Lewandowski, A. Loquet, A. Böckmann and R. G. Griffin, Proton assisted recoupling and protein structure determination, *Journal of Chemical Physics*, 2008, **129**, 245101.

[124] B. Berglund and R. W. Vaughan, Correlations between proton chemical shift tensors, deuterium quadrupole couplings, and bond distances for hydrogen bonds in solids, *Journal of Chemical Physics*, 1980, **73**, 2037–2043.

[125] G. A. Jeffrey and Y. Yeon, The correlation between hydrogen-bond lengths and proton chemical shifts in crystals, *Acta Crystallographica Section B*, 1986, **42**, 410–413.

[126] M. Barfield, Structural dependencies of interresidue scalar coupling h3JNC' and donor 1H chemical shifts in the hydrogen bonding regions of proteins, *Journal of the American Chemical Society*, 2002, **124**, 4158–4168.

[127] L. L. Parker, A. R. Houk and J. H. Jensen, Cooperative hydrogen bonding effects are key determinants of backbone amide proton chemical shifts in proteins, *Journal of the American Chemical Society*, 2006, **128**, 9863–9872.

[128] L. B. Andreas, K. Jaudzems, J. Stanek, D. Lalli, A. Bertarello, T. Le Marchand, D. Cala-De Paepe, S. Kotelovica, I. Akopjana, B. Knott, S. Wegner, F. Engelke, A. Lesage, L. Emsley, K. Tars, T. Herrmann and G. Pintacuda, Structure of fully protonated proteins by proton-detected magic-angle spinning NMR, *Proceedings of the National Academy of Sciences*, 2016, **113**, 9187–9192.

[129] D. Stöppler, A. Macpherson, S. Smith-Penzel, N. Basse, F. Lecomte, H. Deboves, R. D. Taylor, T. Norman, J. Porter, L. C. Waters, M. Westwood, B. Cossins, K. Cain, J. White, R. Griffin, C. Prosser, S. Kelm, A. H. Sullivan, D. Fox, M. D. Carr, A. Henry, R. Taylor, B. H. Meier, H. Oschkinat and A. D. Lawson, Insight into small molecule binding to the neonatal Fc receptor by X-ray crystallography and 100 kHz magic-angle-spinning NMR, *PLoS Biology*, 2018, **16**, 1–27.

[130] S. Penzel, A. Oss, M. L. Org, A. Samoson, A. Böckmann, M. Ernst and B. H. Meier, Spinning faster: protein NMR at MAS frequencies up to 126 kHz, *Journal of Biomolecular NMR*, 2019, **73**, 19–29.

[131] A. A. Malär, S. Dong, G. Kehr, G. Erker, B. H. Meier and T. Wiegand, Char-
acterization of H 2 -Splitting Products of Frustrated Lewis Pairs: Benefit of Fast
Magic-Angle Spinning, *ChemPhysChem*, 2019, 672–679.

[132] A. E. McDermott, F. J. Creuzet, A. C. Kolbert and R. G. Griffin, High-resolution
magic-angle-spinning NMR spectra of protons in deuterated solids, *Journal of
Magnetic Resonance*, 1992, **98**, 408–413.

[133] B. Reif, C. P. Jaroniec, C. M. Rienstra, M. Hohwy and R. G. Griffin, 1 H- 1 H
MAS correlation spectroscopy and distance measurements in a deuterated peptide,
Journal of Magnetic Resonance, 2001, **151**, 320–327.

[134] D. Cala-Paëpe, J. Stanek, K. Jaudzems, K. Tars, L. B. Andreas and G. Pintacuda,
Is protein deuteration beneficial for proton detected solid-state NMR at and above
100 kHz magic-angle spinning?, *Solid State Nuclear Magnetic Resonance*, 2017, **87**,
126–136.

[135] J. S. Waugh, L. M. Huber and U. Haeberlen, Approach to high-resolution NMR
in solids, *Physical Review Letters*, 1968, **20**, 180–182.

[136] P. Mansfield and A. B. Grannell, Improved resolution of small resonance shifts
of dilute nuclear spin systems in solids by pulsed double resonance, *Journal of
Physics C: Solid State Physics*, 1971, **4**, 197–200.

[137] D. P. Burum and W. K. Rhim, Analysis of multiple pulse NMR in solids. III,
Journal of Chemical Physics, 1979, **71**, 944–956.

[138] D. P. Burum and W. K. Rhim, An improved NMR technique for homonuclear dipo-
lar decoupling in solids: Application to polycrystalline ice, *Journal of Chemical
Physics*, 1979, **70**, 3553–3554.

[139] S. Paul, D. Schneider and P. K. Madhu, 1H Homonuclear dipolar decoupling using
symmetry-based pulse sequences at ultra fast magic-angle spinning frequencies,
Journal of Magnetic Resonance, 2010, **206**, 241–245.

[140] D. Sakellariou, A. Lesage, P. Hodgkinson and L. Emsley, Homonuclear dipolar de-
coupling in solid-state NMR using continuous phase modulation, *Chemical Physics
Letters*, 2000, **319**, 253–260.

[141] M. E. Halse and L. Emsley, A common theory for phase-modulated homonuclear decoupling in solid-state NMR, *Phys. Chem. Chem. Phys.*, 2012, **14**, 9121–9130.

[142] K. R. Mote, V. Agarwal and P. K. Madhu, Five decades of homonuclear dipolar decoupling in solid-state NMR: Status and outlook, *Progress in Nuclear Magnetic Resonance Spectroscopy*, 2016, **97**, 1–39.

[143] M. Mehring and J. S. Waugh, Magic-angle NMR experiments in solids, *Physical Review B*, 1972, **5**, 3459–3471.

[144] A. Bielecki, A. C. Kolbert, H. J. De Groot, R. G. Griffin and M. H. Levitt, in *Advances in Magnetic and Optical Resonance*, Academic Press, Inc., 1990, vol. 14, pp. 111–124.

[145] M. H. Levitt, A. C. Kolbert, A. Bielecki and D. J. Ruben, High-resolution 1H NMR in solids with frequency-switched multiple-pulse sequences, *Solid State Nuclear Magnetic Resonance*, 1993, **2**, 151–163.

[146] M. Leskes, P. K. Madhu and S. Vega, A broad-banded z-rotation windowed phase-modulated Lee-Goldburg pulse sequence for 1H spectroscopy in solid-state NMR, *Chemical Physics Letters*, 2007, **447**, 370–374.

[147] S. Paul, R. S. Thakur, M. Goswami, A. C. Sauerwein, S. Mamone, M. Concistrè, H. Förster, M. H. Levitt and P. K. Madhu, Supercycled homonuclear dipolar decoupling sequences in solid-state NMR, *Journal of Magnetic Resonance*, 2009, **197**, 14–19.

[148] M. E. Halse and L. Emsley, Improved phase-modulated homonuclear dipolar decoupling for solid-state NMR spectroscopy from symmetry considerations, *Journal of Physical Chemistry A*, 2013, **117**, 5280–5290.

[149] M. Leskes, P. K. Madhu and S. Vega, Floquet theory in solid-state nuclear magnetic resonance, *Progress in Nuclear Magnetic Resonance Spectroscopy*, 2010, **57**, 345–380.

[150] A. S. Tatton, I. Frantsuzov, S. P. Brown and P. Hodgkinson, Unexpected effects of third-order cross-terms in heteronuclear spin systems under simultaneous

radio-frequency irradiation and magic-angle spinning NMR, *Journal of Chemical Physics*, 2012, **136**, 084503.

[151] A. Garon, R. Zeier and S. J. Glaser, Visualizing operators of coupled spin systems, *Physical Review A - Atomic, Molecular, and Optical Physics*, 2015, **91**, 1–28.

[152] S. Smith, T. Levante, B. Meier and R. Ernst, Computer Simulations in Magnetic Resonance. An Object-Oriented Programming Approach, *Journal of Magnetic Resonance, Series A*, 1994, **106**, 75–105.

[153] F. M. Paruzzo, G. Stevanato, M. E. Halse, J. Schlagnitweit, D. Mammoli, A. Lesage and L. Emsley, Refocused linewidths less than 10 Hz in 1H solid-state NMR, *Journal of Magnetic Resonance*, 2018, **293**, 41–46.

[154] M. Goldman and P. Tekely, Effect of radial RF field on MAS spectra, *Comptes Rendus de l'Academie des Sciences - Series IIc: Chemistry*, 2001, **4**, 795–800.

[155] K. Nishimura, R. Fu and T. A. Cross, The effect of rf inhomogeneity on heteronuclear dipolar recoupling in solid state NMR: Practical performance of SFAM and REDOR, *Journal of Magnetic Resonance*, 2001, **152**, 227–233.

[156] A. Naito, K. Nishimura, S. Kimura, S. Tuzi, M. Aida, N. Yasuoka and H. Saitô, Determination of the Three-Dimensional Structure of a New Crystalline Form of N -Acetyl-Pro-Gly-Phe As Revealed by 13 C REDOR, X-Ray Diffraction, and Molecular Dynamics Calculation , *Journal of Physical Chemistry*, 2002, **100**, 14995–15004.

[157] M. Ernst, Heteronuclear spin decoupling in solid-state NMR under magic-angle sample spinning, *Journal of Magnetic Resonance*, 2003, **162**, 1–34.

[158] P. Hodgkinson, Heteronuclear decoupling in the NMR of solids, *Progress in Nuclear Magnetic Resonance Spectroscopy*, 2005, **46**, 197–222.

[159] P. K. Madhu, Heteronuclear spin decoupling in solid-state nuclear magnetic resonance: Overview and outlook, *Israel Journal of Chemistry*, 2014, **54**, 25–38.

[160] P. Tekely, P. Palmas and D. Canet, Effect of Proton Spin Exchange on the Residual 13C MAS NMR Linewidths. Phase-Modulated Irradiation for Efficient Heteronu-

clear Decoupling in Rapidly Rotating Solids, *Journal of Magnetic Resonance, Series A*, 1994, **107**, 129–133.

[161] M. Ernst, H. Geen and B. H. Meier, Amplitude-modulated decoupling in rotating solids: A bimodal Floquet approach, *Solid State Nuclear Magnetic Resonance*, 2006, **29**, 2–21.

[162] R. S. Thakur, N. D. Kurur and P. K. Madhu, Swept-frequency two-pulse phase modulation for heteronuclear dipolar decoupling in solid-state NMR, *Chemical Physics Letters*, 2006, **426**, 459–463.

[163] M. Weingarth, P. Tekely and G. Bodenhausen, Efficient heteronuclear decoupling by quenching rotary resonance in solid-state NMR, *Chemical Physics Letters*, 2008, **466**, 247–251.

[164] M. Ernst, A. Samoson and B. H. Meier, Low-power XiX decoupling in MAS NMR experiments, *Journal of Magnetic Resonance*, 2003, **163**, 332–339.

[165] M. Kotecha, N. P. Wickramasinghe and Y. Ishii, Efficient low-power heteronuclear decoupling in 13C high-resolution solid-state NMR under fast magic angle spinning, *Magnetic Resonance in Chemistry*, 2007, **45**, 221–230.

[166] M. Weingarth, G. Bodenhausen and P. Tekely, Low-power decoupling at high spinning frequencies in high static fields, *Journal of Magnetic Resonance*, 2009, **199**, 238–241.

[167] M. Weingarth, J. Trébosc, J. P. Amoureux, G. Bodenhausen and P. Tekely, Efficiency at high spinning frequencies of heteronuclear decoupling methods designed to quench rotary resonance, *Solid State Nuclear Magnetic Resonance*, 2011, **40**, 21–26.

[168] V. S. Mithu, S. Paul, N. D. Kurur and P. K. Madhu, Heteronuclear dipolar decoupling in solid-state nuclear magnetic resonance under ultra-high magic-angle spinning, *Journal of Magnetic Resonance*, 2011, **209**, 359–363.

[169] I. J. Shannon, K. D. Harris and S. Arumugam, High-resolution solid state 13C NMR studies of ferrocene as a function of magic angle sample spinning frequency, *Chemical Physics Letters*, 1992, **196**, 588–594.

[170] M. Ernst, H. Zimmermann and B. H. Meier, A simple model for heteronuclear spin decoupling in solid-state NMR, *Chemical Physics Letters*, 2000, **317**, 581–588.

[171] G. Sinning and M. Mehring, Dynamics of Spin Decoupling in Carbon13-Proton NMR, *Chemical Physics Letters*, 1976, **43**, 382–386.

[172] M. Mehring and G. Sinning, Dynamics of heteronuclear spin coupling and decoupling in solids, *Physical Review B*, 1977, **15**, 2519–2532.

[173] I. Frantsuzov, S. K. Vasa, M. Ernst, S. P. Brown, V. Zorin, A. P. M. Kentgens and P. Hodgkinson, Rationalising Heteronuclear Decoupling in Refocussing Applications of Solid-State NMR Spectroscopy, *ChemPhysChem*, 2017, **18**, 394–405.

[174] I. Frantsuzov, M. Ernst, S. P. Brown and P. Hodgkinson, Simulating spin dynamics in organic solids under heteronuclear decoupling, *Solid State Nuclear Magnetic Resonance*, 2015, **70**, 28–37.

[175] A. Equbal, M. Bjerring, P. K. Madhu and N. C. Nielsen, A unified heteronuclear decoupling strategy for magic-angle-spinning solid-state NMR spectroscopy, *Journal of Chemical Physics*, 2015, **142**, 184201.

[176] A. Detken, E. H. Hardy, M. Ernst and B. H. Meier, Simple and efficient decoupling in magic-angle spinning solid-state NMR: The XiX scheme, *Chemical Physics Letters*, 2002, **356**, 298–304.

[177] K. Takegoshi, J. Mizokami and T. Terao, 1H decoupling with third averaging in solid NMR, *Chemical Physics Letters*, 2001, **341**, 540–544.

[178] B. Blümich and H. W. Spiess, Quaternions as a practical tool for the evaluation of composite rotations, *Journal of Magnetic Resonance*, 1985, **61**, 356–362.

Appendices

A. Spin-Tensor Operators

Definition of rank-zero and rank-one tensors for a single spin in the spherical tensor notation are given by [53]

$$
\begin{aligned}
T_{0,0} &= E \\
T_{1,0} &= I_z \\
T_{1,1} &= \frac{-1}{\sqrt{2}} I^+ = \frac{-1}{\sqrt{2}}(I_x + iI_y) \\
T_{1,-1} &= \frac{-1}{\sqrt{2}} I^- = \frac{-1}{\sqrt{2}}(I_x - iI_y)
\end{aligned}
\tag{A.1}
$$

Definition of the rank-zero, -one, and -two tensors for a two-spin system are

$$
\begin{aligned}
T_{0,0} &= \frac{-1}{\sqrt{3}}(\vec{I_1} \cdot \vec{I_2}) \\
T_{1,0} &= \frac{-1}{2\sqrt{2}}(I_1^+ I_2^- - I_1^- I_2^+) \\
T_{1,\pm 1} &= \frac{-1}{2}(I_1^\pm I_{2z} - I_{1z} I_2^\pm) \\
T_{2,0} &= \frac{1}{\sqrt{6}}(3I_{1z} I_{2z} - (\vec{I_1} \cdot \vec{I_2})) \\
T_{2,\pm 1} &= \mp \frac{1}{2}(I_1^\pm I_{2z} + I_{1z} I_2^\pm) \\
T_{2,\pm 2} &= \frac{1}{2}(I_1^\pm \cdot I_2^\pm)
\end{aligned}
\tag{A.2}
$$

The rank-zero, -one, -two, and -three tensors for a three-spin system are defined according to [151]. For brevity, the definition of the Cartesian product is written as $I_{abc} = I_{1a} I_{2b} I_{3c}$.

$$T_{1,-1}(\tau_1^{[3]}) = \frac{2}{\sqrt{15}}[3I_{xxx} - 3iI_{yyy} - i(I_{xxy} + I_{xyx} + I_{yxx}) + (I_{xyy} + I_{yxy} + I_{yyx})$$
$$+ (I_{xzz} + I_{zxz} + I_{zzx}) - i(I_{yzz} + I_{zyz} + I_{zzy})]$$

$$T_{1,0}(\tau_1^{[3]}) = \sqrt{\frac{8}{15}}[(I_{xxz} + I_{xzx} + I_{zxx}) + (I_{yyz} + I_{yzy} + I_{zyy}) + 3I_{zzz}]$$

$$T_{1,1}(\tau_1^{[3]}) = \frac{-2}{\sqrt{15}}[3I_{xxx} + 3iI_{yyy} + i(I_{xxy} + I_{xyx} + I_{yxx}) + (I_{xyy} + I_{yxy} + I_{yyx})$$
$$+ (I_{xzz} + I_{zxz} + I_{zzx}) + i(I_{yzz} + I_{zyz} + I_{zzy})]$$

$$T_{3,-3}(\tau_1^{[3]}) = [(I_{xxx} + iI_{yyy}) - i(I_{xxy} + I_{xyx} + I_{yxx}) - (I_{xyy} + I_{yxy} + I_{yyx})]$$

$$T_{3,-2}(\tau_1^{[3]}) = \sqrt{\frac{2}{3}}[(I_{xxz} + I_{xzx} + I_{zxx}) - (I_{yyz} + I_{yzy} + I_{zyy})$$
$$- i(I_{xyz} + I_{xzy} + I_{yxz} + I_{yzx} + I_{zxy} + I_{zyx})]$$

$$T_{3,-1}(\tau_1^{[3]}) = \frac{1}{\sqrt{15}}[-3(I_{xxx} - iI_{yyy}) + i(I_{xxy} + I_{xyx} + I_{yxx}) - (I_{xyy} + I_{yxy} + I_{yyx})$$
$$+ 4(I_{xzz} + I_{zxz} + I_{zzx}) - 4i(I_{yzz} + I_{zyz} + I_{zzy})]$$

$$T_{3,0}(\tau_1^{[3]}) = \frac{-2}{\sqrt{5}}[(I_{xxz} + I_{xzx} + I_{zxx}) + (I_{yyz} + I_{yzy} + I_{zyy}) - 2I_{zzz}]$$

$$T_{3,1}(\tau_1^{[3]}) = \frac{1}{\sqrt{15}}[3(I_{xxx} + iI_{yyy}) + i(I_{xxy} + I_{xyx} + I_{yxx}) + (I_{xyy} + I_{yxy} + I_{yyx})$$
$$- 4(I_{xzz} + I_{zxz} + I_{zzx}) - 4i(I_{yzz} + I_{zyz} + I_{zzy})]$$

$$T_{3,2}(\tau_1^{[3]}) = \sqrt{\frac{2}{3}}[(I_{xxz} + I_{xzx} + I_{zxx}) - (I_{yyz} + I_{yzy} + I_{zyy})$$
$$+ i(I_{xyz} + I_{xzy} + I_{yxz} + I_{yzx} + I_{zxy} + I_{zyx})]$$

$$T_{3,-3}(\tau_1^{[3]}) = [(-I_{xxx} + iI_{yyy}) - i(I_{xxy} + I_{xyx} + I_{yxx}) + (I_{xyy} + I_{yxy} + I_{yyx})]$$

$$T_{1,-1}(\tau_2^{[3]}) = \frac{1}{\sqrt{3}}[-i(I_{yxx} + I_{xyx} - 2I_{xxy}) - i(I_{yzz} + I_{zyz} - 2I_{zzy})$$
$$+ (I_{xyy} + I_{yxy} - 2I_{yyx}) + (I_{xzz} + I_{zxz} - 2I_{zzx})]$$

$$T_{1,0}(\tau_2^{[3]}) = \sqrt{\frac{2}{3}}[-2(I_{xxz} + I_{yyz}) + (I_{zxx} + I_{xzx}) + (I_{zyy} + I_{yzy})]$$

$$T_{1,1}(\tau_2^{[3]}) = \frac{1}{\sqrt{3}}[-i(I_{yxx} + I_{xyx} - 2I_{xxy}) - i(I_{yzz} + I_{zyz} - 2I_{zzy})$$
$$- (I_{xyy} + I_{yxy} - 2I_{yyx}) - (I_{xzz} + I_{zxz} - 2I_{zzx})]$$

$$T_{2,-2}(\tau_2^{[3]}) = \frac{1}{\sqrt{3}}[(I_{yzx} + I_{zyx}) + (I_{xzy} + I_{zxy}) - 2(I_{xyz} + I_{yxz})$$
$$- (2iI_{xxz} - iI_{xzx} - iI_{zxx}) + (2iI_{yyz} - iI_{yzy} - iI_{zyy})]$$

$$T_{2,-1}(\tau_2^{[3]}) = \frac{1}{\sqrt{3}}[-(2I_{xxy} - I_{xyx} - I_{yxx}) - i(2I_{yyx} - I_{yxy} - I_{xyy})$$
$$+ (2iI_{zzx} - iI_{zxz} - iI_{xzz}) + (2I_{zzy} - I_{zyz} - I_{yzz})]$$

$$T_{2,0}(\tau_2^{[3]}) = \sqrt{2}[(I_{yzx} + I_{zyx}) - (I_{xzy} - I_{zxy})]$$

$$T_{2,1}(\tau_2^{[3]}) = \frac{1}{\sqrt{3}}[(2I_{xxy} - I_{xyx} - I_{yxx}) - i(2I_{yyx} - I_{yxy} - I_{xyy})$$
$$+ (2iI_{zzx} - iI_{zxz} - iI_{xzz}) - (2I_{zzy} - I_{zyz} - I_{yzz})]$$

$$T_{2,2}(\tau_2^{[3]}) = \frac{1}{\sqrt{3}}[(I_{yzx} + I_{zyx}) + (I_{xzy} + I_{zxy}) - 2(I_{xyz} + I_{yxz})$$
$$+ (2iI_{xxz} - iI_{xzx} - iI_{zxx}) - (2iI_{yyz} - iI_{yzy} - iI_{zyy})]$$

$$T_{1,-1}(\tau_3^{[3]}) = [(I_{xyy} - I_{yxy}) + (I_{xzz} - I_{zxz}) - i(I_{yxx} - I_{xyx}) - i(I_{yzz} - I_{zyz})]$$

$$T_{1,0}(\tau_3^{[3]}) = \sqrt{2}[(I_{zxx} - I_{xzx}) + (I_{zyy} - I_{yzy})]$$

$$T_{1,1}(\tau_3^{[3]}) = [-(I_{xyy} - I_{yxy}) - (I_{xzz} - I_{zxz}) - i(I_{yxx} - I_{xyx}) - i(I_{yzz} - I_{zyz})]$$

$$T_{2,-2}(\tau_3^{[3]}) = [(I_{zxy} - I_{xzy}) + (I_{zyx} - I_{yzx}) + i(I_{zxx} - I_{xzx}) + i(I_{yzy} - I_{zyy})]$$

$$T_{2,-1}(\tau_3^{[3]}) = [(I_{yxx} - I_{xyx}) + (I_{zyz} - I_{yzz}) + i(I_{xyy} - I_{yxy}) + i(I_{zyz} - I_{yzz})]$$

$$T_{2,0}(\tau_3^{[3]}) = \sqrt{\frac{2}{3}}[-(2I_{xyz} + I_{xzy} - I_{zxy}) + (2I_{yxz} + I_{yzx} - I_{zyx})]$$

$$T_{2,1}(\tau_3^{[3]}) = [-(I_{yxx} - I_{xyx}) - (I_{zyz} - I_{yzz}) + i(I_{xyy} - I_{yxy}) + i(I_{zyz} - I_{yzz})]$$

$$T_{2,2}(\tau_3^{[3]}) = [(I_{zxy} - I_{xzy}) + (I_{zyx} - I_{yzx}) - i(I_{zxx} - I_{xzx}) - i(I_{yzy} - I_{zyy})]$$

$$T_{0,0}(\tau_4^{[3]}) = \frac{2}{\sqrt{3}}[I_{xyz} - I_{xzy} - I_{yxz} + I_{yzx} + I_{zxy} - I_{zyx}] \tag{A.3}$$

B. Analytical Tensor Components after FSLG Decoupling

The analytical expressions for the two- and three-spin tensors calculated in second- and third-order after FSLG decoupling. The functional forms of the tensors are shown in Figure 6.2 and 6.3, where the simulation parameters can be found. $X_{\ell,m}$ is the projection of the effective Hamiltonian on the spherical tensors defined in Appendix A.

The three-spin components from second-order error calculations are given by

$$
\begin{aligned}
X_{0,0}(\tau_4) &= \frac{1}{\omega_{\mathrm{r}}}(0.591515 + 0.650331\cos(2\theta) + 0.490205\cos(4\theta))\Im(\omega_{1,2}^{(1)} \cdot \omega_{1,3}^{(-1)}) \\
&\quad + (0.289761 + 0.326409\cos(2\theta) + 0.249856\cos(4\theta))\Im(\omega_{1,2}^{(2)} \cdot \omega_{1,3}^{(-2)}) \\
X_{2,0}(\tau_2) &= \sqrt{\frac{3}{2}}X_{0,0}(\tau_4) \\
X_{2,0}(\tau_3) &= -\sqrt{\frac{1}{2}}X_{0,0}(\tau_4) \\
X_{2,1}(\tau_2) &= \frac{1}{\omega_{\mathrm{r}}}(-0.00244743\cos(\theta)\sin(\theta) + 0.000611858\sin(4\theta))\Im(\omega_{1,2}^{(1)} \cdot \omega_{1,3}^{(-1)}) \\
&\quad + (-0.00506846\cos(\theta)\sin(\theta) + 0.00126711\sin(4\theta))\Im(\omega_{1,2}^{(2)} \cdot \omega_{1,3}^{(-2)}) \\
X_{2,-1}(\tau_2) &= -X_{2,1}(\tau_2) = \sqrt{\frac{1}{3}}X_{2,1}(\tau_3) = -\sqrt{\frac{1}{3}}X_{2,-1}(\tau_3) \\
X_{2,2}(\tau_2) &= \frac{1}{\omega_{\mathrm{r}}}(0.00123089 - 0.00123089\cos(4\theta))\Im(\omega_{1,2}^{(1)} \cdot \omega_{1,3}^{(-1)}) \\
&\quad + (0.00256358 - 0.00256358\cos(4\theta))\Im(\omega_{1,2}^{(2)} \cdot \omega_{1,3}^{(-2)}) \\
X_{2,-2}(\tau_2) &= X_{2,2}(\tau_2) = -\sqrt{\frac{1}{3}}X_{2,2}(\tau_3) = -\sqrt{\frac{1}{3}}X_{2,-2}(\tau_3) \tag{B.1}
\end{aligned}
$$

with $\omega_{1,2}^{(\nu)}$ being the Fourier coefficients of the dipolar interaction. Assuming a relative dipole orientation of ϕ, the expressions can be derived as a function of the Euler angles

$$
\begin{aligned}
X_{0,0}(\tau_4) &= \frac{1}{\omega_{\mathrm{r}}} f(\theta) \delta_{1,2} \delta_{1,3} \sin(\alpha) \sin(\beta) \sin(\phi) \\
&\quad (0.125 \cos(\beta)^2 \cos(\phi) + 0.015625 \cos(\phi) \sin(\beta)^2 \\
&\quad - 0.109375 \cos(\alpha) \cos(\beta) \sin(\beta) \sin(\phi)) \\
X_{2,1}(\tau_2) &= \frac{1}{\omega_{\mathrm{r}}} g(\theta) \delta_{1,2} \delta_{1,3} \sin(\alpha) \sin(\beta) \sin(\phi) \\
&\quad (0.125 \cos(\beta)^2 \cos(\phi) + 0.0725938 \cos(\phi) \sin(\beta)^2 \\
&\quad - 0.0524063 \cos(\alpha) \cos(\beta) \sin(\beta) \sin(\phi)) \\
X_{2,2}(\tau_2) &= \frac{1}{\omega_{\mathrm{r}}} h(\theta) \delta_{1,2} \delta_{1,3} \sin(\alpha) \sin(\beta) \sin(\phi) \\
&\quad (0.125 \cos(\beta)^2 \cos(\phi) + 0.0743125 \cos(\phi) \sin(\beta)^2 \\
&\quad - 0.0506875 \cos(\alpha) \cos(\beta) \sin(\beta) \sin(\phi)) \quad \text{(B.2)}
\end{aligned}
$$

The third-order auto-terms projections of the two-spin spherical tensors are given in an analytical form by

$$
\begin{aligned}
X_{0,0} &= X_{1,0} = X_{1,1} = X_{1,-1} = 0 \\
X_{2,0} &= \frac{1}{\omega_{\mathrm{r}}^2} (-0.00598819 \, \omega_{1,2}^{(+2)} \omega_{1,2}^{(-1)} \omega_{1,2}^{(-1)} - 0.00598819 \, \omega_{1,2}^{(-2)} \omega_{1,2}^{(+1)} \omega_{1,2}^{(+1)} \\
&\quad - (0.00506264 \, \omega_{1,2}^{(+2)} \omega_{1,2}^{(-1)} \omega_{1,2}^{(-1)} + 0.00506264 \, \omega_{1,2}^{(-2)} \omega_{1,2}^{(+1)} \omega_{1,2}^{(+1)}) \cos(2\theta) \\
&\quad + (0.00598819 \, \omega_{1,2}^{(+2)} \omega_{1,2}^{(-1)} \omega_{1,2}^{(-1)} + 0.005598819 \, \omega_{1,2}^{(-2)} \omega_{1,2}^{(+1)} \omega_{1,2}^{(+1)}) \cos(4\theta) \\
&\quad + (0.00506264 \, \omega_{1,2}^{(+2)} \omega_{1,2}^{(-1)} \omega_{1,2}^{(-1)} + 0.00506264 \, \omega_{1,2}^{(-2)} \omega_{1,2}^{(+1)} \omega_{1,2}^{(+1)}) \cos(6\theta)) \\
X_{2,1} &= \frac{1}{\omega_{\mathrm{r}}^2} (0.0033459 \, \omega_{1,2}^{(+2)} \omega_{1,2}^{(-1)} \omega_{1,2}^{(-1)} + 0.0033459 \, \omega_{1,2}^{(-2)} \omega_{1,2}^{(+1)} \omega_{1,2}^{(+1)}) \sin(2\theta) \\
&\quad - (0.00122364 \, \omega_{1,2}^{(+2)} \omega_{1,2}^{(-1)} \omega_{1,2}^{(-1)} + 0.00122364 \, \omega_{1,2}^{(-2)} \omega_{1,2}^{(+1)} \omega_{1,2}^{(+1)}) \sin(4\theta) \\
&\quad - (0.00029954 \, \omega_{1,2}^{(+2)} \omega_{1,2}^{(-1)} \omega_{1,2}^{(-1)} + 0.00029954 \, \omega_{1,2}^{(-2)} \omega_{1,2}^{(+1)} \omega_{1,2}^{(+1)}) \sin(6\theta) \\
X_{2,-1} &= -X_{2,1}
\end{aligned}
$$

$$X_{2,2} = \frac{1}{\omega_{\mathrm{r}}^2}(0.000963965\,\omega_{1,2}^{(+2)}\omega_{1,2}^{(-1)}\omega_{1,2}^{(-1)} + 0.000963965\,\omega_{1,2}^{(-2)}\omega_{1,2}^{(+1)}\omega_{1,2}^{(+1)}$$

$$- (0.00317249\,\omega_{1,2}^{(+2)}\omega_{1,2}^{(-1)}\omega_{1,2}^{(-1)} + 0.00317249\,\omega_{1,2}^{(-2)}\omega_{1,2}^{(+1)}\omega_{1,2}^{(+1)})\cos(2\theta)$$

$$+ (0.000641444\,\omega_{1,2}^{(+2)}\omega_{1,2}^{(-1)}\omega_{1,2}^{(-1)} + 0.000641444\,\omega_{1,2}^{(-2)}\omega_{1,2}^{(+1)}\omega_{1,2}^{(+1)})\cos(4\theta)$$

$$+ (0.00156709\,\omega_{1,2}^{(+2)}\omega_{1,2}^{(-1)}\omega_{1,2}^{(-1)} + 0.00156709\,\omega_{1,2}^{(-2)}\omega_{1,2}^{(+1)}\omega_{1,2}^{(+1)})\cos(6\theta))$$

$$X_{2,-2} = X_{2,2} \tag{B.3}$$

Substituting the analytical expressions for the Fourier components of the dipolar coupling, the expressions are obtained in terms of the Euler angles

$$X_{2,0} = \frac{1}{\omega_{\mathrm{r}}^2}u(\theta)\delta_{1,2}^3\sin(\beta)^2\sin(2\beta)^2$$

$$X_{2,1} = \frac{1}{\omega_{\mathrm{r}}^2}v(\theta)\delta_{1,2}^3\sin(\beta)^2\sin(2\beta)^2$$

$$X_{2,2} = \frac{1}{\omega_{\mathrm{r}}^2}w(\theta)\delta_{1,2}^3\sin(\beta)^2\sin(2\beta)^2 \tag{B.4}$$

C. Spin System of Glycine

Table C.1 shows CSA tensors and C.2 the dipolar tensors used for the simulations presented in Chapter 6.4.3 using an 8-spin homonuclear system for glycine.

Table C.1. CSA tensors for the spin system of a 8-spin homonuclear glyince in the PAS at 600 MHz.

CSA tensor	shift (kHz)	δ_{CSA} (ppm)	η_{CSA}	α_{CSA} (°)	β_{CSA} (°)	γ_{CSA} (°)
I_1 (Hα1)	1932	2100	0.8013	-54.76	109.2	96.18
I_2 (Hα2)	2508	-2974.8	0.751	-17.82	103.4	78.42
I_3 (HN)	4752	2085.6	0.998	-2.092	88.39	69.72
I_4 (HN)	4752	2085.6	0.998	-2.092	88.39	69.72
I_5 (HN)	4752	2085.6	0.998	-2.092	88.39	69.72
I_6 (Hα2)	2508	-2974.8	0.751	-17.82	103.4	78.42
I_7 (Hα2)	2508	-2974.8	0.751	-17.82	103.4	78.42
I_8 (Hα1)	1932	2100	0.8013	-54.76	109.2	96.18

Table C.2. Dipolar and J-couplings for the spin system of a 8-spin homonuclear glyince in the PAS at 600 MHz.

dipolar tensor	J coup (Hz)	$\delta_{\mathrm{dip}}\, 2\pi$ (kHz)	α_{dip} (°)	β_{dip} (°)	γ_{dip} (°)
$I_1 I_2$	0	-52245	0	70.7704	120.471
$I_1 I_3$	0	-13595	134.371	96.5903	14.8764
$I_1 I_4$	0	-13595	134.371	96.5903	14.8764
$I_1 I_5$	0	-11213	134.371	96.5903	14.8764
$I_1 I_6$	0	-2983.4	0	42.7559	143.03
$I_1 I_7$	0	-11683	0	135.41	69.0396
$I_1 I_8$	0	-4926.5	0	113.094	234.532
$I_2 I_3$	0	-13387	-105.815	85.9751	47.2049
$I_2 I_4$	0	-13387	-105.815	85.9751	47.2049
$I_2 I_5$	0	-11041	-105.815	85.9751	47.2049
$I_2 I_6$	0	-9027.6	0	31.8856	167.065
$I_2 I_7$	0	-9027.6	0	148.114	12.9347
$I_2 I_8$	0	-2213.4	0	115.015	255.244
$I_3 I_4$	0	-30665	0	81.8395	28.4886
$I_3 I_5$	0	-24851	0	81.8395	28.4886
$I_3 I_6$	0	-6475.4	-124.44	138.512	-96.44
$I_3 I_7$	0	-2553.1	-53.6713	118.981	35.751
$I_3 I_8$	0	-8747	79.9454	130.848	-83.2699
$I_4 I_5$	0	-23441	0	81.8395	28.4886
$I_4 I_6$	0	-6475.4	-124.44	138.512	-96.44
$I_4 I_7$	0	-2553.1	-53.6713	118.981	35.751
$I_4 I_8$	0	-8747	79.9454	130.848	-83.2699
$I_5 I_6$	0	-6475.4	-124.44	138.512	-96.44
$I_5 I_7$	0	-2553.1	-53.6713	118.981	35.751
$I_5 I_8$	0	-8747	79.9454	130.848	-83.2699
$I_6 I_7$	0	-1152.5	0	148.771	0
$I_6 I_8$	0	-899.91	0	134.988	275.494
$I_7 I_8$	0	-1641.1	0	84.3594	239.803

D. AU Program for Heteronuclear Decoupling Optimization

A model AU program written within the course of this thesis for the optimization of heteronuclear decoupling using externally generated shape files as input for the decoupling pulses.

```
/*********************************************************************/
/* TPPMcomp
/* Short Description: TPPM compensation, cosine phase mod
/* AU program that perfroms measurements with different phases
/* and pulse lengths. The shape files are generated by MATLAB
/* and automatically loaded for the respective measurement
/*
/* Keywords: Transient Compensation
/* Description/Usage: See Description with MATLAB Script
/* Author(s)
/* Name: Johannes Hellwagner
/* Organisation: ETH Zurich
/* Email: johe@nmr.phys.chem.ethz.ch
/* First Version
/*********************************************************************/

AUERR = TPPMcomp(curdat);
QUITMSG("--- TPPMcomp finished ---")

#include <ShapeIO/ShapeIOC.h>
```

```c
#include <stdio.h>
#include <inc/exptUtil>

char myname[64] = "180829_glycine_1p8_CM_ref";
char myuser[64];
char path[PATH_MAX] = "/opt/topspin3.5p15/exp/stan/nmr/lists/wave/user/";
double freq;
double tstep;
int nt;
int nph;
int ntr;
int myexpno = 1;
int tmpexpno = 999; //***
int myprocno = 1;

int cp(const char* source_file, const char* target_file);
int read_paramfile_main();
int read_paramfile_sub(char rel_path[PATH_MAX], char* curdat);

int TPPMcomp(const char* curdat) {
  char tmp1[PATH_MAX];
  char source_file[PATH_MAX];
  char target_file[PATH_MAX];
  char line[PATH_MAX];
  char line_sub[PATH_MAX];
  char msg[PATH_MAX];
  int i,j,k;
  int expTime = 0;

  read_paramfile_main();

  DATASET(myname,myexpno,myprocno,disk,myuser);
  STOREPAR("TD",4096)
  STOREPAR1("TD",nt*nph)
```

```
STOREPARS("TD",4096)
STOREPAR1S("TD",nt*nph)
sprintf(line,"TPPM_cosine/tp%d/ph%d/",1,1);
read_paramfile_sub(line,curdat);


DATASET(myname,tmpexpno,myprocno,disk,myuser); //***

//for (j = 1; j <= ntr; j++) {
  //for (i = 1; i <= nph; i++) {
   for (k = 1; k <= nt; k++) {
     sprintf(line,"TPPM_cosine/tp%d/ph%d/",k,1);
     read_paramfile_sub(line,curdat);

      expTime += CalcExpTime();
      //IEXPNO***
   }
  //}
//}
//DEXPNO***

PrintExpTime(expTime*nph,nph*nt);

//expno = myexpno;
//change i,j,k
for (k = 1; k <= nt; k++) {

 sprintf(line,"TPPM_cosine/tp%d/",k);
  read_paramfile_sub(line,curdat);

  for (i = 1; i <= nph; i++) {
      strcpy(tmp1,path);
      strcat(tmp1,line);
      sprintf(line_sub,"ph%d/",i);
```

```
        strcat(tmp1,line_sub);


        strcpy(source_file,tmp1);
        strcat(source_file,"rise.shape");
        strcpy(target_file,path);
        strcat(target_file,"rise.shape");
        cp(source_file,target_file);
        strcpy(source_file,tmp1);
        strcat(source_file,"p.shape");
        strcpy(target_file,path);
        strcat(target_file,"p.shape");
        cp(source_file,target_file);
        strcpy(source_file,tmp1);
        strcat(source_file,"fall.shape");
        strcpy(target_file,path);
        strcat(target_file,"fall.shape");
        cp(source_file,target_file);

   //SETCURDATA
        ZG
        ERRORABORT
        WSER(i+(k-1)*nph,myname,myexpno,myprocno,disk,myuser)
        //IEXPNO
        ERRORABORT
      }
    }
  //DEXPNO***

  return 0;
}

int read_paramfile_main() {
char param_file[PATH_MAX];
  FILE* file;
```

```
  strcpy(param_file,path);
  strcat(param_file,"TPPM_cosine/.param");

  file = fopen(param_file,"r");
  fscanf(file,"%s\n", &myuser);
fscanf(file,"%lf\n",&freq); // MHz
fscanf(file,"%lf\n",&tstep);
  fscanf(file,"%d\n", &nt);
  fscanf(file,"%d\n", &nph);
  fscanf(file,"%d\n", &ntr);
  close(file);

  return 0;
}

int read_paramfile_sub(char rel_path[PATH_MAX], char* curdat) {
  char param_file[PATH_MAX];
  FILE* file;
  int nrise;
  int nrep;
  int nfall;
  double trise;
  double trep;
  double tfall;

  strcpy(param_file,path);
  strcat(param_file,rel_path);
  strcat(param_file,".param");

  file = fopen(param_file,"r");
fscanf(file,"%d\n", &nrise);
  fscanf(file,"%d\n", &nrep);
  fscanf(file,"%d\n", &nfall);
```

```
close(file);


  trise = nrise*tstep;
  trep = nrep*tstep;
  tfall = nfall*tstep;
  //cp_TPPM_shape_pulse.mari

  STOREPAR("PULPROG",    "cp_dec_phi_tp_loop_shape3.johe")
  STOREPAR("TD",         4096) // ?
  //FETCHPAR("TD",TD)
  //STOREPAR("AQ",          0.0306600) //?
  //STOREPAR("RG",          128)
  STOREPAR("DW",         15.0)
  STOREPAR("DE",         6.5)
  STOREPAR("D 1",        6.0)
  STOREPAR("DS",         0)
  STOREPAR("NS",         4)
  STOREPAR("P 15",       1000.0)
  STOREPAR("PLW 1",      27.0)
  STOREPAR("P 3",        2.5)
  STOREPAR("P 12",       trise)
  STOREPAR("P 13",       trep)
  STOREPAR("P 14",       tfall)
  STOREPAR("PLW 2",      28.0)
  STOREPAR("PLW 10",     104.0)
  STOREPAR("PLW 12",     728.0)
  STOREPAR("SPNAM 0",    "tan40_60-80.juga")
  STOREPAR("SPNAM 12",   "rise.shape")
  STOREPAR("SPNAM 13",   "p.shape")
  STOREPAR("SPNAM 14",   "fall.shape")


  return 0;
```

```c
}

int cp(const char* source_file, const char* target_file) {
  char ch;
  FILE* source;
  FILE* target;
  source = fopen(source_file, "r");
  target = fopen(target_file, "w");

  if(source == NULL) {
    exit(EXIT_FAILURE);
  }
  if(target == NULL) {
    fclose(source);
    exit(EXIT_FAILURE);
  }

  while((ch = fgetc(source)) != EOF)
    fputc(ch, target);
  fclose(source);
  fclose(target);
  return 0;
}
```

E. Pulse-Transient Compensation: MATLAB Implementation

The following section provides the MATLAB scripts adapted and modified from [84] for the automated pulse-transient compensation.

E.1. MATLAB Scripts

The following are the four parent scripts that build the backbone of the compensation and call specific subfunctions. The four scripts are the definition of the relevant pulse parameters (C00_Parameters.m), the initialization of the communication with the oscilloscope (C01_Initialize.m), the determination of the impulse-response function (C02_GetH.m), and the generation and verification of the compensated pulse, which is shown exemplary for the PMLG sequence (C03_LinearResponse_PMLG.m).

C00_Parameters.m

```matlab
1  close all
2  %% NMR spectrometer PC host name and login
3  % mounts topspin folder for userdefined shapes on local computer
4  fname    =   'data_';                    % Filename of .mat file, where data is saved
5  username =   'johe';                     % spectrometer login username
6  machine  =   'oersted';                  % hostname or IP of spectrometer
7  path_to_topspin = '/opt/topspin3.5pl5';  % topspin main folder on spectrometer,
        ususally /opt/topspinX.X.X
8  timepoint_now = datestr(now,'mmddyy_HHMM');
9
10
11 %% Spectrometer Properties and Impulse Response Measurement Parameters
12 freq     = 300.0887996e6;                % Spectrometer Frequency
13 tstep    =   50e-9;                       % downsampled timeresolution
14 mls_seed =   [1 1 0 1 1 0 1 1 0 1];      % input seed for MLS, length is order of MLS
15 scrf     =   0.5;                         % maximal MLS amplitude
```

```matlab
16  tauref    =    10e-6;                        % lenght of reference pulse
17  plw_mls   =    10;                           % Powerlevel for MLS sequence in Watt
18  d1        =     1;                           % recycle delay in sec
19
20  %% Scope Options
21  ip        =    '169.254.221.44';             % IP of Tektroniks 7104
22  Fs        =    10e9;                           % Sampling Rate
23  scCH1     =    0.1;                           % scaling of Channel 1 in volts per div
24  recL      =    [1 2 4 10 20 40 100 200 400 1e3]*1e-6;  % possible Record lengths in
        seconds
25
26  [~,tmp] =    min(abs(recL-tstep*(tauref/tstep+5e-6/tstep+1.5*2^length(mls_seed))));
27  deltaT  =    recL(tmp+1);                     %  Record length
28
29  %% Parameters for transient compensation
30  cutoff       = 0.015;         % Cutoff under which FT of compensated shape is set to zero
31  rf_wanted    = 50;            % desired rf field in kHz
32  rf_topspin   = 100;           % rf corresponding to value of 100 in shape
33  plw_rf       = 85;            % Powerlevel in W corresponding to rf_topspin (Hz)
34
35
36  %% Target Shape
37  % single pulse
38  tau_p        =    5e-6;       % pulse length in s
39  tau_edge     =    0.4e-6;      % edge time in s
40  phi1         =    0;          % phase of pulse
41  commentstr  =   'automated compensation';
42
43  save parameters.mat
44
45
46
47  %% Mount Spectrometer drive
48  o1_mountspectrometer(username,machine,path_to_topspin);
49
50  if exist('shapes','dir')==0     % create tmp dir for shapes
51      mkdir shapes
52  end
```

C01_Initialize.m

```matlab
1
2
3  %% Generate MLS Sequence and CW pulse as well as target shape
4  [mls_in,mls_out]=a1_makemls(mls_seed,tstep,scrf,tauref);
5
6  eval(['!mv ./shapes/mls' num2str(length(mls_seed)) '.shape ./shapes/mls.auto']);
7  eval(['!mv ./shapes/cw_mls' num2str(length(mls_seed)) '.shape ./shapes/cw.auto']);
8
```

```
 9  o1_write_paramfile('.param',username,'zg_1shape','cw.auto',freq,length(mls_out),tstep,
        plw_mls,1,1,1)

10

11  o1_copyshapes( './shapes/cw.auto' );
12  o1_copyshapes( './shapes/mls.auto' );
13  o1_copyshapes( './shapes/.param' );

14

15  fprintf(  '### Execute AU program "autocomp.jowi" and press Enter! ###\n' )
16  pause()
17  q=0;

18

19  % check if the oscilloscope is clocked externally

20

21  while(q<1)
22  reply2 = input(' ### Is the scope triggered on the same basis as the spectrometer clock
        ? Y/N [Y]: ', 's');
23  if isempty(reply2)
24      reply2 = 'Y';
25  end

26

27  if  ismember(reply2,['Y','y','yes'])~=1

28

29    pause(1)
30    o1_triggerscope()
31    pause(2)

32

33    %% Record CW pulse to determine Frequency for Mixing Down
34      cw_raw   = tek_read_trigg(ip,deltaT,Fs,scCH1,1,freq);
35      cw_proc  = tek_proc_autophase(cw_raw,tstep,1000:1200);

36

37      [~,fitrange]=a1_find_start_cw(cw_proc, (tstep*0.5*length(mls_out))); % Part of CW
          pulse without phase transients
38      % in 99% of the cases this is correct, keep it in??
39      figure(1)
40      fitrange = a2_ask_for_correct_range(fitrange,cw_proc.single.y1);
41      phaserange_cw = fitrange;                                          % Determine Frequency
          from phase drift
42      delta_f  = tek_calcfreq(cw_proc,fitrange);                        % determine freq
          difference from phase drift
43      freq_opt = freq-delta_f;                                          % Correct frequency for
          downsampling
44      cw_raw.param.freq=freq_opt;
45      cw_proc  = tek_proc_autophase(cw_raw,tstep,phaserange_cw);

46

47      cw       = tek_combine(cw_raw,cw_proc);
48      fprintf(' ### Optimized Frequency: %4.7f MHz ###\n', (freq_opt/1e6));

49

50      figure(1)
51      plot(1:length(cw_proc.single.y1),[real(cw_proc.single.y1);imag(cw_proc.single.y1)])
52      title('Downmixing of CW pulse with updated frequency');
53      pause(0.1)
```

```matlab
54        save -append parameters.mat freq_opt
55  else
56        freq_opt=freq;
57        pause(1)
58        o1_triggerscope()
59        pause(2)
60
61        %% Record CW pulse to determine Frequency for Mixing Down
62            cw_raw   = tek_read_trigg(ip,deltaT,Fs,scCH1,1,freq);
63            cw_proc  = tek_proc_autophase(cw_raw,tstep,1000:1200);
64
65            [~,fitrange]=a1_find_start_cw(cw_proc, (tstep*2.5*length(mls_out))); % Part of
                  CW pulse without phase transient
66            cw_raw.param.freq=freq_opt;
67            cw       = tek_combine(cw_raw,cw_proc);
68            figure(1)
69            plot(1:length(cw_proc.single.y1),[real(cw_proc.single.y1);imag(cw_proc.single.
                  y1)])
70            title('Downmixing of CW pulse with updated frequency');
71            pause(0.1)
72            save -append parameters.mat freq_opt
73  end
74
75  reply1 = input(' ### Did the quadrature demodulation work? Y/N [Y]: ', 's');
76  if isempty(reply1)
77        reply1 = 'Y';
78  end
79
80  if  ismember(reply1,['Y','y','yes'])~=1
81        q=0;
82  else
83        q=1;
84  end
85
86  end
```

C02_GetH.m

```matlab
1  %% Record Response of MLS sequence
2
3
4  o1_write_paramfile('.param',username,'zg_1shape','mls.auto',freq,length(mls_out),tstep,
       plw_mls,ns_mls,1,1)
5  o1_copyshapes( './shapes/.param' );
6  pause(2)
7  o1_triggerscope()
8  pause(2)
9
10 mls_raw          = tek_read_trigg(ip,deltaT,Fs,scCH1,1,freq_opt);
11 mls_proc         = tek_proc_autophase(mls_raw,tstep,floor(tauref/tstep));
```

```matlab
12
13  figure(2)
14  plot(1:length(mls_proc.t),[real(mls_proc.y);imag(mls_proc.y)])
15  title('Response of MLS sequence')
16  pause(0.1)
17
18  [idx_mls,phra_mls]  = a1_find_start(mls_proc,tstep);
19  if ns > 1
20      mls_raw         = tek_read_trigg(ip,deltaT,Fs,scCH1,ns,freq_opt);
21  end
22  mls_proc            = tek_proc_autophase(mls_raw,tstep,phra_mls);
23  mls_proc.input.mls_in = mls_in;
24  mls_proc.input.scrf    = scrf;
25
26
27  %% Calcualte Impulse Response
28
29  % determine beginning of second MLS cycle
30  rr          =  idx_mls+floor(15/(tstep/1e-6))+1*length(mls_in)+(1:length(mls_in));
31  h       =  a12_deconv(mls_in,mls_proc.y(rr),length(mls_in),0);
32
33   % shift impulse response such that maximum is at position 40
34
35  [~,idx_h]         =  max(abs(h));
36  h                 =  circshift(h.',40-idx_h).';
37  fprintf('### Baseline Correction of h. Check, that there is no signal in selected
          region! ###\n')
38  %rr3               =  a2_ask_for_correct_range(1:20,h);
39  rr3=1:20;
40  mls_proc.h_blc  =  h-mean(h(rr3(1):rr3(end)));
41  mls_proc.h      =  h;
42
43  mls             = tek_combine(mls_raw,mls_proc);
44
45
46  figure(3)
47  plot(1:length(mls.h),[real(mls.h_blc);imag(mls.h_blc)])
48  title('Impulse Response Function')
49
50
51  fprintf(' ### Select range of h(t) for compensation ###\n')
52  idx_h   = find(abs(mls.h_blc)>0.02*max(abs(mls.h_blc)),1,'first'); % find rising edge
          of h
53  mls.rr2 = (idx_h)+(0:99);
54  mls.rr2 = a2_ask_for_correct_range(mls.rr2,mls.h_blc);
55
56  figure(10)
57  plot(linspace(-0.5,0.5,length(mls.h_blc))/0.05,abs(fftshift(fft(mls.h_blc))))
58
59   eval(['save  ',fname, timepoint_now ' cw mls'])
```

C03_LinearResponse_PMLG.m

```matlab
[target_shape, scale] = a2_gen_ashaped_pulse(tau_p,tstep,tau_edge,phi1);
a12_exporttotopspin_3shape(target_shape.wanted.*scale,10+[1 target_shape.np],rf_wanted,
    rf_topspin,'./shapes/','target',tstep,commentstr,0)

[comp_in]=a2_perform_compensation(mls,target_shape,cutoff);

exportrange1          = a12_exporttotopspin_3shape(comp_in.shape,[comp_in.idx comp_in.idx
    +comp_in.np],rf_wanted,rf_topspin,'./shapes/','comp.auto',tstep,commentstr,1);
comp_in.exportrange = exportrange1;
comp_in.exp_shape   = comp_in.shape(exportrange1(1):exportrange1(end));
!mv ./shapes/comp.auto.shape ./shapes/comp.auto
o1_copyshapes('./shapes/comp.auto')

[~,tmp] =   min(abs(recL-2*comp_in.np*tstep));
deltaT  =   recL(tmp+1);


%% Record Uncompensated pulse
o1_write_paramfile('.param',username,'zg_1shape','target.auto',freq,target_shape.np,
    tstep,plw_rf,ns,1,1)
o1_copyshapes( './shapes/.param' );
pause(1)
o1_triggerscope()

fprintf( '### I will start pulsing the uncompensated pulse... ###\n' )
pause(3)


uncomp_raw     = tek_read_trigg(ip,deltaT,Fs,scCH1,1,freq_opt);
uncomp_proc    = tek_proc_autophase(uncomp_raw,tstep,100:150);

[~,fitrange] = a1_find_start(uncomp_proc,  0.5*tau_p  ); % Part of  pulse without phase
    transients
figure(1)

fitrange      = a2_ask_for_correct_range(fitrange,uncomp_proc.single.y1);
uncomp_proc   = tek_proc_autophase(uncomp_raw,tstep,fitrange);

uncomp_resp   = tek_combine(uncomp_raw,uncomp_proc);

figure(4)
plot(1:length(uncomp_proc.single.y1),[real(uncomp_proc.single.y1);imag(uncomp_proc.
    single.y1)])
title('Downmixing of Uncompensated pulse ');
pause(0.1)
clear comp_raw comp_proc



```

```matlab
45
46  %% Record Compensated pulse
47  o1_write_paramfile('.param',username,'zg_1shape','comp.auto',freq,comp_in.exportrange(
        end)-comp_in.exportrange(1),tstep,plw_rf,ns,1,1)
48  o1_copyshapes( './shapes/.param' );
49  pause(1)
50  o1_triggerscope()
51
52  fprintf( '### I will start pulsing the compensated pulse... ###\n' )
53  pause(5)
54
55
56  comp_raw      = tek_read_trigg(ip,deltaT,Fs,scCH1,1,freq_opt);
57  comp_proc     = tek_proc_autophase(comp_raw,tstep,fitrange);
58
59  comp_resp     = tek_combine(comp_raw,comp_proc);
60
61  figure(5)
62  plot(1:length(comp_resp.Y),[real(comp_resp.Y);imag(comp_resp.Y)])
63  title('Downmixing of Compensated pulse ');
64  pause(0.1)
65  clear comp_raw comp_proc
66
67
68  fprintf('### Compensated Pulse. Press Enter to continue !')
69
70  pause
71
72
73  %% Generation of Compensated PMLG pulse with shaped phase ramps
74  % generates 3 PMLG pulses and takes the middle one to be exported
75
76  CCC=a2_gen_PMLG_ramp_angle(8e-6,50e-9,0,acos(1/sqrt(3)),125e3);
77  CCCp=a2_gen_PMLG_ramp_angle(8e-6,50e-9,0.4e-6,acos(1/sqrt(3)),125e3);
78  [CCCc]=a2_perform_compensation(mls,CCCp,cutoff);
79  exportrange1         = a12_exporttotopspin_3shape(CCCc.shape,12+CCCc.np/3+[1 CCCp.np
        /3],60,120,'./shapes/','compPMLG_ramp_corr_thetam',tstep,commentstr,0);
80  exportrange1         = a12_exporttotopspin_3shape(CCC.wanted,10+CCC.np/3+[1 CCC.np
        /3],120,120,'./shapes/','PMLG_ramp_thetam_100',tstep,commentstr,0);
81  o1_write_paramfile('.param',username,'zg_1shape','compPMLG_ramp_corr_thetam.shape',freq
        ,CCCc.np/3,tstep,plw_rf,ns,1,1)
82
83  o1_copyshapes('./shapes/*PMLG*.shape')
84  o1_copyshapes( './shapes/.param' );
85  pause(1)
86  o1_triggerscope()
87  pause(5)
88  comppmlg_raw      = tek_read_trigg(ip,deltaT,Fs,scCH1,1,freq_opt);
89  comppmlg_proc     = tek_proc_autophase(comppmlg_raw,tstep,fitrange);
90  comppmlg_resp     = tek_combine(comppmlg_raw,comppmlg_proc);
91
```

```matlab
92
93  figure(6)
94  subplot(211)
95  plot(1:length(comppmlg_resp.Y),[abs(comppmlg_resp.Y)])
96  subplot(212)
97  plot(1:length(comppmlg_resp.Y),[angle(comppmlg_resp.Y)])
98
99  save -append parameters.mat fitrange exportrange1
100 eval(['save ',fname, timepoint_now ' -append *_resp'])
101
102
103 fprintf('### Compensated PMLG Pulse!')
```

E.2. Additional MATLAB Scripts

E.2.1. Data Handling of Shape Files

a1_find_start.m

```matlab
1  %% Find rising edge of reference pulse of MLS sequence (or start of cw pulse)
2  %
3  %  Input :
4  %    data        = struct containing field .y or single.y1 with downsampled data
5  %    tau_plateau = time, where pulse is not distorted (plateau of
6  %                  recangular pulse) in sec
7  %
8
9  function [idx,phaserange]=a1_find_start(data, tau_plateau)
10 tau_trans   = 2.5;                      % approximate transient time in us
11 if isfield(data,'y')
12     y       = abs(data.y);
13 else
14     y       = abs(data.single.y1);
15 end
16     tstepu  = data.t(2) ;               % timestep in us
17 tau_plateau = tau_plateau*1e6;          % time in us
18
19
20 a           = max( y );                 % Maximum Amplitude of signal
21 idx         = find( y >0.1*a,1,'first'); % find rising edge of reference pulse
22
23
24 % Should be in the middle of reference pulse
25 phaserange  = idx+floor(tau_trans/tstepu)+(1:floor(tau_plateau/tstepu));
```

a1_find_start_cw.m

```matlab
1   %% Find start of cw pulse
2   %
3   %   Input :
4   %       data            = struct containing field .y or single.y1 with downsampled data
5   %       tau_plateau     = time, where pulse is not distorted (plateau of
6   %                         recangular pulse) in sec
7   %
8
9   function [idx,phaserange]=a1_find_start_cw(data, tau_plateau)
10  tau_trans    = 2.5;                      % approximate transient time in us
11  if isfield(data,'y')
12      y         = abs(data.y);
13  else
14      y         = abs(data.single.y1);
15  end
16  tstepu   = data.t(2) ;                   % timestep in us
17  tau_plateau = tau_plateau*1e6;           % time in us
18
19
20  a            = max( y );                 % Maximum Amplitude of signal
21  idx          = find( y >0.1*a,1,'first'); % find rising edge of reference pulse
22
23
24  % Should be in the middle of reference pulse
25  phaserange   = idx+30*floor(tau_trans/tstepu)+(1:floor(tau_plateau/tstepu));
```

a1_makemls.m

```matlab
1   %% Generate Bruker shape file with MLS sequence
2   %   contains a reference pulse of length tau_ref and 4 repetitions of a mls
3   %   sequence generated by mls_seed.
4   % Input:
5   %     mls_seed = vector of length n containing only ones and zeros
6   %                used to generate MLS-n sequence; n_max of 32 supported
7   %     tstep    = time resolution for MLS sequence in s, eg 50e-9 for 50ns
8   %     scrf     = scaling of MLS amplitude relative to reference pulse, eg
9   %                    0.5 for 50% scaling
10  %     tauref   = length of reference pulse in seconds, ege 10e-6 for 10us
11  %
12  % Output:
13  %     mls_in   = one MLS-n cycle
14  %     mls_out  = reference pulse and 4 MLS cycles
15  %
16
17  function [mls_in,mls_out]=a1_makemls(mls_seed,tstep,scrf,tauref)
18
19  np_ref=floor(tauref/tstep);
```

```matlab
20  np_delay=floor(10e-6/tstep); % 10 us delay between ref pulse and start of MLS to
        account for ring down
21  tstep=tstep/1e-9;
22
23  [c,seq]=LFSR( mls_seed );
24  LL=length(seq);
25  p=seq;
26  p(p==1)=-1;
27  p(p==0)=1;
28  mls_in=p;
29
30  comstring=['MLS-',num2str(length(mls_seed)), ', Input Seed: [',num2str(mls_seed),']'];
31  mls_out=[ones(1,np_ref),zeros(1,np_delay),mls_in*scrf,mls_in*scrf,mls_in*scrf];
32  a12_exporttotopspin_3shape(mls_out,[1 length(mls_out)],100,100, './shapes/', ['mls',
        num2str(length(mls_seed))] ,tstep*1e9 ,comstring,0);
33  a12_exporttotopspin_3shape(ones(size(mls_out)),[1 length(mls_out)],scrf*100,100, './
        shapes/', ['cw_mls',num2str(length(mls_seed))] ,tstep*1e9 ,'CW pulse',0);
34
35  fprintf([' ### MLS Sequence and CW pulse stored in directory ''./shapes''!          ###\
        n'...
36            ' ### Copy them to the Spectrometer and start pulsing a ' num2str(length(
                mls_out)*tstep/1000) 'us CW pulse! ###\n'])
37
38
39  %% Generate MLS Sequence
40  % script taken from MatlabCentral
41  %
42  % Copyright (c) 2010, Nikesh Bajaj
43  % All rights reserved.
44  %
45  % Redistribution and use in source and binary forms, with or without
46  % modification, are permitted provided that the following conditions are
47  % met:
48  %
49  %     * Redistributions of source code must retain the above copyright
50  %       notice, this list of conditions and the following disclaimer.
51  %     * Redistributions in binary form must reproduce the above copyright
52  %       notice, this list of conditions and the following disclaimer in
53  %       the documentation and/or other materials provided with the distribution
54  %     * Neither the name of the AMU nor the names
55  %       of its contributors may be used to endorse or promote products derived
56  %       from this software without specific prior written permission.
57  %
58  % THIS SOFTWARE IS PROVIDED BY THE COPYRIGHT HOLDERS AND CONTRIBUTORS "AS IS"
59  % AND ANY EXPRESS OR IMPLIED WARRANTIES, INCLUDING, BUT NOT LIMITED TO, THE
60  % IMPLIED WARRANTIES OF MERCHANTABILITY AND FITNESS FOR A PARTICULAR PURPOSE
61  % ARE DISCLAIMED. IN NO EVENT SHALL THE COPYRIGHT OWNER OR CONTRIBUTORS BE
62  % LIABLE FOR ANY DIRECT, INDIRECT, INCIDENTAL, SPECIAL, EXEMPLARY, OR
63  % CONSEQUENTIAL DAMAGES (INCLUDING, BUT NOT LIMITED TO, PROCUREMENT OF
64  % SUBSTITUTE GOODS OR SERVICES; LOSS OF USE, DATA, OR PROFITS; OR BUSINESS
65  % INTERRUPTION) HOWEVER CAUSED AND ON ANY THEORY OF LIABILITY, WHETHER IN
```

```matlab
66  % CONTRACT, STRICT LIABILITY, OR TORT (INCLUDING NEGLIGENCE OR OTHERWISE)
67  % ARISING IN ANY WAY OUT OF THE USE OF THIS SOFTWARE, EVEN IF ADVISED OF THE
68  % POSSIBILITY OF SUCH DAMAGE.
69
70
71  function[c,seq]=LFSR(s)
72  %s=initial state of LFSR, you can choose any lenght of LFSR
73  %example: s=[1 1 0 0 1] for 5 bit LFSR
74  %t=tap positions, e.g.t=[5 2]
75  % c will be matrix containing the states of LFSR raw wise
76  % seq= generated sequence
77  %-------------------------------------------------------------
78  % If any doubt, confusion or feedback please contact me
79  % NIKESH BAJAJ
80  % bajaj.nikkey@gmail.com (+91-9915522564)
81  % Asst. Professor at Lovely Profesional University
82  % Masters from Aligarh Muslim University,INDIA
83  %-------------------------------------------------
84
85  tap2=[0,1];
86  tap3=[0,2];
87  tap4=[0,3];
88  tap5=[1,4];
89  tap6=[0,5];
90  tap7=[0,6];
91  tap8=[1,2,3,7];
92  tap9=[3,8];
93  tap10=[2,9];
94  tap11=[1,10];
95  tap12=[0,3,5,11];
96  tap13=[0,2,3,12];
97  tap14=[0,2,4,13];
98  tap15=[0,14];
99  tap16=[1,2,4,15];
100 tap17=[2,16];
101 tap18=[6,17];
102 tap19=[0,1,4,18];
103 tap20=[2,19];
104 tap21=[1,20];
105 tap22=[0,21];
106 tap23=[4,22];
107 tap24=[0,2,3,23];
108 tap25=[7,24];
109 tap26=[0,1,5,25];
110 tap27=[0,1,4,26];
111 tap28=[2,27];
112 tap29=[1,28];
113 tap30=[0,3,5,29];
114 tap31=[2,30];
115 tap32=[1,5,6,31];
116
```

```matlab
117  n=length(s);
118  eval(['t=1+tap',num2str(n),';']);
119
120  fprintf(' # Taps at Positions: [ ');
121  c(1,:)=s;
122  m=length(t);
123  for i=1:m
124      fprintf([num2str(t(i)),' ']);
125  end
126  fprintf(']\n');
127
128
129  for k=1:2^n-2;
130  b(1)=xor(s(t(1)), s(t(2)));
131  if m>2;
132      for i=1:m-2;
133      b(i+1)=xor(s(t(i+2)), b(i));
134      end
135  end
136  j=1:n-1;
137  s(n+1-j)=s(n-j);
138  s(1)=b(m-1);
139  c(k+1,:)=s;
140  end
141  seq=c(:,n)';
142  %-------------------------------------------------------
143  %                   VERIFICATION
144  %-------------------------------------------------------
145  %Verification
146   m=length(seq);
147  code= seq;
148  %Balance Property
149  Ns=0; % number of 1s
150  Zs=0; % number of 0s
151  for k=1:m
152      if seq(k)==1;
153          Ns=Ns+1;
154      else
155          Zs=Zs+1;
156      end
157  end
158  if Ns==Zs+1
159      % disp('The Code satisfies Balance Property ')
160  else
161      disp('# Warning: The Code does NOT satisfy Balance Property')
162  end
163      % fprintf('  number of 1s and 0s are %i %i  \n\n',Ns,Zs)
164  %Run Length Property
165  b=code;
166  r(1:20)=0;
167  i=1;
```

```matlab
168   while b (1) == b ( m );
169       b = circshift ( b , [1 1]);
170   end
171   if b ( m ) ==0;
172       b ( m +1) =1;
173   else
174       b ( m +1) =0;
175   end
176   for k =1: m ;
177       if b ( k ) == b ( k +1);
178           i = i +1;
179       else
180           r ( i ) = r ( i ) +1;
181               i =1;
182       end
183   end
184   i =0;
185   while r (20 - i ) ==0;
186       r (20 - i ) =[];
187       i = i +1;
188   end
189   l = length ( r );
190   p =0;
191   for k =1: l -2
192       if r ( k ) ==2* r ( k +1)
193           p = p +1;
194       end
195   end
196   if r ( l -1) == r ( l );
197       p = p +1;
198   end
199
200   if p == l -1;
201     %  disp ('The code satisfies RUN LENGTH property ')
202   else
203       disp ('# Warning: The code does NOT satisfy RUN LENGTH property ')
204   end
205   % fprintf ('  The run length is as follow\n')
206   %disp ( r );
207   %Autocorrelation
208   rx = code ;
209   for k =1:2* m +1;
210       ry = circshift ( rx , [1 k -1]);
211       a =0;
212       d =0;
213       for i =1: m ;
214           if rx ( i ) == ry ( i );
215               a = a +1;
216           else
217               d = d +1;
218           end
```

```
219        end
220        rxx(k)=(a-d)/m;
221    end
222    %y=0;
223    %n=0:0.1:2*m+1;
224
225
226    %plot(-m:m,rxx)
227    %hold on
228    %plot(n,y,'-k', 'linewidth',2)
229    %line([-m-1 m+1], [0 0], [1 1],'color', 'k')
230    %title('Autocorrelation of sequence')
231    %xlabel('Shift')
232    %ylabel('Autocorreleation Function')
233    %hold off
234    %axis([-m m min(rxx)-.02 1+.2])
235    p3=0;
236    if rxx(2:m)== -(1/m);
237        p3=1;
238    end
239    if p3==1;
240        %disp('The Code satisfies the Autocorrelation Property')
241    else
242        disp('# Warning: The Code does NOT satisfy the Autocorrelation Property')
243    end
```

a12_deconv.m

```
1     function [x,H,Y,X,window1]=a12_deconv(h,y,np,sc)
2
3    [ax,bx]=size(y);
4    if ax>bx
5        y=y.';         % check input
6    end
7
8    [ah,bh]=size(h);
9    if ah>bh
10       h=h.';          % check input
11    end
12
13
14   Y= fftshift(fft(y,np));
15   H= fftshift(fft(h,np));
16   X= (Y)./ (H);
17
18
19
20   window1=ones(1,np);
21
22
```

```matlab
23   % adaptive filter cutoff
24
25   if sc ~= 0
26
27   window1(abs(H)<sc*max(abs(H)))=0;
28   end
29
30       x=ifft(ifftshift(  X.*window1  ) );
```

a12_exporttotopspin_3shape.m

```matlab
 1   %% Export Function
 2   %
 3   % Input
 4   %   shape      :     rf field (vector of complex numbers)
 5   %   range      :     if vector of length 2 -> start and end of shape
 6   %   rf_wanted  :     rf-field in kHz, that plateau should correspond to
 7   %   rf_topspin :     rf_field specified by Powerlevel in Topspin (corresponding
 8   %                       to value of 100 in shape)
 9   %   fol        :     export folder
10   %   fname      :     file name for export (ending .shape will be attached
11   %                       automatically)
12   %   timestep   :     timestep for shape in seconds, eg. 50e-9 fpr 50ns
13   %   commentstr :     description to be put in the shape file
14   %   checkrange :     set to 1 to manually check selected ranges in vector
15   %                       before export
16
17   function  range=a12_exporttotopspin_3shape(shape,range,rf_wanted,rf_topspin,fol,fname,
         timestep,commentstr,checkrange)
18
19
20   if ismember(commentstr,['',' ',0])
21       commentstr=['compensation ' datestr(now)];
22   end
23   timestep=timestep/1e-9;
24
25   fname=fullfile(fol,fname);
26
27   % Convert to Amplitude / Phase Data
28   amp=abs(shape);
29   ph=(angle(shape)*180/pi);
30
31   ascale=100*rf_wanted/rf_topspin;
32
33   if max(amp*ascale) > 100
34       fprintf('# ATTENTION: VALUE (%.2f) IN SHAPE > 100 ! \n', max(amp*ascale));
35   else
36     if(range==2)                    % single shape export
37           fprintf(' ### Exporting full shape \n')
38       if ismember(checkrange,['y','Y',1])
```

```matlab
39              range=a2_ask_for_correct_range(range,amp);
40              range=[range(1) range(end)];
41        end
42        write_shape_file(fname, amp, ph, ascale, commentstr, range)
43
44
45      else
46              error(' ### Length of range must be 2 (single shape export)!\n')
47      end
48
49
50
51  end
52
53
54  %Output file also specified to TopSpin 3.5 and higher
55
56  function write_shape_file(fname, amp, ph, ascale, commentstr, range)
57  % Write Outputfile
58  fid=fopen( [fname '.shape'] ,'w');
59  fprintf(fid,'##TITLE= Externally Generated Shape \n');
60  fprintf(fid,'##JCAMP-DX= 5.00 Bruker JCAMP library\n');
61  fprintf(fid,'##DATA TYPE= Shape Data\n');
62  fprintf(fid,['##ORIGIN= ',commentstr, '\n']);
63  fprintf(fid,'##OWNER= <johe>\n');
64  fprintf(fid,['##DATE= ',datestr(today),' \n']);
65  fprintf(fid,'##TIME= 00:00:00\n');
66  fprintf(fid,['##$SHAPE_PARAMETERS= \n']);
67  fprintf(fid,'##MINX= 0.000000E00\n');
68  fprintf(fid,'##MAXX= 1.000000E02\n');
69  fprintf(fid,'##MINY= 0.000000E00\n');
70  fprintf(fid,'##MAXY= 3.600000E02\n');
71  fprintf(fid,'##$SHAPE_EXMODE= Excitation\n');
72  fprintf(fid,'##$SHAPE_TOTROT= 1.800000E02\n');
73  fprintf(fid,'##$SHAPE_TYPE= Inversion\n');
74  fprintf(fid,'##$SHAPE_USER_DEF= \n');
75  fprintf(fid,'##$SHAPE_REPHFAC= \n');
76  fprintf(fid,'##$SHAPE_BWFAC= 0.000000E00\n');
77  fprintf(fid,'##$SHAPE_BWFAC50= \n');
78  fprintf(fid,'##$SHAPE_INTEGFAC= 0.000000E00\n');
79  fprintf(fid,'##$SHAPE_MODE= 0\n');
80  fprintf(fid,['##NPOINTS= ',num2str(range(end)-range(1)+1),' \n']);
81  fprintf(fid,'##XYPOINTS= (XY..XY)\n');
82
83  %%%%%%%%%%%%%%%%%%%%%%%%%%%%%%%%%%%%%%%%%%%%%%%%%%%%%%%%%%%%%%%%%%%%%%%%%
84
85  for i=range(1): range(end)
86      fprintf (fid,'%E, %E\n',amp(i)*ascale,mod(ph(i),360));
87  %   fprintf (fid,'%E, %E\n',amp(i)*ascale, ph(i) );
88
89  end
```

```
90   fprintf ( fid , '##END = \n ') ;
91
92   fclose ( fid ) ;
```

a2_ask_for_correct_range.m

```matlab
1    function rr2 = a2_ask_for_correct_range ( rr2_in , h_blc )
2
3    figure (1)
4    plot (1: length ( h_blc ) ,[ real ( h_blc ); imag ( h_blc ) ])
5    hold on
6    plot ([ rr2_in (1)  rr2_in (1) ], 1.1*[ min ([ real ( h_blc ) , imag ( h_blc ) ])  max ([ real ( h_blc ) , imag (
         h_blc ) ]) ] , 'k - - ' )
7    plot ([ rr2_in ( end )  rr2_in ( end ) ], 1.1*[ min ([ real ( h_blc ) , imag ( h_blc ) ])  max ([ real ( h_blc ) ,
         imag ( h_blc ) ]) ] , 'k - - ' )
8    hold off
9
10
11   reply = input ([ ' ### Is the pre - selected region [ ' , num2str ( min ( rr2_in )) , ': ' , num2str ( max
         ( rr2_in )) , '] okay ? Y/N [Y]: '] , 's ') ;
12   if isempty ( reply )
13       reply = 'Y ';
14   end
15   rr2 = rr2_in ;
16
17   if  ismember ( reply ,[ 'Y ' , 'y ' , 'yes ' ])~=1
18     q =0;
19     while q ==0
20       x_s = input ( ' ### First point ? ') ;
21       x_e = input ( ' ### Last point ? ') ;
22       if isempty ( x_s )  ||  isempty ( x_e )
23           q =0;    % stay in loop
24       else
25           rr2 = floor ( x_s ): floor ( x_e ) ;
26           q =1;    % leave the loop
27       end
28
29     end
30
31   else
32       rr2 = rr2_in ;
33   end
34
35   if ( rr2 (1)  < 1 )
36
37       rr2 =1: rr2 ( end ) ;
38           fprintf ([ ' ### Lower limit exceeds size of shape . It was set to ' num2str ( rr2
               (1)) '! \n ' ])
39    end
40
```

```matlab
41  if (rr2(end) > length(h_blc))
42          rr2 =rr2(1) : length(h_blc);
43          fprintf([' ### Upper limit exceeds size of shape. It was set to ' num2str(rr2(
                end)) '! \n'])
44  end
45
46
47  figure(1)
48  plot(1:length(h_blc),[real(h_blc);imag(h_blc)])
49  hold on
50  plot([rr2(1) rr2(1)], 1.1*[min([real(h_blc),imag(h_blc)]) max([real(h_blc),imag(h_blc)
        )]],'k--' )
51  plot([rr2(end) rr2(end)], 1.1*[min([real(h_blc),imag(h_blc)]) max([real(h_blc),imag(
        h_blc)])],'k--' )
52  hold off
```

a2_gen_ashaped_pulse_flipangle.m

```matlab
1   function [target_shape, scale]= a2_gen_ashaped_pulse_flipangle(pulse_length,tstep,
        edge_time,ph)
2
3
4   ns=floor(pulse_length/tstep);
5   ns_edge=round(edge_time/tstep);
6
7   if edge_time ~=0
8
9   amplitude1=ones(1,ns);
10  phase1=ones(1,ns)*ph;
11  sinedge=sin(((-ns_edge/2+1):(ns_edge/2-1))/2/(ns_edge)*2*pi);
12
13  amplitude1(1:(ns_edge-1))=(sinedge+1)/2;
14  amplitude1(ns-ns_edge+2:ns)=(-sinedge(1:end)+1)/2;
15  %amplitude1(ns)=0;
16
17  else
18
19      amplitude1=ones(1,ns);
20      phase1=ones(1,ns)*ph;
21
22  end
23
24  scale=sum(amplitude1)/ns;
25  pulse=amplitude1.*exp(complex(0,phase1));
26
27
28  target_shape.wanted     = zeros(1,2^nextpow2(length(pulse)+10));
29  target_shape.wanted(10+(1:length(pulse)))     = pulse;
30  target_shape.np         = length(pulse);
31  target_shape.tau_p      = pulse_length;
```

```matlab
32   target_shape.tstep      = tstep;
33   target_shape.tau_edge   = edge_time;
```

a2_gen_PMLG_ramp_angle.m

```matlab
1    function [target_shape]= a2_gen_PMLG_ramp_angle(p_length,tstep,edge_time,psi,nu_eff)
2
3    np=floor(p_length/tstep);
4    ns_edge      = floor(edge_time/tstep);
5    total_a=zeros(1,2*np);
6    total_ph=zeros(1,2*np);
7
8    [~, a90 ,~]=gen_ampshaped_pulse1(np,ns_edge,0);
9
10   sc90 = np/sum(a90);
11
12   total_a(1:np)=sc90*a90;
13
14   nu_eff_app=total_a(1:np)*nu_eff;
15   nu_1=sin(psi)*nu_eff_app;
16   nu_off=sqrt(nu_eff_app.^2-nu_1.^2);
17   total_ph(1:np)=cumtrapz(tstep/2:tstep:p_length-tstep/2,nu_off(1:np)*2*pi);
18
19   total_a (np+(1:np))=sc90*a90;
20   total_ph(np+(1:np))=fliplr(cumtrapz((tstep/2:tstep:(p_length-tstep/2)),fliplr(nu_off(1:
         np))*2*pi))+pi;
21
22    %total_sym = (total_a.*exp(complex(0,mod(total_ph,360)/180*pi)));
23    total_sym = (total_a.*exp(1i*total_ph));
24   fprintf(['total pulse length= ' num2str(p_length*2/1e-6) ' mus, rf=' num2str(nu_eff*sin
         (psi)) ' kHz \n'])
25
26   target_shape.wanted     = total_sym;
27   target_shape.np         = length(total_sym)*3;
28   target_shape.tau_p      = p_length;
29   target_shape.tstep      = tstep;
30   target_shape.tau_edge   = edge_time;
31
32
33
34   function [pulse,amplitude1,phase1]= gen_ampshaped_pulse1(ns,ns_edge,ph)
35
36
37
38   if ns_edge ~=0
39
40   amplitude1=ones(1,ns);
41   phase1=ones(1,ns)*ph;
42   sinedge=sin(((-ns_edge/2+1):(ns_edge/2-1))/2/(ns_edge)*2*pi);
43
```

```matlab
44  amplitude1(1:(ns_edge-1))=(sinedge+1)/2;
45  amplitude1(ns-ns_edge+1:ns-1)=(-sinedge+1)/2;
46  amplitude1(ns)=0;
47
48  else
49
50      amplitude1=ones(1,ns);
51      phase1=ones(1,ns)*ph;
52
53  end
54
55  pulse=amplitude1.*exp(complex(0,phase1));
```

a2_perform_compensation.m

```matlab
1   function [comp]=a2_perform_compensation(mls,target_shape,cutoff)
2
3   scrf = mls.input.scrf;
4   h    = mls.h_blc;
5
6   comp.wanted = target_shape.wanted;
7   comp.h      = h;
8   comp.rr2    = mls.rr2;
9   comp.cutoff = cutoff;
10  comp.np     = target_shape.np;
11
12
13  comp.shape  =   a12_deconv( comp.h(comp.rr2),comp.wanted,length(comp.wanted),cutoff);
14
15  comp.shape  =   a2_shift_shape(comp.wanted,comp.shape);
16  comp.idx    =   find_shapestart(comp.shape);
17  comp.shape  =   comp.shape*scrf;
18  comp.shape  =   comp.shape./mean(abs(comp.shape(comp.idx+0.5*comp.np+(1:10))));
19  figure(2)
20  plot(1:length(comp.shape),[real(comp.shape );imag(comp.shape);real(comp.wanted)])
21
22
23
24  function [idx]=find_shapestart(shapedata)
25   a          = max(abs(shapedata));              % Maximum Amplitude of signal
26  idx         = find(shapedata>0.05*a,1,'first'); % find rising edge of reference pulse
```

a2_shift_shape.m

```matlab
1   %% Shift compensated shape such it overlays with target.
2   %
3   function comp_out=a2_shift_shape(target_in,comp_in)
4
```

```matlab
 5
 6  [c,lags] = xcorr(abs(target_in),abs(comp_in)); % c is the correlation, should have a
       clear peak
 7  s = lags(c==max(c)); % s is the shift we need
 8
 9
10  if isrow(comp_in)
11      comp_out = circshift(comp_in.',s).';
12  else
13      comp_out = circshift(comp_in,s);
14  end
```

E.2.2. Communication with the Spectrometer Computer

o1_copyshapes.m

```matlab
1  % copy shapefile to spectrometer
2
3  function o1_copyshapes(fname)
4
5  eval(['!cp ' fname ' ~/spcmount/' ])
```

o1_mountspectrometer.m

```matlab
 1  %% Mount spectrometer waveform folder on local machine
 2  %  Adjusted for NMR net at ETH
 3  %
 4  %  username : spectrometer operator, e.g. 'johe'
 5  %  machine  : computer name, e.g. 'oersted' or 'flory'
 6  %  path_to_topspin : path to topspin main folder, usually: /opt/topspin3.X
 7
 8  function o1_mountspectrometer(username,machine,path_to_topspin)
 9
10
11  if exist('/home/transient/spcmount','dir')
12          !fusermount -u /home/transient/spcmount
13      !yes | rm -r /home/transient/spcmount
14  end
15      mkdir /home/transient/spcmount
16
17  eval(['!sshfs ' username '@' machine '.ethz.ch:' path_to_topspin '/exp/stan/nmr/lists/
       wave/user /home/transient/spcmount/'])
```

o1_triggerscope.m

```matlab
1  function o1_triggerscope()
```

```matlab
2
3
4  % create serial port object
5  s=serial('/dev/ttyS0','DataBits',8);
6  % connect serial port
7  fopen(s);
8
9  % give out trigger signal
10 fwrite(s,1)
11
12 % close object and delete from memory
13 fclose(s);
14 delete(s);
15
16
17 % Accoustic feedback
18 Fs=8192;
19 y1= sin(0:1000).';
20 soundsc(y1,Fs);
```

o1_write_paramfile.m

```matlab
1  %% Write Prameterfile
2  %
3  % DISCLAIMER: this only works with Topspin Versions 3.5 and higher!!!
4  %
5  % Input:
6  %   fname       : filename, AU program looks for .param_cw, .param_mls,
7  %                   .param_uncomp, .param_comp
8  %   username    : name of topspin user, eg. 'jowi'
9  %   pulpro      : name of pulse program, eg. 'zg_1shape'
10 %   spnam       : name of pulse program, eg. 'comp.shape'
11 %   freq        : carrier frequency in Hz, eg. 75.12346e6
12 %   np          : number of points of shape, eg. 200
13 %   tstep       : timestep in seconds, eg. 50e-9
14 %   plw         : rf amplitude in Watt, eg. 50
15 %   ns          : number of scans for averaging of shape
16 %   d1          : recycle delay between scans in seconds
17 %   go_on       : continue (=1) or stop (=0) optimization
18 function o1_write_paramfile(fname,username,pulpro,spnam,freq,np,tstep,plw,ns,d1,go_on)
19
20 fid=fopen(['./shapes/' fname],'w');
21 fprintf(fid,'%d\n',go_on);
22 fprintf(fid,'%s\n',username);
23 fprintf(fid,'%s\n',pulpro);
24 fprintf(fid,'%s\n',spnam);
25 fprintf(fid,'%f\n',freq/1e6);
26 fprintf(fid,'%d\n',np);
27 fprintf(fid,'%f\n',tstep*1e6);
28 fprintf(fid,'%f\n',plw);
```

```
29  fprintf(fid,'%d\n',ns);
30  fprintf(fid,'%f\n',d1);
31
32  fclose(fid);
```

E.2.3. Data Recording with Tektronix Oscilloscope

tek_calcfreq.m

```
1   %% Determine optimal frequency for mixing down
2   %
3   % Input:
4   %   procdata    = output from tek_read, should be a digitized CW pulse
5   %   range       = cw range (no transients) for fit
6   %
7   % Output:
8   %   deltaf      = difference frequency
9   function deltaf=tek_calcfreq(procdata,range)
10
11
12  % linear fit of phase
13  a=polyfit(procdata.t(range),phase(procdata.y(range)),1);
14  % slope of phase is the difference frequency
15  deltaf=a(1)/2/pi/1e-6;           %1e-6 convertes from us to seconds (t is in us)
```

tek_combine.m

```
1   %% Combine raw and processed data
2   % Input
3   %   rawdata  = output from tek_read()
4   %   procdata = output from tek_proc()
5   %
6   % Output
7   %   data     = combination of both
8
9   function data=tek_combine(rawdata,procdata)
10
11  data.raw            = rawdata.single;
12  data.raw.t          = rawdata.t;
13
14  data.proc           = procdata.single;
15  data.proc.t         = procdata.t;
16
17  data.param          = rawdata.param;
18  data.param.tstep    = procdata.param.tstep;
19  data.param.phaserange = procdata.param.phaserange;
20
21  data.y              = procdata.y;
```

```matlab
22  data.t                = procdata.t;
23
24  if isfield(procdata,'input')
25      data.input.mls=procdata.input.mls_in;
26      data.input.scrf=procdata.input.scrf;
27      data.h=procdata.h;
28      data.h_blc=procdata.h_blc;
29  end
30  if isfield(procdata,'rr2')
31      data.rr2=procdata.rr2;
32
33  end
```

tek_proc_autophase.m

```matlab
1   %% Mixing down of recorded data
2   %
3   % Input:
4   %    rawdata      = output-struct of tek_read()
5   %    tstep        = time resolution for mixed-down data in seconds,
6   %                     eg. 50e-9 for 50ns
7   %    refpulse     = length of reference pulse in downsampled data, eg 200 points
8   %                     if refpulse is a vector it is the range where phase is
9   %                     set to zero
10  % Output:
11  %    procdata     = struct containing processed data
12  %        .param   = time resolution in s
13  %        .single.y(i) = processed data of single scans i
14  %        .y           = average over .single.y(i)
15  %        .t           = time axis
16
17  function procdata=tek_proc_autophase(rawdata,tstep,phaserange)
18  procdata.param.tstep=tstep;
19  tstep=tstep/1e-9;
20  y_proc=0;
21
22  for k=1:rawdata.param.ns
23
24      [y,t,phaserange1]=proc_rawdata(rawdata.single.(['y' num2str(k)]),...
25                                  rawdata.param.Fs,rawdata.param.freq,...
26                                  tstep,phaserange);
27      procdata.single.(['y' num2str(k)]) =   y;
28      y_proc=y_proc+y;
29
30  end
31  procdata.t=t;
32
33  procdata.y=y_proc/(rawdata.param.ns);
34  procdata.param.phaserange=phaserange1;
35  fprintf('### Processing finished! ###\n');
```

```matlab
36
37
38   % Process Measured Transients to a format, which can be used for plotting
39   % and further procesing.
40
41   % ns     : Number of measured transients (Averaging for better S/N), np=1:5
42   % Fs     : Sampling Rate. eg. sr=2.5e9 for 2.5 Gigasamples
43   % freq   : Carrier Frequency, e.g. freq= 75.2394e6
44   % tstp   : Time-Step of output shape in NANO-seconds! eg tstp = 50 for 50 ns
45   % phaserange: range of first pulse to determine correct phase
46
47
48   function [shape_trans,t_trans,phaserange]=proc_rawdata(tmp,Fs,freq,tstp,phaserange)
49
50
51
52
53   x=length(tmp);
54   [s]=max(abs(tmp));
55
56     t=(0:(x-1))/Fs;                        % generate time-base
57
58
59
60
61   % chek if final output time step makes sense
62   [~,posi] = min( abs(t-tstp*1e-9) );
63   if (rem(x,posi-1)~=0)
64       error('Error: Timestep nor comensurate with number of Points');
65   end
66
67
68
69   refr = s*cos((2*pi*freq*t));
70   refi = s*sin((2*pi*freq*t));
71
72
73   %% Generate lowpass filter
74
75   % Filter Design such that pass band ends at 80% of the carrier frequency
76   % and stop band is at 120% of the carrier frequency
77
78   fpass=2*0.8* freq/ Fs;
79   fstop=2*1.2* freq/ Fs;
80
81   % pass-band variation in dB
82   Ppass=0.001;
83   % stop-band attenuation in dB
84   Pstop=50;
85
86   % lowpass filter desing
```

```matlab
 87  Hf=fdesign.lowpass('Fp,Fst,Ap,Ast',fpass,fstop,Ppass,Pstop);
 88  Heq=design(Hf,'butter');
 89
 90
 91      % Baseline-Correction;
 92      tmp=tmp-(sum(tmp)/x);
 93
 94      % Multiply with carrier and form complex signal
 95      tmp=squeeze((refr.*tmp)+1i*(refi.*tmp));
 96
 97      % Apply the filter forward and backward for zero-phase filtering
 98      tmp=filter(Heq,tmp);
 99      tmp=flipdim(filter(Heq,flipdim(tmp,2)),2);
100      tmp=mean(reshape(tmp,posi-1,x/(posi-1)));  % Get shape with desired timestep
101
102      % Phase the signals to the same reference phase
103      if numel(phaserange)==1
104          %idx_k=phaserange;
105          refp=zeros(size(tmp));
106          refp(100+(1:phaserange))=1;
107          [corr1,corrax]=xcorr(refp,tmp);
108          phaserange=100-corrax(corr1==max(corr1))+(floor(0.25*phaserange):floor(0.75*
                 phaserange));
109      end
110      p=mean(phase(tmp(  phaserange  ) ));
111      tmp=tmp*exp(-1i*p);
112      tmp=tmp./mean(abs(tmp( phaserange )));
113
114
115
116
117  t_trans=t(1:posi-1:x)*1e6;
118  shape_trans=tmp;
```

tek_read_trigg.m

```matlab
 1  %% Establish VXI connection to scope, read data from Channel1 and process it
 2  %
 3  % Input:
 4  %    deltaT  = acquistion length of scope in seconds, eg. 20e-6 for 20us
 5  %    Fs      = sample rate of scope in Samples/s, eg. 5e9 for 5Gs/s
 6  %    scCH1   = scaling of Channel 1 in Volts/div, eg. 0.1
 7  %    ns      = number of transients, eg. 5 for 5 transients
 8  %
 9  % Output:
10  %    data    = struct containing important parameters and rawdata
11  %      .param : channel impedance, trigger position, record length, sampling
12  %               frequency and number of scans
13  %      .single: .y(i) = rawdata of single scans i
14  %      .t           = corresponding time axis
```

```matlab
15
16  function data=tek_read_trigg(ip,deltaT,Fs,scCH1,ns,freq)
17
18  twait=1.5;                % seconds delay between two measurements (should be bigger than
        D1)
19  timeout=30;          % timeout in seconds
20
21  [deviceObj,interfaceObj]=tek_connect(ip);
22
23
24  data.param       = tek_setpara(deviceObj,interfaceObj,deltaT,Fs,scCH1);
25  data.param.freq = freq;
26  data.param.ns    = ns;
27  data.param.time = datestr(now);
28  data.param.ip    = ip;
29
30  % empty record to warm up scope
31  set(deviceObj.Acquisition(1), 'State', 'run');
32
33
34  for k=1:ns
35  [data.single.(['y' num2str(k)]),t]=...
36      tek_record(deviceObj,interfaceObj,twait,timeout);
37  end
38  data.t=t;
39
40
41  disconnect(deviceObj);
42  delete([deviceObj interfaceObj]);
43
44  fprintf('### All data Recorded! ###\n');
45  clear rawdata proc param Fs tstep  y t ns freq deltaT k phaserange
46
47  %% Connect to Scope
48  % Input
49  % ip = ipaddress of scope, eg. '169.254.221.43'
50
51  function [deviceObj,interfaceObj]=tek_connect(ip)
52
53  % one might need to change this if different visa interface is used!
54  interfaceObj = instrfind('Type', 'visa-tcpip', 'RsrcName',  ['TCPIP0::',num2str(ip),'::
        inst0::INSTR'], 'Tag', '');
55
56  % Create the VISA-TCPIP object if it does not exist
57  % otherwise use the object that was found.
58  if isempty(interfaceObj)
59      interfaceObj = visa('NI', ['TCPIP0::',num2str(ip),'::inst0::INSTR']);
60  else
61      fclose(interfaceObj);
62      interfaceObj = interfaceObj(1);
63  end
```

```matlab
64
65   % Create a device object.
66   deviceObj = icdevice('tektronix_tds7104_johe.mdd', interfaceObj);
67
68   % Disconnect device object from hardware.
69   disconnect(deviceObj);
70
71
72   interfaceObj = get(deviceObj, 'interface');
73
74   % Allow for a 10,000 point waveform with a little extra room.
75
76   set(interfaceObj, 'InputBufferSize', 20000000);
77
78   connect(deviceObj);
79
80
81   if strcmp( deviceObj.Status, 'open') == 1
82       fprintf('### Connection Established Successfully! ###\n')
83   end
84
85
86
87   %% Set Parameters on scope
88   % deltaT = time in sec which we want to acquire
89   % Fs     = sampling rate in Samples/s
90   % scCH1  = volts per div for channel 1 scaling
91   % set Impedance to 50 Ohm on every Channel
92
93   function para=tek_setpara(deviceObj,interfaceObj,deltaT,Fs,scCH1)
94
95
96   recL=deltaT*Fs;
97
98   set(deviceObj.Channel(1), 'Impedance', 'fifty');
99   set(deviceObj.Channel(4), 'Impedance', 'fifty');
100
101  set(deviceObj.Acquisition(1), 'Control', 'single');
102  set(deviceObj.Acquisition(1), 'Mode', 'sample');
103
104  set(deviceObj.Trigger(1), 'Mode', 'normal');
105  set(deviceObj.Trigger(1), 'Source', 'channel4');
106  set(deviceObj.Trigger(1), 'TriggerType', 'edge');
107  set(deviceObj.Trigger(1), 'Level', 0.5);
108
109  set(deviceObj.Horizontal,'Position',1);
110  set(deviceObj.Horizontal,'TriggerPos',0);
111  set(deviceObj.Horizontal,'RecordLength',recL);
112  set(deviceObj.Horizontal,'SamplingRate',Fs);
113
114  set(deviceObj.Channel(1),'scale',scCH1)
```

```matlab
115
116  set(deviceObj.Waveform(1), 'FirstPoint', 1);
117  set(deviceObj.Waveform(1), 'EndingPoint', recL);
118
119
120
121  para.impedance=get(deviceObj.Channel(1), 'Impedance');
122  para.position=get(deviceObj.Horizontal,'Position');
123  para.recordlength=get(deviceObj.Horizontal,'RecordLength');
124  para.Fs=get(deviceObj.Horizontal,'SamplingRate');
125
126  fprintf('### Parameters set! Check output for validity! ###\n');
127
128
129
130  function [y,t]=tek_record(deviceObj,interfaceObj,twait,timeout)
131
132
133  set(deviceObj.Acquisition(1), 'State', 'run');
134  pause(twait/2)
135
136  % trigger scope via audio output
137  o1_triggerscope
138
139  fprintf('### Trigger Pulse Sent... ###\n')
140  fprintf('### Waiting for Pulse from Spectrometer... ###\n')
141  pause(twait/2)
142      if strcmp(get(deviceObj.Trigger(1),'State'),'ready')==1
143          pause(twait/2)
144      end
145
146
147  groupObj = get(deviceObj, 'Waveform');
148  groupObj = groupObj(1);
149
150   [y,t] = invoke(groupObj, 'readwaveform', 'channel1');
151  pause(1);
152   fprintf('### Data Recorded! ###\n')
```

E.3. AU Program for TopSpin

This AU program needs to be run in TopSpin to establish the communication with the compensation computer. The pulse program `zg1_shape` is started automatically and executed with the generated shape files.

```
/****************************************************************
/* Short Description : impulse_response
/* AU program that communicates with MATLAB to determine
/* impulse response function via MLS
/****************************************************************
/* Keywords : Transient Compensation
/*
/****************************************************************
/* Description/Usage: See Description with MATLAB Script
/*
/****************************************************************
/* Author(s)   :
/* Name : Johannes Wittmann,
   mod by: Johannes Hellwagner
/* Organisation : ETH Zurich
/* Email : johe@nmr.phys.chem.ethz.ch
/****************************************************************
/* Name Date Modification:
/* johe  14.06.2017 Third Version
/****************************************************************
/*
$Id: zg_dfs,v 1.7.8.1 2012/01/19 16:39:31 wem Exp $
*/

AUERR = autocomp(curdat);
QUIT

#include <ShapeIO/ShapeIOC.h>
```

```c
#include <stdio.h>


int read_and_set_param(char fname_in,
char myexpname[40], int myexpno, const char* curdat)
{
  char    myspnam[40], mypulpro[40], myusername[10], outputfile[PATH_MAX];
  FILE *file;
  int     np, ns, startstop;
  double      freq, tstep, plw, d1, tau;
  double      plw_sat, plw_max, tau_max;

  plw_sat = 5.0;  // Powerlevel (W) for Saturation pulses
  plw_max = 100;  // max allowed Powerlevel (W)
  tau_max = 5000;  // max allowed pulse length

// Open File for reading
 if (getParfileDirForWrite(".param", SHAPE_DIRS, outputfile) < 0)
  {
    Proc_err(DEF_ERR_OPT, "%s: %s", "parameterfile", outputfile);
    return -1;
  }

  file = fopen(outputfile,"r");
fscanf(file,"%d\n" ,&startstop); // 0: stop 1: go to next experiment
fscanf(file,"%s\n" ,&myusername); // Current User
fscanf(file,"%s\n" ,&mypulpro); // Pulseprogram
fscanf(file,"%s\n" ,&myspnam); // Shape Name
fscanf(file,"%lf\n",&freq); // Spectrometer Frequency in MHz
fscanf(file,"%d\n" ,&np); // nr of points of pulse
fscanf(file,"%lf\n",&tstep); // and corresponding timestep in us
fscanf(file,"%lf\n",&plw); // amplitude in Watt
fscanf(file,"%d\n" ,&ns); // number of scans for averaging
fscanf(file,"%lf\n",&d1); // Recycle Delay in sec
```

```
    close(file);


// Check for meaningful and non-destructive Values
if ( plw > plw_max )
   ERRORABORT

tau = (double)(np*tstep);
   if ( tau > tau_max )
   ERRORABORT

 // Set Parameters for Experiment
  DATASET(myexpname,myexpno,1,disk,myusername)
  STOREPAR("PULPROG",mypulpro)
  STOREPAR("SFO1",freq)
  STOREPAR("P 21",tau)
  STOREPAR("PLW 21",plw)
  //STOREPAR("SPW 2",plw)    // if no fast shape
  STOREPAR("SPNAM 2",myspnam)
  STOREPAR("SPOFFS 2",0.0)
  STOREPAR("P 1",500.0) // 5 ms saturation before
  STOREPAR("L 10",10)
  STOREPAR("PLW 1",plw_sat)
  STOREPAR("NS",ns)
  STOREPAR("D 1",d1)
  STOREPAR("RG",1)
  STOREPAR("TD",128)
  STOREPAR("DW",10.0)


   return startstop;
}

int autocomp(const char* curdat)
{
```

```
char  myexpname[20], myusername[10], buf[20];
FILE *file;
int     np, ns, startstop;
double        freq, tstep, plw, d1, tau;
double        plw_sat, plw_max, tau_max;

strcpy(myexpname,"autocomp");   // Define EXPN Name
plw_sat = 5.0;  // Powerlevel (W) for Saturation pulses
plw_max = 100;  // max allowed Powerlevel (W)
tau_max = 5000;  // max allowed pulse length
startstop = 1;

SETCURDATA;

//#########################
// Pulsing
//#########################

while (startstop > 0) {
startstop = read_and_set_param(".param",myexpname, 1,curdat);
ZG;
  ssleep(0.5);
}


  ERRORABORT

  return 0;


}
```

Acknowledgement

in the world. **Gabriele Roder** for taking care of all bureaucracy related issues and all the help that never came without a small story, comment, or joke. **Alexander Däpp** for building, fixing, and modifying every small electrical piece that was brought to him. **Andreas 'Andideep' Hunkeler** for making everything imaginable out of materials that I sometimes have not heard of but always having the right solution to the posed problems. **Manuel Ochsner** for the synthesis of countless glycine derivates. **Daniel Zindel** for synthesis, chemistry, and life help and just being a very pleasant occasional hiding place from the problems in the lab. And the numerous coffees and beers that were drank together throughout this journey.

If you are forgotten in this not complete list of people, be assured that you live on in my memory.

To **my family**, who has stood by my side since I left Klagenfurt for Zürich at the young age of 20 and has supported me unconditionally to this day.

And finally, to **Nellie** for sticking with me, being there, supporting me, motivating me, and reminding me that after all my PhD has been a great experience.

Curriculum Vitae

Name:	Johannes Hellwagner
Date of birth:	July 26, 1991
Place of birth:	Linz (Republic of Austria)
Nationality:	Austria

Education

2015 – present	**PhD studies** at ETH Zürich (Zürich, Switzerland) *The Design of Experimentally Robust Pulse Sequences in Solid-State NMR* supervisor: Prof. Dr. Matthias Ernst
2015	**MSc Chemistry** at UC Berkeley (Berkeley, California, USA) **MSc thesis:** *Accurate Delay Control and Characterization of Single Attosecond Pulses* supervisor: Prof. Dr. Stephen R. Leone
2014 – 2015	**MSc Chemistry** at ETH Zürich (Zürich, Switzerland)
2011 – 2014	**BSc Chemistry** at ETH Zürich (Zürich, Switzerland)
2002 – 2010	**Matura** at BG/BRG Mössingerstrasse (Klagenfurt, Kärnten, Austria)
09/2007 – 12/2007	**Exchange Semester** at St. Francis College (Cork, Ireland)

Work Experience

09/2015 – present   **ETH Zürich, Laboratory for Physical Chemistry**
PhD Researcher

09/2015 – present   **ETH Zürich, Laboratory of Physical Chemistry**
Teaching assistant

02/2015 – 06/2015   **UC Berkeley, Laboratory for Attosecond Physics**
Researcher

Conference Contributions

Apr 2018   59$^{\text{th}}$ ENC 2018, Orlando, Florida, USA
Poster: *The Influence of Pulse Transients on Pulse Sequences in Solid-State NMR*
Student Travel Stipend Recipient

Sep 2017   The 10$^{\text{th}}$ Alpine Conference on solid-state NMR, 2017, Chamonix, France
Presentation: *Understanding and Counteracting Pulse Transients in Solid-State NMR*

Jul 2016   EUROMAR 2016, Aarhus, Denmark
Poster: *Optimizing radio-frequency driven recoupling (RFDR) using transient compensation*

Languages

German   Native language

English   Fluent

French   Intermediate

Publications

[1] M.G. Jain, K.R. Mote, **J. Hellwagner**, ... , P.K. Madhu, V. Agarwal, *J. Chem. Phys.*, **2019**, *150*, 134201

[2] **J. Hellwagner**, ... , M. Ernst, *J. Magn. Reson.*, **2018**, *287*, 65-73

[3] **J. Hellwagner**, ... , P.K. Madhu, M. Ernst, *J. Chem. Phys.*, **2017**, *146*, 244202

[4] L.A. Straasø, R. Shankar, K.O. Tan, **J. Hellwagner**, ... , A.B. Nielsen, *J. Chem. Phys.*, **2016**, *145*, 034201

[5] J.J. Wittmann, V. Agarwal, **J. Hellwagner**, ... , M. Ernst, *J. Biomol. NMR*, **2016**, *66* (4), 233-242

[6] H. Timmers, M. Sabbar, **J. Hellwagner**, ... , S. Leone, *Optica*, **2016**, *3* (7), 707-710

[7] R. Rajeev, **J. Hellwagner**, ... , H.J. Wörner, *Light: Science & Applications*, **2016**, *5*, e16170